A STUDY OF HADRON ENERGY ESTIMATION IN ICAL@INO AND FEASIBILITY OF A PET DEVICE BASED ON MULTI-GAP RPCs

By

Mohammad Nizam

PHYS01201404006

BHABHA ATOMIC RESEARCH CENTRE, MUMBAI

A thesis submitted to the
Board of Studies in Physical Sciences
In partial fulfillment of requirements
For the Degree of

DOCTOR OF PHILOSOPHY

of

HOMI BHABHA NATIONAL INSTITUTE

November, 2019

Homi Bhabha National Institute

Recommendations of the Viva Voce Board

As members of the Viva Voce Board, we certify that we have read the dissertation prepared by Mohammad Nizam entitled "A STUDY OF HADRON ENERGY ESTIMATION IN ICAL@INO AND FEASIBILTY OF A PET DEVICE BASED ON MULTI-GAP RPCs" and recommend that it maybe accepted as fulfilling the dissertation requirement for the Degree of Doctor of Philosophy.

Chair -	Dr. B. K. Nayak	Date: 10-07-2020
Guide/Convener -	Prof. S. Uma Sankar	Date: 10-07-2020
Member 1 -	Dr. B. Satyanarayana	Date: 10-07-2020
Member 2 -	Prof. Raj Gandhi	Date: 10-07-2020
Member 3 -	Prof. Amol Dighe	Date: 10-07-2020
Member 4 (External examiner) -	Prof. Pradeep Sarin	Date: 10-07-2020

Final approval and acceptance of this dissertation is contingent upon the candidate's submission of the final copies of the dissertation to HBNI.

I hereby certify that I have read this dissertation prepared under my direction and recommend that it may be accepted as fulfilling the dissertation requirement.

Date:

Place: 10-07-2020
Mumbai

Guide
Prof. S. Uma Sankar

STATEMENT BY AUTHOR

This dissertation has been submitted in partial fulfillment of requirements for an advanced degree at Homi Bhabha National Institute (HBNI) and is deposited in the Library to be made available to borrowers under rules of the HBNI.

Brief quotations from this dissertation are allowable without special permisiion, provided that accurate acknowledgement of source is made. Requests for permisiion for extended quotation from or reproduction of this manuscriptin whole or in part may be granted by the Competent Authority of HBNI when in his or her judgement the proposed use of the material is in the interests of scholarship. In all other instances, however, permission must be obtained from the author.

Date: November 18, 2019

Place: Mumbai **Mohammad Nizam**

Enrolment Number : PHYS01201404006

DECLARATION

I, hereby declare that the investigation presented in the thesis has been carried out by me. The work is original and has not been submitted earlier as a whole or in part for a degree / diploma at this or any other Institution / University.

Date: November 18, 2019

Place: Mumbai

Mohammad Nizam

Enrolment Number : PHYS01201404006

Dedicated
to
my family

ACKNOWLEDGEMENTS

Foremost, I would like to express my immense gratitude to my Ph.D supervisor Prof. S. Uma Sankar for the continuous support of my Ph.D study and research, for his patience, motivation, enthusiasm, and immense knowledge. His expertise in the field of particle physics and the excellent teaching methods greatly helped me in further improving my analytical and theoretical skills. His guidance helped me during all phases of my Ph.D and writing of this thesis. I could not have imagined having a better advisor and mentor for my Ph.D study.

I am sincerely grateful to my co–supervisor Dr. B. Satyanarayana for the indispensable guidance and inspiration in the detector and instrumentation technology. His excellent grasp over the particle physics instrumentation helped me in troubleshooting the problems and challenges faced during my experiments in the INO RPC lab. He has always been a constant pillar of support from the very begining of my Ph.D studies.

I am truely grateful to Prof. Gobinda Majumder for helping and guiding me at various stages of MRPC work. I thank Dr. Moon Moon Devi for her crucial help during the early stages of MRPC work and many discussions on MRPCs. I thank Dr. Ali Ajmi for helping me at the begining of Hadron work. I thank Suman Bharti, Suprabh Prakash and Ushak Rahaman for helping me in GLoBES software based calculations. I thank Dr. Tarak Thakore and Dr. Kolahal Bhattacharya for various discussions on Nuance and χ^2 calculations. I thank Mr. R. R. Shinde for his continuous support and technical help throughout the MRPC work. I thank Mr. S. Joshi, Mr. Mandar Saraf, Dr. V. B. Chandratre and Ms. Meneka Sukhwani for helping me in refurbishing the Anusparsh and NINO boards for the MRPC setup. I thank Mr. Yuvraj E and Mr. Pathaleshwar for helping me integrating the RPC DAQ into the MRPC setup.

I thank my doctoral committee members, Dr. B. K. Nayak, Prof. Raj Gandhi and Prof. Amol Dighe for their important feedbacks, valuable suggestions and encouragement. I express my sincere gratitute to Prof. V. M. Datar, the project director of INO for his constant support and encouragement. I thank Prof. Md. Naimuddin, Prof. Sajjad Athar, Prof. Sandhya Choubey, Dr. Lalit Pant, Prof. Sudeshna Bannerjee, Prof. Acharya, Prof. Naba Mondal, Prof. V. Nanal, Prof. S. Goswami and all the co-members of the INO Collaboration. I thank Mr. P. Nagaraj and Mr. Pavan Vengala for making the computing facilities available without fail. I express my gratitude to the present and past colleagues at TIFR, Mr. S. Kalmani, Mr. P. Verma, Mr. V. Asgolkar, Mr. S. Chavan and Mr. G. Ghodke who have helped in making the mounting plateform of MRPCs and ensuring the proper operation of the RPC gas system.

I would like to thank the INO collaboration and the INO Graduate Training Program, which gave me an excellent opportunity to carry out my doctoral studies. I also thank TIFR for providing me with all the experimental facilities at the INO RPC lab to perform the experiments. I thank the Department of Atomic Energy (DAE) and the Department of Science and Technology (DST), Government of India and HBNI, for financial supports.

I thank my fellow INO students, Abhijit, Neha, Apoorva, Suryanarayana, Pethuraj, Jaydeep, Dhruv, Jim, Vishal, Hariom, Mamata, Honey, Suraj, Sadashiv and Jones for their support and care. I also thank Rajibul, Sazedur, Ashif and Zoheb for their excellent company. I would also like to thank my teachers, relatives and old friends, who supported and encouraged me during my research endeavor.

Last but not the least, I am extremely grateful to my parents, my wife, my brothers and sisters for having faith in me, supporting me during my struggle and for their unmatched love and sacrifices for me.

List of publications arising from this thesis

Journal Publications

(1) Tensions between the appearance data of T2K and NOvA

(**Mohammad Nizam**, Suman Bharti, Suprabh Prakash, Ushak Rahman and S. Uma Sankar.)

(Modern Physics Letters A 0 0:0 (2019), 2050021.)

(2) Feasibility study for Time Of Flight PET imaging based on six gap glass MRPC

(**Mohammad Nizam**, B. Satyanarayana, R. R. Shinde and G. Majumder

(Journal of Instrumentation 2019 JINST 14 C09010.)

(3) Hadron energy estimation from Atmospheric neutrino events.

(**Mohammad Nizam** and S. Uma Sankar)

(arXiv:1907.04313, accepted in Pramana Journal of Physics (PRAM-D-19-01013))

Conference Proceedings

(1) Feasibility study for development of a PET device based on Multi-gap Resistive Plate Chambers.

(**Mohammad Nizam**, B. Satyanarayana, R. R. Shinde and G. Majumder

(Proceedings of science ICHEP2018 (2019) 884.)

(2) Feasibility study for development of a PET device based on Multi-gap Resistive Plate Chambers.

(**Mohammad Nizam**, B. Satyanarayana and R. R. Shinde

(Springer Proc. Phys. 203 (2018) 567-569)

Date: November 18, 2019

Place: Mumbai **Mohammad Nizam**

ABSTRACT

Neutrino oscillations provide us with the first glimpse of physics beyond the standard model. Neutrino oscillations parameters have been measured with precision except the sign of Δ_{31}, the octant of θ_{23} and the CP violating phase δ_{cp}. The currently running long baseline experiments NOνA and T2K are expected to measure these unknown parameters. The proposed Iron Calorimeter (ICAL) at INO will study the charged current interactions of the muon neutrinos produced in the atmosphere. It has the ability to determine the atmospheric neutrino mass-squared difference Δm^2_{31} and the corresponding mixing angle $\sin^2\theta_{23}$ with good precision, by reconstructing the momentum and the direction of the muon track accurately. Its charge discrimination capability enables it to determine the sign of Δm^2_{31}. In this thesis, we discussed the discovery of neutrino, its flavors and determination of its mass in experiments. We also presented a detailed discussion on the physics of neutrino oscillations in vacuum and matter for both two flavor and three flavor framework. Atmospheric neutrino experiments IMB, Kamiokande, Superkamiokande and Hyper Kamiokande are also discussed in detail. A systematic study to calibrate the energy of hadrons produced in the atmospheric neutrino interaction in ICAL is presented. Hadron energy resolution functions are obtained and a comparison study is done between the data from two monte carlo event generators NUANCE and GENIE. It is also shown that there is a tension between the appearance data of T2K and NOνA. We noted that the two experiments agree on the best fit values of hierarchy and $\sin^2\theta_{23}$ but strongly disagree on the best fit values of δ_{cp}. We carried out a feasibility study of a PET device based on Multi-gap Resistive Plate Chambers (MRPCs). Several six gap MRPCs have been developed and tested over a long period of time. We did a TOF-PET experiment and measured time of flight of 511 keV gammas between two MRPCs. We also measured the time resolution of our detectors at different high voltages for cosmic muons as well as for 511 keV gammas.

SYNOPSIS

1 Introduction

I study the following three problems in this thesis.

- Hadron energy estimation from Atmospheric neutrino events in ICAL.
- Tension between the data of long baseline neutrino experiments.
- Feasibility study of MRPC based PET device.

1.1 ICAL detector

The Iron calorimeter (ICAL) at the India-based neutrino observatory (INO) is a giant magnetized neutrino detector. Its primary goal is to study the interactions of the atmospheric muon neutrinos and anti-neutrinos. It aims to determine neutrino mass hierarchy and also add to the precision of neutrino oscillation parameters [1]. ICAL has a mass of 50 ktons and it consists of three modules, each of which has dimensions 16 m $\times$ 16 m $\times$ 14.4 m. Each module contains 151 layers of 5.6 cm thick iron plates interspersed with resistive plate chambers (RPCs). The iron plates act as targets to atmospheric neutrinos. The charged current (CC) interactions of ν_μ and $\bar{\nu}_\mu$ produce muons. Because of the 1.3 T magnetic field in the iron plates, ICAL can determine the charge of the muon and distinguish between the interactions of ν_μ and $\bar{\nu}_\mu$. There are approximately 30,000 RPCs in the detector. Each RPC has a surface area of 1.84 m $\times$ 1.84 m and carries a potential difference of 10 kV across its electrodes. Copper strips, of width 1.96 cm, are laid in parallel on the top (bottom) surface of the RPC in X (Y) direction. The vertical direction is taken to be the Z-direction. A charge particle, passing through the RPC, creates an avalanche. The signal due to this avalanche is read by the X and

Y copper strips. These readings, together with the RPC layer number, give (X,Y,Z) coordinates of a "hit".

2 Hadron energy estimation from Atmospheric neutrino events

The design of ICAL enables it to reconstruct the track of a muon with good accuracy. At first, the physics capabilities of ICAL were studied using the kinematical information of only the muons [2, 3, 4]. The charged hadrons, produced in the atmospheric neutrino interactions, will also produce hits in the RPCs of the ICAL. Most of the time, the hits due to the hadrons can not be reconstructed into tracks because (a) the energy of a typical hadron is much smaller than the energy of the muon and (b) the hadrons can be absorbed by the detector nuclei. Thus, the inclusion of the hadron energy in the kinematic reconstruction of an event poses a great challenge. Various efforts were made to estimate the hadron energy in ICAL [5, 6]. However, in these efforts, a charged pion of known energy and direction is injected into Geant4 simulator and the corresponding hit pattern was studied. Through these simulations, a correlation between the pion energy and the number of hits was established and the resolution in pion energy was estimated. *It was assumed that these correlations and the resolutions will hold for all hadrons produced in atmospheric neutrino interactions*.

In this work, we did a systematic study of particle production in atmospheric neutrino events. We found that a significant number of baryons are produced in a large fraction of these events. For hadron energy less than 5 GeV, these baryons carry almost all the hadron energy. Therefore, we believe that the hit pattern produced by an isolated, single charged pion does not represent the hit pattern produced by the hadrons in an atmospheric neutrino event properly. We establish a correlation between the hits produced by the baryons and the baryon energy in atmospheric neutrino events. We then obtain a relation between the number of hits produced by all the hadrons in

an atmospheric neutrino event and the hadron energy. We generated 100 years of unoscillated atmospheric neutrino events through the NUANCE event generator [7]. We did a full Geant4 simulation of all the ν_μ-CC and $\bar{\nu}_\mu$-CC events. We selected those events for which the muon track is reconstructed. For these events, we isolated the hits produced by the hadrons by eliminating the muon track hits from the total number of hits. We used this hadron hit bank information to estimate the hadron energy and the energy resolution. In our analysis, we avoid the problem of "ghost hits" [5] by taking the number of hits in an RPC to be the maximum of (number of X strips with a signal, number of Y strips with a signal).

2.1 Baryons in atmospheric neutrino events

in this section, we study the correlation between the energy carried by the baryons and the hits produced by them in ICAL. After obtaining E_{baryon} and baryon_hits for each event, we define a set of ranges of baryon_hits. For each range we plot the histogram of frequency versus E_{baryon} and fit it with Vavilov distribution [8]. From the fits done for an optimal set of ranges, we determined the average energy of the baryons $E_{baryon-mean}$ and the associated resolution σ_{Eb} for each range. The relation between baryon_hits and $E_{\text{baryon}-\text{mean}}$

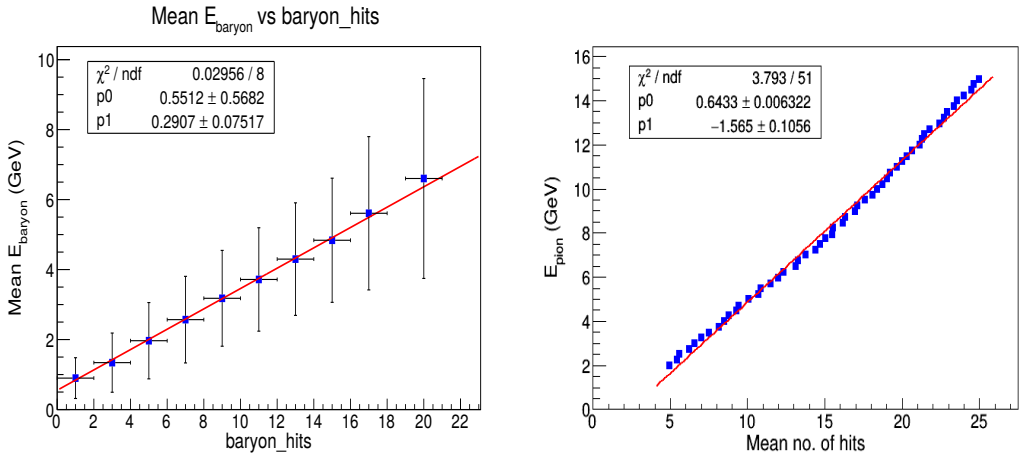

FIGURE 1

is shown in the left panel of figure 1. We compare this relation with the relation obtained from the simulation of isolated pions shown in the right

panel of figure 1. This latter simulation was done in reference [6]. Even though there is a linear relation between the no. of hits and the hadron energy for both baryons and pions, as shown in the two plots in figure 1, the slope of the pion fit is close to the slope of the baryon fit but the intercepts in the two cases are very different. Therefore, we argue that a proper estimation of hadron energy in atmospheric neutrino events requires doing a full Geant4 simulation of these events and establishing a relation between the number of hits produced by the hadrons and the hadron energy.

2.2 Hadron hit bank analysis

In this section, we analyse the hits generated by the hadrons produced in the ν_μ CC events of atmospheric neutrinos. We establish a correlation between these hadron hits and the energy of the hadrons. We also calculate the energy resolution for each given hadron energy. We plotted hadron hits versus $E_{\text{had}-\text{mean}}$ in the left panel of figure 2. We also plotted σ^2_{Eh} versus $E_{\text{had}-\text{mean}}$ in the right panel of figure 2. This energy resolution is parametrized as $\sigma(E)/E = \sqrt{a^2/E + b^2}$ [9].

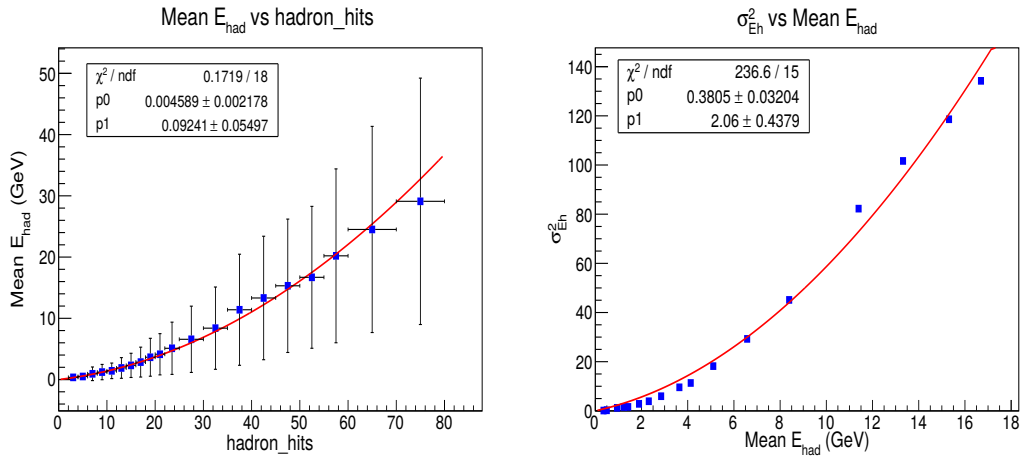

FIGURE 2

We believe that $E_{\text{had}-\text{mean}}$ and σ_{Eh} obtained in this study form the correct representation of hadron energy and its resolution in atmospheric neutrino events. In a previous work, the authors of ref.[9] also have done a similar

study. There are a number of differences in their procedure and in the procedure used in this work. Their data set consists of 1000 years of atmospheric neutrino events, whereas our set consists of 100 years of data. They obtained hadron hit bank information by doing the Geant4 simulation of an event with the muon turned off at the input level. In our case, we did the full Geant4 simulation of all the charged particles in the event and subtracted the hits which went into the track reconstrcution. This is the procedure which will be utilized in the case of actual data. The avalanche produced in an RPC by one charged particle can, quite often, produce hits in two adjacent strips. Thus, the number of hadron hits in an RPC is likely to be larger than the number of charged particles passing through it. This feature is built into Geant4 through the option *multiplicity*. The authors of ref.[9] kept this option *off* and hence obtained a smaller number of hits for a given hadron energy. In our case, we kept the multiplicity option *on* and obtained about 30 to 40% larger numbner of hits for the same hadron energy. This is a more realistic simulation of the detector.

3 Tension between the data of long baseline neutrino experiments

T2K: T2K is a long baseline neutrino oscillation experiment with the ν_μ beam from the J-PARC accelerator in Tokai to the Super-Kamiokande detector 295 km away. The accelerator is oriented in such a way that the detector is at 2.5° off-axis location. Super-Kamiokande is a 22.5 kton fiducial mass water Cerenkov detector, capable of good discrimination between electron and muon neutrino interaction [10]. The neutrino flux peaks sharply at 0.7 GeV which is also the energy of the first oscillation maximum. T2K experiment started taking data in 2009 and ran in neutrino mode with 14.7×10^{20} protons on target (POT) and 7.6×10^{20} POT in anti-neutrino mode [11, 12].

NOνA: NOνA [13] is an another long baseline neutrino oscillation experiment capable of measuring the survival probability $P_{\mu\mu}$ and the oscillation

probability $P_{\mu e}$. The NuMI beam at Fermilab, with the power of 700 kW which corresponds to 6×10^{20} protons on target (POT) per year, produced the neutrinos. The far detector consists of 14 kton of totally active scintillator material and is situated at 810 km away at a 0.8° off-axis location. Due to the off-axis location, the flux peaks sharply at 2 GeV, which is close to the the energy of maximum oscillation of 1.4 GeV. It started taking data in 2014 and ran in neutrino (anti-neutrino) modes with 8.85×10^{20} (12.33×10^{20}) POT.

3.1 Tensions in the data of T2K and NOνA

Each of the two experiments, T2K and NOνA, have taken data in both neutrino and anti-neutrino beam modes. In each case, they have measured muon neutrino disappearance and electron neutrino appearance. The measured values of $|\Delta m^2_{32}|$ from these measurements are consistent with one another and with previous measurements. Regarding the measurement of the unknowns, different pieces of data seem to point in different direction. We observe the following tensions among the data of these two experiments.

- The ν_μ disappearance data of NOνA is consistent with the maximal value of $\sin^2 2\theta_{23} = 1$ whereas the $\bar{\nu}_\mu$ disappearance data requires a non-maximal value.

- The ν_e appearance data of T2K pulls θ_{23} to higher octant whereas the ν_μ disappearance data constrains it to be very close to 45°.

- NOνA observes a reasonably large excess in ν_e and a modest excess in $\bar{\nu}_e$ appearance data whereas T2K observes a very large excess of ν_e appearace events and a suppression (not statistically significant) of $\bar{\nu}_e$ appearance. Thus there is a tension between the appearance data of T2K and NOνA, speacially in $\bar{\nu}_e$ appearance.

3.2 Combined fit to T2K and NOνA data

In this section we present our results of combined fit of the disappearance and the appearance data of T2K and NOνA in both neutrino and anti-neutrino

channels. The data of T2K is taken from reference [14] and that of NOνA from reference [15]. The theoretical expectations for the two experiments are calculated using the software GLoBES [16, 17]. In these calculations, The GLoBES predictions for the expected bin-wise event numbers are matched with those given by the Monte-Carlo simulations of the experiments, quoted in references [14] and [15],for the same input parameters. In calculating the theoretical expectations, the values of $\Delta m^2_{21} = 7.50 \times 10^{-5} eV^2$ and $\sin^2\theta_{12} = 0.307$ are held fixed. There is no allowed region in $\delta_{CP} - \sin^2\theta_{23}$ plane for

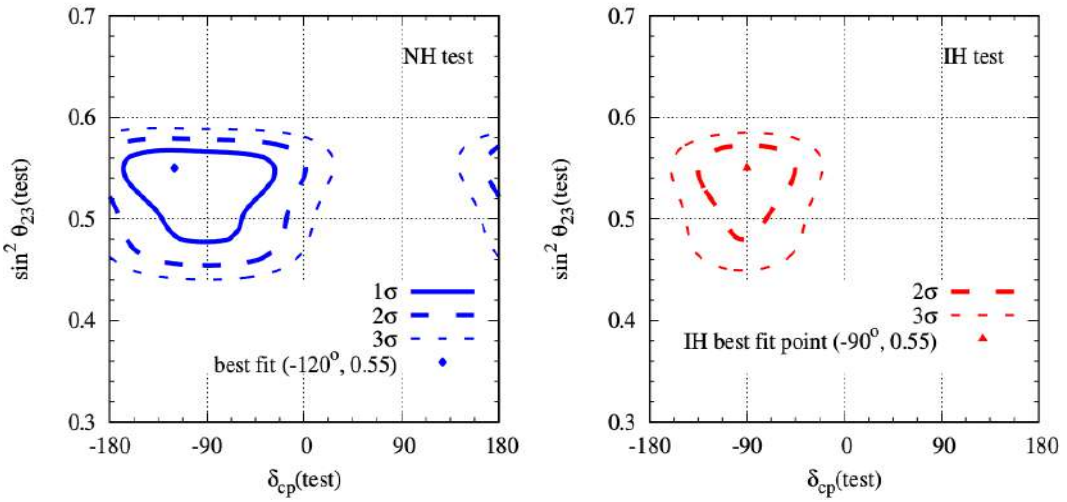

FIGURE 3: Expected allowed regions in $\delta_{CP} - \sin^2\theta_{23}$ plane from the current neutrino and anti-neutrino data of T2K and NOνA. In the left panel, the hierarchy is assumed to be NH and in the right panel, the hierarchy is assumed to be IH. The IH best-fit point has $\Delta\chi^2 = 2.5$.

IH at 1σ. There is a very small allowed region at 2σ with the best-fit point occuring at $(-90°, 0.55)$ with a $\Delta\chi^2 = 2.5$. The best-fit point for IH in our fit is close to the IH best-fit points of T2K and NOνA. This is not surprising because those two points are close to each other. For IH, the whole region of δ_{CP} in upper half plane is ruled out at 3σ because it is disfavoured by both T2K and NOνA. For T2K, the change induced by δ_{CP} in ν_e appearance events is much larger than the change induced by hiearachy. Values of δ_{CP} in upper half plane reduces these events relative to reference point. The large excess seen by T2K relative to the reference point seems to rule out most of the upper half plane of δ_{CP} for NH also, even though this region contains NOνA best-fit point. This same excess seems to place the best-fit value of δ_{CP} in the lower

half plane, with actual value being determined by the relative weights of T2K and NOνA data. The best-fit value of $\sin^2\theta_{23}$ is the average of the best-fit values of T2K and NOvA. Thus it seems as if the $\nu_\mu/\bar{\nu}_\mu$ disappearance data of T2K and NOvA seems to play an equally important role in determining this quantity.

4 Feasibility study of MRPC based PET device

The Multigap Resistive Plate Chamber (MRPC) is a modified version of RPC detector. These detectors consist of many highly resistive plates (e.g. glass) and very thin gas gap between them. The high voltage is applied only on the outermost electrodes and the inner electrodes are all electrically floating. The fast signal is produced by the flow of electrons towards the anode. The resultant signal is the summation from all the gaps which is readout from pickup panels placed at the outside of anode and cathode electrodes. The time resolution of these detectors improves with narrower gas gap. We have developed several glass MRPC detectors to find potential application in medical imaging etc. Here we present the fabrication procedure of the optimized design, the Time Of Flight (TOF) measurements of 511 keV gammas, the time resolution for 511 keV gammas and Geant4 simulations of efficiency.

4.1 Fabrication of MRPCs

We have constructed six-gap glass MRPCs of dimensions 305 mm $\times$305 mm $\times$ 7.5 mm. The dimensions of internal glass plates are 256 mm $\times$ 256 mm $\times$ 0.410 mm. Glass sheets of 2 mm thickness with bulk resistivity of $10^{10} - 10^{12}$ Ω cm, coated with a conductive layer of graphite paint, spaced from one another using spacers of equal thickness, were used as the outer electrodes. Two sided non conducting adhesive tapes were used on both sides of a mylar sheet to make small circular spacers of diameter 4 mm and thickness $\approx$ 250 μm. Twenty five spacers were used to maintain gas gaps. The gas mixture has been optimized to $R134a$ (91.2 %), C_4H_{10} (4.8%) and SF_6 (4%). The pickup panels consist of plastic honeycomb material laminated with copper strips of

width 2.8 cm placed on both the sides of an MRPC orthogonal to each other.

4.2 MRPC for Positron Emission Tomography (PET)

We attempt to demonstrate the possible application of these detectors in medical imaging because of their excellent time resolution. We have mounted two MRPCs horizontally and a radioactive source (^{22}Na) is placed asymmetrically between the two detectors. ^{22}Na emits a positron which annihilates with an electron almost at rest and two gammas of 511 keV are produced with opposite momenta. These photons are detected by the two detectors in coincidence with each other. Each MRPC has eight "X" strips and eight "Y" strips of 2.8 cm width. Lines Of Response (LOR) can be obtained by joining the hit coordinates. The time of flight information gives the exact position of the source on the line of response. The "X" and "Y" coordinates of hits are recorded along with the time of arrival of the photon at the detector. We obtain lines of response by joining the hit coordinates of MRPC1 and MRPC2 only for events with single multiplicity (with one strip hit per plane per detector). The timing Information infers the exact position of the source on the line of response. The difference between timings of two opposite photons is calculated as $\Delta T = t_{MRPC1} - t_{MRPC2}$. There were offset in cable lengths and the TDC path of different channels. To avoid this, we have taken two readings for a fixed distance between the MRPCs. First, the source is kept at the bottom MRPC and we obtain $\Delta T_1 = t_{MRPC1} - t_{MRPC2}$. The same reading is repeated but with source just below the top MRPC and we calculate $\Delta T_2 = t_{MRPC1} - t_{MRPC2}$. Finally we calculate the time of flight TOF=$(|\Delta T_1 - \Delta T_2|)/2$. We took readings for the four values of separation (30 cm, 45 cm, 60 cm and 75 cm) between MRPCs. The opearting voltage of MRPCs was set at 15 kV. Our results of time of flight calculation for these distances have been summarized in table 9.2. The time resolution is the crucial parameter for a TOF-PET device. The Anusparsh boards were used to get both the digital as well as analog information of each event. The analog information is required to apply time walk correction to the TDC data. Data

Distance	ΔT_1 (ns)	ΔT_2 (ns)	TOF (ns)	Exp. TOF (ns)
30 cm	-8.38 $\pm$ 0.05	-6.24 $\pm$ 0.07	1.07 $\pm$ 0.04	1.0
45 cm	-9.24 $\pm$ 0.04	-6.42 $\pm$ 0.04	1.41 $\pm$ 0.03	1.5
60 cm	-9.67 $\pm$ 0.07	-5.60 $\pm$ 0.06	2.03 $\pm$ 0.05	2.0
75 cm	-10.13 $\pm$ 0.07	-5.13 $\pm$ 0.07	2.50 $\pm$ 0.05	2.5

TABLE 1: Measurement of the time of flight (TOF) for various distances between MRPCs

was taken for four values of operating high voltage 15kV, 16 kV, 17 kV and 18 kV with source placed at the bottom MRPC. The separation between the two MRPCs was kept fixed at $\sim$ 30 cm. The profile histograms of ΔT_{Raw} versus QDC_{MRPC2} are fitted to a function $\exp[-p_0/x + p_1] + p_2$. The TDC value of each event is then corrected by using the fit parameters p_0, p_1 and p_2 and the QDC value. The time resolution values are listed in table 9.3.

H.V.	σ_T (ps) (Raw)	σ_T (ps) (Corrected)
15 kV	1157.25 $\pm$ 15.00	1022.00 $\pm$ 14.25
16 kV	757.50 $\pm$ 8.50	679.25 $\pm$ 9.00
17 kV	722.75 $\pm$ 5.00	674.50 $\pm$ 7.75
18 kV	583.75 $\pm$ 7.50	480.75 $\pm$ 5.00

TABLE 2: Time resolution at different high voltages

4.3 Geant4 simulation of Efficiency for 511 keV gammas

MRPCs are gas filled detectors and have excellent effeciency for minimum ionising particles (muons). Efficiency study of our detector for cosmic muons can be found in [18]. MRPCs have very low efficiency for gammas. Since our experiment involves 511 keV gammas produced by ^{22}Na source, we did a Geant4 simulation study to estimate the efficiency of our detector for 511 keV gammas. The MRPC was simulated according to the design details described above. Gammas of energy 511 keV generated by Geant4 monte carlo were showered within a solid angle which covered the entire active detector area. Figure 9.13(a) shows the plot of effeciency versus the number of gaps in the MRPC. The data points are the mean values of efficiency and the errors

are given by $\sigma/\sqrt{(N-1)}$ (where "σ" is the standard deviation and "N" is the number data samples). As it can be seen that the efficiency is very low for 511 keV gammas. Our detector has six gaps which corresponds to an efficiency of $\sim 1\%$. Efficency increases with the increase in the number of gaps. The efficiency can be improved if a high "Z" material is used as a converter, which converts gammas into electrons through photoelectric effect or compton scattering. We did a simulation study to estimate the improvement in efficiency by using PbO as a converter material. A PbO coat was applied on the inner side of an outside electrode. The thickness of the coat was varied from 0.00 mm to 0.50 mm. Ten data sets were obtained for each thickness by shooting 50,000 photons on the coated electrode side of the MRPC.

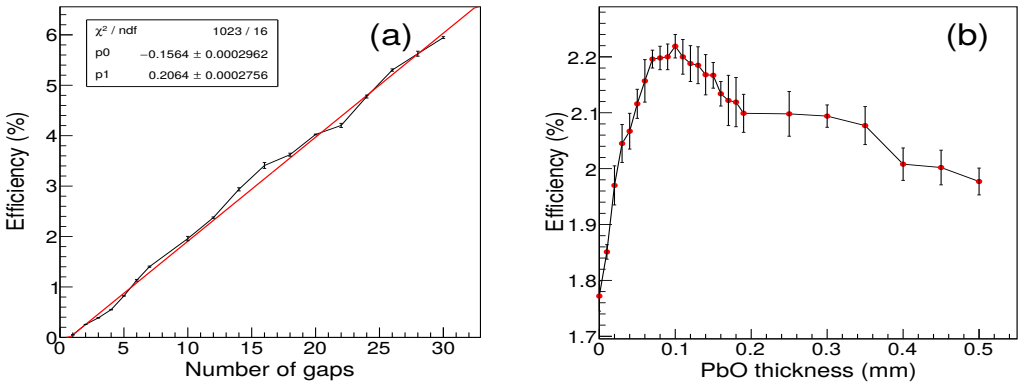

FIGURE 4: (a) Efficiency vs number of gaps and (b) efficiency vs thickness of the PbO coat.

Efficiency was obtained in similar way as obtained above. Figure 9.13(b) shows the efficiency versus PbO coat thickness plot. The data points are the mean values obtained from the ten data sets and the errors are given by $\sigma/\sqrt{(N-1)}$. We see an improvement in effeciency near 0.1 mm thickness of the coat. The number of gaps (6 gaps) was kept fixed for this study.

5 Conclusions

(A) Hadron energy estimation from Atmospheric neutrino events in ICAL: For $E_{had} < 5$ GeV, almost all of the hadron energy is carried by the baryons. The relation between the number of hits and the energy of hadrons is very

different for the two cases when the hadrons are mesons and when the hadrons are baryons. When the events are classified into bins with different number of hadron hits, the resulting spectra are reasonably well described by Vavilov distributions. There is a good correlation between the number of hits and the mean value of E_{Ehad} of the Vavilov distributions. The width (σ) of the Vavilov distributions is related to the mean energy ($E_{\mathrm{had-mean}} = E$) through the expected relation $\sigma(E)/E = \sqrt{(a^2/E + b^2)}$.

(B) Tension between the data of long baseline neutrino experiments: We note that the two experiments (T2K and NOνA) agree on the best fit values of hierarchy and $\sin^2\theta_{23}$ but strongly disagree on the best fit values of δ_{cp}. We did a combined fit of the data of the two experiments. The best fit values of the unknown paramenters in our fit are (NH, $\sin^2\theta_{23} = 0.56$, $\delta_{cp} = -130^\circ$). The best fit point for IH occurs at $\sin^2\theta_{23} = 0.56$, $\delta_{cp} = -90^\circ$ with a $\Delta\chi^2 \approx 2$. The best fit point we obtain are close to the best fit points obtained by NuFit collaboration who did a global analysis of all neutrino data.

(C) Feasibility study of MRPC based PET device: We developed and characterized several six-gap glass MRPCs and extensively studied their performance over a long period of time. We measured Time Of Flight (TOF) of 511 keV gammas produced by (^{22}Na) source between the two MRPCs for different distances between the two detectors. The measured TOF is in good agreement with the expected values. We studied the time resolution of our detector for 511 keV photons at different operating high volatges. The time resolution improves with incresing high voltage. We could go upto 18 kV and the time resolution at this high voltage is $\sim$ 480 ps which includes electronic jitter of $\sim$ 120 ps. The time walk correction using the analog information from the Anusparsh boards significantly improves the time resolution. We did Geant4 simulation to estimate the efficiency of our detector for 511 keV gammas for different number of gaps in an MRPC. The efficency increases with increasing number of gas gaps. The efficiency of our detector can also be improved by using a PbO coat on the inner side of one of the outside electrodes.

Contents

List of Figures

List of Tables

List of Abbreviations

ASIC	Application Specific Intigrated Circuit
CAMAC	Computer Automated Measurement And Control
CC	Charged Current
DAQ	Data Aquisition
DIS	Deep Inelastic Scattering
DUNE	Deep Underground Neutrino Experiment
ECL	Emitter – Coupled Logic
GEANT	GEometry And Tracking
HK	Hyper-Kamiokande
HV	High Voltage
ICAL	Iron CALorimeter
IH	Inverted Hierarchy
IMB	Irvin-Michigan-Brookhaven collaboration
INO	India–based Neutrino Observatory
JUNO	Jiangmen Underground Neutrino Observatory
KamLAND	Kamioka Liquid Scintillator Anti Neutrino Detector
LVDS	Low – Voltage Differential Signaling
MINOS	Main Injector Neutrino Oscillation Search
MRPC	Multigap Resistive Plate Chamber
MSW	Mikheyev – Smirnov – Wolfenstein
NC	Neutral – Current
NH	Normal Hierarchy
NIM	Nuclear Instrumentation Module
NOνA	NuMI Off-axis ν_e Appearance
ORCA	Oscillation Research with Cosmics in the Abyss

PINGU	Precision IceCube Next Generation Underground
QE	Quasi – Elastic
RENO	Reactor Experiment for Neutrino Oscillations
RPC	Resistive Plate Chamber
RS	Resonance Scattering
SK	Super Kamiokande
T2K	Tokai to Kamioka
TDC	Time – to – Digital Converter
TOF	Time – Of – Flight

Chapter 1

Introduction to neutrinos

Wolfgang Pauli proposed a very light, neutral spin $\frac{1}{2}$ weakly interacting particle to restore the energy conservation in β- decay which was later termed as "Neutrino" meaning "the little neutral one". Neutrinos are now known to exist in three flavours and they are the second-most abundant particles in the universe after the photon. We will introduce them and the experiments which discovered them systematically in the following sections.

1.1 Electron Neutrino (ν_e)

Experiments of β-decay showed that a neutron in a radioactive nucleus decays into a proton and an electron. The electron has a continous energy spectrum. But kinematically, electrons in β-decay are expected to be emitted with fixed energy. Pauli postulated a new particle "Neutron" to account for this apparent non-conservation of energy. A very light, neutral, spin $\frac{1}{2}$ particle is emitted along with the electron in β-decay and this unseen particle carries away the missing energy. Later in 1932, James Chadwick discovered a massive particle, with mass a little larger than the mass of proton, which was also called 'neutron'. Enrico Fermi named the neutral particle in β-decay as 'neutrino' to avoid the confusion. The neutrinos emitted in the β-decay are now known as electron anti-neutrinos.

1.1.1 Fermi theory of β-decay

The β-decay can be written as

$$ {}^{A}_{Z}X_{N} \rightarrow {}^{A}_{Z+1}X'_{N-1} + e^{-} + \overline{\nu}. \tag{1.1} $$

This is the β^{-} decay where the underlying process is

$$ n \rightarrow p + e^{-} + \overline{\nu}, \tag{1.2} $$

which converts a neutron into a proton with the emission of an electron and an anti-neutrino. Fermi described this process by an effective Hamiltonian.

$$ H_{wk} = G_F \overline{\Psi}_p \gamma_\mu \Psi_n \overline{\Psi}_e \gamma^\mu \Psi_\nu, \tag{1.3} $$

where Ψ_p, Ψ_n, Ψ_e and Ψ_ν are the four component spin $\frac{1}{2}$ fields for proton, neutron, electron and neutrino respectively. The electron spectrum can be computed using the above Hamiltonian. It is found to be

$$ \frac{d\Gamma}{dT_e} = \frac{G_F^2}{2\pi^3}(T_e + m_e)p_e(Q - T_e)\sqrt{(Q - T_e)^2 - m_\nu^2}, \tag{1.4} $$

$$ Q = m_i - m_f - m_e, \tag{1.5} $$

where G_F is the Fermi coupling constant and Q is the Q-value of the β-decay. m_i and m_f are the masses of initial and final nuclei respectively and m_e is the electron mass. T_e = E_e - m_e is the kinetic energy of the electron. G_F is called the Fermi coupling constant which gives the strength of the weak interaction. Maximum kinetic energy of elctron is equal to the Q value of the process for a massless neutrino. For massive neutrinos, T_e attains its maximum value of T_e^{max} = Q - m_ν. Plot of $\frac{d\Gamma}{dT_e}$ vs. T_e is known as the Kurie plot. Kurie plots of the experimental data of all β-decays [19, 20, 21] matched with the predictions of eq. (1.4) which is taken as the proof of the existence of neutrino. Integrating eq. (1.4) over T_e gives the β-decay width. We obtain G_F by comparing this decay width with the experimental measurement of neutron decay lifetime

[22, 23] to obtain

$$G_F = 1.166 \times 10^{-5} GeV^{-2}. \tag{1.6}$$

1.1.2 Cowan Reines experiment

The success of Fermi's theory through 1950s convinced most of physicists about the existence of neutrino but there was no direct evidence of this elusive particle's existence. One possiblity of directly observing the neutrino was to observe inverse β- decay.

$$\overline{\nu} + p \rightarrow n + e^{+}, \tag{1.7}$$

with a threshold energy of 1.80 MeV. Unfortunately, neutrinos interect with matter only through Fermi's weak force which is so weak that the probability of inverse β-decay was predicted to be nearly zero. Hans Bethe and Rudolf Peierls calculated the interaction cross section to be less than "10^{-44} cm^2 (corresponding to a penetrating power of 10^{16} km in solid matter)" and stated that, "It is therefore absolutely impossible to observe processes of this kind with the neutrinos created in nuclear transformations." In order to detect such a rare interaction in a reasonable time one would need both a large amount of matter as a target and a very large flux of neutrinos. Frederick Reines and Clyde Cowan, two scientists at the Los Alamos weapons laboratory, where the atomic bomb had first been developed and built, hypothesized that they could place a neutrino detector close enough to an atomic bomb explosion so that they would have a good chance of detecting that process. In the fall of 1952, following a suggestion by J.M.B. Kellogg, the director of the Physics Division at Los Alamos, Reines and Cowan revised the experimental plan to see if the flux of antineutrinos from a nuclear fission reactor could be used in place of that from an atomic bomb. Although the flux from a reactor was thousands of times lower than that expected from a 50 kiloton atomic bomb, such an experiment could run for months or a year in contrast to the one or two seconds expected for a bomb experiment. The

challange was to reduce the background from other events, which they could do if they could detect the flashes from both the positron and the neutron as separate but related signals. There were also other advantages in the use of a reactor as the source, such as ease in repeating a measurement and the opportunity to extend the observation time to reduce statistical uncertainty. In addition, Reines and Cowan had devised a new method for detecting the antineutrino.They used Savannah river nuclear reactor as a source and a mixture of cadmium chloride ($CdCl_2$) and water. The set up of the Cowan-Reines experiment has been shown in figure 1.1. An incident antineutrino

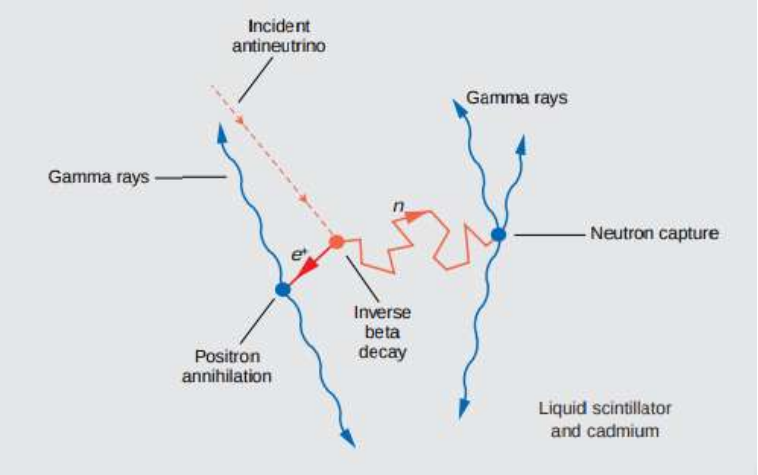

FIGURE 1.1: Schematic diagram of the antineutrino experiment of Reines and Cowan

(red dashed line) interacts with a proton through the weak force. The antineutrino turns into a positron (e^+) and the proton turns into a neutron (n). In the figure above, this reaction is shown to take place in a liquid scintillator. The short, solid red arrow indicates that, shortly after it has been created, the positron encounters an electron. The particle and antiparticle annihilate each other to give rise to two gamma rays. Because energy and momentum have to be conserved, these two gamma rays travel in opposite directions and will cause the liquid scintillator to produce a flash of visible light. In the meantime, the neutron wanders about following a random path (longer, solid red arrow) until it is captured by a cadmium nucleus after some time delay of a few microseconds. The resulting excited nucleus releases about 2.2 MeV

of energy in gamma rays that will again cause the liquid to produce a tiny flash of visible light. This sequence of two flashes of light separated by a few microseconds [24, 25, 26] is the double signature of inverse beta decay and confirms the presence of an anti-neutrino.

1.1.3 Ray Davis' reactor neutrino experiment

A nuclear reactor emits antineutrinos which arise from the negative beta decays of fission products. In 1954, Ray Davis made an attempt to observe an inverse electron capture process $Cl^{37}(\nu,e^-)A^{37}$ which requires neutrinos, using a source emitting anti-neutrinos i.e. a nuclear reactor. If neutrinos and anti-neutrinos are identical in their interactions with nucleons one should be able to observe the process upon carrying the experiment to the required sensitivity. However, if neutrinos and anti-neutrinos differ in their interactions with nucleons one would not expect to induce the reaction

$$\nu + Cl^{37} \rightarrow A^{37} + e^-. \tag{1.8}$$

The minute quantities of argon, produced in this reaction, could be separated from chlorine effectively because argon is chemically inert. This experiment did not observe any argon atoms, i.e. there was no signal [27].

This is explained by the concept of lepton number conservation. The lepton number for electrons and neutrinos is 1, for anti-neutrinos and positrons it's -1 and 0 for rest of the particles. Anti-neutrinos can drive the reaction in eq. (1.7) but cannot cause the reaction in eq. (1.8).

1.2 Muon Neutrino (ν_μ)

In 1962, an experiment was performed at Brookhaven AGS where the interaction of high-energy neutrinos with matter showed the existence of a non-electron type of neutrino [28]. The experiment's aim was to show that the neutrinos obtained by the decay of the pion produce muons but do not

produce electrons, meaning that these neutrinos are different from those involved in β decay.
The experiment looked for following interactions

$$\nu + n \rightarrow p + e^{-}, \tag{1.9}$$

$$\overline{\nu} + p \rightarrow n + e^{+}, \tag{1.10}$$

$$\nu + n \rightarrow p + \mu^{-}, \tag{1.11}$$

$$\overline{\nu} + p \rightarrow n + \mu^{+}. \tag{1.12}$$

The existence of only one type of neutrino implies that neutrino interactions with protons or neutrons should produce as many electrons as muons. If two types of neutrino exist, then there will be no electons produced.

1.2.1 Brookhaven AGS experiment

Schwartz [29] proposed to use high-energy pions which are a natural source of neutrinos: $\pi^{\pm} \rightarrow \mu^{\pm} + (\nu, \overline{\nu})$. A beam of protons from a proton accelerator was allowed to impinge on a target. The pions produced at the target were allowed to travel for some meters. Then they will hit against a shielding wall in front of the detector. Here a part of the pions will decay into high-energy neutrinos.

They shot 15-GeV protons on a 3-in. thick beryllium target, fixed at one end of a straight section 10 ft. long, producing the pions. The flux of particles produced, which moves in the general direction of the detector, strikes a 13.5-m thick iron shield wall at a distance of 21 m from the target. A wall of this thickness can absorb the strongly interacting particles by nuclear interaction (providing an attenuation of the order of 10^{-24} for strongly interacting particles, an attenuation more than sufficient not to alter the results of the experiment) and muons up to 17 GeV by ionization loss. The neutrino interactions are then observed in an aluminum spark chamber located behind the shield.

The spark chamber detector is made by 10 one-ton modules, each one constituted by 9 aluminum plates 44 in.$\times$ 44 in. $\times$ 1 in. thick, separated by $\frac{3}{8}$ in. lucite spacers. To reduce the effect of cosmic rays and AGS-produced muons which penetrate the shield, top, back and front anti-coincidence sheets are added, for a total of 50 counters. The top and back slabs are shielded against neutrino events. Triggering counters are inserted between adjacent chambers and at the end. Figure 1.2. shows the Plan view of AGS neutrino experiment. 113 events were observed, excluding those originated outside the chambers, those which were not originated within a fiducial volume and those of single tracks where the extrapolation of the track backwards for two gaps did not remain within the fiducial volume or where the production angle relative to the neutrino line of flight was more than 60°. There were 49 short single tracks whose visible momentum was less then 300 MeV/c. They were rejected because they include energetic muons that leave the chamber, low-energy neutrino events and the bulk of the neutron produced background. In addition, there were 34 events with single muon tracks of energy more than 300 MeV/c, 22 vertex events with more than one track from a vertex and 8 shower events where the energy deposition is too irregular for them to be muons. The shower events were not accepted and only the 56 events of the first and second types were finally considered. To conclude that two

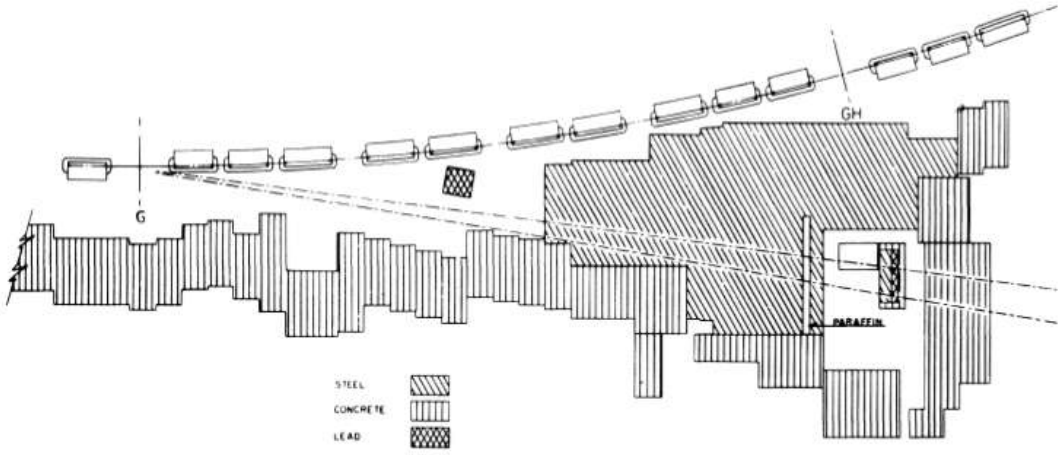

FIGURE 1.2: Plan view of AGS neutrino experiment.

types of neutrino are highly likely to exist, the authors needed to exclude the decays (1.9) and (1.11) from the observed events and to show that the second and fourth decays do not occur with the same rate, as could be expected if the neutrino involved in the interaction (1.10) (which will be indicated with ν_e) and the neutrino involved in the interaction (1.12) (indicated from now on with ν_μ) were the same. First of all they exclude that the events observed could be produced by cosmic rays. The background of these neutrino events is measured experimentally by running with the AGS machine off on the same triggering arrangement except for the Čerenkov gating requirement and is of the order of 1 neutrino-like event in 90 cosmic-ray events. Considering that about 440 cosmic-ray tracks are consistent with the observation, they identify 5 ± 1 cosmic-ray events (consistent with the observation of a small asymmetry seen in the projection of angular distributions of single track events) while the other 51 events are unlikely to be the result of cosmic rays. They also exclude the events that are neutron produced: The origins of the events are uniformly distributed over the fiducial volume, particularly against the last chamber because of the condition that the visible momentum be greater than 300 MeV/c, while nuclear and electromagnetic interactions have both a mean free path of a length shorter than 40 cm. This allows the authors to exclude the decays (1.9) and (1.11). The single particles produced are supposed to be muons because there are little or no nuclear interactions. To explain this the authors consider a simplified situation. In a follow-up experiment, it was observed that for the 400-MeV pions the mean free path for nuclear interactions in the chamber was no more than 100 cm of aluminum. Thus, in the initial experiment they should have observed about 8 nuclear interactions, while no nuclear interaction was observed. The latter consideration allows them to infer that the observed reactions may be due to the decay of pions and kaons. To prove this, in a second background run, the iron was removed from the main shield and was replaced by an equivalent quantity of lead. By changing the conditions this way, the path available for pions was reduced by a factor of 8. The authors observed a reduced rate of events from

1.46 ± 0.2 to 0.3 ± 0.2 per 10^{16} incident protons, which is consistent with the reduction expected for neutrinos produced by the decay of pions or kaons. Finally they considered only the single track events. Of the 34 single muon events, 5 are considered to be cosmic ray background. If we suppose $\nu_e = \nu_\mu$, we expect about 29 electron showers with a mean energy of approximately 400 MeV/c while we observe only 6 candidates of electron showers looking qualitatively very different from the electron events observed at Cosmotron. Later experiments showed that the efficiency of triggering of 400-MeV electrons in the chambers to be 67%. The observation is inconsistent with the prediction based on the hypothesis that $\nu_e = \nu_\mu$.

The calculation of the ratio $(\pi^+ \to e^+ + \nu)/(\pi^+ \to \mu^+ + \nu)$ at $(1.21 \pm 0.07) \times 10^{-4}$ [30], the results of β decay, μ capture and μ decay show that the couplings of single neutrinos with electrons and those of single neutrinos with muons are equal. Hence, we cannot say that the absence of the electrons is caused by the couplings of single neutrinos with electrons. So, the most probable cause of the absence of electron showers is the fact that $\nu_e \neq \nu_\mu$.

Note that the presence of one or two electron events was expected from electron-associated neutrinos produced in the decays $K^+ \to e^+ + \nu_e + \pi^0$ and $K_2^0 \to e^\pm + \nu_e + \pi^\mp$. The authors argue that the absence of the electrons events could be due to the fact that the form factors for the heavy-particle currents in the e-producing reaction is very different from that in the μ-producing reaction at a great momentum transfers. However, this obstacle can be avoided thanks to the calculation [31] which shows that an absolute theoretical lower limit can be established for the rates of the e-producing reaction without a relative comparison with that of the μ-producing reactions. As a matter of fact, using this lower limit we can calculate the number of observed electrons to be greater than 12, with an error of $\pm 30\%$ due to poor knowledge of the flux of the neutrinos. Even though the error is large, it is inconsistent with the observations and, hence, it confirms the hypothesis that $\nu_e \neq \nu_\mu$.
These results require us to expand our definition of lepton number to two distinct quantum numbers:

- Electron Lepton number L_e , which is same as L defined before.
- Muon Lepton number L_μ , which is 1 for μ^- and ν_μ , -1 for their anti-particles and 0 for all other particles.

It is postulated that L_e and L_μ are individually conserved in all reactions. This hypothesis explains why the decays $\mu^- \rightarrow e^- + \gamma$ and $\mu^- \rightarrow e^- + e^- + e^+$ do not occur.

1.3 Tau Neutrino (ν_τ)

In December 1975, the MARK I experimenters at SLAC published a paper by Per1 et al. (1975) entitled " Evidence for Anomalous Lepton Production in e^+ - e^- Annihilation" [32]. They concluded: "the signature e - μ events cannot be explained either by the production and decay of any presently known particles or as coming from any of the well-understood interactions which can conventionally lead to an e and a μ in the final state. A possible explanation for these events is the production and decay of a pair of new particles, each having a mass in the range of 1.6 to 2.0 GeV". In 1977 a paper [33] entitled "Review of Heavy Lepton Production in e^+ e^- Annihilation" concluded:

- All data on anomalous $e\mu$, ex, ee and $\mu\mu$ events produced in e^+ e^- annihilation is consistent with the existence of a mass 1.9 ± 0.1 GeV charged lepton, the τ.
- This data cannot be explained as coming from charmed particle decays.
- Many of the expected decay modes of the τ have been seen. A very important problem is the existence of the $\tau^- \rightarrow \nu_\tau + \pi^-$ decay mode.

In the Mark I collaboration the first demonstration that $B(\tau \rightarrow \nu\pi)$ was substantial came from Gail Hanson [34]. By the middle of 1978 there was no confusion and a $B(\tau \rightarrow \nu\pi)$ close to the expected 10% was established. Thus by the end of 1978 all confirmed measurements agreed with the hypothesis

that the τ was a lepton which was produced by a known electromagnetic interaction and, at least in it's main modes, decayed through the conventional weak interaction.

1.3.1 Invisible Width of Z: LEP Collider

The invisible width from Z decays to neutrinos, $\Gamma_{inv} = N_\nu \Gamma_{\nu\bar{\nu}}$, where N_ν is the number of light neutrino species, is determined from the measurements of the decay widths to all visible final states and the total width,

$$\Gamma_Z = \Gamma_{ee} + \Gamma_{\mu\mu} + \Gamma_{\tau\tau} + \Gamma_{had} + \Gamma_{inv}. \tag{1.13}$$

Because the measured cross-sections depend on products of the partial widths and also on the total width, the widths constitute a highly correlated parameter set. In order to reduce correlations among the fit parameters, an experimentally-motivated set of six parameters is used to describe the total hadronic and leptonic cross-sections around the Z peak. These are

- the mass of the Z, m_Z;
- the Z total width, Γ_Z;
- the "hadronic pole cross-section",

$$\sigma^0_{had} \equiv \frac{12\pi\Gamma_{ee}\Gamma_{had}}{m_Z^2\Gamma_Z^2}; \tag{1.14}$$

- the three ratios

$$R^0_e \equiv \frac{\Gamma_{had}}{\Gamma_{ee}}, R^0_\mu \equiv \frac{\Gamma_{had}}{\Gamma_{\mu\mu}}, R^0_\tau \equiv \frac{\Gamma_{had}}{\Gamma_{\tau\tau}}. \tag{1.15}$$

If lepton universality is assumed, the last three ratios reduce to a single parameter:

$$R^0_l \equiv \frac{\Gamma_{had}}{\Gamma_{ll}}, \tag{1.16}$$

where Γ_{ll} is the partial width of the Z into one massless charged lepton flavour. (Due to the mass of the tau lepton, even with the assumption of

lepton universality, $\Gamma_{\tau\tau}$ differs from Γ_{ll} by about δ_τ = -0.23%.) The six parameters describing the leptonic and total hadronic cross-sections around the Z peak are determined exclusively from the measurements of the four LEP collaborations, due to the large event statistics available and the precise determination of the LEP collision energy.

If the Z had no invisible width, all partial widths could be determined without knowledge of the absolute scale of the cross-sections. Not surprisingly, therefore, the measurement of Γ_{inv} is particularly sensitive to the cross-section scale. Assuming lepton universality, and defining $R^0_{inv} = \frac{\Gamma_{had}}{\Gamma_{ll}}$, Equations (1.14) and (1.15) can be combined to yield

$$R^0_{inv} = \left(\frac{12\pi R^0_l}{\sigma^0_{had} m_Z^2} \right)^{\frac{1}{2}} - R^0_l - (3 + \delta_\tau), \tag{1.17}$$

where the dependence on the absolute cross-section scale is explicit. Assuming that the only invisible Z decays are to neutrinos coupling according to SM expectations, the number of light neutrino generations, N_ν, can then be determined by comparing the measured R^0_{inv} with the SM prediction for $\Gamma_{\nu\bar{\nu}}/\Gamma_{ll}$:

$$R^0_{inv} = N_\nu \left(\frac{\Gamma_{\nu\bar{\nu}}}{\Gamma_{ll}} \right)_{SM} \tag{1.18}$$

The strong dependence of the hadronic peak cross-section on N_ν is illustrated in Figure (1.3). This fit, based on 17 million Z decays [35], gives a precise value

$$N_\nu = 2.9840 \pm 0.0082. \tag{1.19}$$

1.3.2 Tau neutrino discovery: DONuT experiment

The ν_τ was postulated to exist after the discovery of the τ lepton in 1975 [33]. Since that time, much indirect evidence has been gathered implying that the ν_τ exists as the Standard Model third generation neutrino. However, the charged current interactions of a third neutrino had not been observed in the

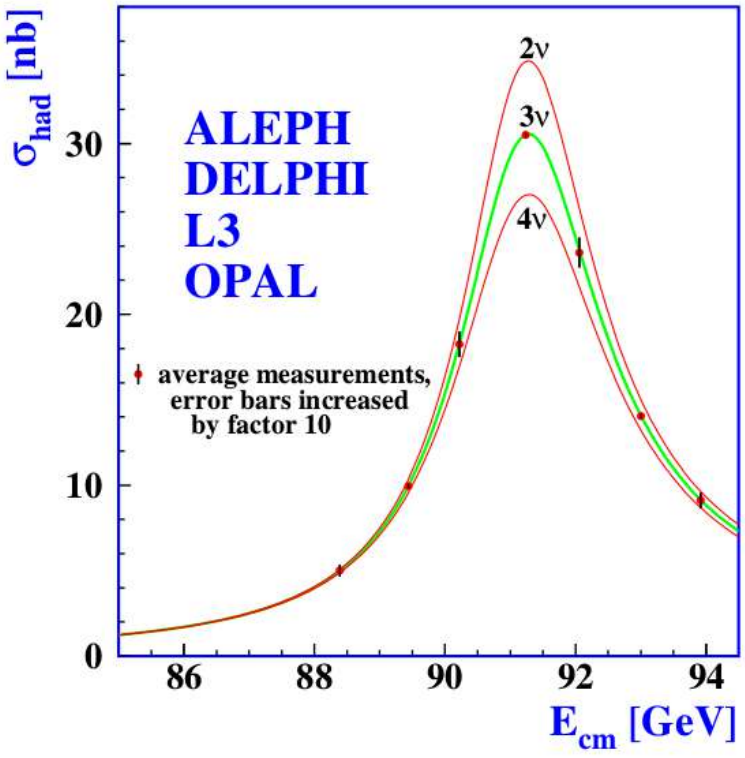

FIGURE 1.3: Measurements of the hadron production cross-section around the Z resonance. The curves indicate the predicted cross-section for two, three and four neutrino species with SM couplings and negligible mass.

same manner as the interactions of the ν_e [24] and the ν_μ [28]. The DONUT experiment [36] was designed to observe the charged current interactions of the ν_τ (2.4) by identifying the τ lepton as the only lepton created at the interaction vertex

$$\nu_\tau + n \rightarrow \tau^- + p. \tag{1.20}$$

At the neutrino energies of this experiment, the τ typically decays within 2 mm of its creation to a single charged daughter (86% branching fraction). Thus the signature of the τ is a track with a kink, signifying a decay characterized by a large transverse momentum. The neutrino beam was created using 800 GeV protons from the Fermilab Tevatron interacting in a meter long tungsten beam dump, which was 36 m upstream from the emulsion target. Most of the neutrinos that interacted in the emulsion target originated in the decays of charmed mesons in the beam dump. The primary source of ν_τ

is the leptonic decay of a D_s meson into τ and $\overline{\nu}_\tau$, and the subsequent decay of the τ to a ν_τ. All other sources of ν_τ are estimated to have contributed an additional 15%. (5 ± 1)% of all neutrino interactions detected in the emulsion were predicted to be from ν_τ with the dominant uncertainty from charm production and $D_s \to \tau\nu$ branching ratio measurements [37]. The mean energies of the detected neutrino interactions were calculated to be 89 GeV, 69 GeV, and 111 GeV, for ν_e, ν_μ, and ν_τ respectively.

To perform the decay search, segments from the redefined scan were realigned and relinked into tracks. Tracks were then fit to form the interaction vertex. Tracks that originated at the interaction vertex and stopped in the scan volume were candidates for decays [36]. Tracks which originated within one or two plates downstream from the end of the stopped track were designated daughters if they had a distance of closest approach to the parent candidate of less than 10 μm. The following selection criteria, which retained 50% of simulated τ events, were used to identify τ decay candidates from the kink candidates:

- At least one segment of the parent track is identified in the emulsion data.
- Only one daughter track was associated with a parent track.
- The parent track was $<$ 5 mm long.
- The daughter angle with respect to the parent track was $>$10 mrad and $<$ 400 mrad.
- The impact parameter of the daughter to the parent track was $<$ 10 μm.
- The impact parameter of the parent track to the interaction vertex was $<$ 10 μm.
- The impact parameter of the daughter track to the primary vertex was $<$500 μm.
- The daughter track momentum was $>$ 1 GeV.

- The transverse momentum of the decay was > 250 MeV.
- None of the tracks originating at the primary interaction vertex was identified as a muon or electron.

In a set of 203 located neutrino interactions [36, 38, 39], four events have a track that meets all the requirements for τ decays, with no evidence of another lepton from the primary vertex. The total background is estimated to be 0.34 ± 0.05 events. Two events are identified as $\tau \rightarrow e\nu_\tau\nu_e$ decays and have negligible level of background from scattering. The probability that the four events are from background sources is 4×10^{-4}, which concludes that these events are evidence that τ neutrino charged current interactions have been observed.

1.4 Determination of Neutrino mass

The huge abundance of neutrinos left over in the universe from the big bang ($336/cm^3$) and their contribution to structure formation as well as the key role of neutrino masses in finding the new Standard Model of particle physics make the absolute value of the neutrino mass one of the most urgent questions of astroparticle physics and cosmology as well as of nuclear and particle physics [40]. The V $-$ A theory of weak interactions [41, 42] proposed that only left chiral Fermions have weak interactions. Since neutrinos have only weak interactions, it may be assumed that only left chiral neutrinos exist [43, 44, 45]. The measurement of neutrino helicity to be -1 confirmed this [46]. If neutrinos are purely left chiral they have to be massless, since one needs both left and right chiral components to construct a massive fermion. However, experimentalists searched for evidence of neutrino mass in a series of increasingly precise experiments.

1.4.1 Electron Neutrino mass from the tritium β decay spectrum

The lower limit is set by neutrino oscillations and the fact that masses are non-negative. The upper limit is set by laboratory measurements on the beta decay of tritium. In beta decay the phase-space available to the electron near the endpoint is modified by neutrino mass, a fact realized immediately by Fermi [47] as he formulated the theory of beta decay. Tritium has been the beta-active nucleus of choice because it has a low endpoint energy, which makes the modification caused by neutrino mass a larger fraction of the total spectrum [48]:

$$^3H \rightarrow {}^3He^+ + e^- + \overline{\nu}_e + 18580eV \tag{1.21}$$

Figure 1.4 defines the requirements of a direct neutrino mass experiment

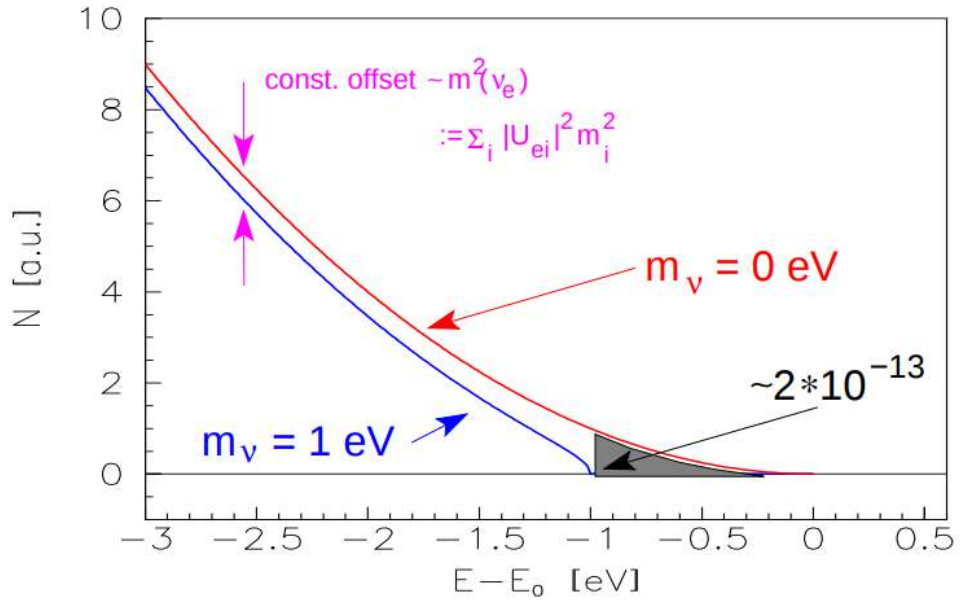

FIGURE 1.4: Expanded β spectrum around its endpoint E_0 for m(ν_e) = 0 (red line) and for an arbitrarily chosen neutrino mass of 1 eV (blue line). In the case of tritium, the gray-shaded area corresponds to a fraction of 2×10^{13} of all tritium β decays

which investigates a β spectrum: The task is to resolve the tiny change of the spectral shape due to the neutrino mass in the region just below the endpoint E_0, where the count rate is going to vanish. Therefore, high energy resolution is required combined with large source strength and acceptance as well as

low background rate. Tritium β decay experiments using a tritium source and a separated electron spectrometer have been performed in search for the neutrino mass for more than 50 years. The electron neutrino mass limit [49, 50, 51] has been improved to $m_{\nu_e} < 2.3$ eV. With the more data coming from the ongoing KATRIN experiment, this limit is expected to lower down to about 0.2 eV [52].

1.4.2 Muon Neutrino mass from the decay $\pi^+ \to \mu^+ \nu_\mu$

A surface muon beam in a magnetic spectrometer along with a silicon microstrip detector was used to measure the muon momentum from the decay $\pi^+ \to \mu^+ \nu_\mu$ at rest [53]. This leads to a squared muon-neutrino mass $m^2_{\nu_\mu}$ = (-0.016 $\pm$ 0.023) MeV^2. which gives an upper limit of 0.17 MeV (C.L.= 0.9) for the muon-neutrino mass.

1.4.3 Tau Neutrino mass from ALEPH experiment

Three- and five-prong τ decays were studied by ALEPH [54] to bound the tau neutrino mass by fitting the distribution of events in the (m_h,E_h) plane (Figure1.5). An upper limit of 18.2 MeV on the tau neutrino mass is obtained at 95% confidence level.

1.5 Neutrino interactions

Neutrinos interact with matter via weak interactions. The first theoretical description of the weak interaction was given by Fermi [20] as an explanation for β-decay. The standard neutrino interactions are described by the leptonic charged current [55]

$$j^\rho_{W,L} = 2 \sum_{\alpha=e,\mu,\tau} \overline{\nu_{\alpha L}} \gamma^\rho \ell_{\alpha L} = \sum_{\alpha=e,\mu\tau} \overline{\nu_\alpha} \gamma^\rho (1-\gamma^5) \ell_\alpha \quad , \tag{1.22}$$

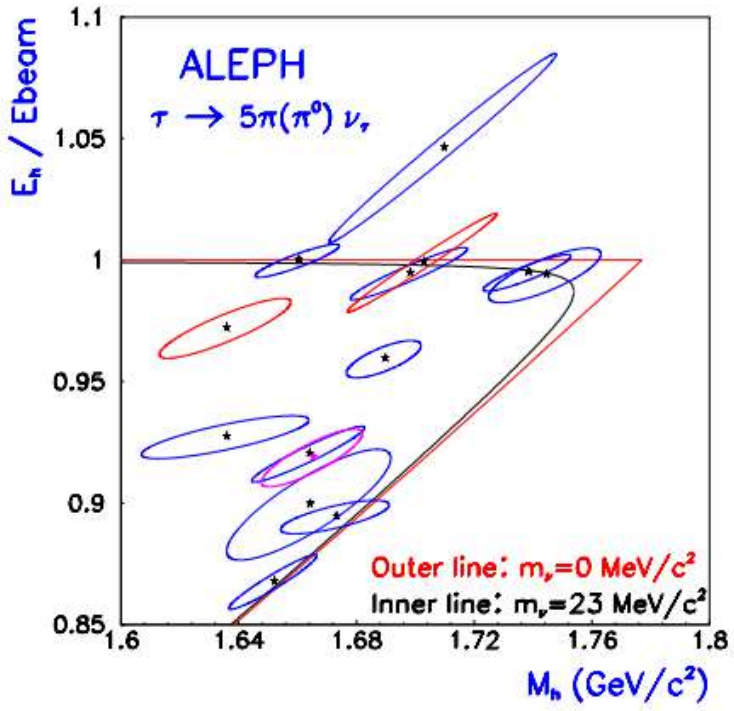

FIGURE 1.5: Distribution in the upper part of the (m_h, E_h) $\tau^- \to 3\pi^- 2\pi^+ (\pi^0)\nu_\tau$ candidates in the data. The two lines show the allowed region for a massless and for a 23 MeV neutrino. The only $\tau^- \to 3\pi^- 2\pi^+ \pi^0 \nu_\tau$ event in the plot is the one with the largest hadronic energy

and the neutrino part of the leptonic neutral current

$$j^{\rho}_{Z,\nu} = 2 \sum_{\alpha=e,\mu,\tau} \overline{\nu_{\alpha L}} \gamma^{\rho} \nu_{\alpha L} = \sum_{\alpha=e,\mu\tau} \overline{\nu_{\alpha}} \gamma^{\rho} (1-\gamma^5) \nu_{\alpha}. \tag{1.23}$$

The leptonic charged-current weak interaction Lagrangian

$$\mathscr{L}^{(CC)}_{I,L} = -\frac{g}{2\sqrt{2}} \left(j^{\rho}_{W,L} W_{\rho} + j^{\rho}_{W,L}{}^{\dagger} W^{\dagger}_{\rho} \right) \tag{1.24}$$

and the corresponding neutrino part of the leptonic neutral-current weak interaction Lagrangian is

$$\mathscr{L}^{(NC)}_{I,\nu} = -\frac{g}{2\cos\theta_w} j^{\rho}_{Z,\nu} Z_{\rho} \quad . \tag{1.25}$$

1.5.1 Neutrino-electron elastic scattering

Neutrinos and anti-neutrinos undergo elastic scattering process with electrons

$$\overset{(-)}{\nu}_{\alpha}(\alpha = e, \mu, \tau) + e^{-} \rightarrow \overset{(-)}{\nu}_{\alpha}(\alpha = e, \mu, \tau) + e^{-}. \tag{1.26}$$

The water Cherenkov solar neutrino detectors use this process which does not have a threshold.

$$\nu_e + e^{-} \rightarrow \nu_e + e^{-}. \tag{1.27}$$

Figure 1.6 shows the two tree-level Feynman diagrams which contribute to the the above process

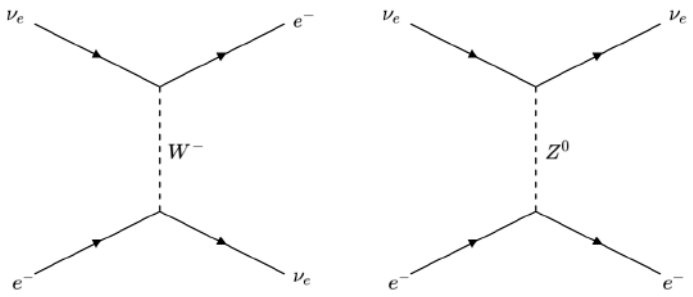

(A) Charged current (B) Neutral current

FIGURE 1.6: Tree level Feynman diagrams for the elastic scattering process $\nu_e + e^{-} \rightarrow \nu_e + e^{-}$.

For the anti-neutrino case, the charged-current t-channel diagram in figure 1.6a is replaced by s-channel diagram in figure 1.7a.

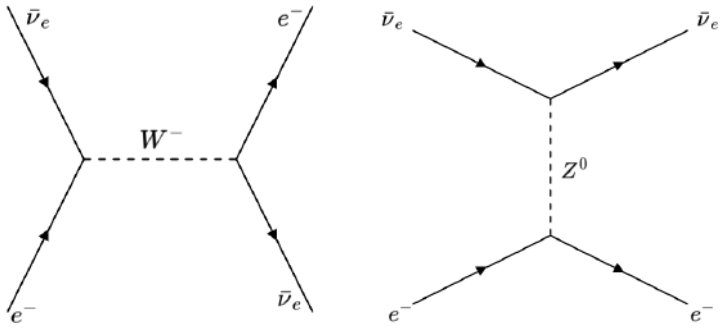

(A) Charged current (B) Neutral current

FIGURE 1.7: Tree level Feynman diagrams for the elastic scattering process $\bar{\nu}_e + e^{-} \rightarrow \bar{\nu}_e + e^{-}$.

The following elastic scattering process also contribute only from the neutral-current diagram in figure 1.8b.

$$\overset{(-)}{\nu}_{\mu,\tau} + e^- \rightarrow \overset{(-)}{\nu}_{\mu,\tau} + e^- . \tag{1.28}$$

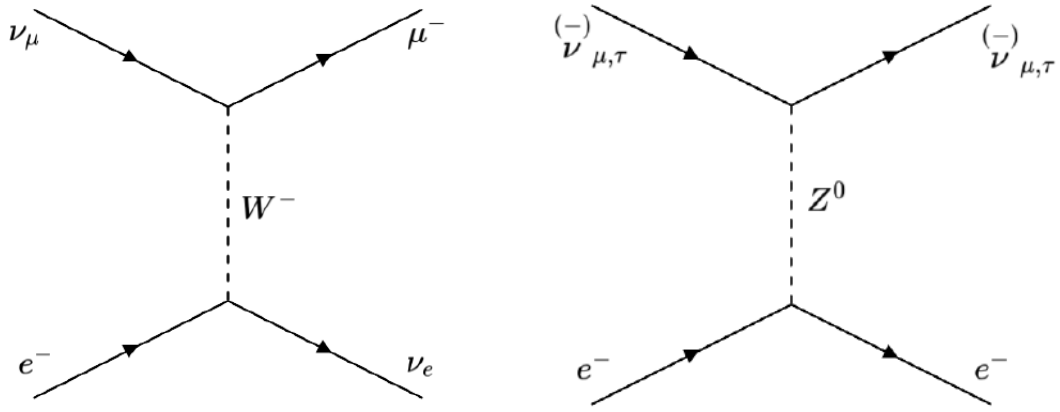

(A) Charged current (B) Neutral current

FIGURE 1.8: Tree level Feynman diagrams for the elastic scattering process $\bar{\nu}_e + e^- \rightarrow \bar{\nu}_e + e^-$.

The effects of the W and Z propagators can be neglected for low energy neutrinos. So, the above processes can be described by the effective charged-current and neutral-current Hamiltonians. The effective low energy Hamiltonian for the elastic scattering process in equation 1.27 is given by

$$\begin{aligned} H_{eff} &= \frac{G_F}{\sqrt{2}} \left\{ \left[\bar{\nu}_e \gamma^\mu (1-\gamma_5) e\right] \left[\bar{e} \gamma_\mu (1-\gamma_5) \nu_e\right] + \left[\bar{\nu}_e \gamma^\mu (1-\gamma_5) \nu_e\right] \left[\bar{e} \gamma_\mu (g_V - g_A \gamma_5) e\right] \right\} \\ &= \frac{G_F}{\sqrt{2}} \left\{ \left[\bar{\nu}_e \gamma^\mu (1-\gamma_5) \nu_e\right] \left[\bar{e} \gamma_\mu (1 + g_V - (1+g_A)\gamma_5) e\right] \right\}. \end{aligned} \tag{1.29}$$

The effective Hamiltonian for the process in equation 1.28 is given by

$$H_{eff} = \frac{G_F}{\sqrt{2}} \left\{ \left[\bar{\nu}_\alpha \gamma^\mu (1-\gamma_5) \nu_\alpha\right] \left[\bar{e} \gamma_\mu (g_V - g_A \gamma_5) e\right] \right\}. \tag{1.30}$$

1.5.2 Neutrino-electron quasielastic scattering

The quasielastic charged-current interaction takes place when muon neutrinos with energy above the μ production threshold

$$\nu_\mu + e^- \rightarrow \nu_e + \mu^-. \tag{1.31}$$

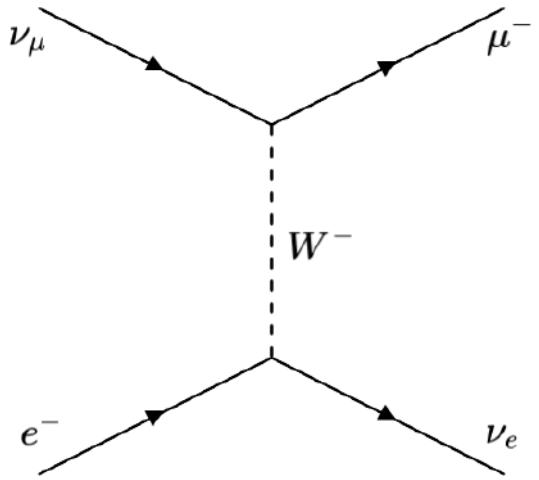

FIGURE 1.9: Feynman diagram for the quasielastic scattering process $\nu_\mu + e^- \rightarrow \nu_e + \mu^-$.

The effective Hamiltonian for this process is

$$H_{eff} = \frac{G_F}{\sqrt{2}} \left\{ \left[\bar{\mu} \gamma^\mu (1 - \gamma_5) \nu_\mu \right] \left[\bar{\nu}_e \gamma_\mu (1 - \gamma_5) e \right] \right\}. \tag{1.32}$$

1.5.3 Neutrino-nucleon quasielastic charge-current reactions

Neutrinos and anti-neutrinos interact with nucleons through quasielastic charge-current scattering which can be written as follows

$$\nu_l + n \rightarrow p + l^-, \tag{1.33}$$

$$\bar{\nu}_l + p \rightarrow n + l^+, \tag{1.34}$$

with $l = e, \mu, \tau$. The process in equation 1.34 with $l = e$, also called the inverse beta decay, has been used in the historical experiment of Cowan and Reines [24, 25, 26].

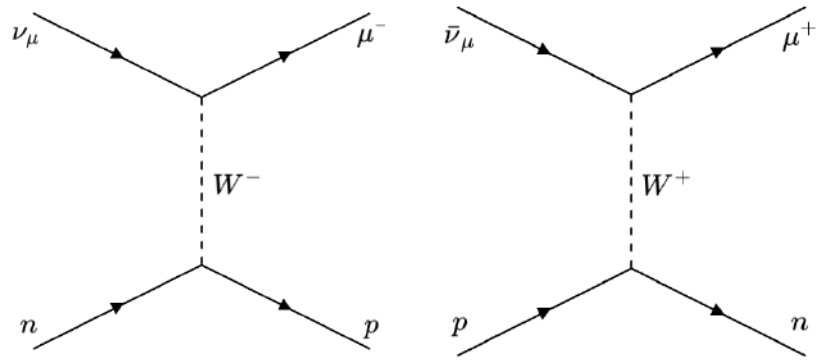

(A) (B)

FIGURE 1.10: Feynman diagrams for the quasielastic charge-current scattering processes $\nu_\mu + n \to p + \mu^-$ and $\bar{\nu}_\mu + p \to n + \mu^+$.

The matrix element for the process in figure 1.10a is give by

$$M = \langle \mu^-, p | H_{eff} | \nu_\mu, n \rangle = \frac{G_F \cos\theta_c}{\sqrt{2}} \left\{ \left[\bar{\mu} \gamma^\mu (1 - \gamma_5) \nu_\mu \right] \left[\bar{p} \gamma_\mu (F_V(q^2) + F_A(q^2)\gamma_5) n \right] \right\}$$
$$F_V(q^2) = \text{vector form factor}, \qquad \cos\theta_c = 0.975 \text{ (cabibo angle)},$$
$$F_A(q^2) = \text{axial-vector form factor} \tag{1.35}$$

1.5.4 Neutrino-nucleon elastic neutral-current reactions

Neutrinos and anti-neutrinos interact elastically with nucleons through the neutral current processes

$$\overset{(-)}{\nu}_l + N \to \overset{(-)}{\nu}_l + N, \tag{1.36}$$

where $N = p, n$. The matrix element for the above process is given by

$$M = \frac{i}{2\sqrt{2}} G_F \bar{\nu}(q_2) \gamma_\mu (1 - \gamma_5) \nu(q_1) \langle N(p_2) | J_Z^\mu | N(p_1) \rangle. \tag{1.37}$$

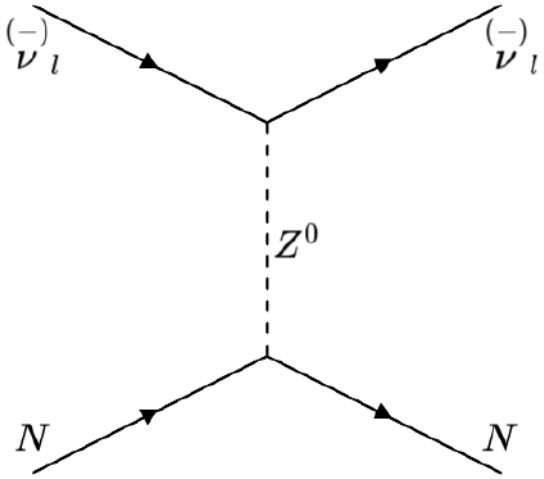

FIGURE 1.11: Feynman diagram for the elastic scattering process.

The most general form for the hadronic weak neutral current is

$$\langle N(p_2)|J_Z^\mu|N(p_1)\rangle = \langle N(p_2)|F_1^Z(Q^2) + F_2^Z(Q^2)\frac{i\sigma^{\mu\nu)}q_\nu}{2M_N} + F_A^Z(Q^2)\gamma^\mu\gamma_5|N(p_1)\rangle, \tag{1.38}$$

where $F_1^Z(Q^2)$, $F_1^Z(Q^2)$ and $F_A^Z(Q^2)$ are Dirac, Pauli and axial vector nucleon weak current form factors respectively.

1.5.5 Neutrino-nucleon resonant scattering

With sufficient energy, neutrino can transform the struck nucleon to an excited state. Through this mechanism, a baryon resonance is produced which quickly decays, most often to a nucleon and single pion final state.

$$\begin{aligned} \nu_l + N &\rightarrow N^* + l^- \\ N^* &\rightarrow \pi^+ + N' \end{aligned} \tag{1.39}$$

where N, N' = n, p. The resonant scattering is the most common means of single pion production in the intermediate neutrino energy region. Following are the seven possible resonant single pion reaction channels (both for

neutrino and antineutrino scattering), three charged current:

$$\begin{aligned} &\nu_\mu + p \to \mu^- + p + \pi^+, \qquad &&\bar{\nu}_\mu + p \to \mu^+ + p + \pi^-, \\ &\nu_\mu + n \to \mu^- + p + \pi^0, \qquad &&\bar{\nu}_\mu + p \to \mu^+ + n + \pi^0, \\ &\nu_\mu + n \to \mu^- + n + \pi^+, \qquad &&\bar{\nu}_\mu + n \to \mu^+ + n + \pi^-, \end{aligned} \tag{1.40}$$

and four neutral current:

$$\begin{aligned} &\nu_\mu + p \to \nu_\mu + p + \pi^0, \qquad &&\bar{\nu}_\mu + p \to \bar{\nu}_\mu + p + \pi^0, \\ &\nu_\mu + p \to \nu_\mu + n + \pi^+, \qquad &&\bar{\nu}_\mu + p \to \bar{\nu}_\mu + n + \pi^0, \\ &\nu_\mu + n \to \nu_\mu + n + \pi^0, \qquad &&\bar{\nu}_\mu + n \to \bar{\nu}_\mu + n + \pi^0, \\ &\nu_\mu + n \to \nu_\mu + p + \pi^-, \qquad &&\bar{\nu}_\mu + n \to \bar{\nu}_\mu + p + \pi^-. \end{aligned} \tag{1.41}$$

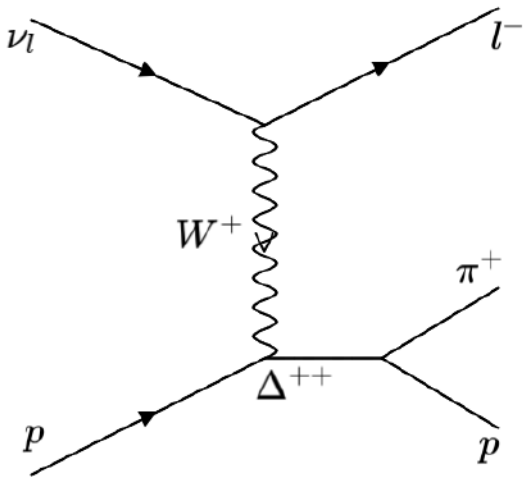

FIGURE 1.12: Feynman diagram for the neutrino-nucleon resonant scattering process $\nu_\mu + p \to \mu^- + p + \pi^+$.

1.5.6 Neutrino-nucleon charged-current deep inelastic scattering

Neutrinos with energies $E_\nu \gg m_N$ undergo the charged-current deep inelastic scattering with nucleons

$$\nu_l + N \to l^- + X, \qquad \bar{\nu}_l + N \to l^+ + X, \tag{1.42}$$

where $N = p, n$ and X represents a set final hadrons. The Fynman diagram for the process $\nu_l(p_\nu) + N(p_N) \rightarrow l^-(p_l) + X(p_X)$ at the lowest order weak interaction perturbation expansion is shown in figure 1.13.

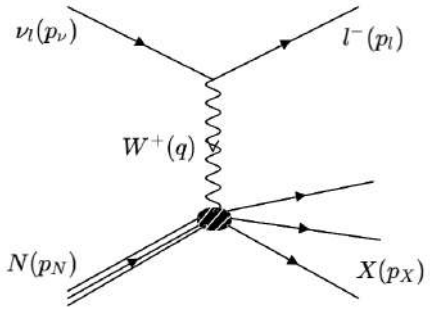

FIGURE 1.13: Feynman diagram for the neutrino-nucleon charged-current deep inelastic scattering process.

The underlying process for ν_μ-proton deep inelastic scattering is $\nu_\mu d \rightarrow \mu^- u$. In the limit $q^2 \ll m_W^2$, the W-boson propagator is $\approx i g_{\mu\nu}/m_W^2$. The matrix element for this process is given by

$$M_{fi} = \frac{g_W^2}{2m_W^2} g_{\mu\nu}[\bar{u}(p_l)\gamma^\mu \frac{1}{2}(1-\gamma^5)u(p_\nu)][\bar{u}(p_X)\frac{1}{2}\gamma^\nu(1-\gamma^5)u(p_N)]. \quad (1.43)$$

1.5.7 Neutrino-nucleon neutral-current deep inelastic scattering

The neutral-current deep inelastic scattering of high enrgy neutrinos with nucleons cab be expressed as follows

$$\overset{(-)}{\nu}_l + N \rightarrow \overset{(-)}{\nu}_l + X, \quad (1.44)$$

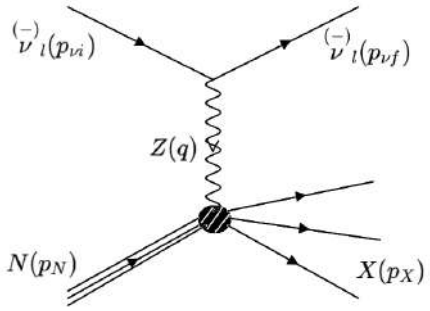

FIGURE 1.14: Feynman diagram for the neutrino-nucleon neutral-current deep inelastic scattering process.

The Feynman diagram of the above process at the lowest order in the weak interaction perturbation expansion is shown in figure 1.14. The kinematical variables are the same as in the charged-current deep inelastic scattering processes, with the obvious replacements $p_\nu \rightarrow p_{\nu i}$ and $p_l \rightarrow p_{\nu f}$, where $p_{\nu i}$ and $p_{\nu f}$ are, respectively, the four-momenta of the initial and final neutrinos.

$$M_{fi} = \frac{g_Z^2}{2m_Z^2} g_{\mu\nu}[\bar{u}(p_{\nu f})\gamma^\mu \frac{1}{2}(1-\gamma^5)u(p_{\nu i})][\bar{u}(p_X)\frac{1}{2}\gamma^\nu(1-\gamma^5)u(p_N)]. \quad (1.45)$$

Figure 1.15 summarizes the existing measurements of CC neutrino and anti-neutrino cross sections across the intermediate energy range [56].

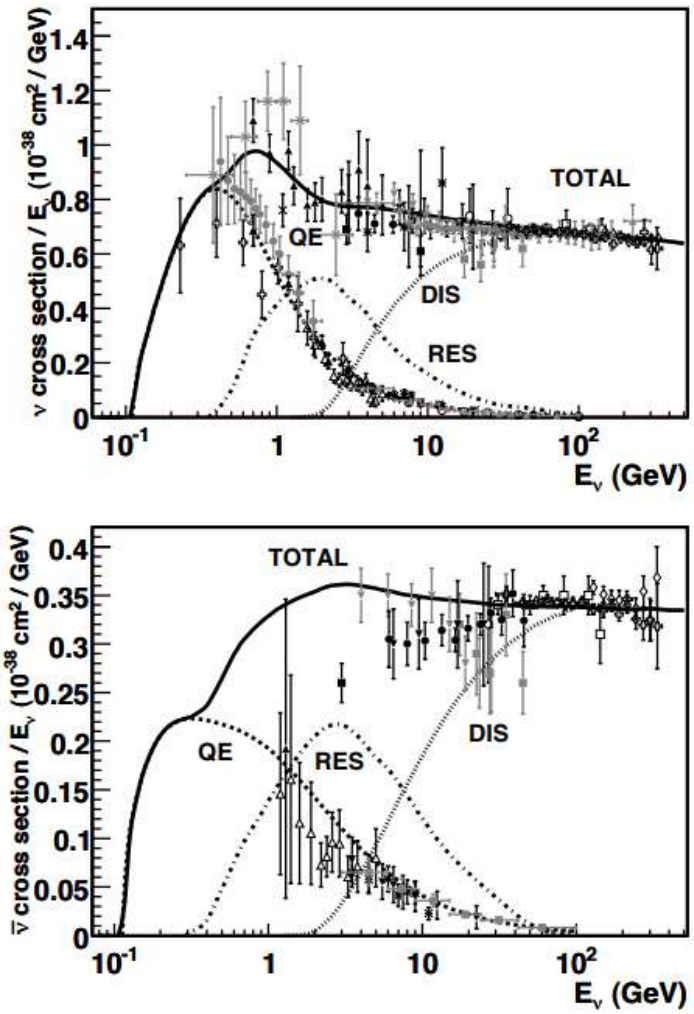

FIGURE 1.15: Total neutrino and antineutrino per nucleon CC cross sections.

Chapter 2

Introduction to neutrino oscillations

One of the most important recent discoveries in particle physics was the discovery of neutrino oscillations in atmospheric neutrino experiments [57] and in solar neutrino experiments [58, 59, 60, 61]. Neutrino oscillations were further studied in the long-baseline accelerator experiments K2K [62], MINOS [63] and T2K [11], in the long baseline reactor experiment KamLand [64] and in the short baseline reactor experiments Daya Bay [65], RENO [66] and Double Chooz [67]. The phenomenon of neutrino oscillations is the only signature of physics beyond standard model. In this chapter, we discuss the physics of neutrino ascillations.

2.1 Neutrino mixing

Neutrino ν_l ($l = e, \mu, \tau$) is produced in the charged current weak decays together with an l^+ or an l^- in the charged current neutrino processes (for example, muon neutrino ν_μ is produced in the decay $\pi^+ \rightarrow \mu^+ + \nu_\mu$ or produces μ^- in the process $\nu_\mu + N \rightarrow \mu^- + X$, etc). Since they are indentified through their interactions, they are called 'interaction' eigenstates or 'flavour eigenstates'. The charge on the produced lepton l^- or l^+ distinguishes between a neutrino or an anti-neutrino. Initially Pontecorvo, inspired by the possibility of $K^0 \leftrightarrow \overline{K^0}$ oscillations suggested by Gell-Mann and Pais [68], proposed the idea of $\nu \leftrightarrow \overline{\nu}$ oscillations [69, 70]. At that time, it was not known that the ν_e

and ν_μ were different. In 1962, Maki, Nakagawa and Sakata (MNS) proposed a theory of neutrino mixing based on two kinds of neutrinos ν_e and ν_μ [71]. Particle states of neutrinos which are different from the flavour eigenstates but are expressed by the linear combinations of the latter were introduced. Heisenberg uncertainty principle implies that in the neutrino production and detection processes it is impossible to reveal small neutrino mass-squared differences. The state of a flavor neutrino ν_l is a linear superposition of states of the neutrinos with definite masses,

$$|\nu_l\rangle = \sum_i U_{li}|\nu_i\rangle. \tag{2.1}$$

Here, U is called the mixing matrix, $|\nu_i\rangle$ is the state of neutrino with mass

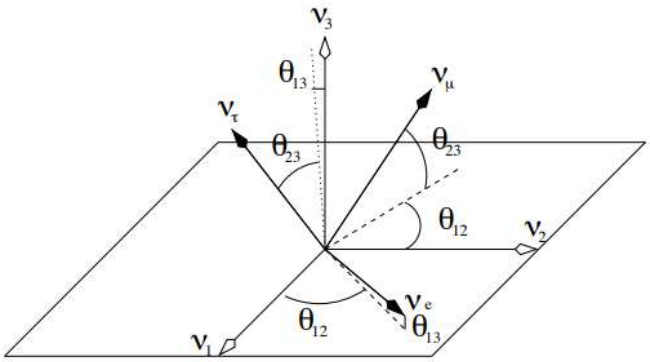

FIGURE 2.1: Flavour and mass axes mixing angles [72]

m_i, momentum $\overrightarrow{p}$ and energy $E_i = \sqrt{p^2 + m_i^2} \approx p + \frac{m_i^2}{2E}$.

Based on the MNS proposal, Eliezer and Swift [73], Fritzsch and Minkowski [74], Bilenky and Pontecorvo [75, 76, 77] developed the theory of two flavour neutrino oscillations in vacuum.

2.2 Two flavour oscillations in vacuum

Here we assume that there are only two flavors ν_e and ν_{mu}. Neutrinos are produced in weak interactions in eigenstates of definite lepton number ($|\nu_e\rangle$ or $|\nu_\mu\rangle$) which are not energy eigenstates. $|\nu_1\rangle$, $|\nu_2\rangle$ are the eigenstates with

eigenvalues m_1 and m_2 for neutrinos at rest. A neutrino of type i with momentum p is an energy eigenstate with eigenvalues $E_i = \sqrt{m_i^2 + p^2}$. A unitary matrix U connects these two sets of states which we can write as

$$U = \begin{pmatrix} U_{\alpha 1} & U_{\alpha 2} \\ U_{\beta 1} & U_{\beta 2} \end{pmatrix}. \tag{2.2}$$

The $|\nu_e\rangle$ and $|\nu_\mu\rangle$ can be written in terms of mass states $|\nu_1\rangle$ and $|\nu_2\rangle$

$$\begin{pmatrix} |\nu_e\rangle \\ |\nu_\mu\rangle \end{pmatrix} = U \begin{pmatrix} |\nu_1\rangle \\ |\nu_2\rangle \end{pmatrix} = \begin{pmatrix} U_{e1} & U_{e2} \\ U_{\mu 1} & U_{\mu 2} \end{pmatrix} \begin{pmatrix} |\nu_1\rangle \\ |\nu_2\rangle \end{pmatrix} \tag{2.3}$$

or we can write more compactly as

$$|\nu_\alpha\rangle = \sum_{i=1,2} U_{\alpha i} |\nu_i\rangle \qquad \alpha = e, \mu. \tag{2.4}$$

Suppose a neutrino beam consisting of a flavour state $|\nu_\alpha(0\rangle$ with a definite flavour α at time $t = 0$ is propagated in free space towards a detector at a distance L. The eigenstates $|\nu_1\rangle$ and $|\nu_2\rangle$ propagate as per the time-dependent Schrodinger equation in free space

$$i\frac{\partial}{\partial t}|\nu_i t\rangle = E_i |\nu_i t\rangle \qquad i = 1, 2. \tag{2.5}$$

The mass eigenstate at a later time t is given by

$$|\nu_j(t)\rangle = e^{-iE_j t}|\nu_j(0)\rangle = e^{-i\phi_j}|\nu_j(0)\rangle. \tag{2.6}$$

The flavour state $|\nu_\alpha\rangle$ at time t will be

$$|\nu_\alpha(t)\rangle = \sum_{j=1,2} U_{\alpha j}|\nu_j(t)\rangle = \sum_{j=1,2} U_{\alpha j} e^{-i\phi_j}|\nu_j(0)\rangle. \tag{2.7}$$

Inverting the mixing matrix yields

$$|\nu_j(0)\rangle = \sum_\gamma U^*_{\gamma j}|\nu_\gamma(0)\rangle. \tag{2.8}$$

Combining equations 2.7 and 2.8 gives

$$\begin{aligned} |\nu_\alpha(t)\rangle &= \sum_{j=1,2} U_{\alpha j} e^{-i\phi_j} \sum_\gamma U^*_{\gamma j} |\nu_\gamma(0)\rangle \\ &= \sum_\gamma \sum_j U^*_{\gamma j} e^{-i\phi_j} U_{\alpha j} |\nu_\gamma(0)\rangle. \end{aligned} \tag{2.9}$$

The amplitude for detecting a $|\nu_\beta\rangle$ at time t

$$\begin{aligned} A(|\nu_\alpha(0)\rangle \to |\nu_\beta(t)\rangle) &= \langle \nu_\beta(t)|\nu_\alpha(0)\rangle \\ &= \sum_\gamma \sum_j U_{\gamma j} e^{i\phi_j} U^*_{\beta j} \langle \nu_\gamma 0|\nu_\alpha(0)\rangle. \end{aligned} \tag{2.10}$$

Orthogonality of the flavour states leads to

$$= \sum_j U_{\alpha j} U^*_{\beta j} = \delta_{\alpha\beta} \tag{2.11}$$

We obtain the oscillation probability by squaring the amplitude. Using the orthogonality relation, we obtain the probability to be

$$\begin{aligned} &P(|\nu_\alpha\rangle \to |\nu_\beta\rangle) = |A(|\nu_\alpha 0\rangle \to |\nu_\beta t\rangle)|^2 \\ &= |\sum_j U_{\alpha j} e^{i\phi_j} U^*_{\beta j}|^2 \\ &= \sum_j U_{\alpha j} e^{i\phi_j} U^*_{\beta j} \sum_k U^*_{\alpha k} e^{-i\phi_k} U_{\beta k} \\ &= \sum_k \sum_j U_{\alpha j} U^*_{\beta j} U^*_{\alpha k} U_{\beta k} e^{-i(\phi_k - \phi_j)} \\ &= (|U_{\beta 1}|^2 |U_{\alpha 1}|^2 + |U_{\beta 2}|^2 |U_{\alpha 2}|^2) + U_{\alpha 1} U^*_{\beta 1} U_{\alpha 2} U^*_{\beta 2} (e^{i(\phi_2 - \phi_1)} + e^{-i(\phi_2 - \phi_1)}) \\ &= (|U_{\beta 1}|^2 |U_{\alpha 1}|^2 + |U_{\beta 2}|^2 |U_{\alpha 2}|^2) + 2U_{\alpha 1} U^*_{\beta 1} U_{\alpha 2} U^*_{\beta 2} cos(\phi_2 - \phi_1). \end{aligned} \tag{2.12}$$

Here the unitary matrix U is a 2×2 rotation matrix which rotates a vector in the flavour basis into a vector in the mass basis:

$$U = \begin{pmatrix} cos\theta & sin\theta \\ -sin\theta & cos\theta \end{pmatrix}. \tag{2.13}$$

So the oscillation probability is

$$\begin{aligned} P(|\nu_\alpha\rangle \to |\nu_\beta\rangle) &= (sin^2\theta cos^2\theta + cos^2\theta sin^2\theta) + 2(cos\theta)(-sin\theta)(sin\theta)(cos\theta)cos(\phi_2 - \phi_1) \\ &= 2cos^2\theta sin^2\theta(1 - cos(\phi_2 - \phi_1)) \\ &= sin^2(2\theta)sin^2\left(\frac{\phi_2 - \phi_1}{2}\right). \end{aligned} \tag{2.14}$$

The phase difference is

$$\phi_2 - \phi_1 = (E_2 - E_1)t. \tag{2.15}$$

Since they have very small mass (< 2 eV), neutrinos with energies $\simeq$ 1 MeV are ultra relativistic. Then we can assume that $t = L$, where L is the distance between source and detector. In the ultra relativistic approximation

$$E_i = \sqrt{p^2 + m_i^2} = p\sqrt{1 + \frac{m_i^2}{p^2}} \approx p\left(1 + \frac{m_i^2}{2p^2}\right), \tag{2.16}$$

where we made the equal momentum approximation, *i.e.* we assumed that both mass eigenstates have the same momentum. In this approximation, we get

$$\phi_2 - \phi_1 = \left(\frac{m_1^2}{2p} - \frac{m_2^2}{2p}\right)L = \frac{\Delta m^2 L}{2E}, \tag{2.17}$$

where $\Delta m^2 = m_1^2 - m_2^2$. Since the neutrinos are ultra relativistic, we approximated $p \simeq E$, which is the average energy of E_1 and E_2. The oscillation probabilities remain essentially the same even without the equal momentum approximation. However, this approximation simplifies the algebra considerably.

Using equation 2.17 in equation 2.14, we get

$$P(|\nu_\alpha\rangle \to |\nu_\beta\rangle) = sin^2(2\theta)sin^2\left(\frac{\Delta m^2 L}{4E}\right). \tag{2.18}$$

Taking care of $\hbar$ and c values and writing L in units of meters and E in units of MeV, we get

$$P(|\nu_\alpha\rangle \rightarrow |\nu_\beta\rangle) = sin^2(2\theta) sin^2\left(1.27\Delta m^2 \frac{L}{E}\right). \tag{2.19}$$

The corresponding survival probability is

$$P(|\nu_\alpha\rangle \rightarrow |\nu_\alpha\rangle) = 1 - P(|\nu_\alpha\rangle \rightarrow |\nu_\beta\rangle). \tag{2.20}$$

A non zero oscillation probability $P(|\nu_e\rangle \rightarrow |\nu_\mu\rangle)$ implies that the mixing angle $\theta \neq 0$ and $\Delta m^2 \neq 0$. Hence, neutrinos should be massive and the masses should be non-degenerate $(m_1 \neq m_2)$. The two flavour oscillations are similar for both neutrinos and anti-neutrinos.

2.3 Three flavour oscillations in vacuum

With the discovery of ν_τ, it became imperative to consider the mixing of all the three flavour states ν_e, ν_μ and ν_τ which results in three mass eigenstates ν_1, ν_2 and ν_3 with masses m_1, m_2 and m_3 respectively. This implies that the mixing matrix is (i) 3×3, (ii) complex and (iii) unitary

$$U = \begin{pmatrix} U_{\alpha 1} & U_{\alpha 2} & U_{\alpha 3} \\ U_{\beta 1} & U_{\beta 2} & U_{\beta 3} \\ U_{\gamma 1} & U_{\gamma 2} & U_{\gamma 3} \end{pmatrix}. \tag{2.21}$$

This is known as the Pontecorvo-Maka-Nakagawa-Sakata (PMNS) matrix which connects the three flavour eigenstates to the three mass eigenstates of neutrino as follows:

$$\begin{pmatrix} |\nu_e\rangle \\ |\nu_\mu\rangle \\ |\nu_\tau\rangle \end{pmatrix} = \begin{pmatrix} U_{e1} & U_{e2} & U_{e3} \\ U_{\mu 1} & U_{\mu 2} & U_{\mu 3} \\ U_{\tau 1} & U_{\tau 2} & U_{\tau 3} \end{pmatrix} \begin{pmatrix} |\nu_1\rangle \\ |\nu_2\rangle \\ |\nu_3\rangle \end{pmatrix}. \tag{2.22}$$

The fact that the matrix is unitary means that we can also write

$$\begin{pmatrix} |\nu_1\rangle \\ |\nu_2\rangle \\ |\nu_3\rangle \end{pmatrix} = \begin{pmatrix} U_{e1}^* & U_{\mu 1}^* & U_{\tau 1}^* \\ U_{e2}^* & U_{\mu 2}^* & U_{\tau 2}^* \\ U_{e3}^* & U_{\mu 3}^* & U_{\tau 3}^* \end{pmatrix} \begin{pmatrix} |\nu_e\rangle \\ |\nu_\mu\rangle \\ |\nu_\tau\rangle \end{pmatrix} \tag{2.23}$$

and

$$\begin{pmatrix} U_{e1} & U_{e2} & U_{e3} \\ U_{\mu 1} & U_{\mu 2} & U_{\mu 3} \\ U_{\tau 1} & U_{\tau 2} & U_{\tau 3} \end{pmatrix} \begin{pmatrix} U_{e1}^* & U_{\mu 1}^* & U_{\tau 1}^* \\ U_{e2}^* & U_{\mu 2}^* & U_{\tau 2}^* \\ U_{e3}^* & U_{\mu 3}^* & U_{\tau 3}^* \end{pmatrix} = \begin{pmatrix} 1 & 0 & 0 \\ 0 & 1 & 0 \\ 0 & 0 & 1 \end{pmatrix}, \tag{2.24}$$

which gives the following useful relations

$$\begin{aligned} U_{e1}U_{e1}^* + U_{\mu 1}U_{\mu 1}^* + U_{\tau 1}U_{\tau 1}^* &= 1 \\ U_{e2}U_{e2}^* + U_{\mu 2}U_{\mu 2}^* + U_{\tau 2}U_{\tau 2}^* &= 1 \\ U_{e3}U_{e3}^* + U_{\mu 3}U_{\mu 3}^* + U_{\tau 3}U_{\tau 3}^* &= 1 \\ U_{e1}U_{\mu 1}^* + U_{e2}U_{\mu 2}^* + U_{e3}U_{\mu 3}^* &= 0 \\ U_{e1}U_{\tau 1}^* + U_{e2}U_{\tau 2}^* + U_{e3}U_{\tau 3}^* &= 0 \\ U_{\mu 1}U_{\tau 1}^* + U_{\mu 2}U_{\tau 2}^* + U_{\mu 3}U_{\tau 3}^* &= 0. \end{aligned} \tag{2.25}$$

To calculate the three flavour oscillation probabilities, we proceed just like the two flavour case. Assume that a neutrino is produced at $t = 0$ in a pure $|\nu_\alpha\rangle$ state.

$$|\psi(t=0)\rangle = U_{\alpha 1}|\nu_1\rangle + U_{\alpha 2}|\nu_2\rangle + U_{\alpha 3}|\nu_3\rangle \tag{2.26}$$

The wavefunction at a later time t is given by

$$\begin{aligned} |\psi(t)\rangle &= U_{\alpha 1}|\nu_1\rangle\, e^{-iE_1 t} + U_{\alpha 2}|\nu_2\rangle\, e^{-iE_2 t} + U_{\alpha 3}|\nu_3\rangle\, e^{-iE_3 t} \\ &= U_{\alpha 1}|\nu_1\rangle\, e^{-i\phi_1} + U_{\alpha 2}|\nu_2\rangle\, e^{-iphi_2} + U_{\alpha 3}|\nu_3\rangle\, e^{-i\phi_3} \quad \alpha = e, \mu, \end{aligned} \tag{2.27}$$

As in the two flavor case, we assume ultra relativistic neutrinos and make the equal momentum approximation. This leads to

$$\phi_i = E_i t = \left(p + \frac{m_i^2}{2p} \right) L. \tag{2.28}$$

Combining equation 2.22 and 2.25 gives

$$\begin{aligned} |\psi(t)\rangle = U_{\alpha 1} e^{-i\phi_1} (U_{e1}^* |\nu_e\rangle + U_{\mu 1}^* |\nu_\mu\rangle + U_{\tau 1}^* |\nu_\tau\rangle) \\ + U_{\alpha 2} e^{-i\phi_2} (U_{e2}^* |\nu_e\rangle + U_{\mu 2}^* |\nu_\mu\rangle + U_{\tau 2}^* |\nu_\tau\rangle) \\ + U_{\alpha 3} e^{-i\phi_3} (U_{e3}^* |\nu_e\rangle + U_{\mu 3}^* |\nu_\mu\rangle + U_{\tau 3}^* |\nu_\tau\rangle), \end{aligned} \tag{2.29}$$

which can be rearranged as

$$\begin{aligned} |\psi(t)\rangle = (U_{\alpha 1} U_{e1}^* e^{-i\phi_1} + U_{\alpha 2} U_{e2}^* e^{-i\phi_2} + U_{\alpha 3} U_{e3}^* e^{-i\phi_3}) |\nu_e\rangle \\ + (U_{\alpha 1} U_{\mu 1}^* e^{-i\phi_1} + U_{\alpha 2} U_{\mu 2}^* e^{-i\phi_2} + U_{\alpha 3} U_{\mu 3}^* e^{-i\phi_3}) |\nu_\mu\rangle. \\ + (U_{\alpha 1} U_{\tau 1}^* e^{-i\phi_1} + U_{\alpha 2} U_{\tau 2}^* e^{-i\phi_2} + U_{\alpha 3} U_{\tau 3}^* e^{-i\phi_3}) |\nu_\tau\rangle \end{aligned} \tag{2.30}$$

The oscillation probability $P(\nu_\alpha \to \nu_\beta)$ is

$$P(\nu_\alpha \to \nu_\beta) = |\langle \nu_\beta | \psi(t) \rangle|^2 = \left| U_{\alpha 1} U_{\beta 1}^* e^{-i\phi_1} + U_{\alpha 2} U_{\beta 2}^* e^{-i\phi_2} + U_{\alpha 3} U_{\beta 3}^* e^{-i\phi_3} \right|^2. \tag{2.31}$$

Using the identity

$$|z_1 + z_2 + z_3|^2 = |z_1|^2 + |z_2|^2 + |z_3|^3 + 2\Re(z_1 z_2^* + z_1 z_3^* + z_2 z_3^*), \tag{2.32}$$

equation 2.31 can eventually be written as

$$\begin{aligned} P(\nu_\alpha \to \nu_\beta) = \delta_{\alpha\beta} - 4 \sum_{i>j} Re(U_{\alpha i}^* U_{\beta i} U_{\alpha j} U_{\beta j}^*) sin^2 \left(\Delta m_{ij}^2 \frac{L}{4E} \right) \\ + 2 \sum_{i>j} Im(U_{\alpha i}^* U_{\beta i} U_{\alpha j} U_{\beta j}^*) sin \left(\Delta m_{ij}^2 \frac{L}{2E} \right), \end{aligned} \tag{2.33}$$

where $\Delta m^2_{ij} = m^2_i - m^2_j$. The PMNS matrix is expressed by three rotation matrices and a complex phase

$$U = \begin{pmatrix} 1 & 0 & 0 \\ 0 & cos\theta_{23} & sin\theta_{23} \\ 0 & -sin\theta_{23} & cos\theta_{23} \end{pmatrix} \begin{pmatrix} cos\theta_{13} & 0 & sin\theta_{13}e^{-i\delta_{CP}} \\ 0 & 1 & 0 \\ -sin\theta_{13}e^{-i\delta_{CP}} & 0 & cos\theta_{13} \end{pmatrix} \begin{pmatrix} cos\theta_{12} & sin\theta_{12} & 0 \\ -sin\theta_{12} & cos\theta_{12} & 0 \\ 0 & 0 & 1 \end{pmatrix} \tag{2.34}$$

or

$$U = \begin{pmatrix} c_{12}c_{13} & s_{12}c_{13} & s_{13}e^{-i\delta_{CP}} \\ -s_{12}c_{23} - c_{12}s_{23}s_{13}e^{i\delta_{CP}} & c_{12}c_{23} - s_{12}s_{13}s_{23}e^{i\delta_{CP}} & c_{13}s_{23} \\ s_{12}s_{23} - c_{12}s_{13}c_{23}e^{i\delta_{CP}} & -c_{12}s_{23} - s_{12}s_{13}c_{23}e^{i\delta_{CP}} & c_{13}c_{23} \end{pmatrix}, \tag{2.35}$$

where $c_{ij} = \cos\theta_{ij}$ and $s_{ij} = \sin\theta_{ij}$. Probabilities with $\alpha \neq \beta$ are called "oscillation probabilities" and the probabilities with $\alpha = \beta$ are called "survival probabilties". The expression for survival probability simplifies to

$$P(\nu_\alpha \to \nu_\alpha) = 1 - 4\sum_{i>j} |U_{\alpha i}|^2 |U_{\alpha j}|^2 sin^2\left(\Delta m^2_{ij}\frac{L}{4E}\right) \tag{2.36}$$

The oscillation probability for the anti-neutrino case is given by

$$\begin{aligned} P(\bar{\nu}_\alpha \to \bar{\nu}_\beta) = \delta_{\alpha\beta} &- 4\sum_{i>j} Re(U^*_{\alpha i}U_{\beta i}U_{\alpha j}U^*_{\beta j}) sin^2\left(\Delta m^2_{ij}\frac{L}{4E}\right) \\ &-2\sum_{i>j} Im(U^*_{\alpha i}U_{\beta i}U_{\alpha j}U^*_{\beta j}) sin\left(\Delta m^2_{ij}\frac{L}{2E}\right) \end{aligned} \tag{2.37}$$

2.3.1 Neutrino mass heirarchy

If the data from the solar neutrino experiments [58, 59, 60, 61] is interpreted in terms of two flavor neutrino oscillations, a mass squared difference Δm^2_{sol} in the range $\left(10^{-5}, 10^{-4}\right)$ eV^2 is obtained. Similarly, when the atmospheric neutrino data is interpreted in terms of two flavor neutrino oscillations, a mass squared difference Δm^2_{atm} in the range $\left(10^{-3}, 10^{-2}\right)$ eV^2 is obtained. In three flavor oscillations, we can define two independent mass squared differences: $\Delta m^2_{21} = m^2_2 - m^2_1$ and $\Delta m^2_{31} = m^2_3 - m^2_1$. The third mass squared difference is a linear combination of these two. Without loss of generality, we

can identify $\Delta m^2_{\text{sol}} = \Delta m^2_{21}$ and $\Delta m^2_{\text{atm}} = \Delta m^2_{31}$. Given that Δm^2_{atm} is more than an order of magnitude larger than Δm^2_{sol}, we can say that $\Delta m^2_{32} \approx \Delta m^2_{31}$. Solar neutrino data require Δm^2_{21} to be positive but there is no constraint on the sign of Δm^2_{31} so far. This sign ambiguity, called "neutrino mass hierarchy problem", leads to two possible patterns of neutrino masses: (a) $m_3 > m_2 > m_1$ called "normal heirarchy (NH)" and (b) $m_2 > m_1 > m_3$ called "inverted heirarchy (IH)". These two patterns are shown schematically in the figure 2.2.

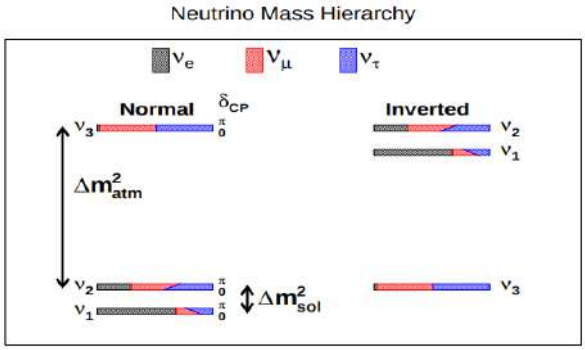

FIGURE 2.2: Normal and inverted netrino mass heirarch [78].

2.4 Effective 2-flavour oscillations from 3-flavour oscillations

To observe the effect of neutrino oscillations, it is desirable to have

$$|\Delta m^2_{ij}| \frac{L}{E} \sim 1. \tag{2.38}$$

Since Δm^2_{21} is much smaller than $|\Delta m^2_{31}|$, it is possible to satisfy the above condition for either Δm^2_{21} or $|\Delta m^2_{31}|$ in a given experiment. If $|\Delta m^2_{21}| L/E \sim 1$ is satisfied, $|\Delta m^2_{31}| L/E \gg 1$ and the corresponding oscillations are averaged out. If $|\Delta m^2_{31}| L/E \sim 1$ is satisfied, $|\Delta m^2_{21}| L/E \ll 1$ and the corresponding oscillations will be too small to be observable. These features enable us to simplify the expressions of three flavor survival probabilities into those of effective two flavor survival probabilities.

2.4.1 Long baseline reactor experiments

These experimets utilize large fluxes of electron anti-neutrinos, with energies of the order of a few MeV, produced in nuclear reactors by β^--decays of heavy nuclie. The experiments are designed such that

$$\Delta m^2_{21}\frac{L}{E} \sim 1 \qquad \text{and} \qquad \Delta m^2_{31}\frac{L}{E} >> 1. \tag{2.39}$$

The oscillations due to m^2_{31} are averaged out due to either the size of the production region or experimental energy resolution. For $L/E \sim 10^4$ m-MeV^{-1} equation 2.36 gives the effective survival probability

$$P(\bar{\nu}_e \to \bar{\nu}_e) = 1 - \cos^2(\theta_{13})\sin^2(2\theta_{12})\sin^2\left(1.27\Delta m^2_{21}\frac{L}{E}\right) - \frac{1}{2}\sin^2(2\theta_{13}). \tag{2.40}$$

CHOOZ experiment [79] has shown that $\sin^2(2\theta_{13}) \leq 0.1$. In the approximation of neglecting θ_{13}, we get the effective two flavor survival probability

$$P(\bar{\nu}_e \to \bar{\nu}_e) = 1 - \sin^2(2\theta_{12})\sin^2\left(1.27\Delta m^2_{21}\frac{L}{E}\right). \tag{2.41}$$

KamLAND: Kamioka Liquid Scintillator AntiNeutrino Detector (KamLAND) experiment was proposed in 1994 to study the oscillations of electron anti-neutrinos emitted from far away nuclear reactors. It is located at the Kamioka mine beneath the mountains of Japanese Alps, about 200 km west of Tokyo. Almost all the 26 reactors are located nearly 180 km away from the Kamioka mine. The KamLAND liquid scintillator (LS) is a chemical cocktail of 80% dodecane, 20% pseudocumene (1,2,4-trimethylbenzene) and 1.36 g/liter of PPO (2,5-diphenyloxazole) as a fluorescent medium. After entering the detector, electron anti-neutrino undergoes inverse β-decay. The emitted positron deposits its energy and then anhilates to two γ-rays (each with 511 keV). Thus, the inverse β-decay reaction provides a clear signature of the prompt e^+ followed by delayed photon due to neutron absorption, with definite time correlation. Following critera were used to identify the $\bar{\nu}_e$ events

- fiducial volume (radius < 5m),
- prompt e^+ and delayed γ time correlation 0.5 μs < ΔT < 660 μs,
- vertex correlation ΔR(| prompt - delay |)<1.6m,
- delayed γ energy (1.8<$E_{delayed}$<2.6 MeV)

This experiment has observed both the flux suppression and spectral distortion caused by neutrino oscillation and gave $\Delta m^2_{21} = (8.2 \pm 0.6) \times 10^{-5} eV^2$ and $tan^2\theta_{21} = 0.1 - 10$ [64].

2.4.2 Long baseline accelerator experiment

These neutrino experiments are operated with muon neutrino or anti-neutrino beam produced by the decay in flight of pions and kaons created by shooting a proton beam to a target. The source-detector distance is about $10^2 - 10^3$ km. If the experiment is designed such that

$$\Delta m^2_{31} \frac{L}{2E} \sim 1 \qquad \text{and} \qquad \Delta m^2_{21} \frac{L}{2E} << 1, \tag{2.42}$$

then the oscillations due to the smaller Δm^2_{21} remain a small correction which can be neglected. The effective muon neutrino survival probability with $\theta_{13} << 1$ is given by

$$P(\nu_\mu \to \nu_\mu) = 1 - \sin^2(2\theta_{23}) \sin^2 \left(1.27 \Delta m^2_{32} \frac{L}{E}\right) \tag{2.43}$$

MINOS: Main Injector Neutrino Oscillations Search(MINOS) uses an accelerator produced beam from the Fermilab (USA) Main Injector accelerator. The peak of the low energy neutrino beam is adjusted to be about 3 GeV. The MINOS far detector is a magnetized steel scintillator detector with 5 ktons of mass located 735 km away in the Soudan mine; in addition MINOS has a near detector using the same tech- nology with 1 kton of mass placed $\sim$ 1 km away from the beam production target. Both near and far detectors are placed on the NuMI beam line axis. These detectors are tracking, sampling

calorimeters, consist of 2.54 cm thick iron plates interleaved with scintillator planes composed of 1 cm thick, 4.1 cm wide alternating orthogonal scintillator strips with read out using multi-anode photomultipliers. The Near Detector has a 23.7t fiducial mass and the Far Detector has a 4.2 kt fiducial mass. Both detectors are magnetized with a toroidal magnetic field to focus negatively charged particles. A charged current interaction of a muon neutrino in MINOS is characterized by a muon track with one or more hadronic showers [80]. MINOS obtained $|\Delta m^2_{32}| = (2.43 \pm 0.13) \times 10^{-3} eV^2$ (68% C.L) and $\sin^2(2\theta_{23}) = 0.90$ (90% C.L) [81].

2.4.3 Short baseline reactor experiment

These experiments also utilize large isotropic fluxes of electron antineutrinos produced in nuclear reactors by β^--decays of heavy nuclei. A typical energy of reactor ν_e's is of the order of a few MeV and the source–detector distance in the reactor short baseline experiments is ~ 1 km with following condition

$$\Delta m^2_{31} \frac{L}{2E} \sim 1 \qquad \text{and} \qquad \Delta m^2_{21} \frac{L}{2E} << 1. \tag{2.44}$$

With the above approximations, the survival probability for these experiments becomes

$$P(\bar{\nu}_e \to \bar{\nu}_e) = 1 - \sin^2(2\theta_{13}) \sin^2\left(1.27 \Delta m^2_{31} \frac{L}{E}\right). \tag{2.45}$$

Daya Bay: The Daya Bay experiment is located at the Daya Bay nuclear power complex near Shenzhen, China. It had three cylindrical nested fluid volumes separated by two acrylic vessels. The innermost volume contansied 20 tons of linearly-alkyl-benzene-based liquid scintillator, doped with 0.1% gadolinium. Scintillation light was collected by reflectors on the top and bottom of the detector and by 192 photomultiplier tubes (PMTs) on the

walls of the detectors. The Daya Bay analysis used coincident events to reduce ambient radiative background. The detectors were optimized to observe the prompt positron and delayed neutron of the inverse beta decay process. Events were seleceted after rejecting flashing PMT events and applying a muon veto. Inverse beta decay candidate were chosen from promt-delayed coindence events which satisfied the following cuts

- energy of prompt signal between 0.7 and 12 MeV,
- delayed signal energy between 6 and 12 MeV,
- time between prompt and delayed events between 1 and 200 μ s,
- no signals 400 μ s before or 200 μ s after the delayed neutron event.

In the standard 3-neutrino framework, Daya Bay yields $\sin^2 2\theta_{13} = 0.089 \pm 0.010$ [82]

RENO: Reactor Experiment for Neutrino Oscillation (RENO) is another short baseline reactor neutrino oscillation experiment in South Korea. It uses anti-neutrinos emitted from the Yonggwang nuclear power plant. There are identical near and far $\bar{\nu}_e$ detectors located at 294 m and 1383 m, respectively, from the center of six reactor cores. The reactor $\bar{\nu}_e$ is detected through the inverse β-decay process using hydrocarbon liquid scintillator with 0.1% Gadolinium (Gd) as target. The inverse β-decay events are selected against background with following criterion

- coincidence of a prompt positron signal and a delayed signal from neutron capture by Gd(n-Gd) ($\Delta T \sim 28 \mu s$),
- the prompt signal energy $\sim$ 1.02 MeV (two γ-rays from positron annihilation in addition to the positron kinetic energy,
- The delayed signal with several γ-rays with total energy of $\sim$ 8 MeV.

The best-fit value obtained by RENO is $\sin^2 2\theta_{13} = 0.113 \pm 0.013$ [83]

Double Chooz: Double Chooz is also a short-baseline neutrino oscillation experiment in Chooz, France. The far detector is located at an average distance

of 1,050 m from the two reactor cores, in a hill topology with 300 meters water equivalent (m.w.e.) rock overburden to shield cosmic muons. Double Chooz has a calorimetric liquid scintillator detector made of four concentric cylindrical vessels optimized for detection of reactor neutrinos. The central region of the detector consists of three concentric cylinders, collectively called the inner detector (ID). The innermost cylinder is the 10.3 m^3 target. This is surrounded by a γ-catcher (GC) (22.5 m3). The target liquid is a PXE-based liquid scintillator doped with Gd at a concentration of 1 g/l, while the γ-catcher (GC) liquid is an undoped liquid scintillator. Outside the γ-catcher is the buffer, a 105 cm thick layer of non-scintillating mineral oil contained in a stainless steel tank. Light from the target and γ-catcher volumes is collected by 390 low background 10-inch PMTs installed on the inner wall of the buffer tank. Outside the buffer tank, and optically isolated from it, is the inner veto (IV), a 50 cm thick layer of liquid scintillator in a steel tank. The IV is equipped with 78 8-inch PMTs and serves as a veto for cosmic rays and fast neutrons entering the detector. The IV is surrounded by a 15 cm thick layer of demagnetized steel which suppresses γ-catcher from radioactivity in the surrounding rock. Above the IV is the outer veto (OV) detector, a scintillator-strip-based muon tracking system. The inverse β-decay signal is a twofold coincidence of a prompt positron energy deposition, E_{prompt}, and a delayed gamma energy deposition, E_{delay}, resulting from a neutron capture on hydrogen or Gd. The separation in time and space, Δt and Δr, of the coincident events are determined by neutron capture physics. Neutron capture times are 200 μs in the γ-catcher and 30 μs in the target, where the presence of Gd greatly increases the neutron capture probability [84]. The best value obtained by Double Chooz is $\sin^2 2\theta_{13} = 0.090 \pm 0.035$ [85].

2.4.4 Sign of Δm^2_{31}, octant of θ_{23} and value of δ_{CP}

The data from solar neutrino experiments have established that Δm^2_{21} is positive but there is no information on the sign of Δm^2_{31}. Long baseline experiments have shown that the value of $\sin^2 \theta_{23}$ is close to 1, which gives rise to

the octant ambiguity of θ_{23}. Following are the unaswered quastions about neutrino oscillations:

- what is the sign of Δm^2_{31} and correct neutrino mass hierarchy? +ve (NH) or -ve (IH)?
- what is the octant of θ_{23}? $\theta_{23} < \pi/4$ or $\theta_{23} > \pi/4$?
- What is the value of CP violating phase $\delta_{\rm CP}$?

To answer these quastions, various experiments are running and are being planned.

1. ***T2K and NOνA***: These are the long baseline accelator neutrino experiments which measure $\mathrm{P}(\nu_\mu \rightarrow \nu_e)$ and $\mathrm{P}(\bar{\nu}_\mu \rightarrow \bar{\nu}_e)$. But these probabilities depend on all the above three unknowns therefore these two experiments give a number of degenerate solutions which are difficult to resolve (a detailed discussion in chapter 8).

2. ***DUNE***: This is an upcoming long baseline accelerator neutrino experiment. Degenerate solutions can be avoided by using DUNE data due to larger matter effects.

3. ***JUNO and RENO 50***: T2K and NOνA can measure the effective mass quare differece [86]

$$\Delta m^2_{\mu\mu} \simeq \sin^2\theta_{12}\Delta m^2_{31} + \cos^2\theta_{12}\Delta m^2_{32} + \sin 2\theta_{12}\sin\theta_{13}\tan\theta_{23}\cos\delta\Delta m^2_{21}, \tag{2.46}$$

JUNO and RENO 50 can measure

$$\Delta m^2_{ee} \simeq \cos^2\theta_{12}\Delta m^2_{31} + \sin^2\theta_{12}\Delta m^2_{32}, \tag{2.47}$$

We can also calculte the difference of these effective quantities

$$|\Delta m^2_{\mu\mu}| - |\Delta m^2_{ee}| = \pm\Delta m^2_{21}(\cos 2\theta_{12} - \sin 2\theta_{12}\sin\theta_{13}\tan\theta_{23}\cos\delta). \tag{2.48}$$

where the positive and negative signs correspond to normal and inverted mass hierarchies, respectively. Accurate measurement of $\Delta m^2_{\mu\mu}$ and Δm^2_{ee} at the level of 1% or so can give sign of Δm^2_{31}. This is very difficult because it needs inverse β-decay energy reconstruction at (2-3)% level.

4. ***INO***: India-based Neutrino observatory (INO) is an upcoming atmospheric neutrino experiment which will look for matter effects in atmosphric neutrino events. Hyper Kamiokande (HK) also plans to do the same.

Chapter 3

Matter dependent neutrino oscillations

In 1978, L. Wolfenstein [87] considered the problem of neutrinos travelling in matter. He showed that the coherent forward elastic scattering of neutrinos with the partciles in the medium (electron, proton and neutron) can be parametrised in the form of a potential. This potential modifies the mass eigenvalues and the mixing of the neutrinos. The effective mixing angle can be larger than the mixing angle in vacuum for suitable density of matter. S. P. Mikheev and A. Yu. Smirnov discovered that when neutrinos travel in a medium with varying density [88, 89, 90], there can be a region along the neutrino path for which the effective mixing angle takes the maximal value ($\pi/4$). This resonant amplification of the mixing angle is called the "MSW effect". This effect is needed to explain the energy dependence of the solar neutrino survival probability. It also requires $\Delta m^2_{\text{sol}} = \Delta m^2_{21}$ to be positive.

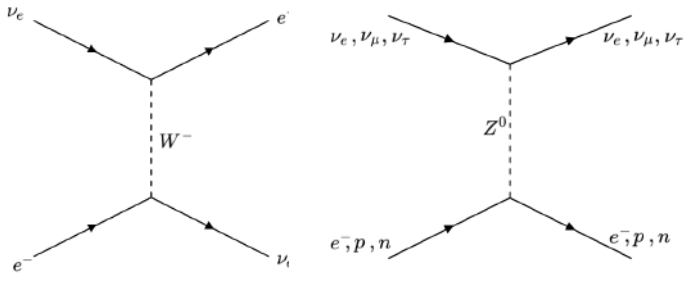

(A) CC scattering

(B) NC scattering

FIGURE 3.1: Feynman diagrams of the elastic scattering processes. CC potential V_{CC} is generated through W exchange and NC potential V_{NC} is generated through Z exchange.

3.1 Effective matter potential

Propagating through matter, neutrinos are subjected to effective potentials due to the interaction with the medium through coherent forward elastic weak CC and NC scatterings. The feynman diagrams of CC and NC scattering are shown in figure 3.1. The effective CC hamiltonian corresponding to the feynman diagram 3.1a for an electron neutrino propagating in a homogeneous and isotropic gas of unpolarized electrons

$$H_{eff}^{CC} = \frac{G_F}{\sqrt{2}}[\bar{\nu}_e\gamma^\rho(1-\gamma^5)\nu_e][\bar{e}\gamma_\rho(1-\gamma^5)e]. \tag{3.1}$$

This Hamiltonian leads to the charge current potential V_{CC} is given by

$$V_{CC} = \sqrt{2}G_F N_e \tag{3.2}$$

where N_e is the electron density of the medium. Based on the form of the interaction given in eq.3.1, we note that the potential V_{CC} is experianced only by ν_e. There is no such potential for ν_μ and ν_τ.

The NC interactions lead to a corresponding potential V_{NC}. In the electroweak model, the NC interactions of each of the neutrino flavors are the same. Therefore, we have the same V_{NC} for ν_e, ν_μ and ν_τ. Therefore, the net matter potential for flavor ν_α is

$$V_\alpha = V_{CC}\delta_{\alpha e} + V_{NC}. \tag{3.3}$$

3.2 Neutrino mixing in matter

Similar to the vacuum oscillation case, we start with a neutrino in flavor state $\alpha(\alpha = e, \mu, \tau)$ and the mass eigenstate k (k=1,2,3) with momentum $\overrightarrow{p}$ connected through the mixing matrix U

$$|\nu_\alpha\rangle = \sum_k U_{\alpha k}^* |\nu_k\rangle. \tag{3.4}$$

$|\nu_k\rangle$ with momentum $\overrightarrow{p}$ is an eigenstate of vacuum hamiltonian H_0:

$$H_0|\nu_k\rangle = E_k|\nu_k\rangle, \qquad \text{with} \qquad E_k = \sqrt{p^2 + m_k^2} = p + m_k^2 \tag{3.5}$$

The total hamiltonian in matter, with the inclusion of matter effect, becomes

$$H = H_0 + H_m, \qquad \text{with} \qquad H_m|\nu_\alpha\rangle = V_\alpha|\nu_\alpha\rangle. \tag{3.6}$$

Consider a neutrino with initial flavor α. The time evolution of ν_α is given by the Schrödinger equation

$$i\frac{d}{dt}|\nu_\alpha(t)\rangle = H|\nu_\alpha(t)\rangle. \tag{3.7}$$

The transition amplitude of $\nu_\alpha \to \nu_\beta$ after a time t is given by

$$\psi_{\alpha\beta}(t) = \langle\nu_\beta|\nu_\alpha(t)\rangle. \tag{3.8}$$

The time evolution of the transition amplitude is

$$i\frac{d}{dt}\psi_{\alpha\beta}(t) = \sum_\eta \left(\sum_k U_{\beta k} E_k U^*_{\eta k} + \delta_{\beta\eta} V_\beta\right) \psi_{\alpha\eta}(t) \tag{3.9}$$

The evolution equation can be rewritten as

$$i\frac{d}{dt}\psi_{\alpha\beta}(t) = \left(p + \frac{m_1^2}{2E} + V_{NC}\right)\psi_{\alpha\beta}(t) + \sum_\eta \left(\sum_k U_{\beta k}\frac{\Delta m^2_{k1}}{2E} U^*_{\eta k} + \delta_{\beta e}\delta_{\eta e} V_{CC}\right)\psi_{\alpha\eta}(t). \tag{3.10}$$

The first term in the above equation generates the same phase for all flavours which does not affect the flavor transions. Therefore, the relevant evolution equation for the flavor transition amplitudes is

$$i\frac{d}{dt}\psi_{\alpha\beta}(t) = \sum_\eta \left(\sum_k U_{\beta k}\frac{\Delta m^2_{k1}}{2E} U^*_{\eta k} + \delta_{\beta e}\delta_{\eta e} V_{CC}\right)\psi_{\alpha\eta}(t). \tag{3.11}$$

Writing eq.3.11 in matrix form

$$i\frac{d}{dx}\Psi_\alpha = H_F\Psi_\alpha, \tag{3.12}$$

where the effective hamiltonian H_F is given by

$$H_F = \frac{1}{2E}(U\mathbb{M}^2U^\dagger + \mathbb{A}). \tag{3.13}$$

The explicit forms of various terms in equations 3.12 and 3.13 are

$$\Psi_\alpha = \begin{pmatrix} \psi_{\alpha e} \\ \psi_{\alpha\mu} \\ \psi_{\alpha\tau} \end{pmatrix}, \quad \mathbb{M}^2 = \begin{pmatrix} 0 & 0 & 0 \\ 0 & \Delta m^2_{21} & 0 \\ 0 & 0 & \Delta m^2_{31} \end{pmatrix}, \quad \mathbb{A} = \begin{pmatrix} A_{CC} & 0 & 0 \\ 0 & 0 & 0 \\ 0 & 0 & 0 \end{pmatrix}, \tag{3.14}$$

where

$$A_{CC} = 2EV_{CC} = 2\sqrt{2}EG_FN_e. \tag{3.15}$$

3.3 2-flavor oscillations in matter

Before discussing the complicated case of 3-flavor oscillations, first we consider the simpler case of 2-flavor oscillations in matter. We take the initial neutrino to be an electron neutrino. The time evolution equation can be written as

$$i\frac{d}{dt}\begin{pmatrix} \psi_{ee} \\ \psi_{e\mu} \end{pmatrix} = \frac{1}{4E}\begin{pmatrix} -\Delta m^2\cos 2\theta + A_{CC} & \Delta m^2\sin 2\theta \\ \Delta m^2\sin 2\theta & \Delta m^2\cos 2\theta - A_{CC} \end{pmatrix}\begin{pmatrix} \psi_{ee} \\ \psi_{e\mu} \end{pmatrix}, \tag{3.16}$$

where $\Delta m^2 = m_2^2 - m_1^2$ and θ is the vacuum mixing angle, defined by

$$\nu_e = \cos\theta\nu_1 + \sin\theta\nu_2, \quad \nu_\mu = -\sin\theta\nu_1 + \cos\theta\nu_2. \tag{3.17}$$

The effective Hamiltonian matrix is diagonalised by an orthogonal transformation

$$U_M^T H_F U_M = H_M, \tag{3.18}$$

where

$$H_M = \frac{1}{4E} diag(-\Delta m^2_M, \Delta m^2_M), \tag{3.19}$$

is the effective hamiltonian matrix in the mass basis in matter. The diagonalising matrix

$$U_M = \begin{pmatrix} \cos\theta_M & \sin\theta_M \\ -\sin\theta_M & \cos\theta_M \end{pmatrix} \tag{3.20}$$

is the effective mixing matrix in matter. The effective mass squared difference is given by

$$\Delta m^2_M = \sqrt{(\Delta m^2 \cos 2\theta - A_{CC})^2 + (\Delta m^2 \sin 2\theta)^2}. \tag{3.21}$$

The effective mixing angle in matter θ_M is given by

$$\tan 2\theta_M = \frac{tan2\theta}{1 - \dfrac{A_{CC}}{\Delta m^2 cos2\theta}}. \tag{3.22}$$

The effective mixing angle θ_M in matter assumes the maximal value $(\pi/4)$ when A_{CC} becomes equal to

$$A^R_{CC} = \Delta m^2 \cos 2\theta. \tag{3.23}$$

This mechanism is called the "*MSW effect*". A_{CC} is positive in normal matter therefore, there can be a resonance only if $\theta < \pi/4$. The matter potential is reversed for anti-neutrinos hence the resonance can occur only for $\theta > \pi/4$. We can also write

$$\sin 2\theta_M = \frac{\Delta m^2 \sin 2\theta}{\Delta m^2_M}, \quad \cos 2\theta_M = \frac{\Delta m^2 \cos 2\theta - A_{CC}}{\Delta m^2_M}. \tag{3.24}$$

The evolution equation in terms of the effective mixing angle in matter can be written as

$$i\frac{d}{dt}\begin{pmatrix} \psi_{ee} \\ \psi_{e\mu} \end{pmatrix} = \frac{1}{4E}\begin{pmatrix} -\Delta m^2_M \cos 2\theta_M & \Delta m^2_M \sin 2\theta_M \\ \Delta m^2_M \sin 2\theta_M & \Delta m^2_M \cos 2\theta_M \end{pmatrix}\begin{pmatrix} \psi_{ee} \\ \psi_{e\mu} \end{pmatrix}. \tag{3.25}$$

We calculate the oscillation probabilities in a manner similar to the vacuum oscillation case. The 2-flavour mixing of neutrinos in terms of mass eigenstates in matter can be written as

$$\begin{aligned} |\nu_e\rangle &= |\nu_{1m}\rangle \cos\theta_M + |\nu_{2m}\rangle \sin\theta_M, \\ |\nu_\mu\rangle &= -|\nu_{1m}\rangle \sin\theta_M + |\nu_{2m}\rangle \cos\theta_M \end{aligned} \tag{3.26}$$

We assume that the initial neutrino flavor is ν_e, at a later time t, the flavor state is given by

$$|\nu(t)\rangle = |\nu_{1m}\rangle e^{-i\frac{\Delta m^2_M}{4E}t} \cos\theta_M + |\nu_{2m}\rangle e^{i\frac{\Delta m^2_M}{4E}t} \sin\theta_M. \tag{3.27}$$

The probability of detecting $|\nu(t)\rangle$ as $|\nu_\mu\rangle$ at time t is

$$\begin{aligned} P_M(\nu_e \to \nu_\mu) &= |\langle \nu_\mu | \nu(t)\rangle|^2 \\ &= |-\sin\theta_M . e^{-i\frac{\Delta m^2_M}{4E}t} \cos\theta_M + \cos\theta_M . e^{i\frac{\Delta m^2_M}{4E}t} \sin\theta_M|^2 \\ &= |\sin\theta_M \cos\theta_M (e^{i\frac{\Delta m^2_M}{4E}t} - e^{-i\frac{\Delta m^2_M}{4E}t})|^2 \\ &= \sin^2 2\theta_M \sin^2\left(\frac{\Delta m^2_M}{4E}t\right). \end{aligned} \tag{3.28}$$

For ultrarelativistic neutrinos, t can be replaced by L (the neutrino path-length)

$$P_M(\nu_e \to \nu_\mu) = \sin^2 2\theta_M \sin^2\left(\Delta m^2_M \frac{L}{4E}\right) \tag{3.29}$$

and the survival probability is given by

$$P_M(\nu_e \to \nu_e) = 1 - \sin^2 2\theta_M \sin^2\left(\Delta m^2_M \frac{L}{4E}\right) \tag{3.30}$$

It is to be noted that in the above discussion, we have assumed that the neutrinos propagate in matter of a constant density. For varying matter densities, one has to consider the corresponding variations in the expressions for Δm^2_M and θ_M.

3.4 3-flavor oscillations in matter

In three flavor case, the Schrödinger equation for neutrinos propagating through matter of constant density can be written as

$$i\frac{d}{dt}|\nu_\alpha\rangle = H_F|\nu_\alpha\rangle, \tag{3.31}$$

where the effective hamiltonian H_F is given by

$$H_F = \frac{1}{2E}(U\mathbb{M}^2U^\dagger + \mathbb{A}), \tag{3.32}$$

with

$$\mathbb{M}^2 = \begin{pmatrix} 0 & 0 & 0 \\ 0 & \Delta m^2_{21} & 0 \\ 0 & 0 & \Delta m^2_{31} \end{pmatrix}, \quad \mathbb{A} = \begin{pmatrix} A_{CC} & 0 & 0 \\ 0 & 0 & 0 \\ 0 & 0 & 0 \end{pmatrix}. \tag{3.33}$$

The mixing matrix U can be written as

$$U(\theta_{12},\theta_{13},\theta_{23},\delta_{\rm CP}) = O_{23}(\theta_{23})U_{13}(\theta_{13},\delta_{\rm CP})O_{12}(\theta_{12}), \tag{3.34}$$

and $U_{13}(\theta_{13},\delta_{\rm CP}) = U_{\delta_{\rm CP}}O_{13}U^\dagger_{\delta_{\rm CP}}$, where

$$U_{\delta_{\rm CP}} = \begin{pmatrix} e^{i\delta_{\rm CP}/2} & 0 & 0 \\ 0 & 1 & 0 \\ 0 & 0 & e^{-i\delta_{\rm CP}/2} \end{pmatrix}. \tag{3.35}$$

Therefore, $U = U_{23}(\theta_{23})U_{\delta_{\rm CP}}O_{13}U^\dagger_{\delta_{\rm CP}}U_{12}(\theta_{12})$ and $\mathbb{A} = U_{23}(\theta_{23})U_{\delta_{\rm CP}}\mathbb{A}U^\dagger_{\delta_{\rm CP}}U^\dagger_{23}$. Equation 3.31 can be written as

$$i\frac{d}{dt}|\nu_\alpha\rangle = \frac{1}{2E}[U_A(U_B\mathbb{M}^2U_B^\dagger + \mathbb{A})U_A^\dagger]|\nu_\alpha\rangle, \tag{3.36}$$

where $U_A = U_{23}(\theta_{23})U_{\delta_{\rm CP}}$ and $U_B = U_{13}U^\dagger_{\delta_{\rm CP}}U_{12}(\theta_{12})$. Equation 3.36 can be written as

$$i\frac{d}{dt}|\nu_\alpha\rangle = \frac{1}{2E}[U_A(\mathbb{M}^2_M)U_A^\dagger]|\nu_\alpha\rangle, \tag{3.37}$$

with

$$\begin{aligned}\mathbb{M}_M^2 &= \frac{1}{2E}(U\mathbb{M}^2U^\dagger + \mathbb{A}).\\ &= U_B \begin{pmatrix} 0 & 0 & 0 \\ 0 & \Delta m_{21}^2 & 0 \\ 0 & 0 & \Delta m_{31}^2 \end{pmatrix} U_B^\dagger + \begin{pmatrix} A_{CC} & 0 & 0 \\ 0 & 0 & 0 \\ 0 & 0 & 0 \end{pmatrix} \\ &= M_0 + M_1\end{aligned} \tag{3.38}$$

where

$$M_0 = U_B \begin{pmatrix} 0 & 0 & 0 \\ 0 & 0 & 0 \\ 0 & 0 & \Delta m_{31}^2 \end{pmatrix} U_B^\dagger + \begin{pmatrix} A_{CC} & 0 & 0 \\ 0 & 0 & 0 \\ 0 & 0 & 0 \end{pmatrix} \tag{3.39}$$

and

$$M_1 = U_B \begin{pmatrix} 0 & 0 & 0 \\ 0 & \Delta m_{21}^2 & 0 \\ 0 & 0 & 0 \end{pmatrix} U_B^\dagger. \tag{3.40}$$

Using the one mass squared difference (OMSD) because $\Delta m_{21}^2 \ll \Delta m_{31}^2$, we can neglect Δm_{21}^2. The matter modified mass squared matrix in OMSD approximation is

$$\mathbb{M}_M^2 = M_0 = \begin{pmatrix} A + \Delta m_{31}^2 \sin^2\theta_{31} & 0 & \Delta m_{31}^2 \sin\theta_{31}\cos\theta_{13} \\ 0 & 0 & 0 \\ \Delta m_{31}^2 \sin\theta_{31}\cos\theta_{13} & 0 & \Delta m_{31}^2 \cos^2\theta_{31} \end{pmatrix}. \tag{3.41}$$

We can find a matrix U_B^m which diagonalises the $\mathbb{M}_M^2$. The matter modified PMNS matrix, in OMSD approximation, can be written as

$$U_{OMSD} = U_A U_B^m = \begin{pmatrix} \cos\theta_{13}^m & 0 & \sin\theta_{13}^m \\ -\sin\theta_{23}\sin\theta_{13}^m.e^{i\delta_{\rm CP}} & \cos\theta_{23} & \sin\theta_{23}\cos\theta_{13}^m.e^{i\delta_{\rm CP}} \\ -\cos\theta_{23}\sin\theta_{13}^m.e^{i\delta_{\rm CP}} & -\sin\theta_{23} & \cos\theta_{23}\cos\theta_{13}^m.e^{i\delta_{\rm CP}} \end{pmatrix}. \tag{3.42}$$

where

$$\tan 2\theta_{13}^m = \frac{\Delta m_{31}^2 \sin 2\theta_{13}}{\Delta m_{31}^2 \cos 2\theta_{13} - A_{CC}}. \tag{3.43}$$

The oscillation and survival probabilities for neutrinos propagating through a constant density matter, under OMSD approximation are

$$\begin{aligned}
P_{ee}^m &= 1 - \sin^2 2\theta_{13}^m \sin^2\left(1.27\frac{\Delta m_{31}^2 L}{E}\right), \\
P_{\mu e}^m &= \sin^2 2\theta_{13}^m \sin^2\theta_{23} \sin^2\left(1.27\frac{\Delta m_{31}^2 L}{E}\right), \\
P_{\mu\mu}^m &= 1 - \cos^2\theta_{13}^m \sin^2 2\theta_{23} \sin^2\left(1.27\frac{(\Delta m_{31}^2 + A + \Delta {m_{31}^2}^m)L}{2E}\right) \\
&- \sin^2\theta_{13}^m \sin^2 2\theta_{23} \sin^2\left(1.27\frac{(\Delta m_{31}^2 + A - \Delta {m_{31}^2}^m)L}{2E}\right) \\
&- \sin^4\theta_{23} \sin^2 2\theta_{13}^m \sin^2\left(1.27\frac{\Delta {m_{31}^2}^m L}{E}\right)
\end{aligned} \tag{3.44}$$

and similarly for other channels. The matter modified mass squared difference $\Delta {m_{31}^2}^m$ is defined as

$$\Delta {m_{31}^2}^m = \sqrt{(\Delta m_{31}^2 \cos 2\theta_{13} - A)^2 + (\Delta m_{31}^2 \sin 2\theta_{13})^2}. \tag{3.45}$$

M_1 can be considered as perturbation for a non-zero 1-2 mixing. Applying standard perturbation theory, we can calculate the eigenvalues and the diagonalizing matrix of the matter modified mass square matrix in flavour basis. By doing so, it is straight forward to calculate the oscillation probabilities. The probability of muon neutrino oscillating into electron neutrino is

$$\begin{aligned}
P_{\mu e}^m &= \sin^2 2\theta_{13} \sin^2\theta_{23} \frac{\sin^2\hat{\Delta}(1-\hat{A})}{(1-\hat{A})^2} \\
&+ \alpha \cos\theta_{13} \sin 2\theta_{12} \sin 2\theta_{13} \sin 2\theta_{23} \cos(\hat{\Delta} + \delta_{CP}) \frac{sin\hat{\Delta}\hat{A}}{\hat{A}} \frac{\sin\hat{\Delta}(1-\hat{A})}{1-\hat{A}} \\
&+ \alpha^2 \sin^2 2\theta_{12} \cos^2\theta_{13} \cos^2\theta_{23} \frac{\sin^2\hat{\Delta}\hat{A}}{\hat{A}^2}.
\end{aligned} \tag{3.46}$$

upto second order in Δm^2_{21} [91, 92, 93], where $\hat{\Delta} = \Delta m^2_{31} L/4E$, $\hat{A} = A/\Delta m^2_{31}$ and $\alpha = \Delta m^2_{21}/\Delta m^2_{31}$. In the above equation, $\Delta m^2_{31}>0$ for NH and $\Delta m^2_{31} < 0$ for IH. The probability for muon anti-neutrino oscillating into electron anti-neutrino can be written by changing the signs of δ_{CP} and A in equation 3.46. Therefore for neutrino (anti-neutrino), $\hat{A}$ is positive (negative) for NH and negative (positive) for IH. Therefore, $P_{\mu e}$ is sensitive to both hierarchy and δ_{CP}. The first term in equation 3.46 is proportional to $\sin^2\theta_{23}$, which makes $P_{\mu e}$ sensitive to the octant of θ_{23}. If uncertainty in θ_{13} is large, then $P_{\mu e}$ becomes sensitive to θ_{13} as well. The dependencies of $P_{\mu e}$ on hierarchy, δ_{CP} and octant of θ_{23} give rise to eight fold degeneracy problem [94]. We will discuss about the degeneracies in the chapter 8.

Chapter 4

Atmospheric neutrinos

4.1 Atmospheric neutrino flux

High energy particles, mostly protons, from galactic and extragalactic sources are continously bombarding earth's atmosphere. These so called "primary cosmic rays" interact with the nuclei of air molecules in the atmosphere and produce secondary particles such as pions, kaons and muons. These secondary particles further decay to neutrinos through following decay chains. These neutrinos are called "atmospheric neutrinos".

$$\begin{aligned} \pi^{\pm} &\rightarrow \mu^{\pm} + \nu_{\mu}(\bar{\nu}_{\mu}), \\ \mu^{\pm} &\rightarrow e^{\pm} + \bar{\nu_{\mu}}(\nu_{\mu}) + \nu_{e}(\bar{\nu_{e}}). \end{aligned} \tag{4.1}$$

The contribution due to kaons is small compared to that of pions for neutrinos in few GeV range. This cascading process of neutrino production is illustrated in the schematic diagram shown in figure 4.1. The average height of the neutrino production is 15 km above the ground. The primary cosmic-ray flux varies with the energy, approximately as $E^{-2.7}$ in the GeV to TeV energy range. Therefore, the atmospheric neutrino flux rapidly decreases with the increasing energy. It is to be noted that mainly two flavors ν_e and ν_μ neutrinos, along with their anti-particles are produced in the atmosphere. At low energy, approximately two (ν_μ plus $\bar{\nu}_\mu$) are produced for each (ν_e plus $\bar{\nu}_e$). The flavor ratio

$$r \equiv \frac{\nu_\mu + \bar{\nu}_\mu}{\nu_e + \bar{\nu}_e} \tag{4.2}$$

is predicted to be very close to 2 by detailed calculations of the neutrino flux as shown in 4.2. It increases with increasing energy because more and more muons reach the ground before they decay. The atmospheric neutrino fluxes are modulated with the 11 year solar cycle due to the modulation in the primary cosmic rays fluxes. This ratio is calculated with an accuracy better than a few percent in the GeV energy range. Therefore, it is a good means to inevestigate neutrino oscillations.

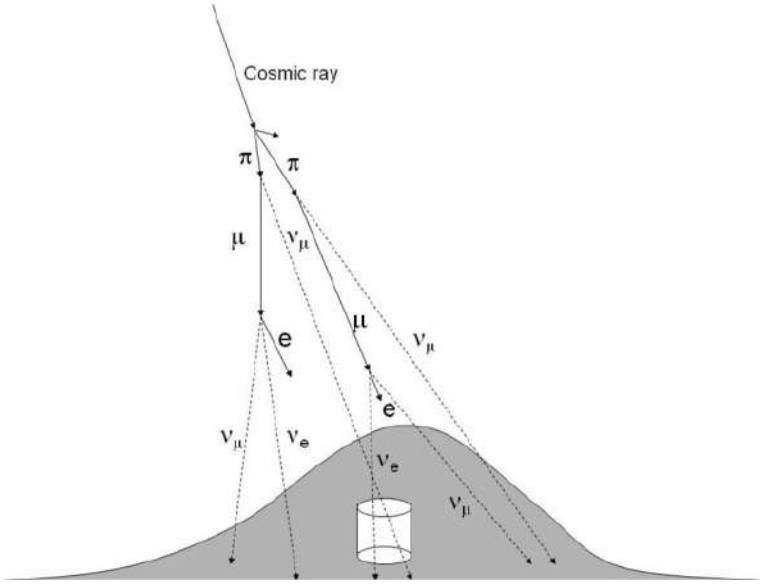

FIGURE 4.1: Production of atmospheric neutrinos.

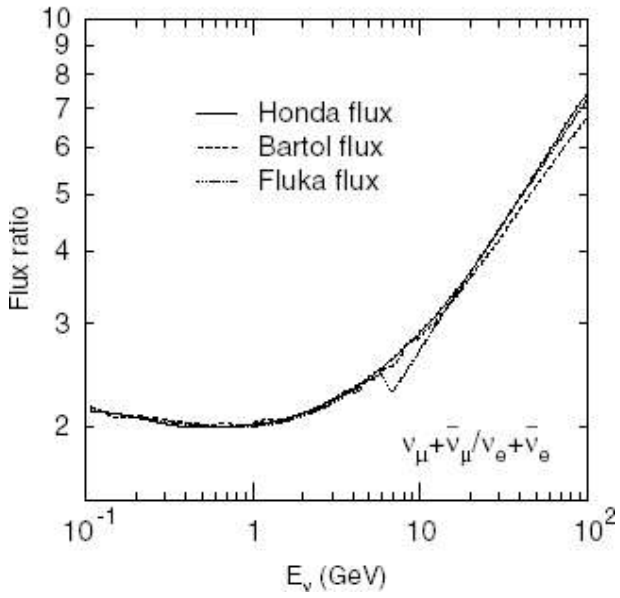

FIGURE 4.2: $\nu_\mu + \bar{\nu}_\mu / \nu_e + \bar{\nu}_e$ ratio of the atmospheric neutrino flux versus neutrino energy [95].

An important characteristic of the atmospheric neutrino flux is the up-down symmetry. If a neutrino enters the Earth at a point with zenith angle θ_{in} should leave the Earth at a point with zenith angle θ_{out} with $\theta_{in} = \pi - \theta_{out}$. This is shown in figure 4.3. Since the cosmic rays arrive on earth from all direction with equal rate, there must be a neutrino going in the opposite direction with same entry and exit angles. Hence, the rates of up-going and down-going neutrinos are equal. Therfore an up-down assymmtry of neutrino flux is a compelling evidence for neutrino oscillations. Figure 4.4 shows

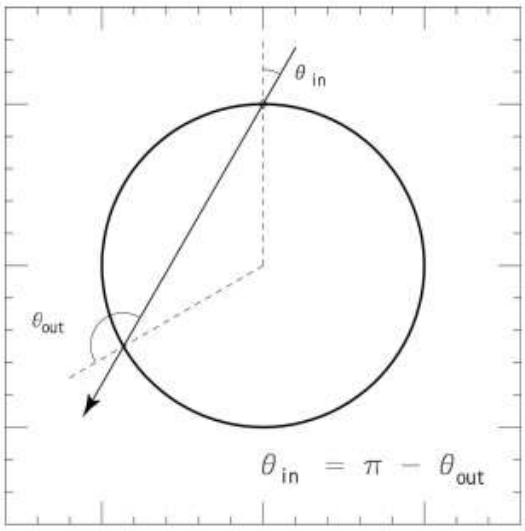

FIGURE 4.3: Trajectory of a neutrino which enters the Earth at an angle θ_{in} and exit at θ_{out}.

the calculated zenith-angle dependence of the atmospheric neutrino flux for 3.2 GeV neutrino energy at different locations [96]. It can be seen from this figure that the flux is up-down symmetric. However, below this, the flux is not exactly up-down symmetric because the geomagnetic field of earth significantly bends the low energy cosmic-ray particles. Thus the flux of low energy, down-going neutrinos depends on the local geomagnetic field above the detector. But the flux of low energy , up-going neutrinos, the geomagnetic field effect is averaged out by integrating over all angles. As it can be seen from the figure 4.4, the flux is typically maximum near horizontal ($\cos\theta_z = 0$), where muons travel maximum distance and most likely to decay. The ratio in 4.2 increases for high energy vertical neutrinos, where

muons have less chance of decay, so the second reaction in equation 4.1 is less probable. Figure 4.4 shows the atmospheric neutrino fluxes (averaged over all azimuthal angles at 3.2 GeV) variation with zenith angle for different sites.

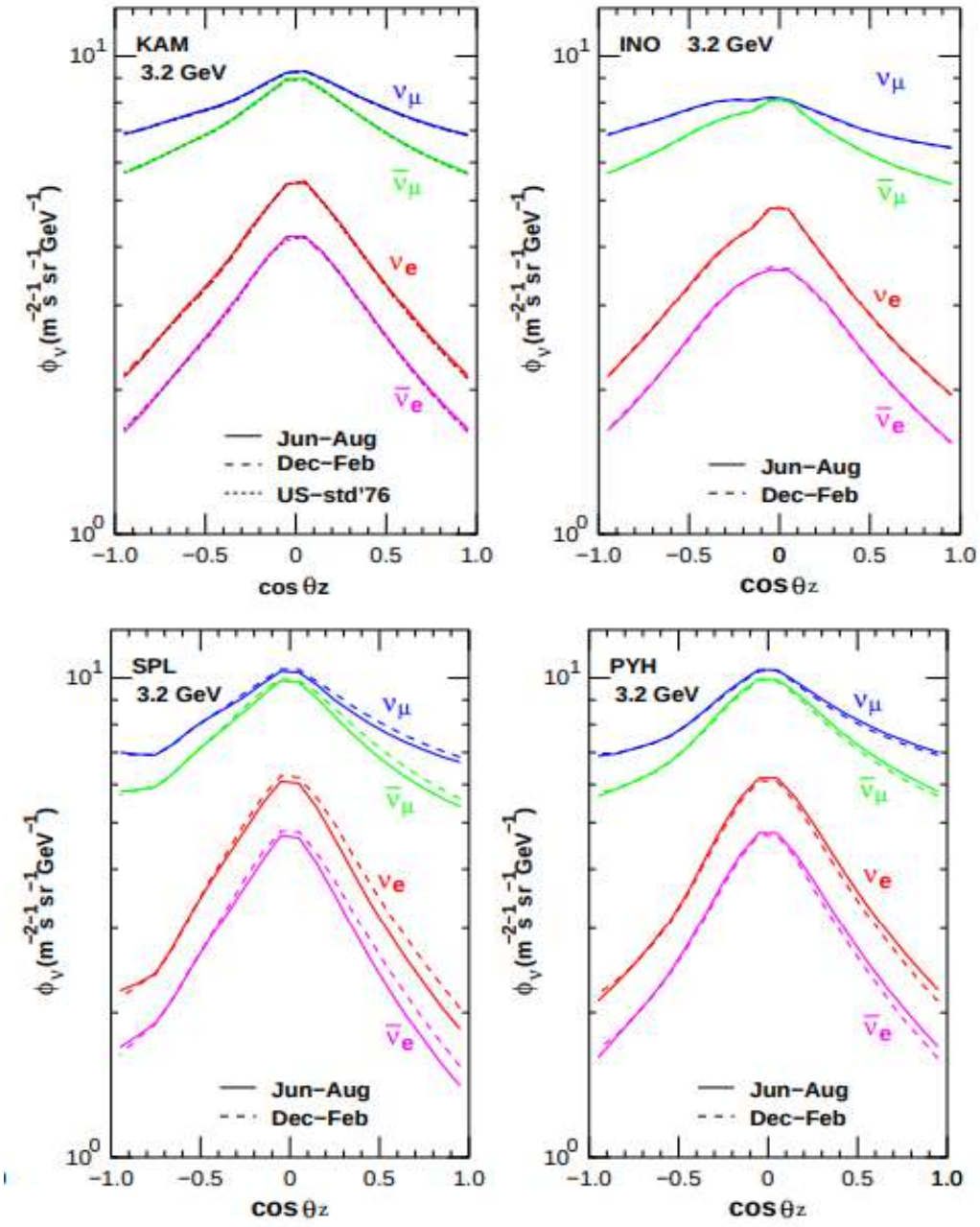

FIGURE 4.4: Zenith ngle dependence of atmospheric neutrino fluxes averaged over all azimuth angles at 3.2 GeV for different sites [96]. KAM stands for the SK site, INO for the INO site, SPL for the Soth Pole and PYH for the Pyhäsalmi mine.

4.2 Uncertainities in the atmospheric neutrinos flux

There are a large number of atmospheric neutrino flux calculations, each of which uses different aaproaches, different interaction models and different representations of the primary cosmic-ray spectrum [97, 98, 99, 100, 101, 102, 103].

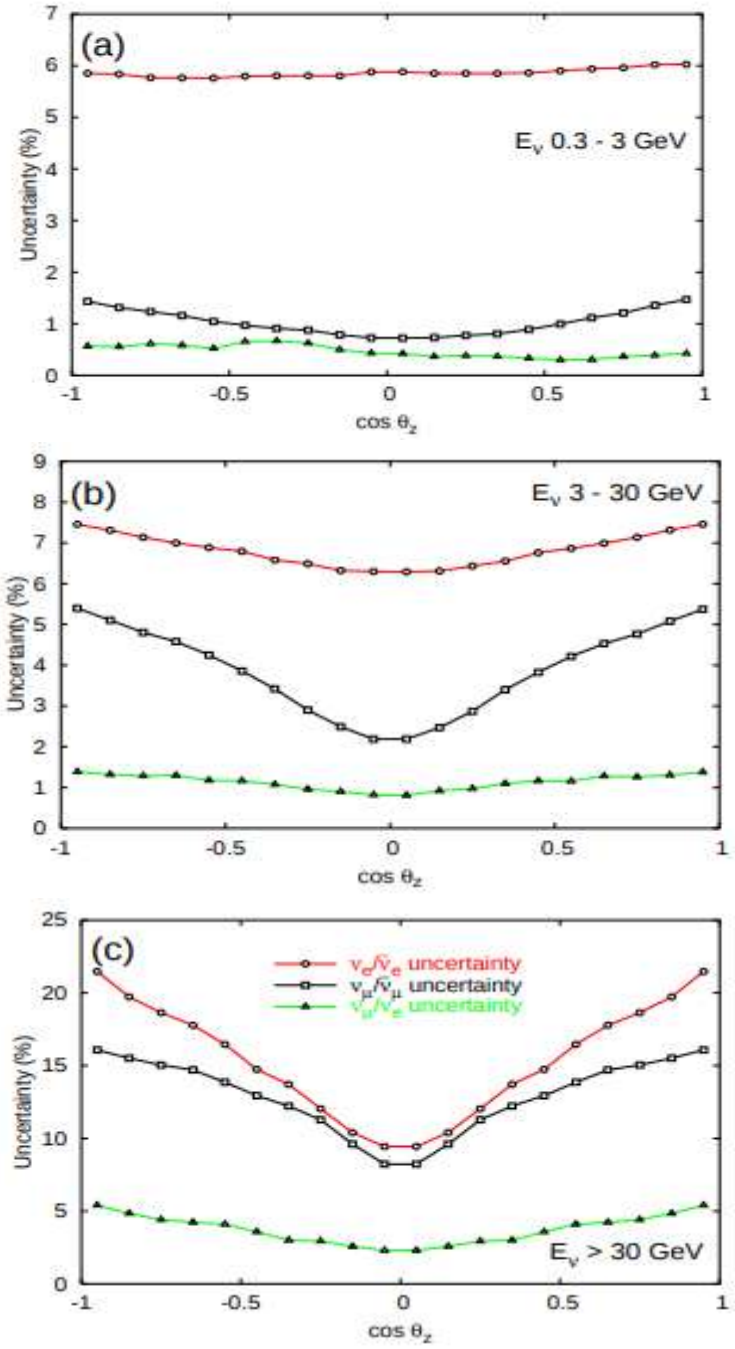

FIGURE 4.5: Uncertainities in neutrino type ratios as a function of zenith angle for different energy ranges [104]

Figure 4.2 shows the flavor ratios for the three different calculations which agree to better than 5%. On the other hand, the uncertainity in the normalization of the neutrino flux is larger and increases with energy. Overall uncertainty is at the level of $\pm 15\%$ in the GeV range.

Figure 4.5 shows the variation of neutrino-type ratios with zenith angle. The red lines with circles correspond to $\nu_e/\bar{\nu}_e$, black lines with square represent $\nu_\mu/\bar{\nu}_\mu$ and the green lines with triangles show $(\nu_\mu + \bar{\nu}_\mu/\nu_e + \bar{\nu}_e)$. Uncertainties in the ratios are much smaller because uncertainties in the primary spectrum and in hadronic interactions cancel in lowest order in the ratios. The uncertainty in the flavor ratio of equation 4.2 is of order $\pm 1\%$ for $E_\nu <$ 30 GeV. The uncertainties (6-7% for $\nu_e/\bar{\nu}_e$ and 1-5% for $\nu_\mu/\bar{\nu}_\mu$) are larger than r because they are more sensitive to the charge ratio of the parent mesons [104].

4.3 Atmospheric neutrino anomaly

Atmospheric neutrinos were first detected in 1965 by the Kolar Gold Field experiment in India [105] and an experiment led by Fred Reines in South Africa [106]. In these experiments, muons created by neutrino interactions in the rock surrounding the detector were observed. The neutrino detectors were placed deep underground ($\sim$ 8000 metres water equivalent (m.w.e)). Therefore the charged particles traversing the detectors almost horizontally were essentially of atmospheric neutrino origin. The first detection of atmospheric neutrino induced muon signal was anounced by these experiments almost simultaneously. IMB [107] and Kamiokande II experiment [108] were set up to search for proton decay with a lifetime of less than 10^{32} years, as predicted by early Grand Unified Theories. These experiments first reported a discrepency between the predicted atmospheric neutrino fluxes and that which was observed in the detector. They measured the number of e-like and μ-like events, which were mostly CCν_e and CCν_μ interactions, respectively.

It was found that the number μ-like events had a significant deficit compared with the Monte Carlo prediction., while the number of e-like events were in good agreement with the prediction. The flavor ratio of the of the atmospheric neutrino flux in equation 4.2 has been calculated to an accuracy of better than 5% in the relevent energy range. The value of the double ratio, $(\nu_\mu + \bar{\nu}_\mu / \nu_e + \bar{\nu}_e)_{Data} / (\nu_\mu + \bar{\nu}_\mu / \nu_e + \bar{\nu}_e)_{M.C}$, is measured to be less than 1. These measurements triggered the current interest in atmospheric neutrino oscillations.

Another interesting puzzle regarding atmospheric neutrinos was the up-down asymmetry. Kamiokande studied the zenith angle dependence of multi-GeV fully-contained events and partially contained events. Neutrinos entering the Earth with different zenith angles travel different pathlengths. Thus the neutrino oscillation probability is a function of the zenith angle of the neutrino direction. Vertically downward-going neutrinos travel about 15 km while vertically upward-going neutrinos travel about 13000 km before interacting in a detector located near the surface of the Earth. The kamiokande data revealed that the deficit of μ-like events depends on the neutrino zenith angle. Further in 1998, the Super-Kamiokande (SK) experiment with much larger data statistics proved that neutrino data contained evidence for neutrino oscillations [109].

4.4 Atmospheric neutrino experiments

The atmospheric neutrino interaction rate is about 200 $kt^{-1}year^{-1}$ and the background rate at the surface due to cosmic ray particles is much larger i.e. $\sim 2 \times 10^2 m^{-2} s^{-1}$ [110]. Therefore, it is not possible to carry out atmospheric neutrino experiments at the surface. Muons consist of a large fraction of a secondary cosmic rays at the surface which lose their energy only by ionization. The atmospheric neutrino detector must be located deep underground to significantly cut the muon flux. The variation of cosmic ray muon flux

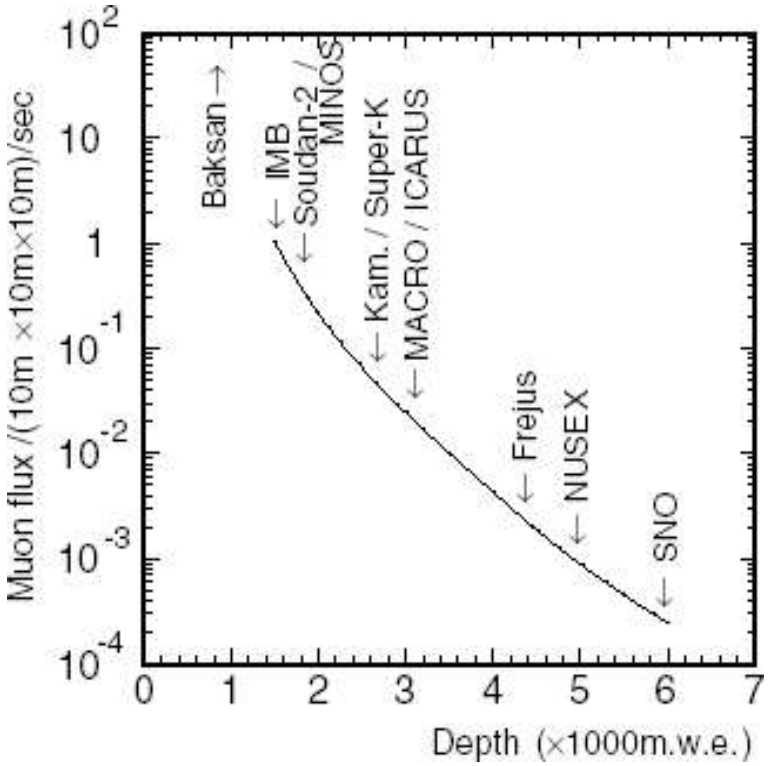

FIGURE 4.6: Cosmic ray muon flux versus depth of the detectors [111].

with the depth of the detector is shown in figure 4.6 for different experiments. The rate of cosmic ray muons should be compared with the observed atmospheric neutrino rate in the fiducial volume of the corresponding detector. It was found that the ratio of cosmic ray muon rate and the atmospheric neutrino event rate was $\sim 2 \times 10^4$ in Super-Kamiokande. There are mainly two types of atmospheric neutrino detectors, (a) water Cherenkov detectors and (b) fine-grained tracking detectors. We describe these detectors in the follwing subsections.

4.4.1 IMB

The first very large water Cherenkov detector was built by the Irvine-Michigan-Brookhaven (IMB) collaboration [112]. Charged particles with a velocity β>0.752 produce Cherenkov radiation in a cone about the particle direction. Water Cherenkov detectors use Cherenkov raditiation from relativistic charged

particles produced by the neutrino interaction with nucleus to observe an atmospheric neutrino event. The opening angle of the cone approaches 42° as $\beta \rightarrow 1$. Sufficiently purified water is transparent to the Cherenkov light which allows it to be collected by photomultipliers tubes (PMTs). A 2-dimentional array of PMTs record the hit time and the pulse height. The timing information with resolution of a few nanoseconds is used for vertex position reconstruction and the pulse height (total number of photo-electrons) corrsponds to the energy of the particles crossing Cherenkov threshold.

The IMB detector was situated 65 km east of Cleveland, Ohio in a salt mine operated by Morton. It started taking data in 1982 and ended in 1991. It used 3.3 kton of liquid water which filled a cube $\sim$ 15 m on a side. The full detector dimensions were $22.5 \times 17 \times 18 m^3$ and the total mass was 8 kton. The first phase of IMB (IMB-I) detector used 2048 13 cm hemispherical PMTs each of 5-inch diameter. In the first upgrade (IMB-2), light collection was improved by installing 2feet $\times 2 feet \times 0.5$ wave shifting plates. The final upgrade (IMB-3) detector was equiped with 2048 20 cm PMTs coupled with waveshifters.

This experiment reported that out of the total number of single track candidates, 34 events had a muon decay signal while 43 were expected [113]. Similar deficit in muon decay events was established by the Kamiokande experiment.

4.4.2 Kamiokande

The Kamiokande was also a water Cherenkov detector located at a depth of depth of 2700 meters water equivalent in the Kamioka mine in Japan [114, 115]. The first phase of the experiment was operated without the anticounter layer and was called kamiokande-I. The detector was upgraded to the second phase "Kamiokande-II", with a new electronics system capable of recording the arrival time of each PMT signal along with its charge. Continous water purification and removal of radioactive contamination improved the low-energy neutrino detection capability. PMT gain was doubled which

improved resolution for low-energy electrons and event vertex reconstruction. The second upgrade took place in 1990 when all the dead PMTs were replaced and the entire electronics were replaced with a more compact, low power system. Each PMT in the inner detector was equiped with a reflector to collect more light. This phase was called Kamikande-III. An schematic diagram of the detector is shown in the figure 4.7. Pure water with a mass of 3,000 tons filled a 16 m high and 15.6 m diameter cylindrical steel tank. The inner detector with 13.1 m height, 14.4 m diameter and 2,140 tons mass was viewed by 948 PMTs. The top and bottom of the inner detector had 164 and 160 PMTs respectively. This inner detector was surrounded by a 4π water Cherenkov anticounter layer viewed by 123 PMTs. The observed data was divided into two sets, (a) sub-GeV data set with $E_{vis} < 1.33$ GeV and (b) multi-GeV data set with $E_{vis} > 1.33$ GeV. The mult-GeV data was further divided into two categories (i) fully contained events and (ii) partially-contained events which have their interaction vertex in the fiducial volume and at least one visible track leaving the inner detector. The selection criteria for fully contained multi-GeV events was as follows [115].

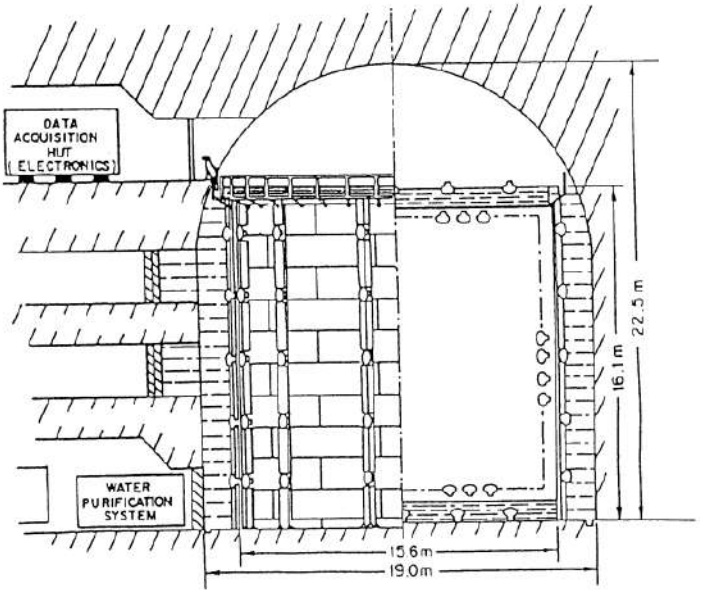

FIGURE 4.7: Schematic diagram of the Kamiokande-II(III) detector [115].

- E_{vis}>1.33 GeV
- total hit PMTs of the anti-counter$\leq$ 5
- the vertex position of the event should be at least 1 m inside the PMT plane.

The fiducial volume for these events was 1.35 kton. Total 195 such fully contained events were observed during 8.2 kton.yr of exposure. The selection criteria for the partially-contained events was

- total photoelectron (p.e.) numbers of the inner counter > 1500
- elimination of entering tracks by calculating the probability that a track is a cosmic ray muon.
- at most one cluster of hit PMTs in the anti-counter
- total p.e. numbers of the anti-counter > 20
- total hit PMTs of the anti-counter > 5
- the reconstructed vertex position should be at least 1.5 m inside the PMT plane.

The fiducial volume for these events is 1.04 kton. Total 118 partially contained events were observed during 6.0 kton.yr of the detector exposure. The μ/e ratio was obtained by combining the multi-GeV fully contained and partially contained events

$$\frac{(\mu/e)_{data}}{(\mu/e)_{MC}} = 0.57 \pm 0.07 \tag{4.3}$$

This ratio was averaged over the complete zenith angle. It as also shown that the mult-GeV data had a zenith angle dependence unlike the sub-GeV data which was isotropic.

4.4.3 Super-Kamiokande

Supar-Kamiokande (SK), the world's largest water Cherenkov detector, is located in the Mozumi mine of the Kamioka Township, Japan [116]. The detector is operated by the Super-Kamiokande Collaboration which is a joint Japan-US research collaboration. It was designed to further improve upon the experience gained by its scientific predeccessors, the Kamiokande and IMB. SK started data taking in April,1996. The detector consists of a welded stainless-steel tank with dimentions 42 m high and 39 m diameter. The total water capacity is 50,000 tons. Within the tank, here is a stainless steel framework of thickness 55 cm is equiped with arrays of inward-facing and outward-facing PMTs. The inward-facing array consists of 11,146 Hamamatsu hemispherical PMTs of type R3600, 50 cm diameter. The inward-facing PMTs, and the volume of water they view are called as the Inner Detector (ID). The outward-facing array consists of 1885 hemispherical PMTs of type R1408, 20 cm diameter. This outward-facing array along with the volume they see is called Outer Detector (OD). Figure 4.8 gives a cross-sectional view of the SK detector.

Neutrino events produced in the ID are identified as "fully contained" (FC) if there is no activity in the OD. Depending on the size and shape of the emitted Cherenkov light, the events were classified as single-ring electron-like (e-like), single-ring muon-like (μ-like), or mult-ring. The "partially contained" events were characterised with OD light pattern consistent with exiting particles. SK also records upward going muons which are assumed to be products of neutrino interactions in the rock below the detector. The upward muons are identified with the Cherenkov light of an entering muon. If OD data shows that this upward muon also leaves the detector, it is called "through-going upward muon", otherwise it is tagged as a "stopping upward muon".

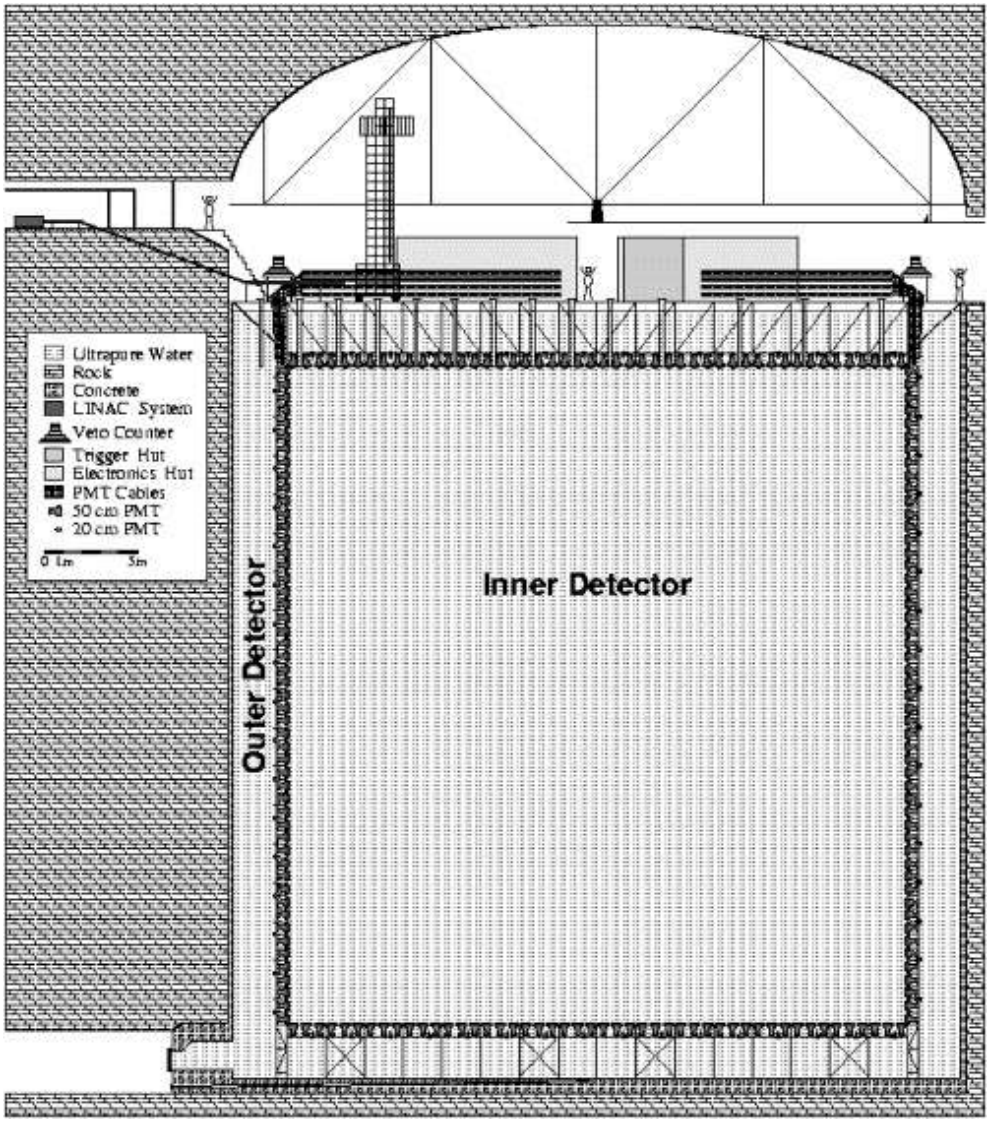

FIGURE 4.8: A cross-sectional view of the SK detector [116].

An analysis was done using SK data from a 25.5 kton.yr exposure collected between May 1996 and October 1997 [117]. The follwing selection criteria was imposed,

- no significant OD activity,
- total charge collected in the ID > 200 p.e.s, which corresponds to 22 MeV for electrons and 190 MeV for muons,
- the ratio (maximum p.e. in any single PMT)/(total p.e.s) is less than 0.5,

- the time interval from the preceeding event > 100 μs, to reject electrons from stopping muon decays.

$\sim$ 6,000 events were classified as fully-contained events. Out of these, 3,462 neutrino event candidate were reconstructed in the fiducial volume with $E_{vis} > 30MeV$. To calculate the μ/e ratio, only single ring event were considered. In the sub-geV sample, $E_{vis} < 1.33GeV$, and electron and muon momentum greater than 100 and 200 MeV respectively. From this sub-GeV data sample, the following ratio was obtained

$$R \equiv \frac{(\mu/e)_{DATA}}{(\mu/e)_{MC}} = 0.61 \pm 0.03. \tag{4.4}$$

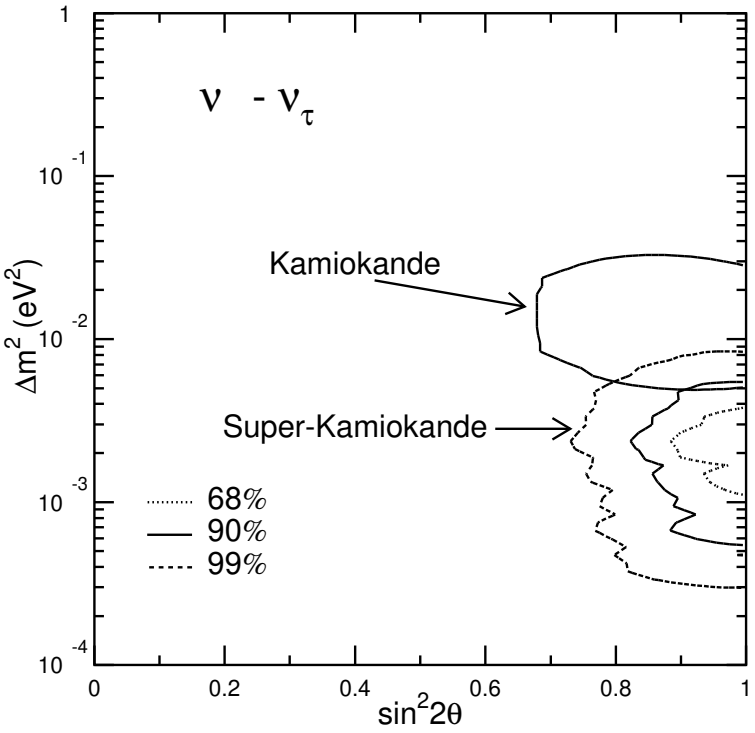

FIGURE 4.9: $\sin^2 2\theta$ and Δm^2 based on 33.0 kton.yr of Super-Kamiokande data [118].

In an another study using SK data, this ratio was calculated for both the sub-GeV and multi-GeV events [118]. For sub-GeV sample $R = 0.63 \pm$

0.03 and for multi-GeV sample $R = 0.65 \pm 0.05$. Along with the small values of R, this study confirmed the zenith angle dependence of the number μ-like events in the detector. They concluded that these results could only be explained by two flavor $\nu_\mu \leftrightarrow \nu_\tau$ oscillations with $\sin^2 2\theta > 0.82$ and $5 \times 10^{-}4 < \Delta m^2 < 6 \times 10^{-3} eV^2$ at 90% confidence level. Figure 4.9 shows the Superkamiokande results along with allowed region obtained by the Kamiokande experiment.

The latest analysis [119] uses atmospheric neutrino data collected during each of the SK run periods equivalent to a total livetime of 5,326 days, 2519 of which are from SK-IV. There are total 19 analysis samples defines for each SK run periods. The Zenith angle distributions of each sample are shown in figure 4.10. The data are separated into three broad categories, fully contained (FC), partially contained (PC) and upwardgoing muons (Up-μ) that are further sub-divided into the final analysis samples. Fully contained events have a reconstructed vertex within the 22.5 kton fiducial volume, defined as the region located more than 2 m from the ID wall, and with no activity in the OD. The FC data are sub-divided based upon the number of observed Cherenkov rings, the particle ID (PID) of the most energetic ring, and visible energy or momentum into combinations of single- or multi-ring, electron-like (e-like) or muon-like (μ-like), and sub-GeV (E_{vis} < 1330.0 MeV) or multi-GeV (E_{vis} > 1330.0 MeV). Additional selections are made based on the number of observed electrons from muon decays and the likelihood of containing a π^0. After all selections there are a total of 14 FC analysis samples. Events with a fiducial vertex but with energy deposition in the OD are classified as PC. Based on the energy deposition within the OD, PC events are further classified into "stopping" and "through-going" subsamples. The Up-μ sample is composed of upward-going muon events produced by neutrino interactions in the rock surrounding SK or in the OD water. Accordingly, light deposition in both the OD and ID is expected and the sample is divided into "through-going" and "stopping" subsamples for events that cross or stop within the ID, respectively. Through-going events with energy deposition consistent

with radiative losses are separated into a "showering" subsample.

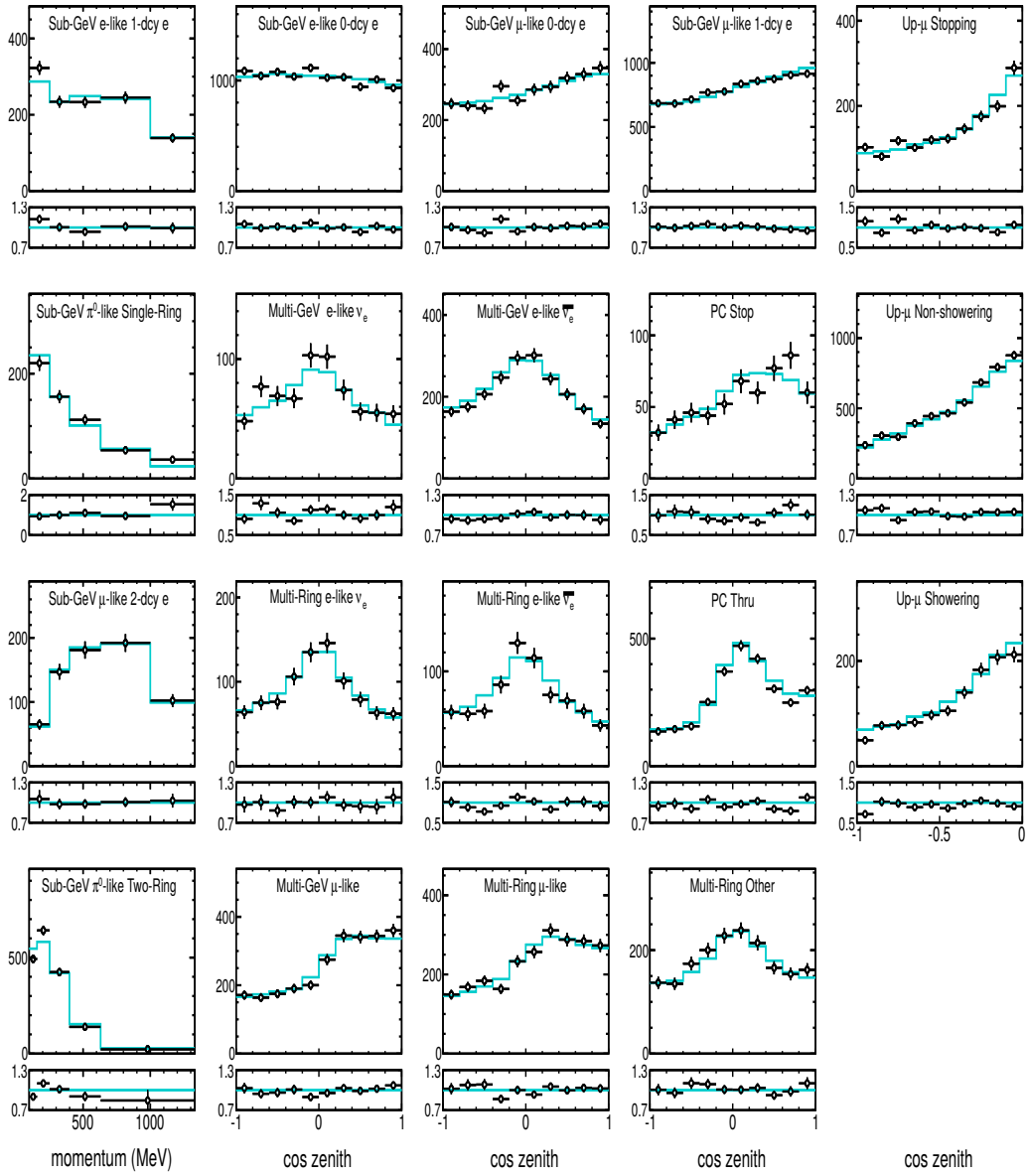

FIGURE 4.10: Data and MC comparisons for the entire Super-K data divided into 19 analysis samples. Lines denote the best fit MC assuming the normal hierarchy. Narrow panels below each distribution show the ratio of the data and MC [119].

The analysis used the fixed values of the oscillation paratmeters, $\Delta m^2_{21} = (7.53 \pm 0.18) \times 10^{-5}$, $\sin^2\theta_{12} = 0.304 \pm 0.014$ and $\sin^2\theta_{13} = 0.0219 \pm 0.0012$. These values are obtained from solar neutrino data, KamLAND reactor experiment data and short baseline reactor neutrino data. Figure 4.11 shows

the allowed regions for $|\Delta m^2_{32,31}|$, $\sin^2\theta_{23}, \theta_{13}$ and δ_{CP} obtained by only SK data.

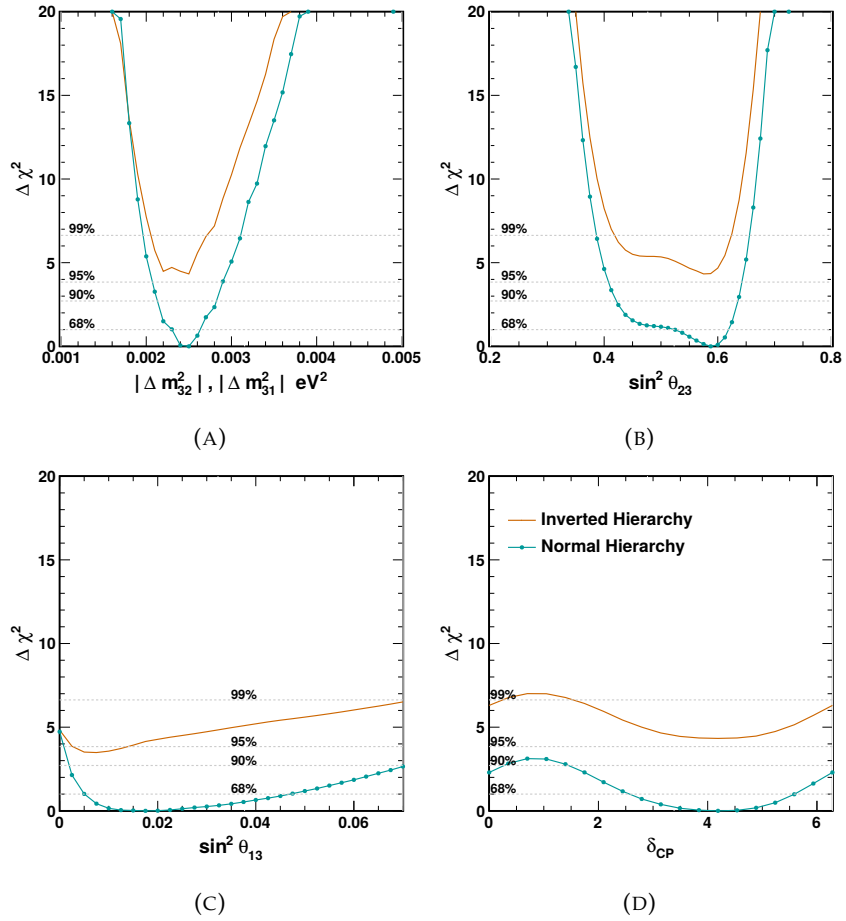

FIGURE 4.11: Allowed regions for neutrino oscillation parameters from the SK atmospheric neutrino data only.

The SK data rules out $\sin^2\theta_{13} = 0.0$ at approximately 2σ. It shows a weak preference for the higher octant of θ_{23} disfavouring the maximal mixing ($\sin^2\theta_{23} = 0.5$) at around 1σ significance. These features are in agreement with the expectations from $\nu_\mu \rightarrow \nu_e$ oscillations driven by non-zero θ_{13}. The best fit value of δ_{CP} is found to be 4.18(3.84) radians for normal (inverted) fit. Figure 4.12 shows the consistency of these results with the matter induced oscillations. For $\sin^2\theta_{13} = 0.0219 \pm 0.0012$, the data prefers the normal hierarchy with standard matter effects ($\alpha = 1.0$). Purely vacuum oscillations ($\alpha = 0.0$) are ruled out at 1.6 σ.

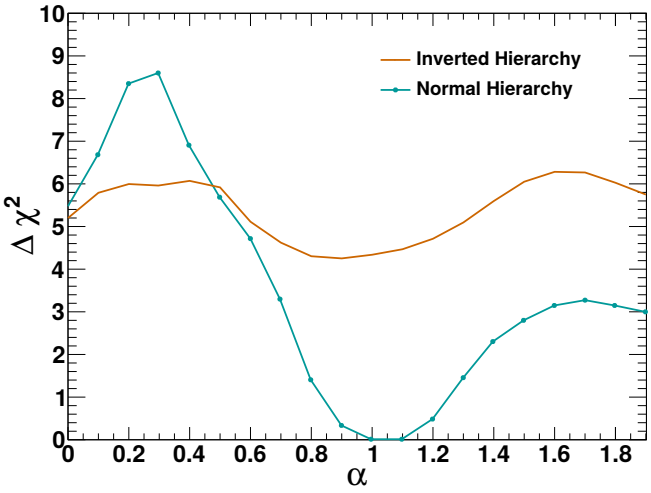

FIGURE 4.12: Constraints on the matter effect parameter α from the Super-K atmospheric neutrino data fit assuming $\sin^2\theta_{13} = 0.0219 \pm 0.0012$ [119].

The Super-kamiokande atmospheric neutrino data over a 328 kton.yr exposure of the detector indicates a weak preference for the normal mass hierarchy, disfavouring the inverted mass hierarchy at 93.9% assuming oscillation parameters at the analysis best fit point. Assuming the normal mass hierarchy the constraints on the atmospheric neutrino mixing parameters are $\sin^2\theta_{23} = 0.588^{+0.031}_{-0.064}$ and $\Delta m^2_{32} = 2.50^{+0.13}_{-0.20}$ with $\delta_{CP} = 4.18^{+1.41}_{-1.61}$. Over the range of parameters allowed at 90% C.L. the inverted mass hierarchy is disfavoured by between 81.9% and 96.7% by the SK data only.

4.5 Future atmospheric neutrino experiments

Hyper-Kamiokande: Hyper-Kamiokande (HK) is one of the most promising next-generation atmospheric neutrino detectors based on the well tested technology used in SK. It will be a megaton-class water Cherenkov detector with fiducial volume almost 20 times that of SK. It will be located 8 km south of Super-K, in the Tochibora mine, Japan. Figure 4.13 shows the expected sensitivity of HK with 10 years of run and 187 kton fiducial volume [120, 121].

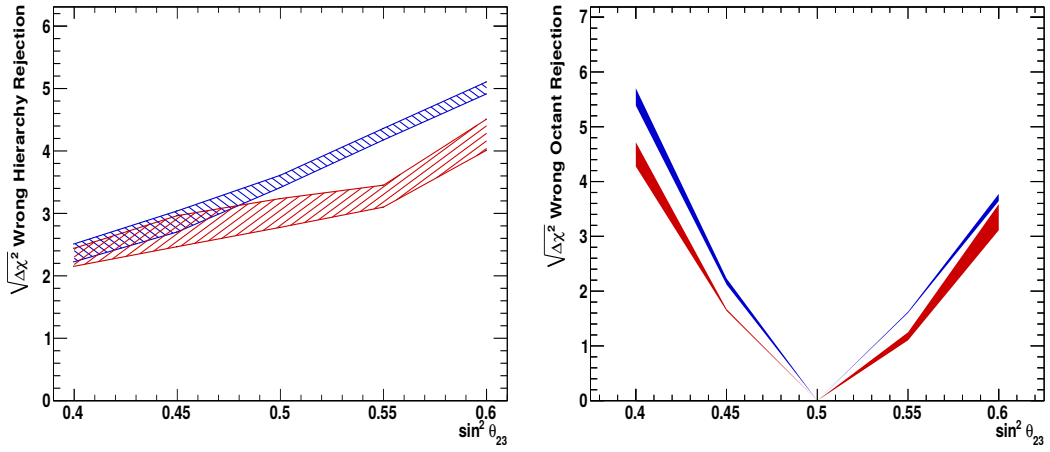

(A) (B)

FIGURE 4.13: HK sensitivity to determine the mass hierarchy (left) and the octant of θ_{23} (right) using atmospheric neutrinos only. Blue (red) band corresponds to normal (inverted) hierarchy and the width of thebands corresponds tp the uncertainity on the δ_{CP}.

HK can determine the mass hierarchy with 3σ significance for various possible values of $\sin^2\theta_{23}$ for normal hieachy. It has lower sentivity for inverted hierarchy but reaches 3σ value for the largest value of $\sin^2\theta_{23}$.

PINGU: The Precision IceCube Next Generation Underground (PINGU) detector is a proposed low energy extension of the IceCube detector [122, 123]. It will have a fiducial volume in the multi-megaton range which makes this detector very promising. It will study the sum of ν and $\bar{\nu}$ interactions as a function of zenith angle and energy differentiating between events with and wthout a track. There will be a signal of Neutrino Mass Hierarchy (NMH) due to the difference between ν and $\bar{\nu}$ cross-section and atmospheric flux. Figure 4.14 depicts the expected difference in the number of events assuming NH and IH.

ORCA: ORCA stands for Oscillation Research with Cosmics in the Abyss. It will be low energy extension of the KM3Net detector in the Mediterranean. With a threshold of a few GeV, ORCA will be able to put stringent constraints on the NMH as well as other oscillation parameters [124]. The expected sensitivity to the NMH is shown in figure 4.15.

INO: The Iron CALorimeter (ICAL) at the India-based Neutrino Observatory (INO) will be a 50 kton magnetized iron calorimeter. Due to its magnetic field, this detector is expected to have excellent charge identification efficiency. The detector and its expected physics capabilities will be described in chapters 5 and 6.

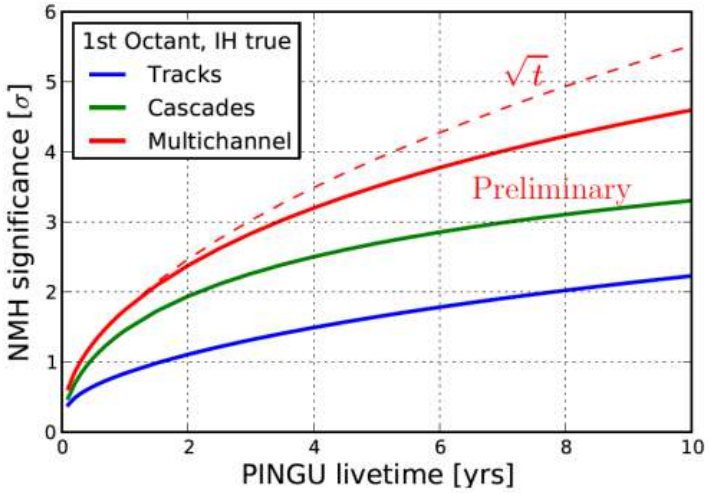

FIGURE 4.14: Expected significance for the rejection of NH as a function of run time, assuming that the IH is true (PINGU). [123].

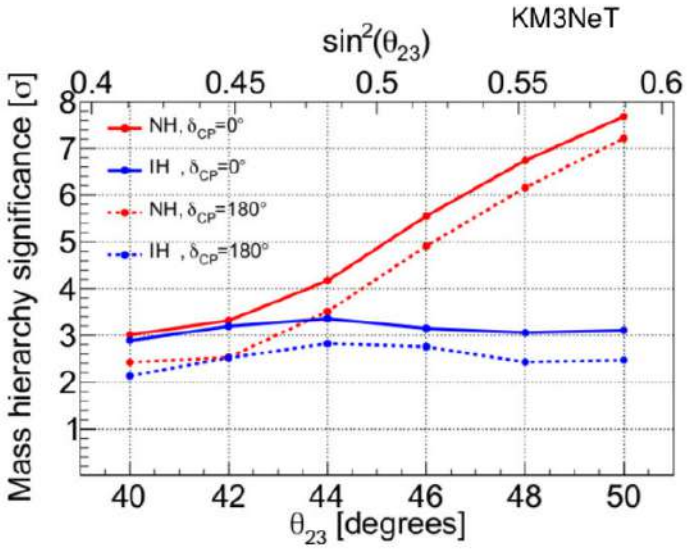

FIGURE 4.15: Expected sensitivity to NMH after 3 years of data taking as reported in KM3Net LoI.

Chapter 5

INO detector

Neutrino experiments in India started in the early sixties. Indian scientists from TIFR in collaboration with groups from Durham University (UK) and Osaka City University (Japan) conducted many front ranking experiments at Kolar Gold Fields (KGF) near the city of Banglore in South India. The first atmospheric neutrino event was observed in early 1965 [105]. The KGF laboratory operated for nearly four decades. The India-based neutrino observatory (INO) project was proposed to do experiments in neutrino physics at the cutting edge. The main goal of INO is to setup an underground laboratory with a gigantic magnetized iron calorimeter (ICAL) to study the atmospheric neutrinos.

5.1 India-based Neutrino Observatory (INO)

The proposed site for INO is located at the Bodi West Hills, near Pottipuram village, in the Theni district of Tamil Nadu, India. The detector will be placed under a mountain peak. The photo in the right panel of figure 5.1 shows a view of the mountain peak under which the cavern will be located. An underground horizontal tunnel, approximately 1900 m long, will be constructed to reach the laboratory. One large and three small laboratory caverns are to be built. The mountain peak provide a rock cover of about 1000 m all around the caverns. Right panel of figure 5.1 shows the reduction of the cosmic muon flux for various underground laboratories. The cosmic muon rejection for this site is almost the same as that at the Gran Sasso laboratory.

Along with studying the atmospheric neutrinos with the main Iron CALorimeter (ICAL) detector, this underground facility is designed to host experiments in other areas of interest such as neutrinoless double beta decay, dark matter search, low-energy neutrino spectroscopy, etc. Initial investigations and R&D in these fields are in progress.

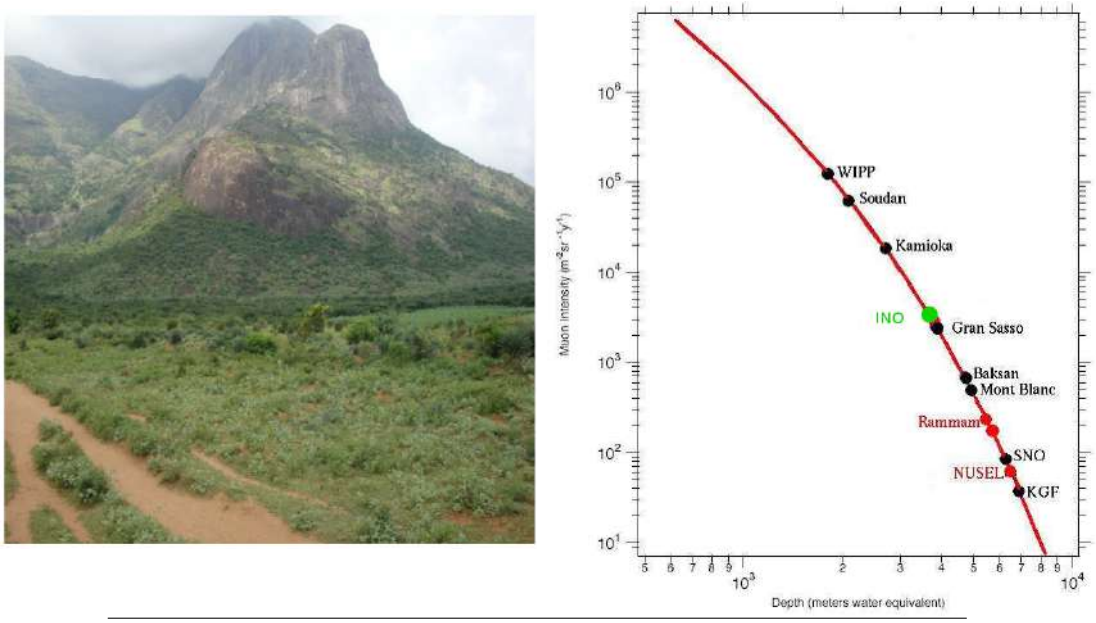

FIGURE 5.1: Left panel: Bodi West Hills (Photo courtesy: M V N Murthy [1]). Right panel: Atmospheric muon background flux as a function of depth [125].

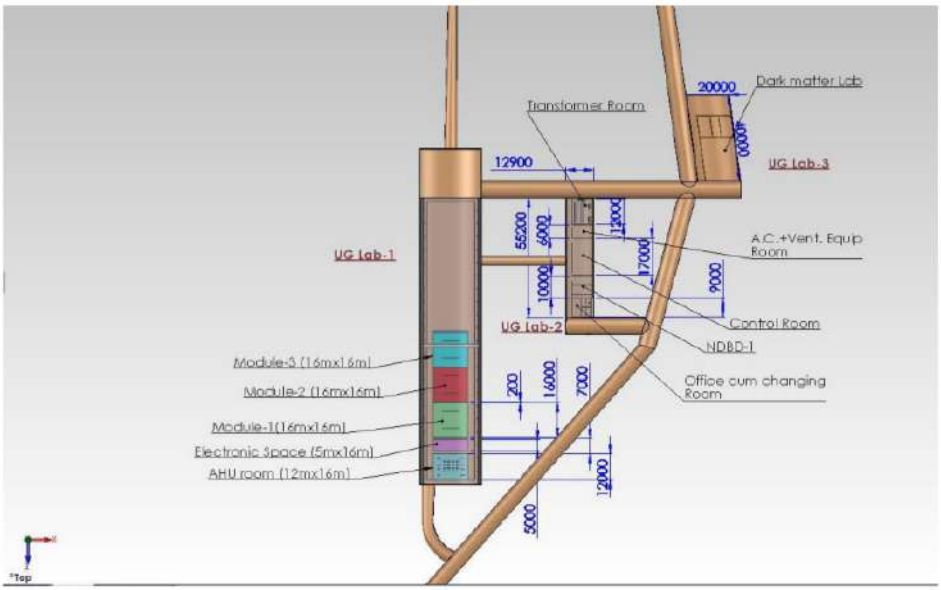

FIGURE 5.2: A sketch of the underground caverns with the positions of different modules [1].

A layout of the laboratory caverns is shown in figure 5.2. The main ICAL detector will sit in the largest cavern called "UG-Lab 1" which is 132.0 m long, 26.0 m wide and 32.5 m high. It is designed to house a proposed 50 kton ICAL detector and later one more neutrino detector ICAL-II of same size. Each ICAL has three modules with dimensions $16m \times 16m \times 14.5m$. Following criteria were taken into account in designing the ICAL detector for INO experiment:

- a large target mass to achieve enough statistics of atmospheric neutrino events in a reasonable time-scale (say 5 years),
- good energy and angular resolution to accurately measure L/E,
- charge identification capability to distinguish between ν and $\bar{\nu}$ events.

5.2 Iron CALorimeter (ICAL)

Figure 5.3 shows a schematic diagram of the proposed ICAL detector. It will have a modular structure with three modules of $16m \times 16m$ with total area $48m \times 16m$. Each module consists a stack of 151 horizontal layers of magnetized iron plates with a thicknes of 5.6 cm. The iron plates are separated by an air gap of 4 cm where the active detector layers will be placed. The total height of each module is 14.5 m.

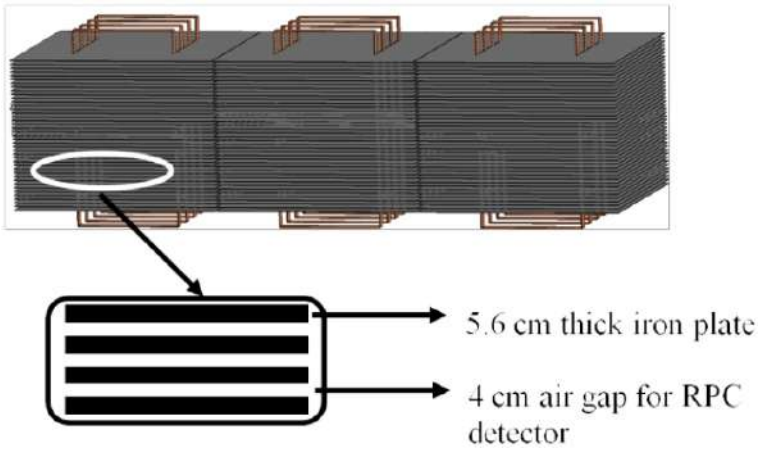

FIGURE 5.3: A layout of the 50 kt ICAL detector [1].

Iron spacers placed every 2 m along both "X" and "Y" directions provide mechanical support to all the layers. The 2 m wide empty space in the transverse "Y" direction help in periodic replacement of the Resistive Plate Chambers (RPCs) which will act as the active detector elements interspersed with the iron plates. Each RPC will have an area of $2m \times 2m$ and will be operated at a high volatge of about 10 kV in avalanche mode. Signals will be read by orthogonal "X" and "Y" strips of about 3 cm width, one on each side of an RPC. This will provide the "X" and "Y" coordinates of the track of the charged particles passing through the RPC and the layer number of the RPC will give the "Z" coordinate. ICAL will be able to dintinguish between the up-going and down-going charge particles due to a good time resolution ($\sim$ 1 ns). Both momentum and the direction of the particles can be reconstructed from the hit pattern observed in the RPCs. The total number of readout channels will be about 3.7 million. The important detector specifications are in table 5.1. RPCs are described in detail in section 5.6.

Number of Modules	3
Size of a Module	16 m $\times$ 16 m $\times$ 14.4 m
Total ICAL dimentions	48 m $\times$ 16 m $\times$ 14.4 m
Number of layers	151
Iron plate thickness	5.6 cm
Gap between Iron plates for RPCs	4 cm
Magnetic Field	1.4 tesla
RPC dimensions	195 cm $\times$ 184 cm $\times$ 2.4 cm
Strip width	2.8 cm
Number of RPCs/Road/Layer	8
Number of Roads/Layer/Module	8
Number of RPC units/Layer	192
Total number of RPCs	28,800
Total number of readout channels	3.7×10^6

TABLE 5.1: The ICAL specifications

5.3 ICAL Magnet

The ICAL serves the twofold purpose. It provides a large volume of target nucleons for neutrino interactions and a detection medium in which the

tracks of secondary charged particles produced in the neutrino-nucleon interactions can be separately reconstructed on the basis of their magnetic rigidity and give an estimate of their momenta. It will be made of 50 kton low carbon steel. ASE1010 or C10 steel have been selected for this purpose. The detector will have a modular structure with dimentions $48m \times 16m \times 14.5m$. The thickness of the steel plates will be $\sim$ 5.6 cm and an air gap of 4.0 cm. The steel plates will be magnetised to a magnetic field of $\sim$ 1.3 T by using copper coils. The following criteria were considered for the ICAL magnet:

- **Field Uniformity**
  Magnetic field should be uniform to achieve best performance of the detector.
- **Modularity**
  A modular structure has to be adopted to realize a magnetized detector of 50 kton steel and ease for its maintenance.
- **Optimized copper to steel ratio**
  Optimized copper to steel ratio to achieve reasonable cost and electrical power consumption.

A toroidal design has been chosen for the ICAL magnet. Preliminary design results are obtained using the 3D commercial code MagNet 6.0 [125]. The copper coil goes through two rectangular slots in the stack of steel plates. Figure 5.4 shows the geometry of the coil in one of the modules of the ICAL magnet and the field lines. The blue colour indicates negligible magnetic field in a region. The length, breadth and the positions of the slots are chosen to generate a uniform field in as large a volume of steel as possible. The design also takes care of the movement of RPC trays from the sides. The small thickness of the copper conductor (1 cm $\times$ 1 cm) and the small width (20 cm) of the coil provide negligible loss of active volume of the detector. A coil with 40,000 amp-turns is employed to produce a field of 1.3 T in one module. The calculated field lines in a typical layer are plotted in figure 5.5. The arrows show the reversal of the field on the two sides of the coils. Over

the entire set of plates the variation is within 0.3%, the field varying by less than 0.15% over a height of $\pm$ 5 m from the centre. The field is quite uniform in the x-direction, varying by less than 0.25% but in the y-direction it starts falling beyond the length of the coil slot ($\pm$ 4 m).

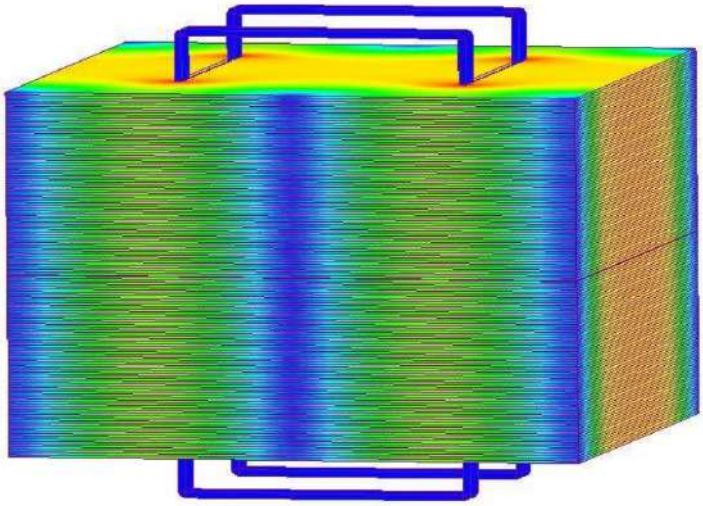

FIGURE 5.4: Magnetic field map of a single module of ICAL [125].

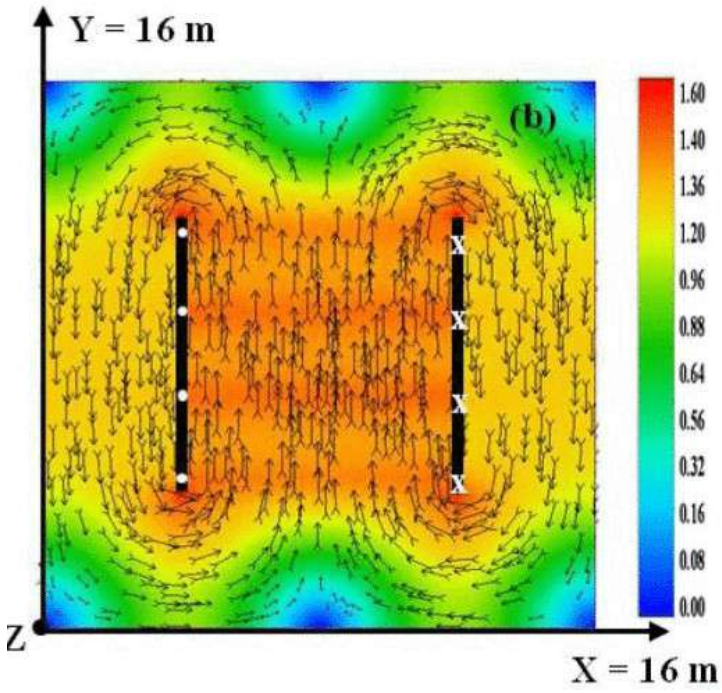

FIGURE 5.5: The X-Y projection of magnetic field of a single module of ICAL [126].

5.4 Gas System

There will be total 28,800 glass RPCs of size $2m \times 2m$ each with a gas gap of 2mm. A total volume of $\sim 216\ m^3$ of gas mixture will be needed. The gas distribution system for such a big detector will be a recycling system with approximately one volume change per day due to cost and pollution considerations. The detector will be divided into many zones with each zone getting gas supply from a separate gas mixing unit. The three gases (freon ($C_2F_4H_2$) also called R-134a, isobutane (C_4H_{10}) and SF_6 or argon) will be sent to mass flow controllers for mixing in appropriate proportions. Mixed gas will be distributed to 24 $\times$ 140 roads through a series of manifolds. Uniform distribution in each road will be maintained by flow resistors. Exhaust pressure and relief bubblers will avoid the over pressure situation. A pilot Closed Loop System (CLS) [127, 128] has been continuously running and being tested for a stack of RPCs at TIFR, Mumbai, for the last 6 years. Following factors were considered to design the CLS.

- **Pressure**

  The gas pressure inside an RPC should be maintained at a constant value. The pressure inside the RPC has to be more than the atmospheric pressure to avoid suction of contaminations into the RPC.

- **Gas flow rate**

  The gas flow rate is controlled in proportion to the deviation of the pressure inside the RPC from the minimum and maximum allowable limit. The equivalent gas flow rate is 360 ml/h through each RPC of 2m $\times$ 2m in size. The gas volume lost due to leakage is compensated by preparing the mixture through Mass Flow Controllers (MFC).

- **Gas composition**

  The transients in the mass flow controller operation will not interfere with the gas mixture composition.

- **Safety**

  The harmful radicals which may damage the surface quality of the glass electrode, formed during the passage of the gas mixture through the detector, should be removed through chemical reaction.

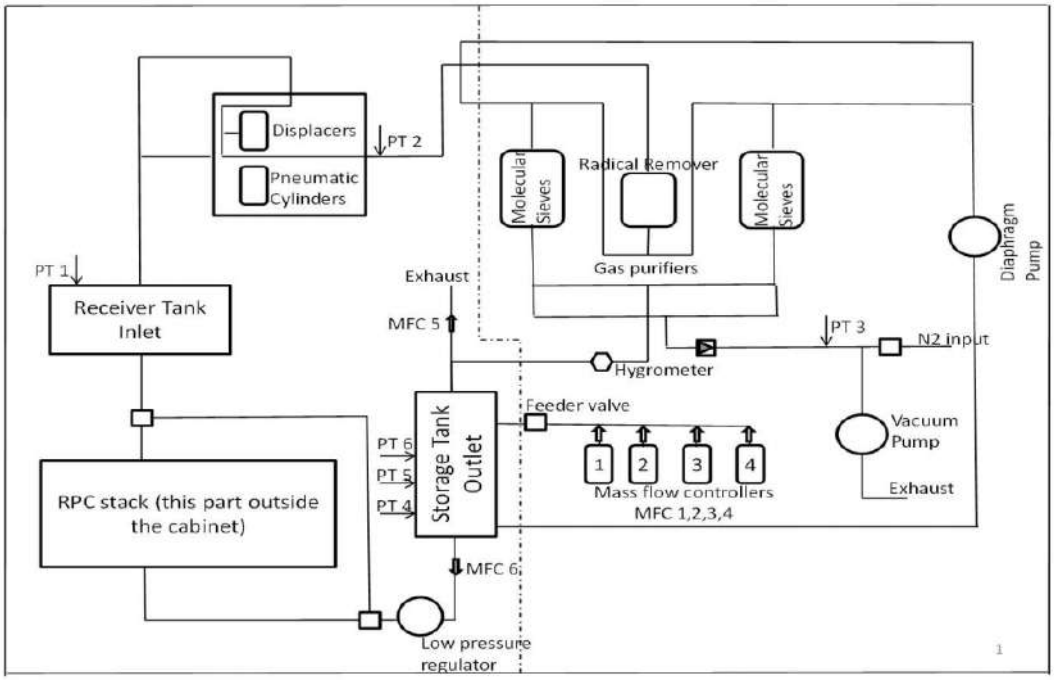

FIGURE 5.6: Block diagram of the Closed Loop Gas System [127].

The CLS, as shown in figures 5.6 and 5.7, supplies gas to 12 RPCs of $2m \times 2m$ in size. A single stage, pneumatically operated positive displacement pump sucks gas mixture from a receiver tank, which is connected to the RPC outlets, at pressures between 1002 mbarA and 1005 mbarA and delivers it to a storage tank at 1650 mbarA through purifiers. When the storage tank pressure drops below 1350 mbarA, the mass flow controllers, start feeding the gas mixture into the storage tank till the pressure is topped up to 1650 mbarA, while maintaining the ratio of the gas mixture at 95:4.5:0.5 of R134a, isobutane and SF_6 respectively (for avalanche mode operation of RPCs). (In the current test setup, SF_6 is being used in place of Argon but ICAL will use Argon.) A Residual Gas Analyser (RGA) is connected to the outlet of the RPC exhaust to study the presence of any breakdown radicals into the gas. Solid state pressure transmitters monitor pressure of gas at 6 points. In

addition, atmospheric pressure is also measured. A Siemens PLC with input and output modules, actuators and a SCADA interface, controls the flow and pressure throughout the loop. A safety routine is built into the logic and various data parameters are logged periodically. In 21 days the leak rate observed in the pilot CLS is 5.4 ml per hour when connected to 4 RPCs of $2m \times 2m$ in size.

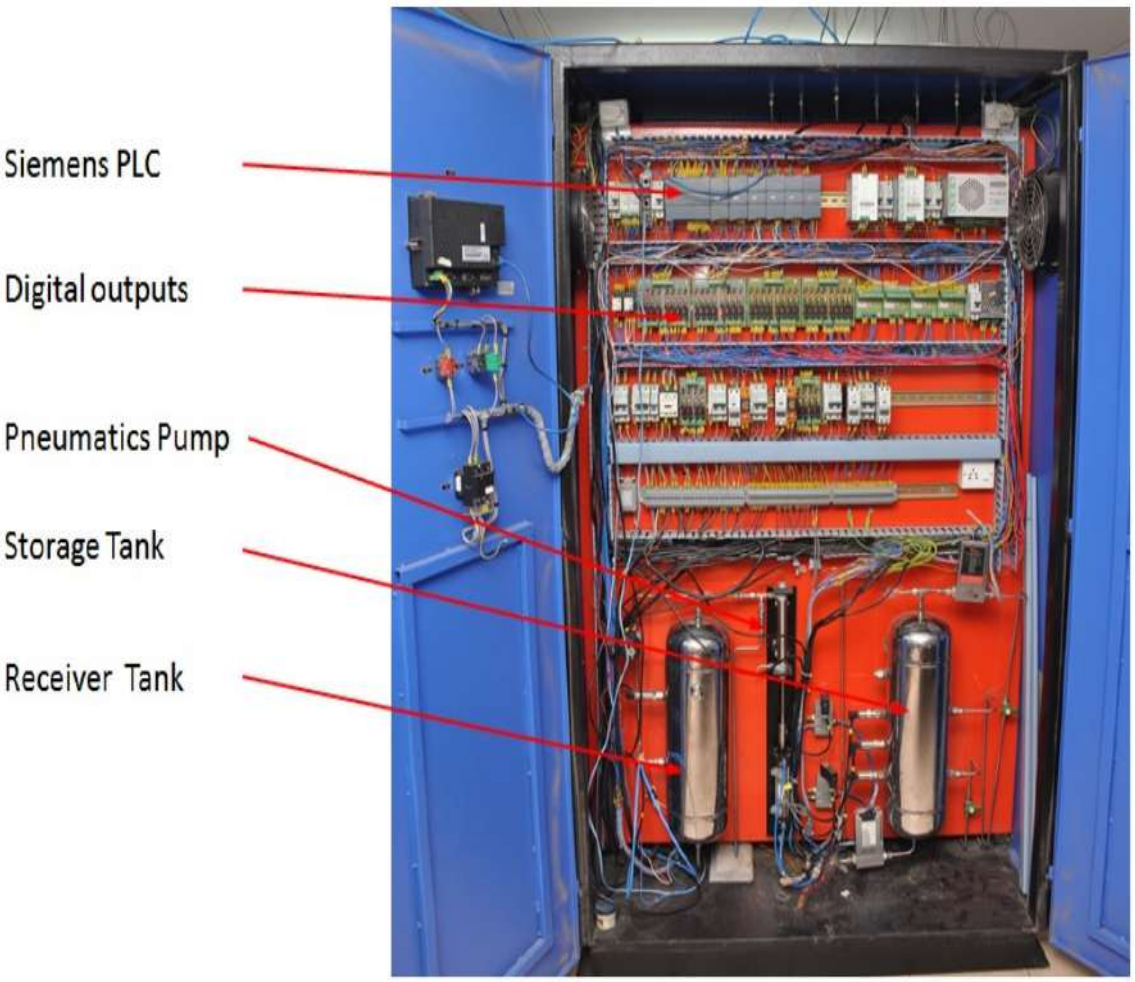

FIGURE 5.7: A Closed Loop Gas System unit functioning at TIFR [127].

5.5 Detector readout system

The Resistive Plate Chambers (RPCs) will be used as the active detector elements in ICAL. RPC offers time resolution of under 1 ns and spatial resolution of better than 1 cm which are the crucial parameters for the ICAL detector. Due to their planar geometry, RPCs are well suited for large area

detectors. They are easy to construct using commonly available materials and can easily be operated over long periods of time which is essential for ICAL detector. RPCs can be constructed using bakelite or glass as electrode materials, ICAL will use glass mainly due to the fact that it is readily available locally at a reasonable cost and has good surface quality. Each RPC detector element for ICAL will be 1.84 m in length and 1.84 m wide. Eight such elements will cover a road of 16 m $\times$ 2 m. Total 28,800 elements will be needed to fill the entire detector volume. The readout of the signals from RPCs will be obtained by outer orthogonal pick-up strips of 30 mm in pitch. INO collaboration has been undertaking a dedicated R&D programme to design, develop and characterize the RPCs.

5.6 Resistive Plate Chamber (RPC)

Resistive Plate Chambers (RPCs) are charged particle detectors consisting of two parallel plate electrodes of high volume resistivity such as glass or bakelite (phenol-formaldehyde polymer) with a gas gap in between. They were introduced in 1981 by R. Santonico and R. Cardarelli [129]. RPCs have very simple design to construct and operate. The main advantages of these detectors include large signal output, excellent time as well as position resolutions and low cost per unit area of coverage. An RPC operates under a constant and uniform electric field produced by two parallel plate electrodes of high bulk resistivity. A mixture of gases with a high absorption coefficient for ultraviolet light and high electronegativity is passed through the gap between the electrodes. The gas is ionised by a charged particle crossing the chamber and the produced free charge carriers trigger avalanches of electrons and start a discharge. The high resistivity of the electrodes ensures that the electric field drops in that limited area only. The state of the detector remains unaffected outside this small area. The ultra-violet absorbing component of the gas mixture absorbs the photons produced by the discharge and prevents secondary discharges. The propagation of the avalanche of electrons induces

a current on external strip electrodes. The outer electrodes are made of a resistive material (usually glass or bakelite) with bulk resistivity between 10^{10} - $10^{12}\Omega - cm$. A thin graphite coat is applied to the outer surfaces of these electrodes and connected to a high voltage power supply in order to create a uniform and intense electric field (about 5 kV/mm) in the gap between them. The gas gap between the electrodes is maintained by small cylindrical spacers (polycorbonate) of diameter $\sim$ 10 mm and a bulk resistivity greater than $10^{13}\Omega - cm$. A simple configuration of RPC is shown in figure 5.8.

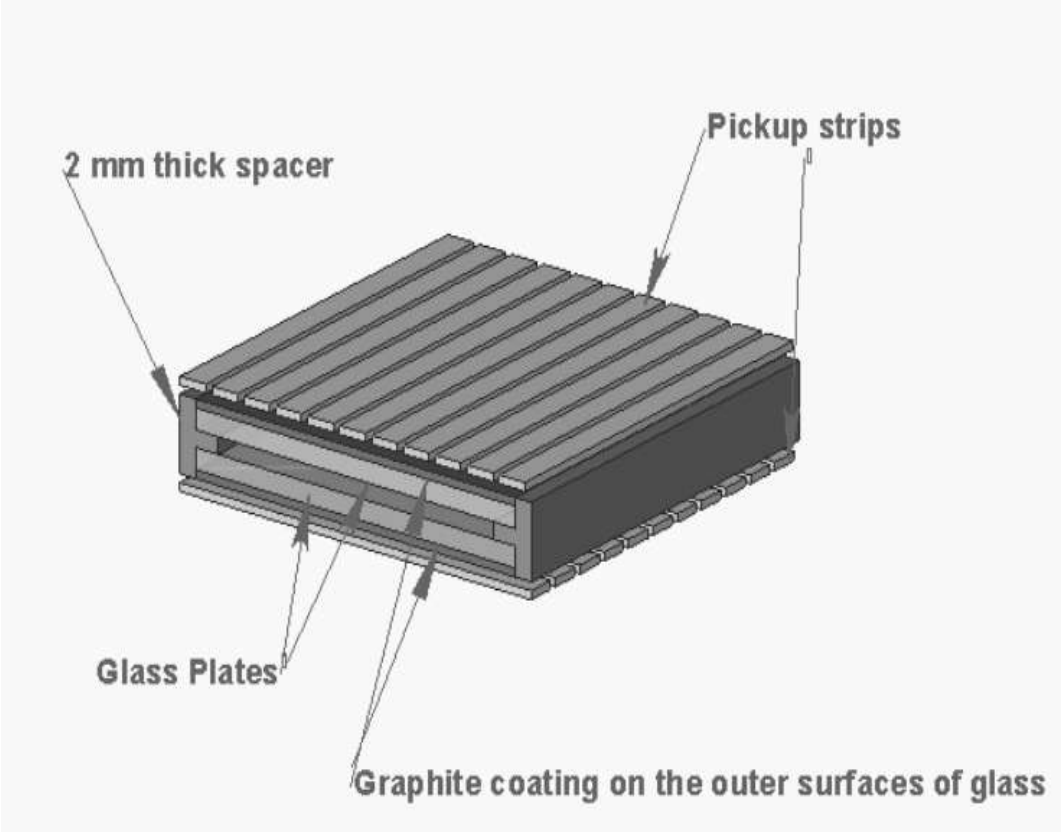

FIGURE 5.8: Schematic diagram of an RPC [125].

The high resistivity of the electrode material prevents the onset of the continous discharge between the electrodes. Therefore, the electric field drops significantly in the localized region of the discharge which subsequently extinguish it. This can be explained by the fact that the typical duration of the discharge is $\sim$10 ns while electrodes are recharged with the time constant (τ) which is of the order of $\rho\varepsilon$ [130], where ρ and ε are the resistivity and

dielectric constant of the electrode material respectively. Assuming, for example, $\varepsilon = 5 \times 10^{12}$ Ω-cm and $\varepsilon = 4 \times \varepsilon_0$ then the time constant $\tau \approx 1.8$ s. The large enough difference between τ and the typical discharge time in the detector makes it sure that the electrodes behave almost like insulators during the discharge. Only a localized area (about 0.1 cm^2) of the electrode surface experiances a high voltage drop which remains inactive for a time interval of order τ. Counting rate capability of an RPC depends on these characteristic times. Glass RPCs are therefore capable of counting rates of up to about 500 Hz/m^2 with a dead-time of less than 1%. The rate capability of bakelite RPCs is comparatively higher due to higher bulk resistivity of bakelite.

The electric signal in an RPC is formed due to the process of electron multiplication. An ionising particle passing through the gas gap creates a number of primary electrons. These n_0 primary electrons are accelerated by the appllied electric field in the form of a group and start the electron multiplication. This process is characterised by the "number of ionisations per unit length" (first Townsend coefficient "α") and by "the number of electrons that are captured by the gas per unit length" (the attachment coefficient "β"). The number of electrons reaching the anode will be given by [131]:

$$n = n_0 e^{\eta x} \tag{5.1}$$

where,

$$\eta = \alpha - \beta \tag{5.2}$$

and the detector gain is defined by

$$M = \frac{n}{n_0} \tag{5.3}$$

The gas mixture could be composed of Argon, Isobutane and an electronegative gas like Freon (R134a) or SF_6. Freon or Argon acts as target for ionising particles while an organic gas like Isobutane helps to quench the photons emitted by recombination processes thus supressing secondary avalanches

away from the primary ones. An electronegative gas limits the amount of free charge in the gas volume. Such gas mixture is specially required to avoid the formation of streamers.

5.6.1 Modes of operation

The value of M decides the mode of operation. M becomes larger than 10^8 in the case of streamer mode, however lower values of M ($\ll 10^8$) characterises the avalanche mode. The mode of operation mainly depends on the parameters α and β which is evident from equations 5.1 and 5.2. High rate applications and detector aging issues made the operation in avalanche mode popular. This is achieved by substantial reduction of the charge produced in the gas gap. The counting rate capability of RPCs is improved by more than an order of magnitude if the occurrence of streamers is suppressed by operating the detector in the avalanche mode. This was also facilitated by the development of new highly quenching $C_2F_4H_2$-based gas mixtures or with addition of small fraction of SF_6 to the gas mixtures. The $C_2F_4H_2$ gas in particular exhibits other attractive features like a moderately high density (resulting in high primary ionisation) and a low operating voltage. While the physics of streamers is difficult to study, the avalanche mode is amenable for detailed simulations of the physics processes in RPCs.

As the streamer signals are quite large (between 50 pC and a few nC), no amplification is needed and the signals can be discriminated against the detection threshold directly.Thus the read out of streamer mode RPCs is quite simple. Double gap chambers operated at electric fields of 40 kV/cm in streamer mode and with 2 mm wide gaps reach efficiencies of 99% and a time resolution around 1 ns. However, the rate capability is limited to a few hundred Hz/cm^2 .

After testing with various gas mixtures, a combination of R134a, Isobutane and SF_6 has been found suitable to operate RPCs in the avalanche mode during ICAL R&D program.

5.7 RPCs for ICAL

The ICAL detector at INO will consist of about 30,000 Resistive Plate Chambers (RPC) of about 2m $\times$ 2m in area as sensitive detector elements to track particles produced by the neutrino interactions inside the detector mass. Two collaborations are involved in the fabrication and study of these gaseous detectors. The group at VECC is involved in the study of Bakelite RPCs and the group at TIFR focuses on glass based RPC's.

The first activity in the R&D of RPCs at TIFR started with the development of a 30 sq.cm RPC. Later a stack of 12 RPCs of 1m $\times$ 1m was develped which now serves as a cosmic-ray telescope. The final ICAL detector will have about 3 million electronic channels and hence a suitable test bench is necessary for testing of the electronics. The stack serves this purpose. The long term stability of these detectors is studied by constantly monitoring the noise rates and the efficiency of the detectors. Detector related studies are complemented by cosmic muon studies. Recent studies include the directionality measurement of cosmic muons and the time offset calibration of the RPCs. The extensive study of sealed RPCs has been done by the collaboration with encouraging results. With the experience gained in the development of 1m $\times$ 1m RPCs, the group at TIFR progressed to fabricate 2m $\times$ 2m RPCs. The team was successful in the endeavor, with currently 10 RPCs in the new stack operational at the transit campus of Inter-Institutional Centre for High Energy Physics (IICHEP), Madurai.

To enable mass production of RPCs for the ICAL detector, the collaboration is now in the process of transferring the technology to the Industry. Some glass factories were approached and their personnel are trained in the fabrication and quality control of the RPCs. Industries are also consulted for the production of the conductive paints. An industrial technique was developed to screen-print the glasses and for the consequent curing of the same. The INO collaboration also looking for industrial interface for the production/design of the pick-up panels of the RPCs.

Chapter 6

INO simulations

The ICAL at INO would observe the atmospheric neutrino interactions by recording the "hits" generated in the active detector element (RPCs) by the final state particles produced in neutrino-nucleus reactions. The energy, direction and flavor of the initial neutrino can be determined by accurately measuring the energy and direction of the resultant charged particles (especially muons). Therefore, precise determination of the energy, direction and charge of the final state muon is crucial to achieve the physics goals of the ICAL. Information on the final state hadrons would further improve the physics sensitivity of the detector. Thus, the ICAL detector should be carefully calibrated to reconstruct the energy and direction of the muon and hadrons alongwith the correct charge of the muon.

Figure 6.1 illustrates the simulation framework for the ICAL. NUANCE Monte Carlo event generator [7] is used to simulate neutrino interactions in the detector. Atmospheric neutrino fluxes as described in Chapter 4 along with various neutrino-nucleus interaction cross-sections which are incoporated in NUANCE to generate the vertex position and the energy-momentum of all final state particles in each event. The output of the NUANCE is then passed through the GEANT4 based ICAL simulation kit. The GEANT4 package is used both to define the detector geometry as well as simulate the detector response for the propagation of particles through the simulated detector volume including the effects of the iron, the RPCs, and the magnetic field. This information is digitized by incorporating the detector efficiency and noise. The information thus available from each event is passed through the

reconstruction algorithms, which attempt, from the hit pattern, to identify a muon track and reconstruct its energy and direction. The detailed simulation procedure is described below.

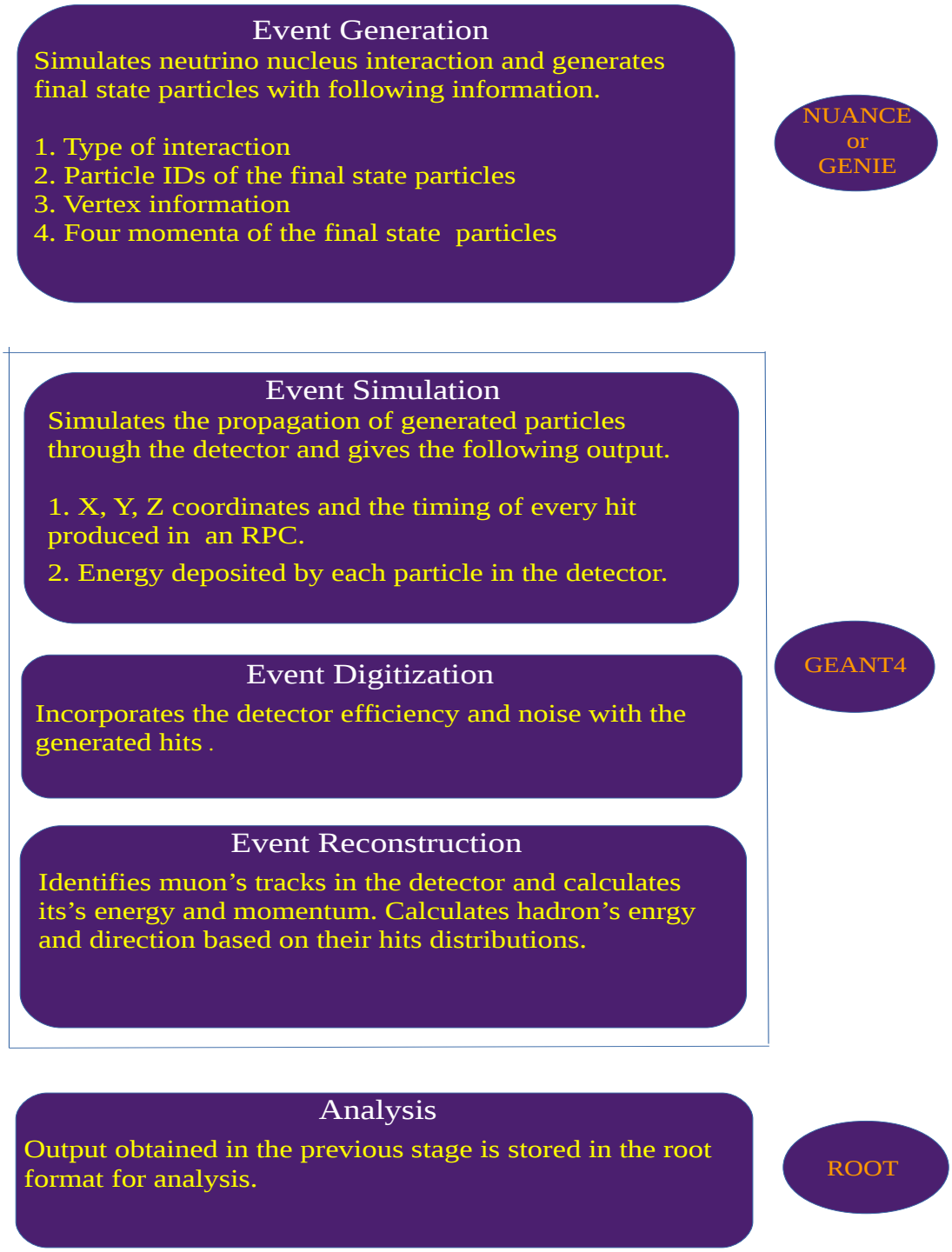

FIGURE 6.1: ICAL detector simulation framework.

6.1 Neutrino event generator

Neutrino event generators are Monte Carlo programs which simulate the neutrino-nucleous interactions using theoretical models. A neutrino with a given 4-vector momentum and a target nucleus are chosen by these generators [132]. The resultant particles are kinematically generated according to the physics lists in the event generator libraries to get the final state particles in the given detector geometry. A variety of scattering mechanisms are included alongwith the elementary cross-sections, hadronization models and nuclear models. Different models with their corresponding range of validity are included to cover the desired phase space. There are can be a kinematic regime outside the scope of all existing models, which requires either the development of a new model or the adoption of a model which can be extrapolated into the region of interest.

A number of neutrino event generators are available, such as ANIS [133], GENIE [134], GiBUU [135, 136], NEGN [137], NEUT [138], NUANCE [7], the FLUKA routines [139], NUNDIS/NUNRES [140], and NuWRO [141]. We are interested in the few-GeV range for atmospheric neutrinos. We have used NUANCE and GENIE to generate atmospheric neutrino events for our present study.

6.1.1 NUANCE

It is a FORTRAN based program, which we have used to simulate atmospheric neutrino events in simple ICAL detector geometry. NUANCE was developed by Dave Casper [7] to generate neutrino events for Super Kamiokande experiment. The detector geometry and the target materials are specified by the user. The list of cross sections and the rates of all the known interaction channels are invoked using the corresponding libraries. Events can be generated either by specifying the number of events or by specifying the exposure time. The information of the generated events is saved in the form of an ascii file. The interaction models used in this program was originally

developed for the IMB experiment. NUANCE include models for following interactions:

- quasi-elastic scattering (QE) which dominate below neutrino energies of 1 GeV,
- resonant scattering (RES) for neutrino energies between 1 and 2 GeV,
- deep inelastic scattering (DIS) which is dominant in the multi-GeV region,
- coherent nuclear processes on nuclei,
- neutrino-electron elastic scattering and inverse muon decay.

The contribution of the last two is negligible in the few GeV energy region of interest. A simple ICAL detector geometry has been defined within NUANCE. It can distinguish between the bound nucleons (with corresponding Fermi energies) and the free nucleons and applies final state nuclear corrections. The NUANCE generator integrates different cross sections weighted by the fluxes for all charged current (CC) and neutral current (NC) channels at each neutrino energy and angle to calculate final event rate. There can be 10-40% uncertainty in cross sections in the intermediate energy ranges [142] based on the interaction channel. NUANCE can also generate neutrino data with different oscillation parameters. The oscillation of atmospheric neutrinos is achieved by assuming the earth's sphere in 25 concentric shells of varying density. The events are first analysed at the NUANCE output level which defines the kinematic limitations on the event reconstruction. Then the NUANCE output is passed through the GEANT4 simulated ICAL detector to study the sensitivity of the ICAL detector to atmospheric neutrinos.

6.1.2 GENIE

GENIE is an acronym for Generates Events for Neutrino Interaction Experiments. It is based on object-oriented/C++ neutrino Monte Carlo Generator. It supplants Fortran neutrino MC generators, such as GENEVE [143], NEUT,

NeuGEN [144] and NUX [145]. GENIE is developed as a neutrino interaction physics Monte Carlo generator which is suited to all nuclear targets, complicated detector geometries and neutrino flavors from MeV to PeV energy scales.

In order to achieve a realistic description of the experimental signature of any detector and all its components, all the neutrino-nucleus interaction processes must be accurately modeled. Most of the theoretical models only partially describe these processes. GENIE includes several such models to properly incorporate all the physics processes. The list of physics models include nuclear, cross-sectional, quasi-elastic scattering, elastic neutral current scattering, baryon resonance production, coherent neutrino-nucleus scattering, non-resonance inelastic scattering, quasi-elastic charm production, deep-inelastic charm production, inclusive inverse muon decay and neutrino-electron elastic scattering. GENIE also uses the AGKY hadronization model (developed for the MINOS experiment) to take care of the transition region, total cross section and the neutrino-induced hadronic multiparticle production modeling.

6.2 GEANT4 detector simulation

GEANT4 [146] is a toolkit based on the C++ programming language for simulating the propagation of particles through different materials. It offers diverse applications for tracking, geometry, physics models and hits. Various physics processes such as electromagnetic, hadronic and optical are included with a large set of long-lived particles, materials and elements, over a wide energy range. It can handle complex geometries to enable its easy and effective use in different sets of applications. It has been used in applications in particle physics, nuclear physics, accelerator design, space engineering and medical physics. It considers the following broad aspects of the simulation of the passage of particles through a detector.

- geometry and materials,

- particle interaction in matter,
- tracking management,
- digitisation and hit management,
- event and track management,
- visualisation and visualisation framework,
- user interface.

The physics processes cover a wide range of energies from 250 eV to the TeV. A block diagram in figure 6.2 illustrates the same flow of dependencies.

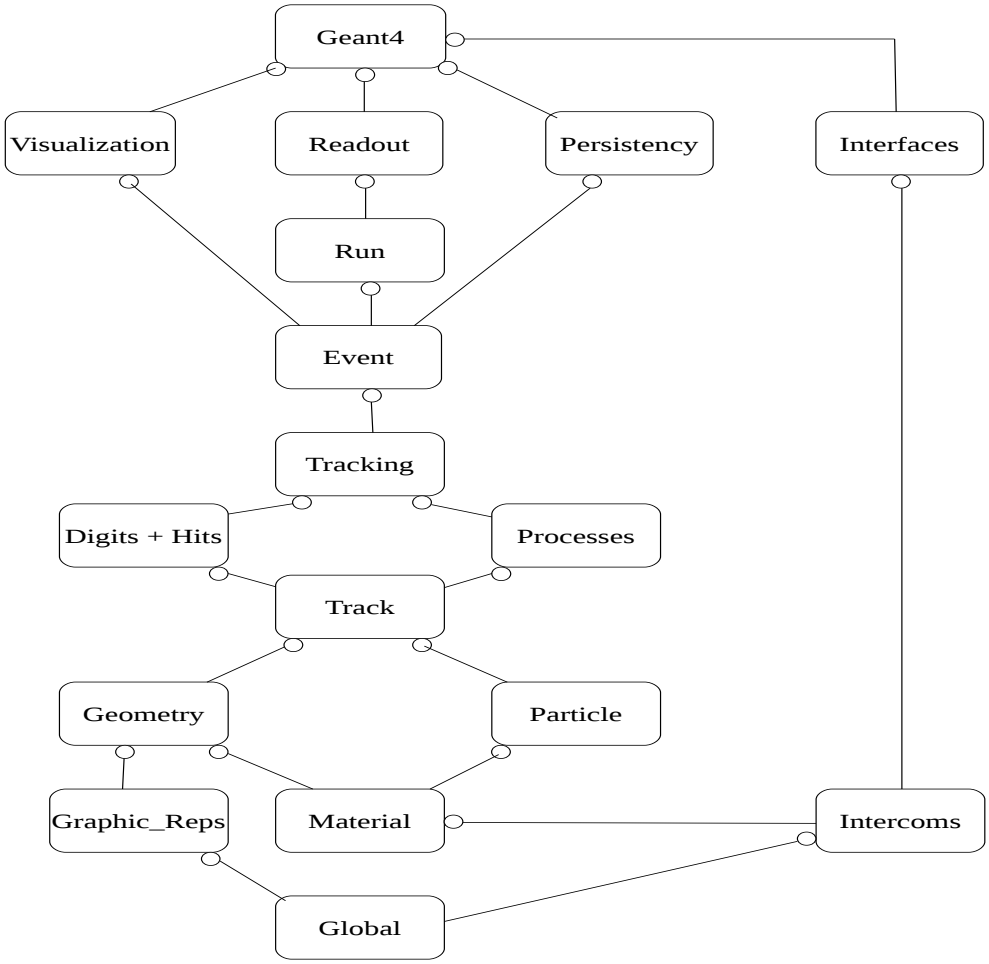

FIGURE 6.2: The Top Level Category Diagram of the Geant4 toolkit. The open circle on the joining lines represents a using relationship;the category at the circle end uses the adjoined category [146].

6.2.1 ICAL geometry

A 50 kt ICAL detector with a modular structure has been simulated using GEANT4 package. There are three modules, each of size 16 m (length) $\times$ 16 m (width) $\times$ 14.5 m (height), with a gap of 20 cm between the modules. Each module consists of 151 horizontal layers of 5.6 cm thick iron plates. The area of each module is 16 m $\times$ 16 m, while each iron plate has dimensions 2 m $\times$ 4 m. There is an air gap of 4 cm between two iron plates. Steel support structures are placed every 2 m in both the x and y directions to support iron sheets. RPCs are placed within the air gaps and have dimensions of 1.84 m $\times$ 1.84 m $\times$ 2.5 cm. A 16 cm horizontal gap is kept between RPCs in both x and y directions to accommodate the support structures. The direction along the placement of modules is labelled as the x-direction and the other horizontal transverse direction is considered as y. The z-axis points vertically upwards. The centre of the second module is taken as the origin. Four copper coils wind around the iron plates which provide a magnetic field in the x-y plane, as shown in chapter 5. These coils are accomodated in vertical slots created at x = $x_{center} \pm 4$ m (where x_{center} is the central x value of each module) extending up to y = $\pm$4 m and cutting through all layers. The field strength in the central region of each module is about 1.5 T in the y-direction, as calculated by MAGNET6.26 software [147].

6.2.2 Active detector element:RPC

Resistive Plate Chambers (RPCs) are the active detector elements for ICAL which has to be interleaved with iron plates in the detector simulation process. Two glass plates of 3 mm thickness are sealed with a gap of 2 mm gap between them. A high DC voltage is applied across them. A mixture of R134A ($\sim$ 95%), isobutane, and small volume of SF_6 gas continually flows through the gap. The working principle of an RPC is described in reference [148].

A copper sheet of 150 micron thickness is placed on the inside of a 5 mm thick honeycomb material located both above and below the glass chamber. Mylar sheets are inserted between the glass plates and the copper sheet. Strips of width 1.96 cm are grooved on this copper sheet with above and below strips transverse to each other. These pick-up strips thus provide the x and y location of the charged particle as it traverses the RPC while the RPC layer number provides the z information. A timing resolution of about 1.0 ns and an efficiency of 95% are incorporated in the simulations based on the observations of RPCs as a part of INO R&D program [148].

6.2.3 Event Simulation and Digitisation

The full ICAL geometry is stored to a machine readable GDML file which also contains the RPC detector components, the support structure, and the gas composition. This GDML file is read by the event reconstruction package. The copper sheets are considered as a continuous material for GEANT4 simulations, however for signal digitization the separate copper strips are considered.

Passage of a charged particle through an RPC induces a signal on the pick-up strips and assigned "X" and "Y" values from the respective pick-up strips. Z coordinate is given by the the layer number information. A time stamp "t" is also recorded alongwith each hit. The threshold energy to produce a hit in an RPC is taken to be 30 eV, with an average efficiency of 95%. The spatial resolutions, the effect of cross-talk (strip multiplicity) are also incorporated, using the results from [148]. Finally, all possible pairs of nearby X and Y hits in a plane are grouped to form a cluster. A typical charged current neutrino interaction event producing a muon track and associated hadron shower is shown in figure 6.3. A typical muon track is clean with one or two hits per layer and crosses an average of 5 layers, whereas the hadron produces a shower with hits generated in a small region only.

6.2.4 Muon track reconstruction in ICAL

Since, muons leave a long clean track, ICAL is designed to reconstruct the energy, direction and charge of a muon produced in an atmospheric neutrino event quite efficiently. Different types of hadrons leave similar hit patterns in ICAL. Therefore individual hadrons can not be reconstructed. Only an averaged information can be obtained due to all the hadrons produced in an event.

The trajectory of a muon bends as it traverses in the magnetized detector. Depending on the direction of the direction of this bending, ICAL can distinguish between a μ^+ and a μ^-. The curvature of the trajectory or the total pathlength can be used to calculate muon momentum. RPC's excellent time resolution ($\sim$ 1 ns) allows the distinction between up-going and down-going muons.

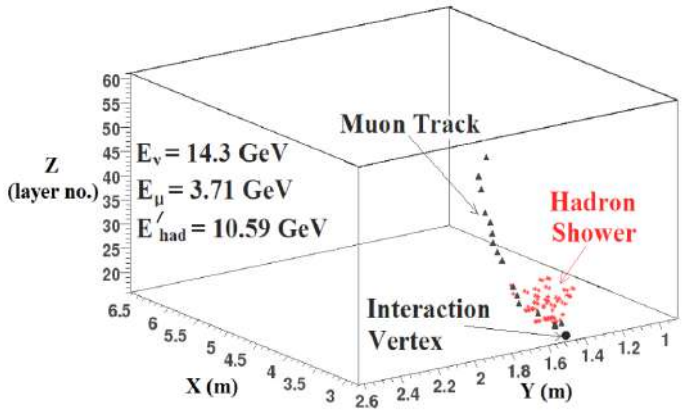

FIGURE 6.3: A typical DIS interaction event in the simulated ICAL.The black filled triangles represent the muon track, while the red stars show the shower created by the hadrons [9].

A track finder package followed by a track fitting algorithm reconstructs both the momentum and charge of the muon.

The track Finder: The (x, y, z) coordinates and the time stamp for each hit are stored for individual events separately. All the adjacent "X" and "Y" hits in a plane are grouped to form a cluster. The track finder algorithm combines clusters formed in adjacent layers through a curve fitting algorithm in order

to obtain a tracklet. Nearby Tracklets are then joined to form a track, and the iteration of this process gives the longest possible track in an event [149]. The average of the time information from all the x and y strip hits in a layer used to decide the direction of the track (upward or downward). At least 5 hits in a track are required to classify it as a muon-like track. The clusters in each layer are then averaged to effective one hit per layer, and the corresponding averaged coordinate and timing information are further processed by the track fitting algorithm.

The track fitter: A Kalman-filter based algorithm is applied to fit the tracks including the effect of the magnetic field. A track is considered with a starting vector

$$X_0 = (X, Y, dX/dZ, dY/dZ, q/p) \tag{6.1}$$

where (X, Y, Z) is the position of the earliest hit as recorded by the finder. The ratio q/p is called the charge-weighted inverse momentum which is taken as zero at the starting point. The initial track direction, from the slopes dX/dZ and dY/dZ, is estimated from the first two layers because the tracks are almost straight in the begining. This initial state vector is then extrapolated to the next layer by calculating the Kalman gain matrix incorporating local magnetic field and the geometry. The state prediction is done using the Kalman filter algorithm and the corresponding error propagation is implemented by a propagator matrix [149]. The state extrapolation takes care of the noise due to multiple scattering as described in [150] and energy loss in the detector material, mostly iron, according to the Bethe formula [151]. The formulae for the propagation of the state and errors [152] have been improved for atmospheric neutrinos with large energy and range. The extrapolated point is compared with the actual hit point in that layer, if any, and the process is iterated. The process of iteration continues till it obtains the best fitted track. The fitted track is then extrapolated backwards to locate the vertex of the interaction. The best fit value of the momentum at the vertex is the reconstructed momentum. The quality of fit better than $\chi^2/\text{ndf} < 10$ is imposed

for the reconstructed tracks to be used in the analysis. The magnitude of the momentum at the vertex is given by q/p. The direction is determined by the slops dX/dZ and dY /dZ and saved in the form of the zenith angle θ and the azimuthal angle ϕ.

6.3 Response of muons in ICAL

The reconstruction of single muons has been studied using the GEANT4 Monte Carlo generated muons at various momentum P_μ and zenith angle θ_μ. The central volume of the ICAL with dimentions 8 m$\times$8 m$\times$10 m has been used to randomly generate the interaction vertex, and 10000 muons at different momenta and zenith angles are propagated. The azimuthal angle is smeared uniformly between 0 to 2π for all the (P_μ, θ_μ) combinations [153]. The muon momentum resolution, zenith angle resolution, charge identification (CID) efficiency and track reconstruction efficiency have been studied. Figure 6.4 shows the important results from this analysis are mentioned below. Figure 6.4a shows the momentum resolution of muons in ICAL. It can be seen from the figure that the resolution improves with increase in momentum upto about 6 GeV. In this energy range, the number of RPC layers in the track and the number of hits in layers increase with increasing energy and magnetic field bends the muon tracks significatly. These factors improve the momentum reconstruction. However, beyond this energy range, the particles tend to exit the detector and leave only a partial track in the detector. The radius of curvature of the track also increases. These effects deteriorate the momentum resolution. Figure 6.4b shows the θ resolution. For all zenith angles and P_{in} >4 GeV/c, the resolution is better than a degree. At 10 GeV/c and beyond, the resolution curves approximately coincide. Figure 6.4c shows the relative charge identification (CID) efficiency. Due to the multiple scattering of muons in the detector, the direction of bending at smaller incident momentum can be wrongly reconstructed, since the number of layers crossed is small. This effect can be seen in the figure as the efficiency at

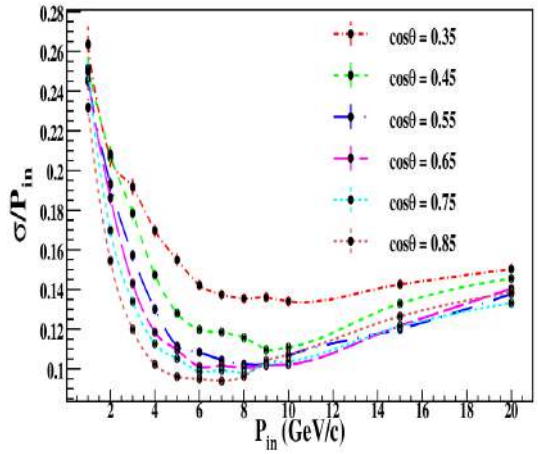

(A) Momentum resolution.

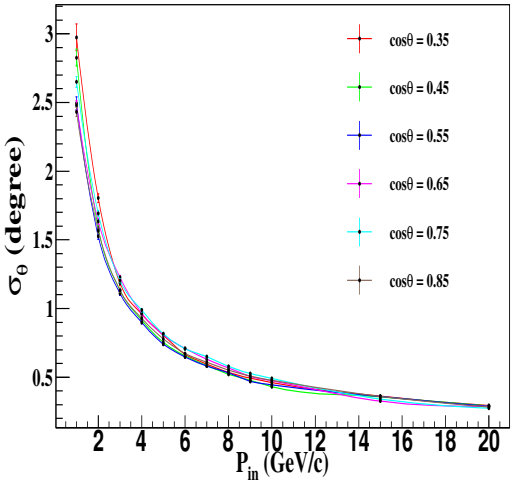

(B) θ resolution.

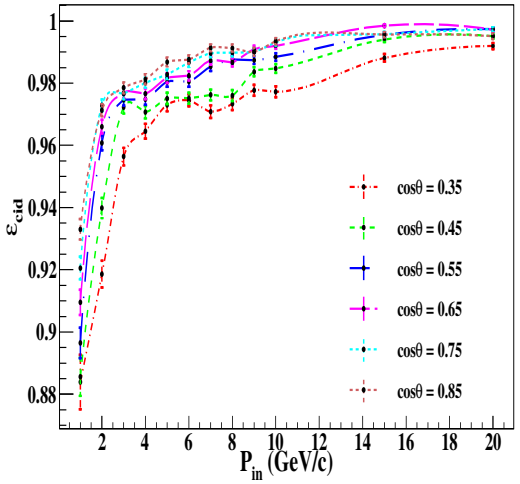

(C) CID reconstruction efficiency.

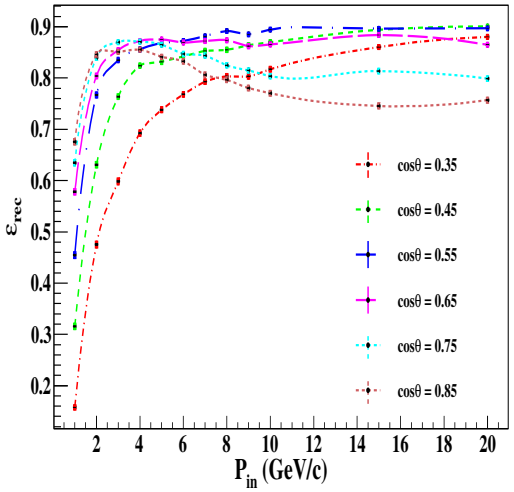

(D) Muon momentum reconstruction efficiency.

FIGURE 6.4: Momentum resolution, θ resolution, CID reconstruction efficiency and momentum reconstruction efficiency as a function of the input momentum and at certain $\cos\theta$ bins [153].

lower energies is relatively poorer. With increase in energy, the track length increases and the reconstruction of the direction of the curvature becomes more accurate. Figure 6.4d shows the relative charge identification (CID) efficiency. The momentum resolution efficiency is marginally smaller than the track reconstruction efficiency, particularly at smaller angles. This efficiency depends on the factors like the incident energy and direction, the magnetic field strength.for momentum values < 4 GeV/c, the reconstruction efficiency increases with increasing incident momentum at all incident angles. This is

due to the increase in the number of hits with increase in incident momentum, as the particle traverses more number of layers. This effect is the most for the particles propagating in a near vertical direction. As the zenith angle increases, the number of layers crossed by the particle becomes smaller. However, at higher energies, the particle at any incident angle crosses sufficient number of layers, and the reconstruc- tion efficiency becomes almost constant. A drop is observed in the reconstruction efficiency of the vertical muons, which is due to the track being partially confined in the detector and the requirement of a single reconstructed track to pick the events to be analyzed.

Chapter 7

Hadron energy estimation from atmospheric neutrino events

7.1 Introduction

The design of ICAL enables it to reconstruct the track of a muon with good accuracy. From this reconstructed track, the charge, the energy and the direction of the muon are estimated with good precision. At first, the physics capabilities of ICAL were studied using the kinematical information of only the muons [2, 3, 4]. The charged hadrons, produced in the atmospheric neutrino interactions, will also produce hits in the RPCs of the ICAL. Most of the time, the hits due to the hadrons can not be reconstructed into tracks because (a) the energy of a typical hadron is much smaller than the energy of the muon and (b) the hadrons can be absorbed by the detector nuclei. Thus, the inclusion of the hadron energy in the kinematic reconstruction of an event poses a great challenge. The first estimate of the hadron energy of atmospheric neutrino events in ICAL was done in ref. [9].

Various efforts were made to estimate the hadron energy in ICAL [5, 6]. However, in most of these efforts, a charged pion of known energy is injected into Geant4 simulator and the corresponding hit pattern was studied. This process was repeated for pions of different energies. Through these simulations, a correlation between the pion energy and the number of hits was established and the resolution in pion energy was estimated. *It was*

assumed that these correlations and the resolutions will hold for all hadrons produced in atmospheric neutrino interactions. The physics capabilities of ICAL are re-calculated using three kinematical variables: muon energy, muon direction and the hadron energy, estimated from the pion simualtions mentioned above. With this "3-D analysis", it was shown that the physics capabilities are enhanced [154, 155].

In this work, we have taken a different approach. We did a systematic study of particle production in atmospheric neutrino events. We found that a significant number of baryons are produced in a large fraction of these events. For hadron energy less than 5 GeV, these baryons carry most of the hadron energy. Therefore, we believe that the hit pattern produced by an isolated, single charged pion does not represent the hit pattern produced by the hadrons in an atmospheric neutrino event properly. We established a correlation between the hits produced by the baryons (called **baryon hit bank**) and the baryon energy in atmospheric neutrino events. This correlation is very different from the correlation found for pions in reference [6]. Later, we did a full Geant4 simulation of all the final state particles of the atmospheric neutrino events in ICAL. From the set of hits produced by these particles, we removed those hits which were included in the track reconstruction. It is assumed that the hits forming the track (the highest energy track, in case there is more than one track) are produced by the muon and the remaining hits are produced by hadrons. We used this **hadron hit bank** information to estimate the hadron energy in atmospheric neutrino events. In both the baryon analysis as well as the hadron analysis we used 100 years of unoscillated atmospheric neutrino events simulated using NUANCE event generator. From these, we have selected those events which contain charged current (CC) interactions of ν_μ and $\overline{\nu}_\mu$.

7.2 Baryons in atmospheric neutrino events

As mentioned in the introduction, we believe that doing a simple simulation of isolated charged pions does not reflect the true picture of hadron production in atmospheric neutrino events.

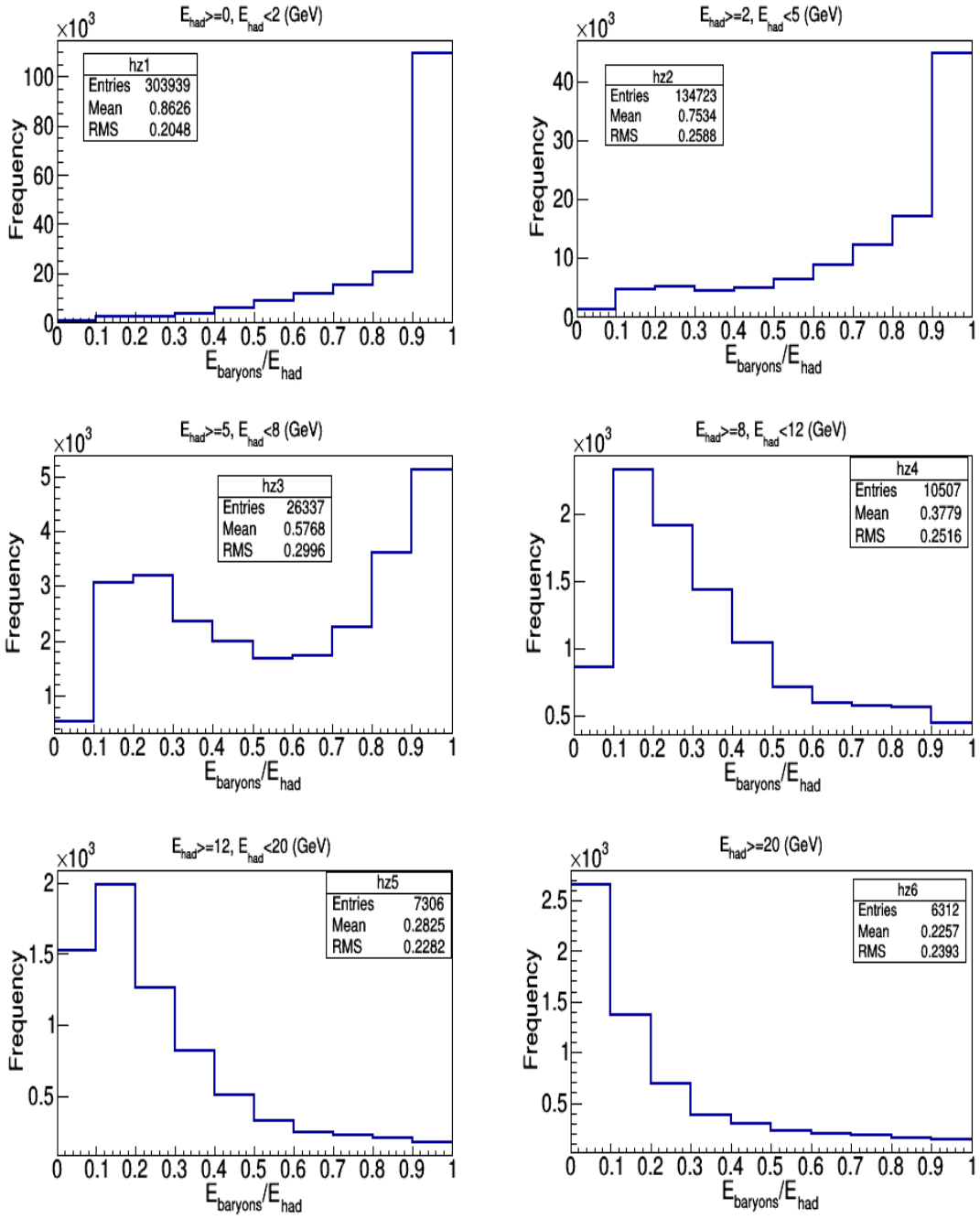

FIGURE 7.1: The ratio $E_{baryons}/E_{had}$ versus frequency

This is so because a fair number of baryons are produced in these events

and they carry a non negligible fraction of the hadron energy. This is illustrated in figure 7.1. From the first two panels of this figure, we see that baryons carry almost all of the hadron energy for a vast majority of events when $0 \leq E_{had} \leq 5$ GeV. For larger values of hadron energy, the energy fraction carried by the baryons becomes smaller untill it becomes negligibly small for $E_{had} > 20$ GeV. Therefore, in this section, we study the correlation between the energy carried by the baryons and the hits produced by them in ICAL.

7.2.1 Baryon hit bank

In order to do this analysis, we need to know (a) the hits produced by these baryons ("baryon_hits") and (b) the total energy carried by all the baryons (E_{baryon}) in each event. To calculate baryon_hits, we used the following method: We took all the ν_μCC events generated by NUANCE and looked at the particle content of all the mesons in these events. We found that essentially all of these mesons are pions and kaons and the heavier mesons form less than 1% of all the mesons. So, we did a Geant4 simulation of these events after turning off the muons, the pions and the kaons. It is expected that the resulting hit bank information is essentially due to the baryons produced in these events. The number of baryon hits as a function of $E_{\text{had}} = E_\nu - E_\mu$ is given in table 7.1, where E_ν and E_μ are given by NUANCE. We define $E_{baryon} = E_\nu - E_\mu - E_{meson}$. It is straight forward to obtain E_{baryon} from NUANCE. After obtaining baryon_hits and E_{baryon} for each event, we define a set of ranges of baryon_hits. For each range we plot the histogram of frequency versus E_{baryon} and fit a Vavilov distribution [8] to each histogram. We tested a number different sets of ranges until we found an optimal set for which the fitted distributions matched the histograms very well.

S. No.	E_{had}	0-6	6-10	10-20	20-30	30-50	50-80	≥ 80
1	0-0.5	51739	74	10	1	2	3	0
2	0.5-1	113992	2391	138	19	5	3	0
3	1-1.5	73984	4543	380	16	6	3	1
4	1.5-2	49786	6126	690	16	5	2	4
5	2-3	56228	13812	2181	22	20	5	0
6	3-4	25375	10855	3261	55	11	6	1
7	4-5	25375	10855	3261	55	11	6	1
8	5-7	12232	6945	3620	75	14	3	2
9	7-10	10656	5613	4627	241	17	2	1
10	10-20	6269	2546	2416	310	33	6	1
11	20-30	6383	2235	2094	533	155	10	2
12	30-50	1725	551	562	220	167	20	2
13	$\geq$50	1096	368	344	182	156	58	6

TABLE 7.1: Baryon hits and E_{had} table.

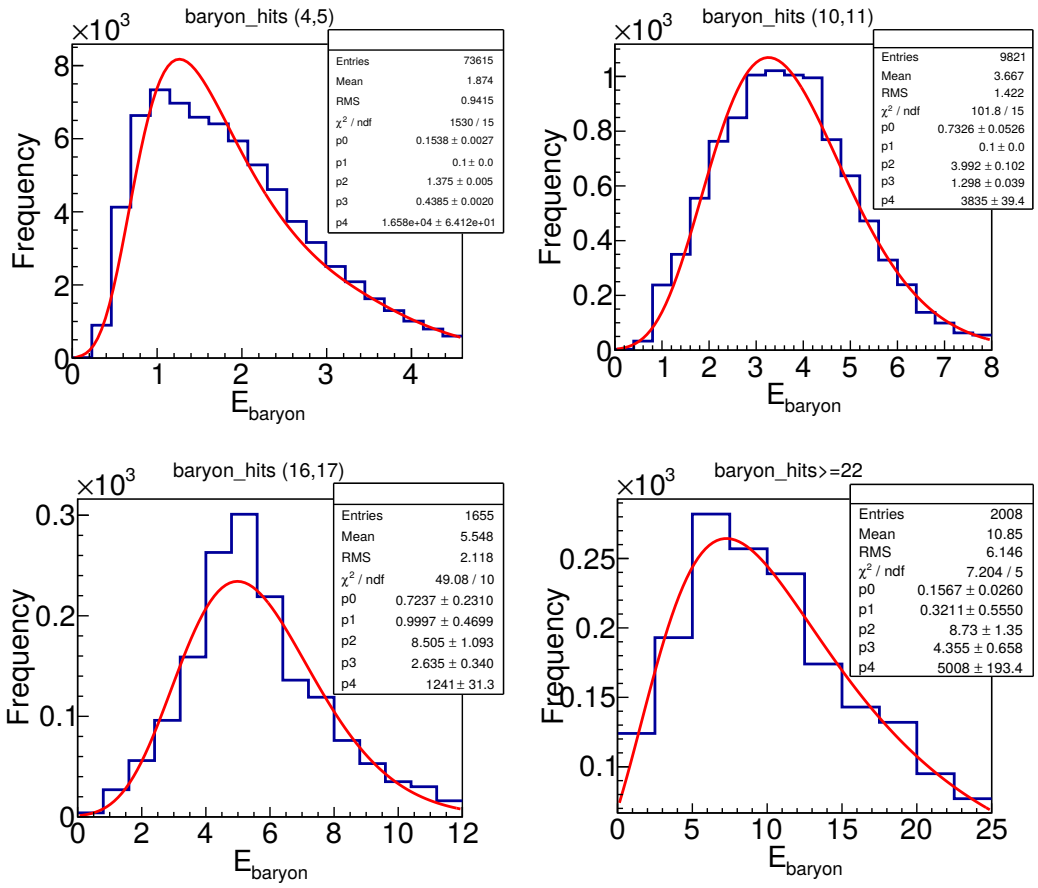

FIGURE 7.2: E_{baryon} distribution for hit ranges (4,5), (10,11), (16,17) and ($\geq$22)

From the fits done for this optimal set of ranges, we determined the average value of $E_{baryon-mean}$ and the associated resolution σ_{Eb} for each range.

These quantities are defined as

$$\begin{aligned} E_{baryon-mean} &= (\gamma - 1 - lnP_0 - P_1)P_3 + P_2, \\ \sigma_{Eb} &= \sqrt{\frac{(2-P_1)}{2P_0}P_3^2}, \end{aligned} \tag{7.1}$$

where "γ" is the Euler's constant and "P_i" are the parameters of the Vavilov fit. A sample of these fits are shown in figure 7.2. The values of $E_{baryon-mean}$ and σ_{Eb} for each baryon_hits range, are listed in table 7.2.

S. No.	baryon_hits	$E_{\text{baryon}-\text{mean}}$	σ_{Eb}
1	0-1	0.898	0.582
2	2-3	1.340	0.845
3	4-5	1.967	1.090
4	6-7	2.569	1.237
5	8-9	3.179	1.369
6	10-11	3.717	1.477
7	12-13	4.299	1.607
8	14-15	4.837	1.774
9	16-17	5.609	2.190
10	18-21	6.603	2.855
11	≥ 22	13.561	10.079

TABLE 7.2: baryon_hits and E_{baryon} table.

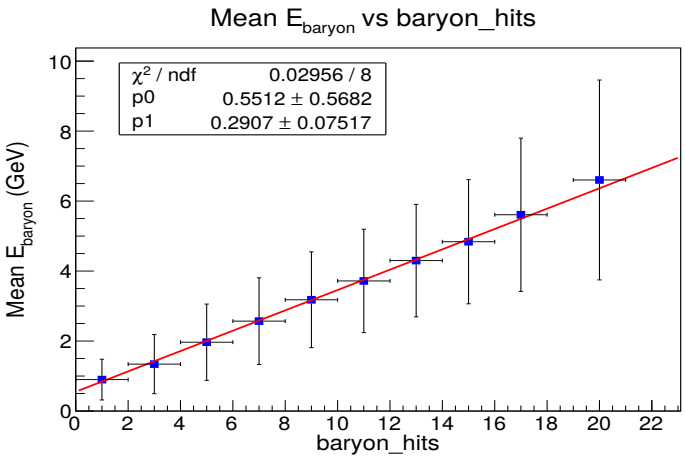

FIGURE 7.3: $E_{\text{baryon}-\text{mean}}$ vs baryon _hits

The relation between baryon_hits and $E_{\text{baryon}-\text{mean}}$ is shown in figure 7.3. The error bars in the x direction span the bin size in the number of hits. The error bars in the y direction extend $\pm\sigma_{Eb}$ from $E_{\text{baryon}-\text{mean}}$. The data in figure 7.3 is well described by the linear fit

$$E_{\text{baryon}-\text{mean}} = 0.55\ (\text{baryon\_hits}) + 0.29. \tag{7.2}$$

We compare this relation with the relation obtained from the simulation of isolated pions. This latter simulation was done in reference [6]. The left panel of figure 2 of this reference gives the plots of "Mean no. of hits" versus E_{pion} for various different thickness values of the iron plates of ICAL. These plots are shown in figure 7.4. The Geant4 simulation used in our analysis used iron plate thickness of 5.6 cm. We took the data for this thickness from figure 7.4 and replotted it in the form E_{pion} versus Mean no. of hits in figure 7.5.

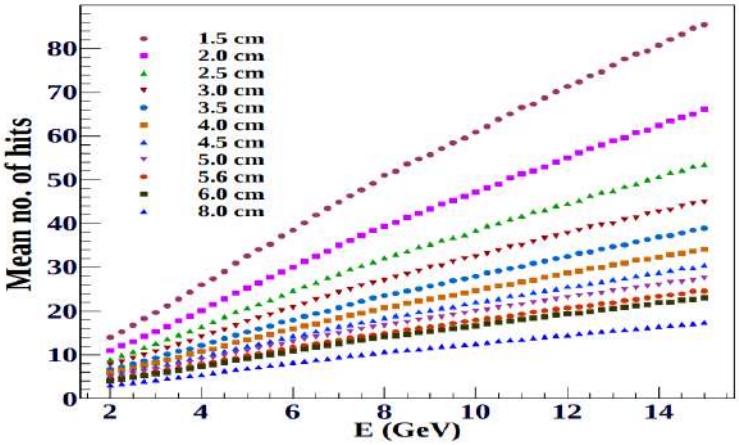

FIGURE 7.4: "Mean no. of hits" versus E_{pion} for various different thickness values of the iron plates of ICAL [6]

We see that the data shows a linear relationship between these two variables and a linear fit gives the relation

$$E_{\text{pion}} = 0.64\ (\text{Mean\_no.\_hits}) - 1.57. \tag{7.3}$$

We see that there is a linear relation between the no. of hits and the hadron energy for pions also. Comparing equations 7.2 and 7.3, we note that the

slopes in the two equations are close but the intercepts are very different. Therefore, we argue that the energy estimate made for pions can not be extended to all hadrons. A proper estimation of hadron energy in atmospheric neutrino events requires doing a full Geant4 simulation of these events and establishing a relation between the number of hits produced by the hadrons and the hadron energy.

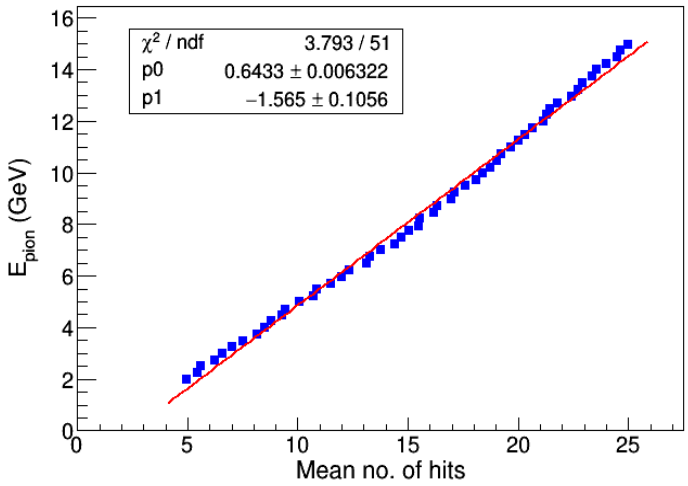

FIGURE 7.5: "Mean no. of hits" for 5.6 cm thick iron plates of ICAL

7.3 Hadron hit bank analysis

In this section, we analyse the hits generated by the hadrons produced in the ν_μ CC events of atmospheric neutrinos. We establish a correlation between these hadron hits and the energy of the hadrons. We will also calculate the energy resolution for each given hadron energy. As mentioned before, such an analysis was performed earlier in ref. [9]. However, there are two important differences between the procedure of ref. [9] and our procedure. We will describe them at the end of the section.

7.3.1 Hadron hit bank

The Geant4 simulation of atmospheric neutrino events gives the full hit bank information due to all the charged particles. The ICAL reconstruction code

looks to form a track with a subset of the total number of hits. If a track is not constructed, the event is not processed any further. If a track is constructed, such a track is identified with a muon. The hits which make up the track are removed from the hit bank information. These remaining hits form **hadron hit bank**. In the analysis below, the events with no hadron hits are discarded. The hadron hit bank is likely to contain ghost hits. To avoid overcounting due to ghost hits, we consider the larger of (number of x-hits, number of y-hits) from the hadron hit bank. This number is defined to be "hadron_hits". The difference between the neutrino energy and the muon energy for a given event, obtained from NUANCE, is defined to be "E_{had}" of that event.

The hit distributions of this hit bank are given in figure 7.6. From the hit distribution, we see that most of the events have less than five hits and a vast majority have less than 10 hits.

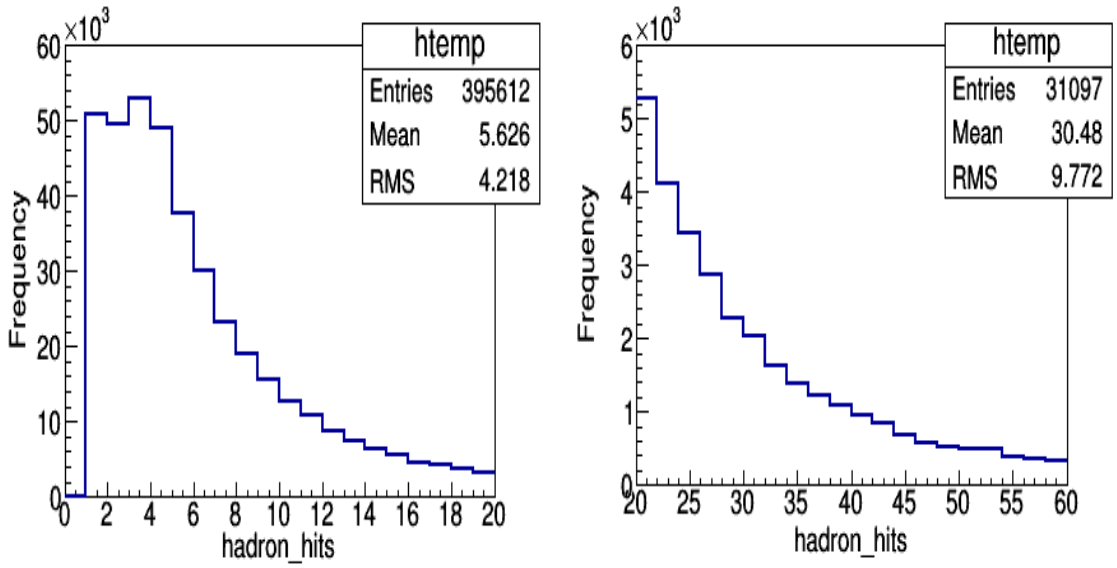

FIGURE 7.6: The left (right) panel shows the distribution for the number of hits $< 20 (\geq 20)$.

We first divided the event sample into different bins, each with it's own range in the number of hits. For each bin, we plotted the histogram of frequency versus E_{had} and fit it to a Vavilov distrbution. Various different hit ranges were tried out and the procedure was repeated till we obtained an optimal set of hit ranges for which the Vavilov distribution provided a good

fit for each of the frequency versus E_{had} histograms. These histograms, along with the fitted Vavilov distributions, are shown in figures 7.7, 7.8, 7.9, 7.10. For the bin with $2-3$ hits, the Vavilov distribution was not a good fit. Therefore this bin was not used in further analysis. Moreover, such low number of hits may occur due to the noise rather than due to charged hadrons. This is another justification for dropping this bin. The hadron hit ranges used and the corresponding Vavilov fit values are shown in table 7.3.

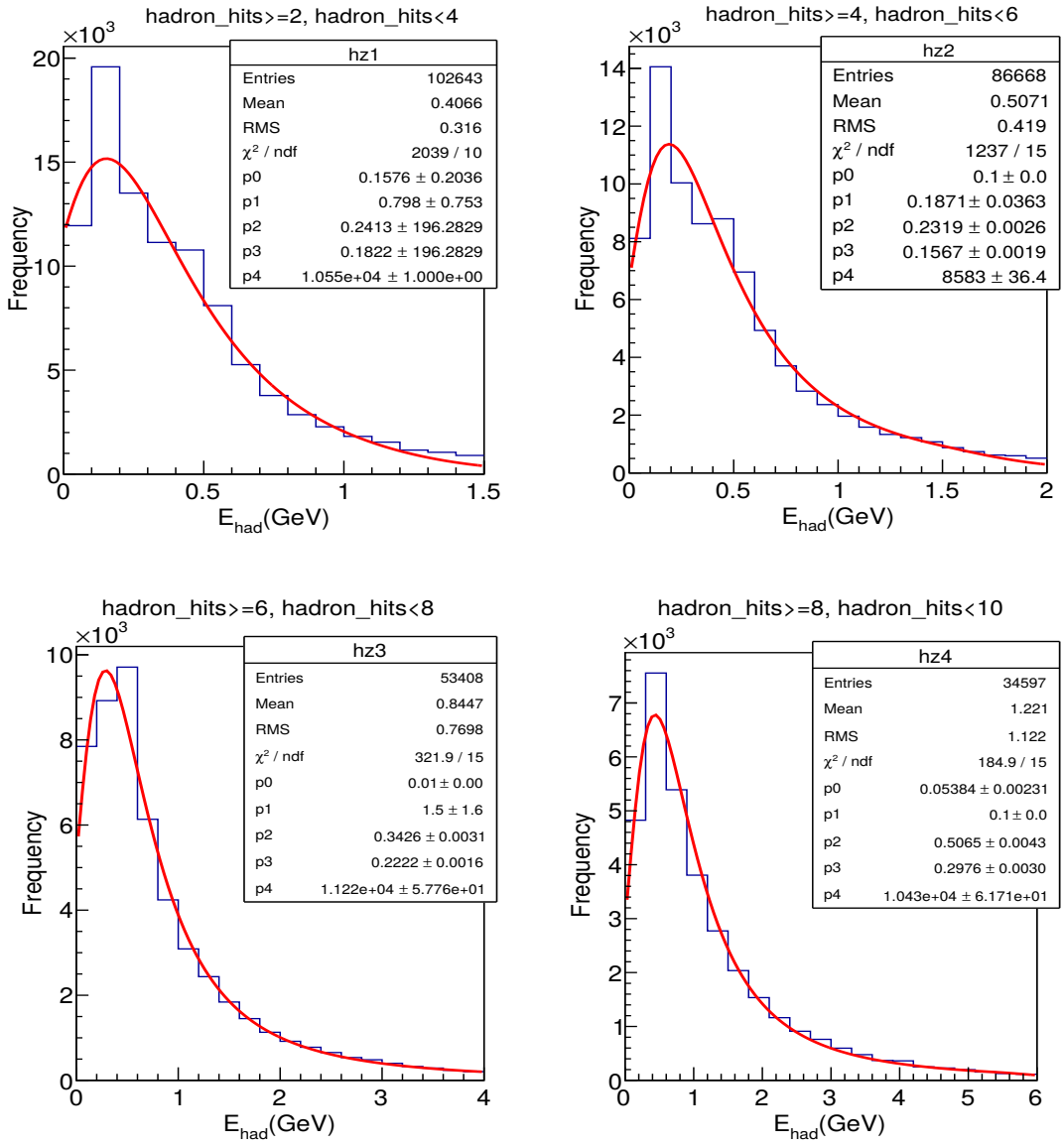

FIGURE 7.7: E_{had} distribution for hit ranges (2,3),(4,5),(6,7),(8,9).

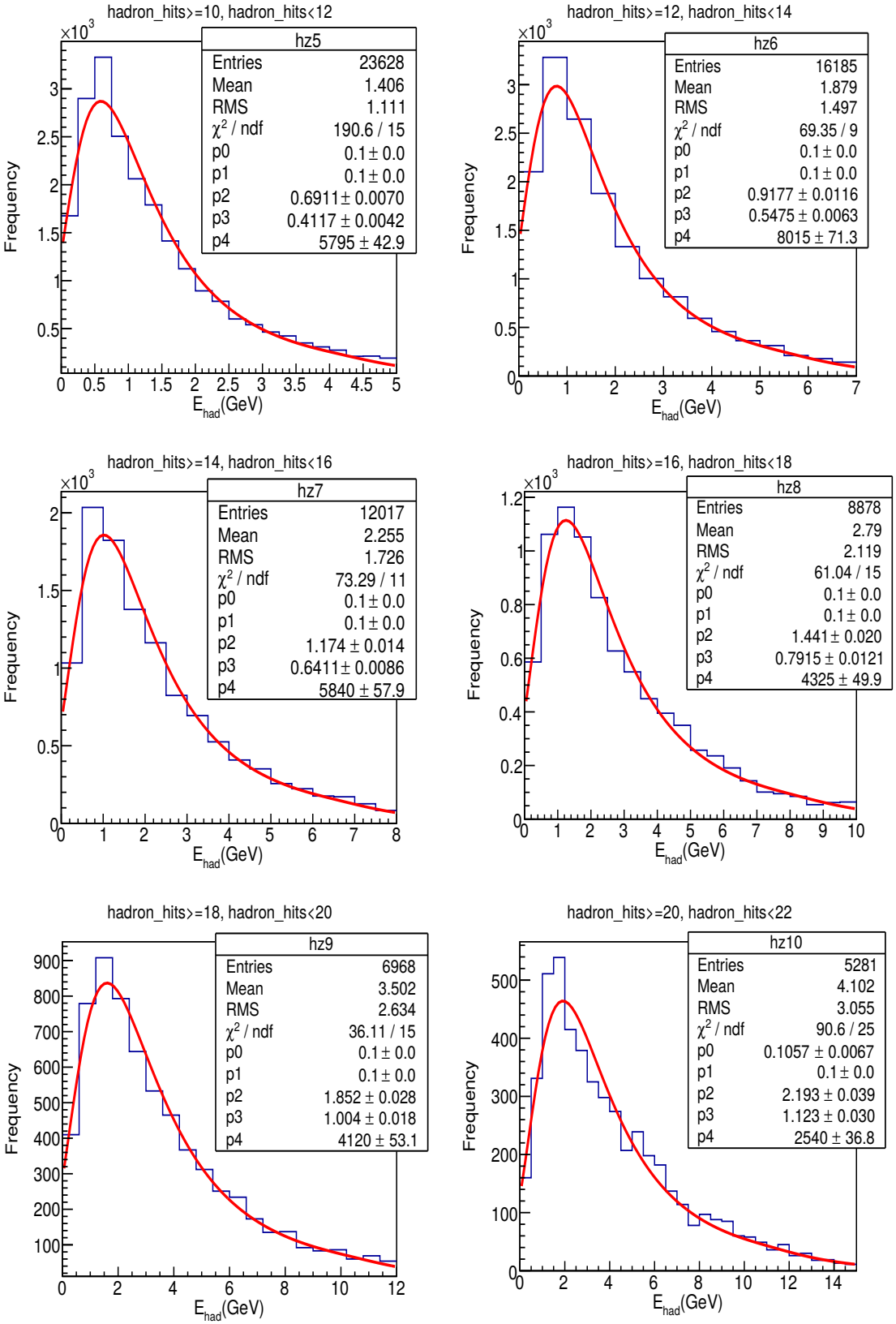

FIGURE 7.8: E_{had} distribution for hit ranges (10,11), (12,13), (14,15), (16,17), (18,19)and (20,21).

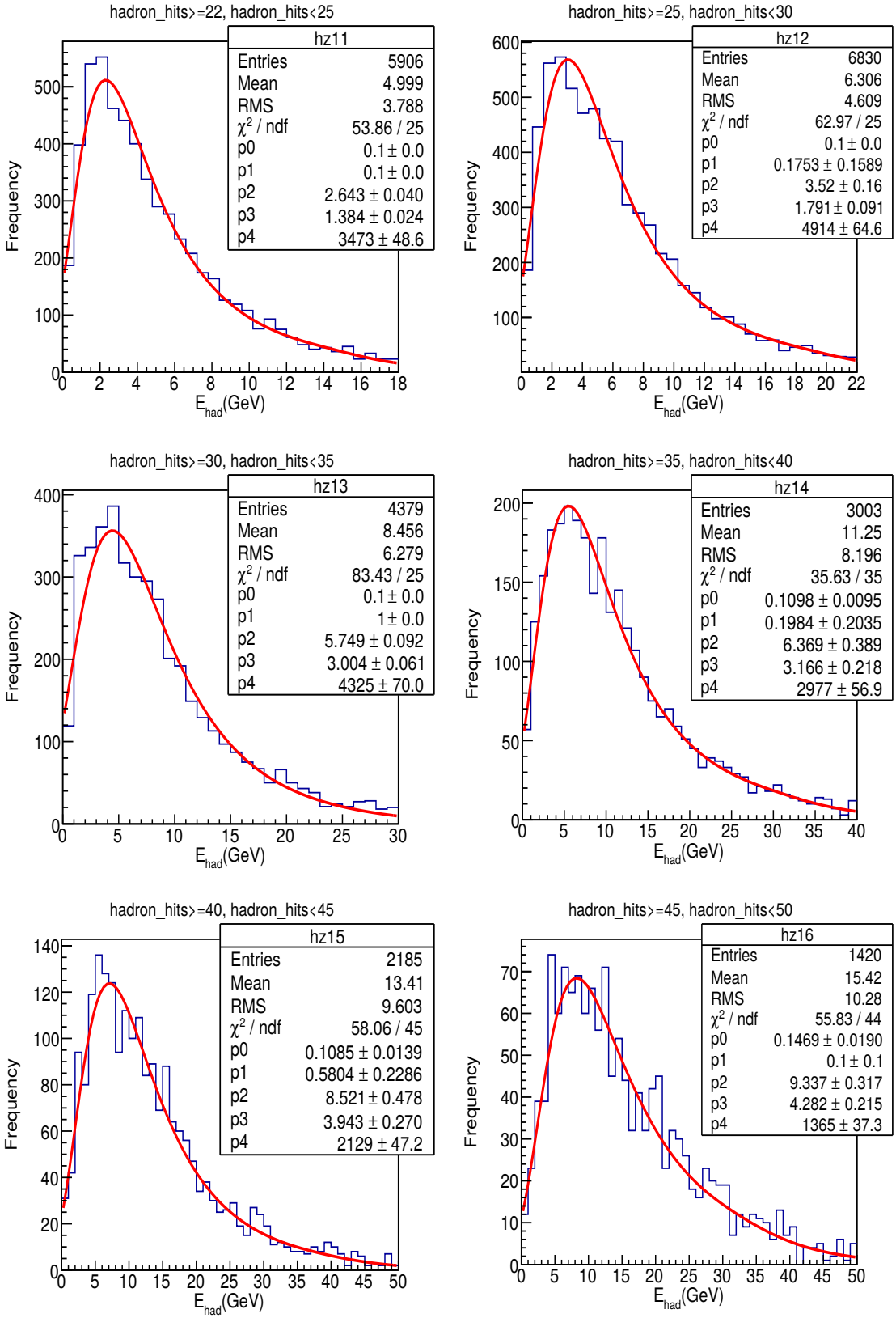

FIGURE 7.9: E_{had} distribution for hit ranges (22,24), (25,29), (30,34), (35,39), (40,44) and (45,49).

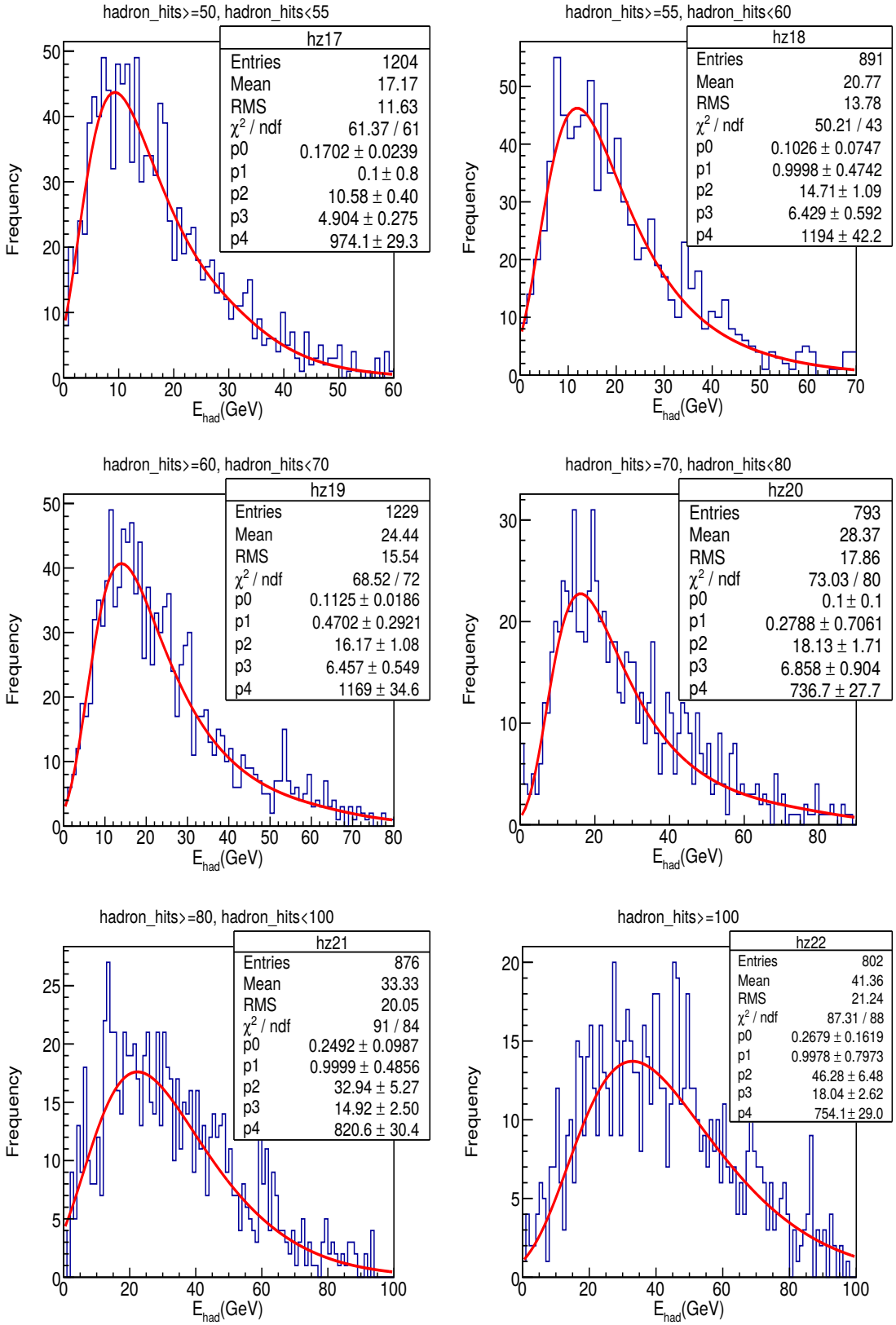

FIGURE 7.10: E_{had} distribution for hit ranges (50,54), (55,59), (60,69), (70,79), (80,99) and ($\geq$ 100).

S. No.	hadron_hits	$E_{\mathrm{had-mean}}$	σ_{Eh}
1	2-3	0.356	0.356
2	4-5	0.497	0.472
3	6-7	0.939	1.111
4	8-9	1.220	1.250
5	10-11	1.424	1.269
6	12-13	1.892	1.687
7	14-15	2.315	1.976
8	16-17	2.850	2.440
9	18-19	3.639	3.094
10	20-21	4.130	3.367
11	22-24	5.106	4.266
12	25-29	6.572	5.411
13	30-34	8.391	6.718
14	35-39	11.397	9.069
15	40-44	13.320	10.083
16	45-49	15.311	10.891
17	50-54	16.694	11.586
18	55-59	20.203	14.196
19	60-69	24.510	16.834
20	70-79	29.105	20.119
21	80-99	32.444	21.135
22	≥ 100	44.4066	24.679

TABLE 7.3: The ranges of hadron hits and the corresponding fit values of Vavilov distributions.

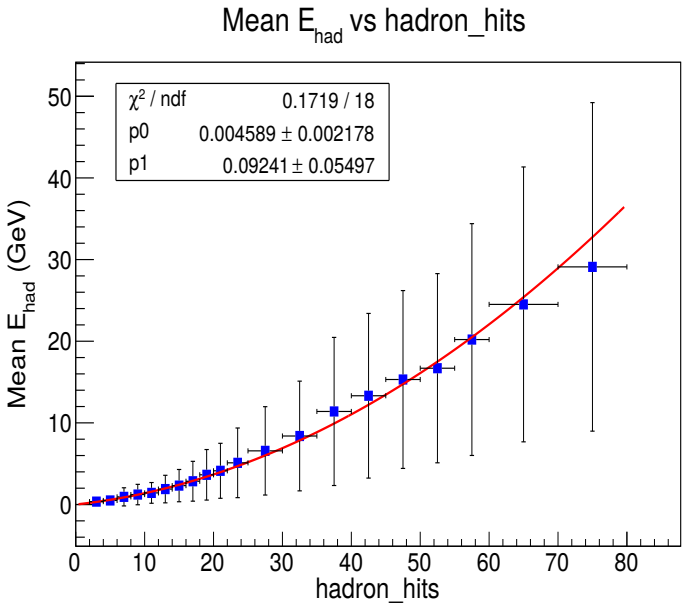

FIGURE 7.11: $E_{\mathrm{had-mean}}$ vs hadron _hits

The values of $E_{\mathrm{had-mean}}$ and σ_{Eh} are calculated for each distribution from the corresponding Vailov fit parameters P_i, using equations similar to those

in eq. (7.1). We plotted hadron hits versus $E_{\text{had}-\text{mean}}$ in figure 7.11. Here again, the error bars in the x direction span the bin size in the number of hits and the error bars in the y direction extend $\pm\sigma_{Eh}$ from $E_{\text{had}-\text{mean}}$. When the data in figure 7.11 was fitted with a linear function, the estimate of hadron energy was too low for hadron hits > 40. Therefore we did a fit with a quadratic function and obtained

$$E_{\text{had}-\text{mean}} \simeq 0.09x + 0.005x^2, \tag{7.4}$$

where x represents the number of hadron hits. We also plotted σ^2_{Eh} versus $E_{\text{had}-\text{mean}}$ in figure 7.12. This energy resolution is parametrized as $\sigma(E)/E = \sqrt{a^2/E + b^2}$ [6]. A fit to the plot gives the values

$$\left(\frac{\sigma_{\text{Eh}}}{E_{\text{had}-\text{mean}}}\right) = \sqrt{\frac{2.1 \pm 0.4}{E_{\text{had}-\text{mean}}} + 0.38 \pm 0.03}, \tag{7.5}$$

leading to $a = 1.45 \pm 0.14$ and $b = 0.62 \pm 0.02$.

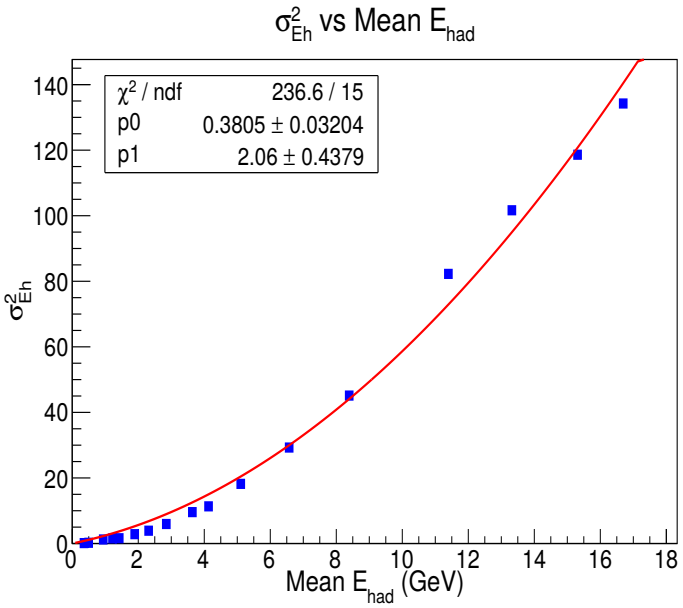

FIGURE 7.12: σ^2_{Eh} vs $E_{\text{had}-\text{mean}}$

In a previous work, the authors of ref.[9] also have used the hadron hit information from the Geant4 simulation of NUANCE generated atmospheric neutrino events. There are a number of differences in the procedure they

used and in the procedure used in this work.

- Their data set consists of 1000 years of atmospheric neutrino events, whereas our set consists of 100 years of data.
- They obtained hadron hit bank information by doing the Geant4 simulation of an event with the muon turned off at the input level. In our case, we did the full Geant4 simulation of all the charged particles in the event and subtracted the hits which went into the track reconstrcution. This is the procedure which will be utilized in the case of actual data.
- The avalanche produced in an RPC by one charged particle can, quite often, produce hits in two adjacent strips. Thus, the number of hadron hits in an RPC is likely to be larger than the number of charged particles passing through it. This feature is built into Geant4 through the option *multiplicity*. The authors of ref.[9] kept this option *off* and hence obtained a smaller number of hits for a given hadron energy. In our case, we kept the multiplicity option *on* and obtained about 30 to 40% larger numbner of hits for the same hadron energy. This is a more realistic simulation of the detector.

Because of points 2 and 3, the procedure we used is modelled more closely to what happens in the detector.

Chapter 8

Tension between the data of long baseline neutrino experiments

8.1 Long baseline neutrino experiments

Super-Kamiokande experiment showed that atmospheric muon neutrinos undergo oscillations into tau neutrinos with a large mixing angle but the probability of oscillation of the atmospheric electron neutrinos is quite small. A fit of the muon neutrino data to the muon neutrino survival probability expression

$$P_{\mu\mu} = 1 - \sin^2 2\theta_{23} \sin^2 \left(1.27 \frac{\Delta m^2_{32} L}{E} \right), \tag{8.1}$$

gives Δm^2_{32} in the range $(2-5) \times 10^{-3}$ eV^2 and $sin^2 2\theta_{23}$ in the range $(0.95-1)$. In the above equation L is neutrino's path length and E is it's energy. Later, a number of accelerator neutrino experiments were constructed to measure the above oscillation parameters more accurately and also to search for CP violation in neutrino oscillations. In all these experiments, a beam of $\nu_\mu / \bar{\nu}_\mu$, produced at an accelerator complex, is directed to a detector which is located at a distance of a few hundred kilometers. The energy of the beam is chosen so that $\Delta m^2_{32} L/E \sim 1$. The signal for oscillations is most prominent for this choice. The data from MINOS experiment, the first such experiment, led to the measurements [156]

$$|\Delta m^2_{32}| = (2.74 \pm 0.44) \times 10^{-3} \text{ eV}^2 \text{ and } \sin^2(2\theta_{23}) > 0.87. \tag{8.2}$$

MINOS experiment also observed electron neutrino appearance events due to $\nu_\mu \rightarrow \nu_e$ oscillations [157]. However, the background for this signal was too large to make any other measurement possible.

The next generation accelerator experiments were designed to optimize the observation of ν_e appearance signal. The detectors were placed at a location which is slightly off the beam axis. This gave rise to a neutrino beam spectrum which is sharply peaked at the design energy. The detectors were also designed to fully reconstruct the neutrino energy. This enables them to supress the background events due to beam ν_e (whose energy is higher than that of the signal events) and the background events due to NC π^0 events (whose energy is lower than that of the signal events). Two such experiments are currently taking data. The first is T2K experiment in Japan and the other is NOνA experiment in the US.

8.1.1 T2K

T2K is a long baseline neutrino oscillation experiment with the ν_μ beam from the J-PARC accelerator in Tokai to the Super-Kamiokande detector 295 km away. The accelerator is oriented in such a way that the detector is at 2.5° off-axis location. Super-Kamiokande is a 22.5 kton fiducial mass water Cerenkov detector, capable of good discrimination between electron and muon neutrino interaction [10]. The neutrino flux peaks sharply at 0.7 GeV which is also the energy of the first oscillation maximum. T2K experiment started taking data in 2009 and ran in neutrino mode with 14.7×10^{20} protons on target (POT) and 7.6×10^{20} POT in anti-neutrino mode [11, 12].

8.1.2 NOνA

NOνA [13] is an another long baseline neutrino oscillation experiment capable of measuring the survival probability $P_{\mu\mu}$ and the oscillation probability $P_{\mu e}$. The NuMI beam at Fermilab, with the power of 700 kW which corresponds to 6×10^{20} protons on target (POT) per year, produced the neutrinos. The far detector consists of 14 kton of totally active scintillator material and

is situated at 810 km away at a 0.8° off-axis location. Due to the off-axis location, the flux peaks sharply at 2 GeV, which is close to the the energy of maximum oscillation of 1.4 GeV. It started taking data in 2014 and ran in neutrino (anti-neutrino) modes with 8.85×10^{20} (12.33×10^{20}) POT.

8.2 Degeneracies in $P(\nu_\mu \to \nu_e)$

The $\nu_\mu \to \nu_e$ appearance signal events in T2K and NOνA are sensitive to the various neutrino oscillation paramenters appearing in the oscillation probability $P_{\mu e}$. For three flavour oscillations, including matter effects, this probability is given by

$$\begin{aligned} P_{\mu e} &= \sin^2 2\theta_{13} \sin^2 \theta_{23} \frac{\sin^2 \hat{\Delta}(1-\hat{A})}{(1-\hat{A})^2} \\ &+ \alpha \cos\theta_{13} \sin 2\theta_{12} \sin 2\theta_{13} \sin 2\theta_{23} \cos(\hat{\Delta} + \delta_{CP}) \frac{sin\hat{\Delta}\hat{A}}{\hat{A}} \frac{\sin\hat{\Delta}(1-\hat{A})}{1-\hat{A}}, \end{aligned} \tag{8.3}$$

where $\hat{\Delta} = 1.27\Delta m^2_{31} L/E$, $\hat{A} = A/\Delta m^2_{31}$ and $\alpha = \Delta m^2_{21}/\Delta m^2_{31}$. The Wolfenstein matter term A is

$$A(eV^2) = 0.76 \times 10^{-4} \rho(gm/cc) E(GeV), \tag{8.4}$$

where E is the energy of the neutrino and ρ is the density of the matter. For anti-neutrinos, $P_{\mu e} = P_{\bar{\mu}\bar{e}}$ is given by a similar expression with $\delta_{CP} \to -\delta_{CP}$ and $A \to -A$. Since $\alpha \approx 0.03$, the term proportional to α^2 in $P_{\mu e}$ is neglected. This expression depends on all the neutrino oscillation parameters. Among them the mass squared difference Δm^2_{21} and the mixing angles θ_{12} and θ_{13} are measured with great accuracy. The magnitude of Δm^2_{32} is measured accurately but its sign is as yet unknown. The case of positive Δm^2_{32} is called normal hierarchy (NH because $m_3 > m_2 > m_1$) and the case of negative

Δm^2_{32} is called inverted hierarchy (IH because $m_2 > m_1 > m_3$). The probabilities $P_{\mu e}$ and $P_{\bar{\mu}\bar{e}}$ are sensitive to hierarchy because of the quadratic and linear powers of $\sin[(1-\hat{A})\hat{\Delta}]/(1-\hat{A})$ in the first and second terms of equation 8.3 respectively. In the case of mixing angle θ_{23}, the value of $sin^2 2\theta_{23}$ is measured to great accuracy. However, the value of $\sin^2\theta_{23}$, derived from this measurement has a large range of $(0.35 - 0.65)$. The case of $\sin^2\theta_{23} > 0.5$ is called higher octant (HO) and that of $\sin^2\theta_{23} < 0.5$ is called lower octant (LO). Before the advent of T2K and NOvA, the value of the CP violating phase $\delta_{\rm CP}$ is completely unknown.

From equation 8.3, we note that $P_{\mu e}$ depends on all the three unknowns mentioned above. That is, on (a) hierarchy (b) octant and (c) $\delta_{\rm CP}$. Therefore, a single measurement of $P_{\mu e}$ can yield multiple, degenerate solutions. To unravel the value of each of the unknowns, we should study the change in $P_{\mu e}$ and in $P_{\bar{\mu}\bar{e}}$ by each of these unknowns. To facilitate this study, we define the following reference set of values for each of the unknown parameters.

- vacuum oscillations (no matter term, $A = 0$).
- maximal value of θ_{23} ($sin^2\theta_{23} = 0.5$)
- no CP violation ($\delta_{\rm CP} = 0$).

We first consider the changes in $P_{\mu e}$ and $P_{\bar{\mu}\bar{e}}$, relative to the reference point, due to a change in one of the above unknowns.

- For NH, $P_{\mu e}$ increases and $P_{\bar{\mu}\bar{e}}$ decreases. The effect is opposite for IH.
- For HO, both $P_{\mu e}$ and $P_{\bar{\mu}\bar{e}}$ increases. They both decrease for LO.
- For $\delta_{\rm CP}$ in the lower half plane (LHP, $-180^\circ < \delta_{\rm CP} < 0$) $P_{\mu e}$ increases and $P_{\bar{\mu}\bar{e}}$ decreases. The effect is opposite for $\delta_{\rm CP}$ in the upper half plane (UHP, $0 < \delta_{\rm CP} < 180^\circ$).

When we consider changes induced by two or three unknowns, it is possible that the change induced by one is cancelled by the change induced by the others. Degenerate solutions occur in such cases. Measurement of both

$P_{\mu e}$ and $P_{\bar{\mu}\bar{e}}$ is helpful in distinguishing between these degenerate solutions. These degeneracies are discussed in detail in reference [158]

The energy of T2K beam at peak flux is quite small ($\sim$ 0.7 GeV). Hence, the matter term for this experiment leads to only a small change in $P_{\mu e}$ and $P_{\bar{\mu}\bar{e}}$ (less than 10 %). The energy of NOνA beam is nearly three times larger with corresponsdingly larger matter term. Such a term induces a change of about 25% in $P_{\mu e}$ and $P_{\bar{\mu}\bar{e}}$. The maximum change induced due to the non-maximal value of θ_{23} is about 20% for both experiments. The change induced by considering maximal CP violation ($\delta_{\rm CP} = \pm 90^\circ$) is in the range $(20-25)\%$ for both experiments. Note that, all three changes are of comparable magnitude for NOνA whereas the change induced by hierarchy in T2K is much smaller than the maximal changes induced by the other two unkownns.

8.3 Tensions in the data of T2K and NOνA

Each of the two experiments, T2K and NOνA, have taken data in both neutrino and anti-neutrino beam modes. In each case, they have measured muon neutrino disappearance and electron neutrino appearance. The measured values of $|\Delta m^2_{32}|$ from these measurements are consistent with one another and with previous measurements. Regarding the measurement of the unknowns, different pieces of data seem to point in different direction. Here, we summarize the results of each piece of data.

- T2K ν_μ disappearance: This data indicates maximal disappearance and hence prefers $\sin^2 2\theta_{23}$ very close to one. It strongly disfavors non-maximal value.

- T2K $\bar{\nu}_\mu$ disappearance: This data also prefers maximal $\sin^2 2\theta_{23}$, though its statistical weight is less than the ν_μ disappearance data.

- T2K ν_e appearance: T2K observes 89 ν_e appearance events whereas 60 events are expected for the reference point. Such a large increase requires the hierarchy to be NH, the octant to be HO and the $\delta_{\rm CP} \approx -90^\circ$.

- T2K $\bar{\nu}_e$ appearance: T2K experiment has observed only seven $\bar{\nu}_e$ appearance events against an expectation of nine events for reference point. This data is not statistically significant.

- NOνA ν_μ disappearance: This data is consistent with $\sin^2 2\theta_{23}$ close to maximal value.

- NOνA $\bar{\nu}_\mu$ disappearance: This data, on the other hand, requires a non-maximal value of $sin^2 2\theta_{23}$.

- NOνA ν_e appearance: NOνA observes 58 ν_e appearnce events compared to 39 events expected for the reference point. This excess is similar to the excess seen by T2K.

- NOνA $\bar{\nu}_e$ appearance: NOνA is the first experiment to establish $\bar{\nu}_e$ appearance signal. They observe a modest excess in this channel also (27 versus 28 for the reference point).

We observe the following tensions among the above data.

- The ν_μ disappearance data of NOνA is consistent with the maximal value of $\sin^2 2\theta_{23} = 1$ whereas the $\bar{\nu}_\mu$ disappearance data requires a non-maximal value.

- The ν_e appearance data of T2K pulls θ_{23} to higher octant whereas the ν_μ disappearance data constrains it to be very close to 45°.

- NOνA observes a reasonably large excess in ν_e and a modest excess in $\bar{\nu}_e$ appearance data whereas T2K observes a very large excess of ν_e appearace events and a suppression (not statistically significant) of $\bar{\nu}_e$ appearance. Thus there is a tension between the appearance data of T2K and NOνA, speacially in $\bar{\nu}_e$ appearance.

In the NOνA experiment, the magnitude of the change in $P_{\mu e}$, due to a change in any one unkown, is the same. A reasonably large excess in ν_e appearance is possible if the changes induced by two unkowns are positive and no change induced by the third unknown. Since matter effects definitely

cause a change, the reasonably large increase points to the hierarchy being NH and one of the two following options:(a) $\sin^2\theta_{23}$ in HO and $\delta_{cp} \approx 0$ or (b)$\sin^2\theta_{23} = 0.5$ and $\delta_{cp} \approx -90^\circ$. Only for the first option, is it possible for the anti-neutrino appearance events to match the expectation for the reference point. If option (b) were true, the $\bar{\nu}_e$ appearance events would have been much less than the expectation for the reference point because both NH and $\delta_{cp} \approx -90^\circ$ suppress these events. For T2K data, the best-fit solution for the unknowns is: hierarchy NH, $\sin^2\theta_{23} = 0.53$ and $\delta_{\rm CP} = -107^\circ$. The best-fit solution of NOνA data is: hierarchy NH, $\sin^2\theta_{23} = 0.56$ and $\delta_{\rm CP} = 0^\circ$. T2K data rules out NO$\nu$A best-fit point at 2σ. whereas NOνA data rules out T2K best-fit point at 1σ.

Both the experiments also did a fit assuming the hierarchy to be IH. For this case, the best-fit solution for T2K is $\sin^2\theta_{23} = 0.53$ and $\delta_{\rm CP} = -82^\circ$. However, this solution is barely allowed at 2σ. For NOνA, the corresponding best-fit solution is $sin^2\theta_{23} = 0.56$ and $\delta_{\rm CP} = -90^\circ$, which is also allowed only at 2σ. It is interesting to note that the $\delta_{\rm CP}$ values of the IH best-fit solutions of the two experiments are reasonably close to each other whereas $\delta_{\rm CP}$ values of the actual best-fit solution are far apart.

8.4 Combined fit to T2K and NOνA data

In this section we present our results of combined fit of the disappearance and the appearance data of T2K and NOνA in both neutrino and anti-neutrino channels. The data of T2K is taken from reference [14] and that of NOνA from reference [15]. The theoretical expectations for the two experiments are calculated using the software GLoBES [16, 17]. In these calculations, The GLoBES predictions for the expected bin-wise event numbers are matched with those given by the Monte-Carlo simulations of the experiments, quoted in references [14] and [15],for the same input parameters. In calculating the theoretical expectations, the values of $\Delta m^2_{21} = 7.50 \times 10^{-5} eV^2$ and $\sin^2\theta_{12} = 0.307$ are held fixed.

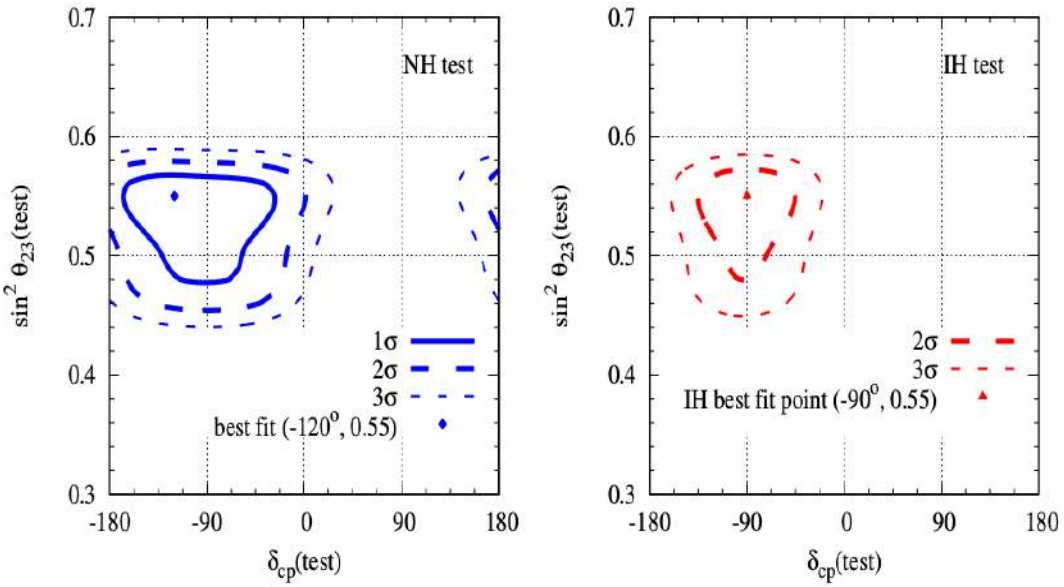

FIGURE 8.1: Expected allowed regions in $\delta_{CP} - \sin^2\theta_{23}$ plane from the current neutrino and anti-neutrino data of T2K and NOν. In the left panel, the hierarchy is assumed to be NH and in the right panel, the hierarchy is assumed to be IH. The IH best-fit point has $\Delta\chi^2 = 2.5$.

The other oscillation parameters are varied in the following ranges: $\Delta m^2_{31} = (2.494 \pm 3 \times 0.065) \times 10^{-3} eV^2, \sin^2\theta_{23} = (0.4, 0.65), \sin^2 2\theta_{13} = (0.084 \pm 3 \times 0.003)$ and $\delta_{CP} = (-180°, 180°)$. In the appearance mode, there are 24 energy bins each in neutrino and anti-neutrino channels for T2K and 6 each for NOνA. The corresponding numbers for the disappearance mode are 42 for T2K and 19 for NOνA. Thus the fit involves a total of 182 data points. In computing the χ^2 between the data and the theoretical expectation, prior is added for $\sin^2 2\theta_{13}$. The results of our fit are shown in figure 8.1. In generating these plots, we assumed a 10% overall systematic error for each channel of both experiments. The χ^2 for the best fit point is 209.7, which occurs for NH. The best-fit point in $\delta_{CP} - \sin^2\theta_{23}$ plane occurs at $(-120°, 0.55)$.

There is no allowed region in $\delta_{CP} - \sin^2\theta_{23}$ plane for IH at 1σ. There is very small allowed region at 2σ with the best-fit point occuring at $(-90°, 0.55)$ with a $\Delta\chi^2 = 2.5$. The best-fit point for IH in our fit is close to the IH best-fit points of T2K and NOνA. This is not surprising because those two points are close to each other. For IH, the whole region of δ_{CP} in upper half plane is ruled out at 3σ because it is disfavoured by both T2K and NOνA. For T2K,

the change induced by δ_{CP} in ν_e appearance events is much larger than the change induced by hiearachy. Values of δ_{CP} in upper half plane reduces these events relative to reference point. The large excess seen by T2K relative to the reference point seems to rule out most of the upper half plane of δ_{CP} for NH also, even though this region contains NOνA best-fit point. This same excess seems to place the best-fit value of δ_{CP} in the lower half plane, with actual value being determined by the relative weights of T2K and NOνA data. The best-fit value of $\sin^2\theta_{23}$ is the average of the best-fit values of T2K and NOvA. Thus it seems as if the $\nu_\mu/\bar{\nu}_\mu$ disappearance data of T2K and NOvA seems to play an equally important role in determining this quantity.

Chapter 9

Feasibility study of a PET device based on MRPCs

9.1 Introduction

The Multigap Resistive Plate Chamber (MRPC) is a modified version of RPC detector wherein the gas gap between the electrodes is further divided into multiple gaps by introducing electrically floating highly resistive plates. The MRPC was first conceptualized and developed in 1996 [159]. These detectors consist of many highly resistive plates (e.g. glass) and very thin gas gap between them. The high voltage is applied only on the outermost electrodes and the inner electrodes are all electrically floating.The signals are readout from X- and Y-planes pickup panels placed at the outside of anode and cathode electrodes. The time resolution of these detectors improves with narrower gas gap. Studies done by several groups have shown a time resolution lower than 100 ps for various MRPC configurations [160].

The working principle of an MRPC is similar to that of a single gap RPC except that the electrically floating electrodes limits the avalanche to grow beyond a certain level and provides less jitter in timing signal. Figure 9.1 illustrates an MRPC in the steady state condition. Excessive growth of the avalanche is limited by intermediate plates, and hence a higher electric field can be applied to the detector operated in the avalanche mode, compared to that of a single gap structure. This is advantageous in terms of the time resolution and rate capability of the device.

The electrically floating interior resistive plates are maintained at equal voltages due to the flow of positive ions and electrons between them. The voltage across each gap is the same and on an average each gap produces equal number of avalanches. The average net current to any of the internal plates would be zero since there is an identical flow of electrons and ions in each gas gap. The outer electrodes with graphite coat are transparent to the fast signal generated by the avalanches inside each gas gap. The avalanche in any of the gaps will induce a signal to the outermost electrodes, as the inner electrodes are transparent to the fast signals. The fast signal is produced by the flow of electrons towards the anode. The resultant signal is the summation from all the gaps which is readout from pickup panels placed at the outside of anode and cathode electrodes. MRPCs may consist of a single stack or two stacks packed together [161]. A higher operating voltage has to be applied due to larger over all gap compared to a single gap RPC. MRPCs can have potential application in Positron Emission Tomography (PET) due to their precision time measurement [162, 163, 164] and good spatial resolution [165]. Several glass MRPC detectors have been developed to find potential application in TOF detectors, medical imaging etc. Here we present the development and fabrication procedure of the optimized design, characterization and the experimental setup of TOF-PET experiment, the trigger and data acquisition system, data analysis and Geant4 simulations of efficiency.

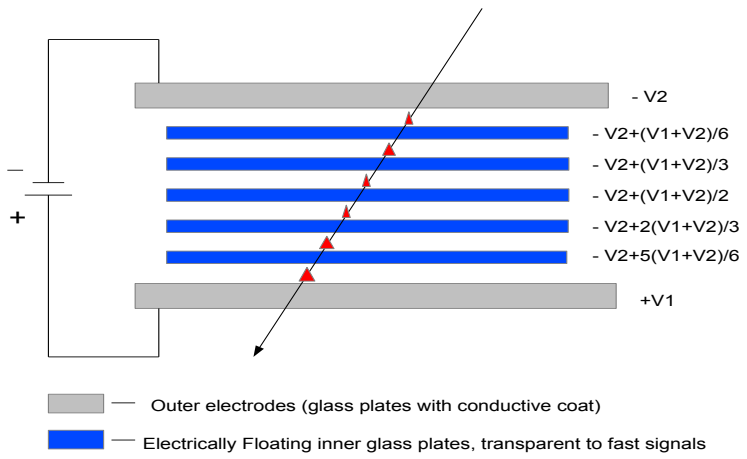

FIGURE 9.1: Potentials across the sub-gaps of an ideal MRPC detector.

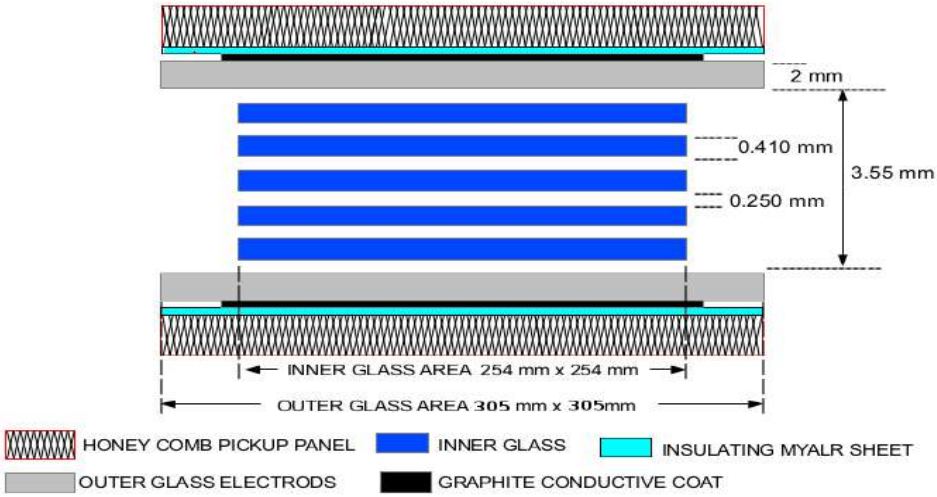

FIGURE 9.2: A schematic diagram of our detector.

9.2 Fabrication and Characterization of MRPCs

9.2.1 Fabrication

We have constructed several six-gap glass MRPCs of dimensions 305 mm $\times$ 305 mm $\times$ 7.5 mm. A schematic of the detector geometry with dimensions of various components is shown in figure 9.2. The dimensions of internal glass plates are 256 mm $\times$ 256 mm $\times$ 0.410 mm. Glass sheets of 2 mm thickness, coated with a conductive layer of graphite paint of NEROLAC brand, were used for the outer electrodes. The surface resistivity of the conductive coat was in the range of 0.5 - 1 M$\Omega/\square$. Two sided non conducting adhesive tapes were used on both sides of a mylar sheet to make small circular spacers of diameter 4 mm and thickness $\approx$ 250 μm. Twenty five spacers were used to maintain gas gaps.

Figure 9.3(a) shows placement of the spacers. There is a gap of around 2.7 cm between the edges of external and internal electrodes. The gas mixture might end up flowing through that path of thickness 3.55 mm, instead of flowing through a very narrow (0.250 mm) gas gap, which would offer much higher resistance to the gas flow. In order to ensure a proper flow of gas mixture through gap between the internal plates, we introduced blockers at

appropriate places (one each near the gas inlets and two each near the gas outlets). Figures 9.3(b) and 9.3(c) shows the design and placement of the blockers, side spacers and gas nozzles respectively. The gas mixture has been optimized to $R134a$ (91.2 %), C_4H_{10} (4.8%) and SF_6 (4%). The pickup panels consist of plastic honeycomb material laminated with copper strips of width 2.8 cm placed on both the sides of an MRPC orthogonal to each other. Figure 9.3(d) shows a fully assembled detector. Further details of our detector can be found in [18].

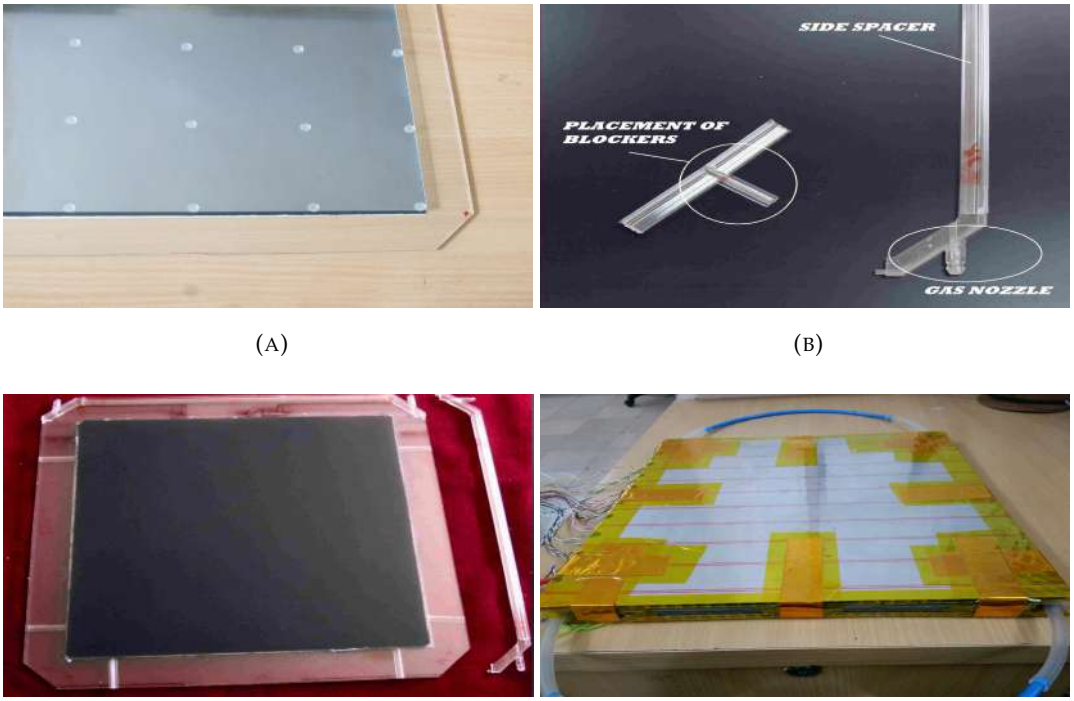

(A) (B)

(C) (D)

FIGURE 9.3: (a) Placement of spacers, (b) blockers and side spacers, (c) placement of blockers and side spacers and (d) a fully assembled MRPC with pickup panels.

9.2.2 Characterization

We have characterized the two MRPCs used in our Time of Flight experiment. A cosmic ray muon telescope was setup using three scintillator paddles of 2 cm width. The two scintillator paddles were placed above the two MRPCs under test and the third paddle was placed below the MRPCs. All the three paddles were aligned along the central strip of both MRPCs. The

effective area of the telescope was 25 cm $\times$ 2 cm. A view of the characterization setup is shown in figure 9.4(a). P1, P2 and P3 are the scintillator paddles whose coincidence is given as the trigger to the Data Acquisition System (DAQ). A schematic of the DAQ system is shown in figure 9.5. The trigger is formed by the coincidence of discriminated signals of P1, P2 and P3. The signals from MRPC1 and MRPC2 are recorded with this trigger. We need both digital as well as analog outputs from the preamplifiers for correcting time walk of Time to Digital Converter (TDC) data. Anusparsh boards [166] are used as preamplifiers to obtain time and charge information simultaneously. Anusparsh is a front end ASIC designed for the ICAL experiment. It is an 8-channel amplifier and discriminator. It also provides analog output of the amplifier stage for a selected channel. The amplifier comprises of a regulated cascode trans-impedance amplifier, followed by two stages of differential amplifier. The threshold is common to all discriminator channels. Outputs of the discriminators are Low Voltage Differential Signals (LVDS). The charge information is obtained from the analog output of the Anusparsh and used for the calibration of the TDC data. A picture of the Anusparsh boards designed and fabricated at TIFR is shown in figure 9.4(b). The analog outputs are directly fed to the ADC inputs to get the charge information. The LVDS outputs are first converted into NIM signals. These NIM signals are discrimated and fed into the TDC module to get timing information of the MRPC signals with respect to the trigger and into the scaler module to get individual noise rates and efficiencies of MRPC1 and MRPC2.

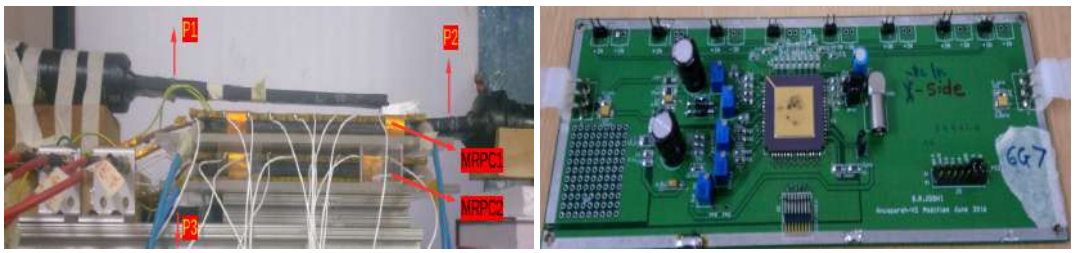

(A) (B)

FIGURE 9.4: (a) A view of the Characterization setup and (b) the Anusparsh board.

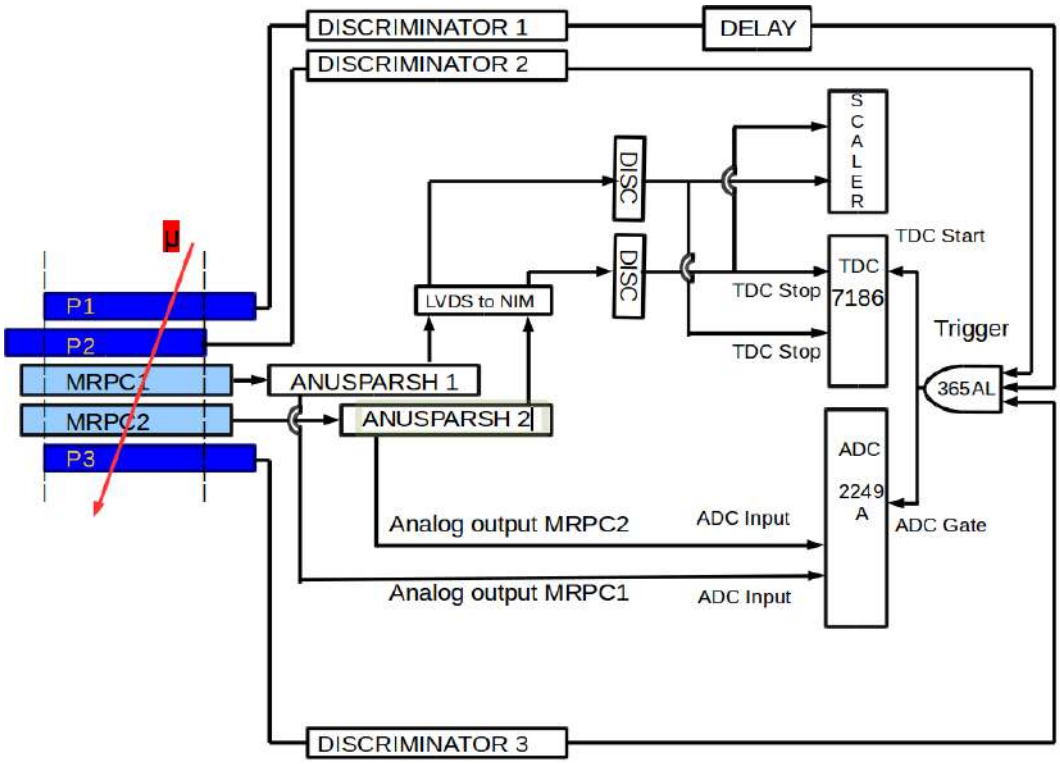

FIGURE 9.5: DAQ of the characterization setup

The noise rates verus applied high voltages, I-V charcteristics and the muon detection efficiencies versus applied high voltages of MRPC1 and MRPC2 are shown in figures 9.6(a,b and c) respectively. We also studied time resolutions of MRPC1 and MRPC2 with this characterization setup using the cosmic muons. The TDC data of individual MRPCs were corrected by using the charge information of each event obtained by Anusparsh boards. Figures 9.6(d and g) and 9.6(e and h) show the TDC counts versus QDC counts histograms and profile histogram of MRPC1 and MRPC2. The profile histograms were fitted to a function $\exp[-p_0/x + p_1] + p_2$. The TDC value of each event is then corrected by using the fit parameters p_0, p_1 and p_2 and the QDC value. The calibration is done using the following equation

$$TDC_{corrected} = TDC_{raw} - T_{calib} \tag{9.1}$$

where T_{calib} is the correction obtained using the fit parameters from the profile histogram. Figures 9.6(f) and 9.6(i) shows the corrected TDC distributions of MRPC1 and MRPC2 respectively.

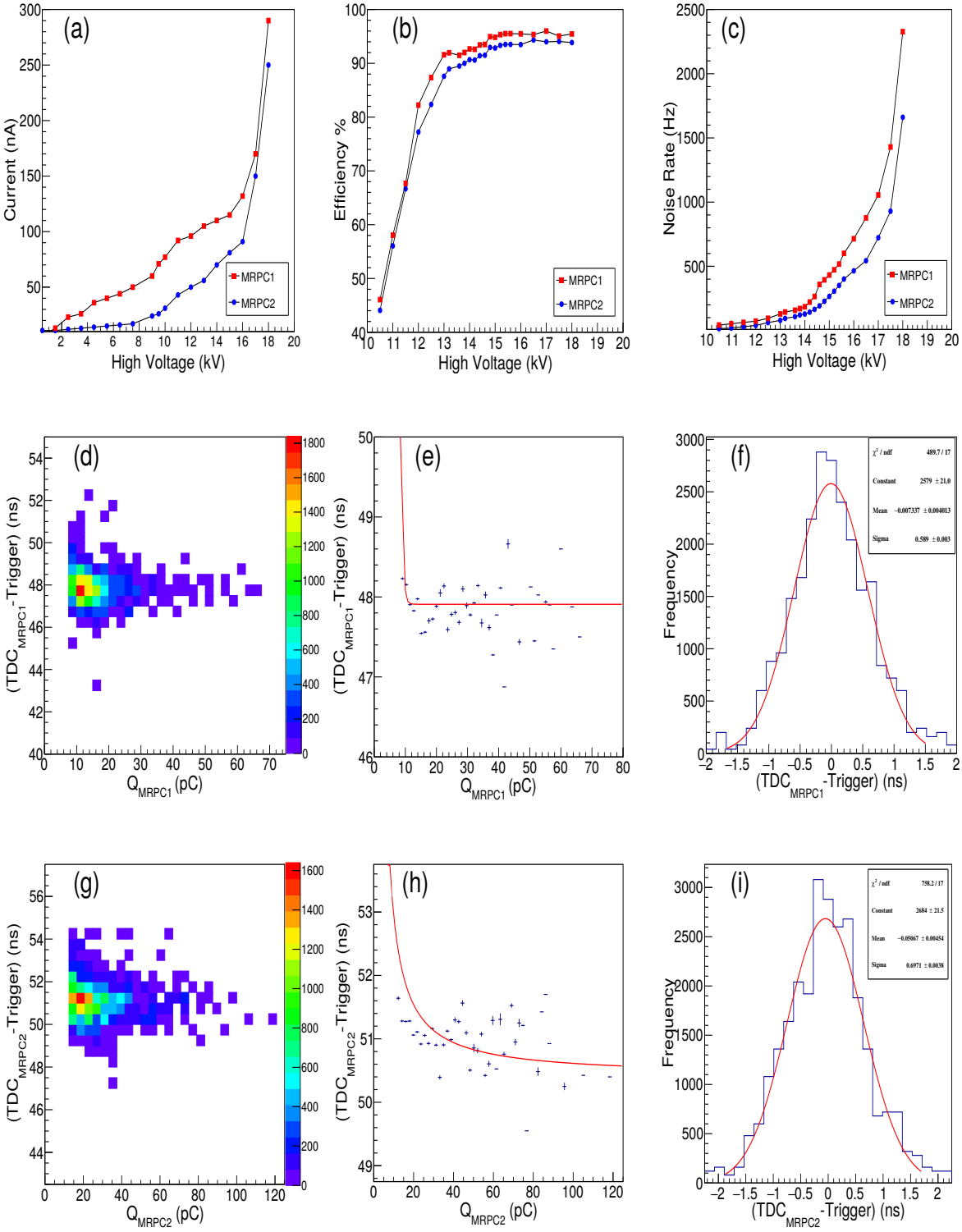

FIGURE 9.6: Characterization plots (a) Noise rates, (b) chamber current (I) vs applied high voltage (V), (c) efficiency versus applied high voltage, (d) TDC versus QDC histogram of MRPC1, (e) Profile histogram of MRPC1, (f) the time walk corrected TDC distribution of MRPC1, (g) TDC versus QDC histogram of MRPC2, (h) Profile histogram of MRPC2 and (i) the time walk corrected TDC distribution of MRPC2.

The time resolutions of MRPC1 and MRPC2 with respect to the trigger (scintillator paddles) after applying the time walk correction are $\sim$ 589 ps and $\sim$ 697 ps respectively. An electronic jitter of $\sim$ 20 ps along the TDC path of each channel was measured by feeding signals from a pocket pulser. The time difference between MRPC1 and MRPC2 (ΔT) is shown in figure 9.7. The time resolution for ΔT is $\sim$ 390 ps which includes the 20 ps electronic jitter. Different characterization values of MRPC1 and MRPC2 are listed in table 9.1.

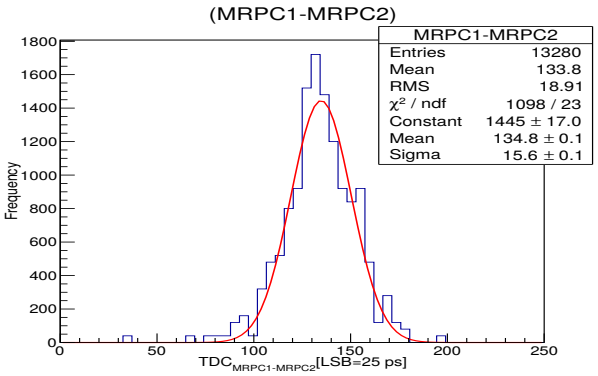

FIGURE 9.7: ΔT distribution (MRPC1 - MRPC2).

	Noise rate (Hz)	Current (nA)	Efficiency (%)	σ_T Corrected (ps)
MRPC1-Trigger	$\sim$ 2350	$\sim$ 290	$\sim$ 92	$\sim$ 589
MRPC2-Trigger	$\sim$ 1700	$\sim$ 250	$\sim$ 94	$\sim$ 697
MRPC1-MRPC2				$\sim$ 390

TABLE 9.1: Noise rates, chamber currents, efficiencies and corrected timing resolutions of MRPC1 and MRPC2 at $\sim$ 18 kV operating voltage.

9.2.3 Time resolution with signal readout from both ends of a strip

We modified the signal readout system of our detector in order to achieve a better time resolution. The pickup strips of both the top and bottom planes of each detector are placed parallel to each other. The signal is read in differential mode from both ends of strips. Only the central strips are read from both MRPC1 and MRPC2. The trigger is formed by the scintillator paddles as described in 9.2.2. The data is recorded in a 4-channel, 2.5 GHz bandwidth oscilloscope as shown in figure 9.8.

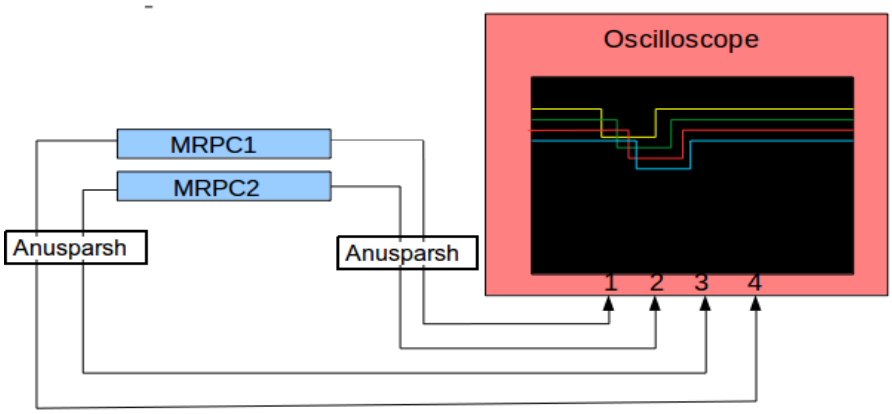

FIGURE 9.8: Setup for measurement of time resolution with readout from both ends of a pickup strip.

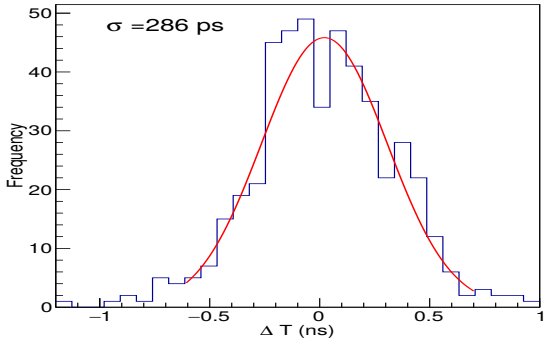

FIGURE 9.9: ΔT distribution

The timing data from left and right ends of the central strip of both MRPC1 and MRPC2 is averaged to correct for the position dependence of time [167]. The time difference between MRPC1 and MRPC2 is shown in figure 9.9. The obtained time resolution from this method is $\sim$ 286 ps.

9.3 MRPC for Positron Emission Tomography (PET)

Positron Emission Tomography (PET) is an advanced diagnostic method to monitor the effects of therapies like oncology, cardiology, neurology, psychiatry or gastrology. It is used to determine the spatial and temporal distribution of concentrations of some pharmaceutical substances in the body. The patient is administered a substance containing a radioactive isotope which emits positrons. As the rate of assimilation of these special substances depends

on the type of the tissues, regions of the diseased cells can be recognized with high accuracy [168]. The currently used detectors for PET imaging are the scintillator-based detectors, e.g., Bismuth germanate (BGO) or Lutetium orthosilicate (LSO), due to their excellent light output and very good energy resolution. But their high cost, limitations due to a short field of view and long dead time of the electronics, attempts are being made to find a better alternative. MRPCs offer a good alternative to the scintillator-based PET due to their excellent time resolution and position resolution with a comparatively lower cost of fabrication. We have mounted two MRPCs horizontally and a radioactive source (^{22}Na) is placed asymmetrically between the two detectors. ^{22}Na emits a positron which annihilates with an electron almost at rest and two gammas of 511 keV are produced with opposite momenta. These photons are detected by the two detectors in coincidence with each other. Each MRPC has eight "X" strips and eight "Y" strips of 2.8 cm width. Lines Of Response (LOR) can be obtained by joining the hit coordinates. The time of flight information gives the exact position of the source on the line of response.

9.3.1 The Experimental setup and DAQ

A pair of scintillator paddles (P3 and P4) of dimensions 44 cm $\times$ 44 cm are placed above the top MRPC and another pair of scintillator paddles (P1 and P2) are placed below the bottom MRPC such that the MRPCs are well within the area of scintillator paddles. The coincidence signal of all four scintillator paddles is used as a veto to remove the cosmic muon background. The signals from pickup strips are readout by Anusparsh ASIC described in section 2. We read only three "X" and three "Y" central strips of each MRPC to form the trigger. The LVDS output of Anusparsh is converted to NIM signal. These are discriminated and fanned out for the MLU (LeCroy 365AL Dual 4-Fold Majority Logic Unit), Scalers and the TDC (Phillips Scientific 7186 Time-to-Digital Converter). In the coincidence unit path, the "X" strips and "Y" strips are ORed separately and the ORed signals of X and Y planes are ANDed. The

resultant AND output of each MRPC are finally ANDed to form the trigger. In the TDC path, the discriminated NIM output of each strip is delayed by adding appropriate lenghts of cables such that the signal is well within the trigger window and then they are used as TDC stop. The analog outputs of Anusparsh boards are directly fed into the ADC inputs. Figure 9.10 (bottom panel) illustrate the DAQ system. We have used only the "X" plane timing data of MRPCs to calculate the time of flight in this experiment. Figure 9.10 (top panel) shows a view of the experimental setup.

9.3.2 Time of flight measurement

The "X" and "Y" coordinates of hits are recorded along with the time of arrival of the photon at the detector. We obtain lines of response by joining the hit coordinates of MRPC1 and MRPC2 only for events with single multiplicity (with one strip hit per plane per detector). The timing Information infers the exact position of the source on the line of response. The difference between timings of two opposite photons is calculated as $\Delta T = t_{MRPC1} - t_{MRPC2}$. There were offset in cable lengths and the TDC path of different channels. To avoid this, we have taken two readings for a fixed distance between the MRPCs. First, the source is kept at the bottom MRPC and we obtain $\Delta T_1 = t_{MRPC1} - t_{MRPC2}$. The same reading is repeated but with source just below the top MRPC and we calculate $\Delta T_2 = t_{MRPC1} - t_{MRPC2}$. Finally we calculate the time of flight TOF=$(|\Delta T_1 - \Delta T_2|)/2$. We took readings for the four values of separation (30 cm, 45 cm, 60 cm and 75 cm) between MRPCs. The opearting voltage of MRPCs was set at 15 kV. Our results of time of flight calculation for these distances have been summarized in table 9.2. The figures 9.11(a), 9.11(c), 9.11(e) and 9.11(g) show the ΔT_1 distributions of the central strips with source at bottom MRPC and 9.11(b), 9.11(d), 9.11(f) and 9.11(h) show the ΔT_2 distributions of the central strips with source at top MRPC. We can see from these figures that the peak corresponding to the source signal sits over a uniform random noise. The position of the peak depends on the

position of source. When the source is placed at the bottom (top) MRPC, the peak is on the left (right) side of the central value.

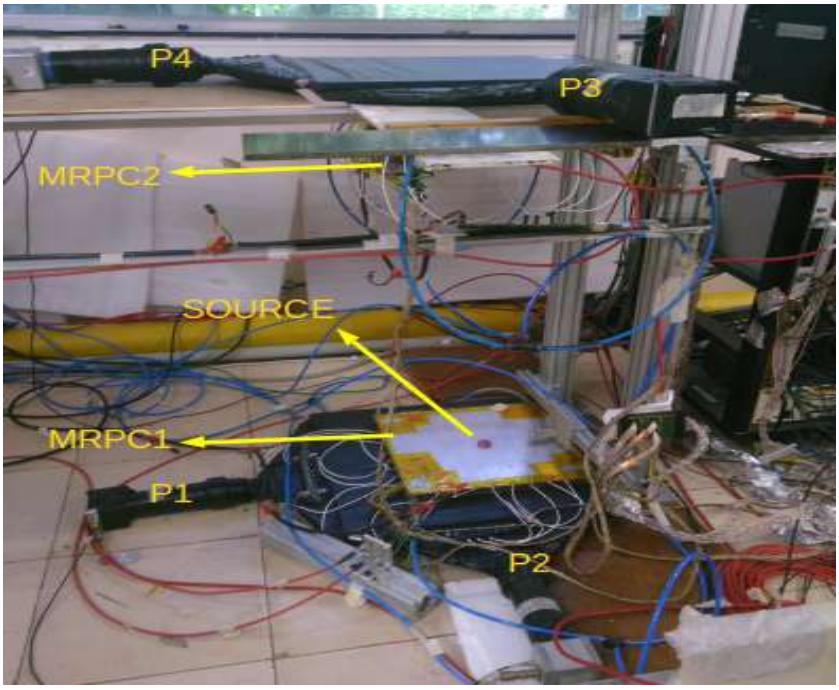

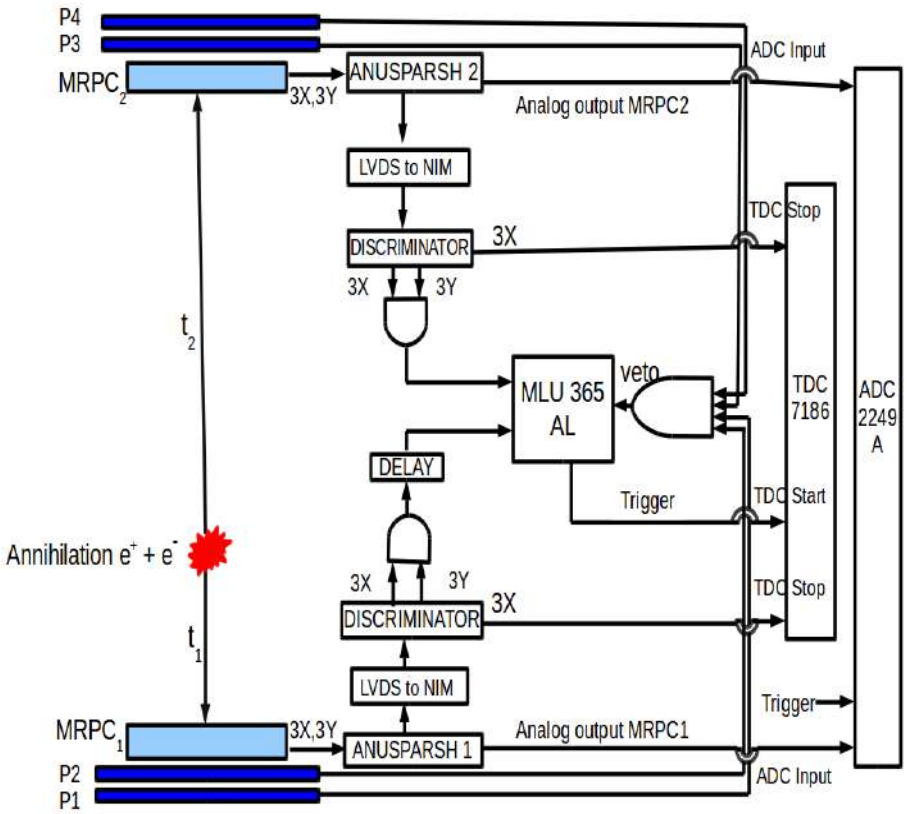

FIGURE 9.10: Top panel: A view of the setup. Bottom panel: Block diagram of the setup.

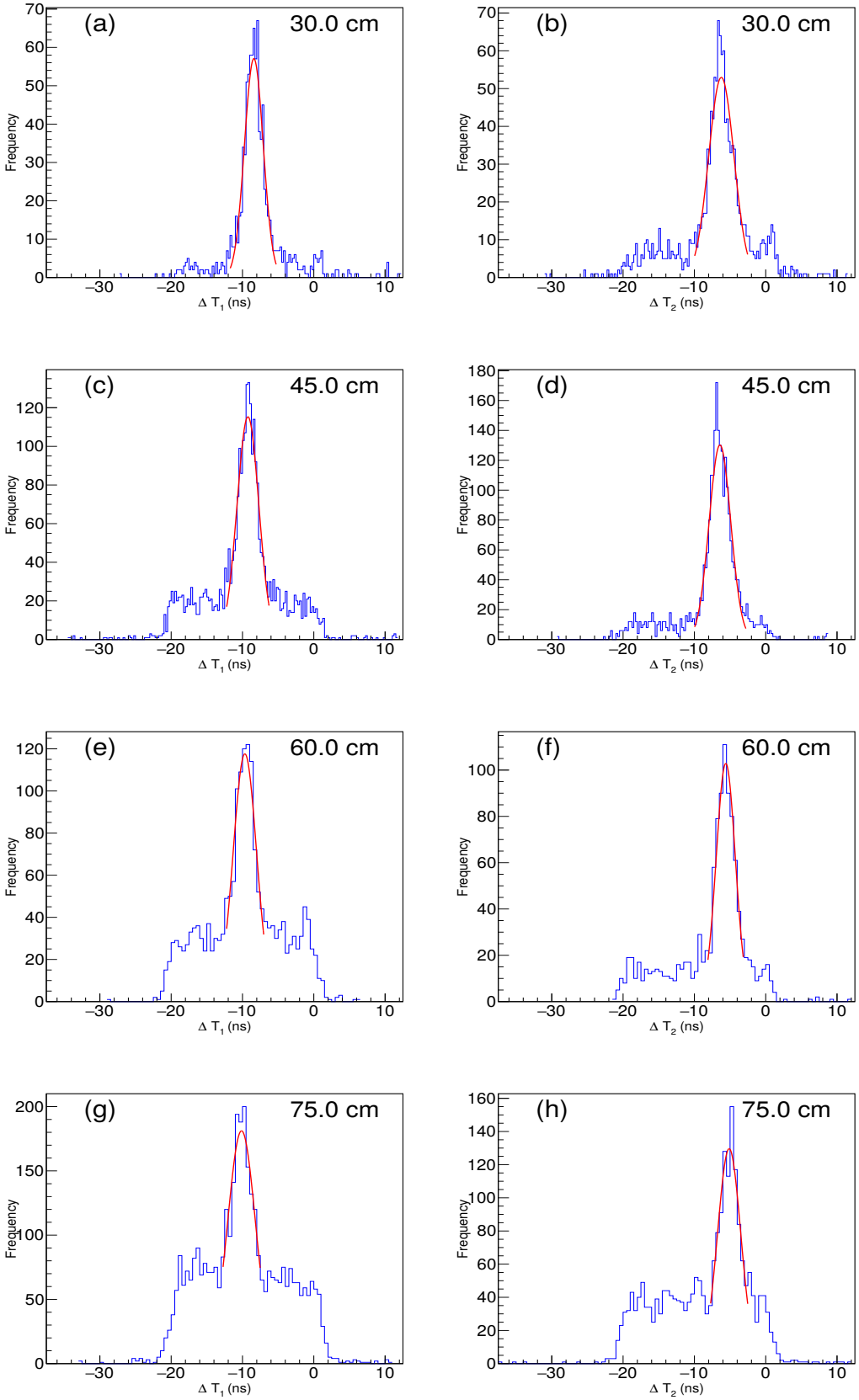

FIGURE 9.11: ΔT distributions for various distances between MRPCs.

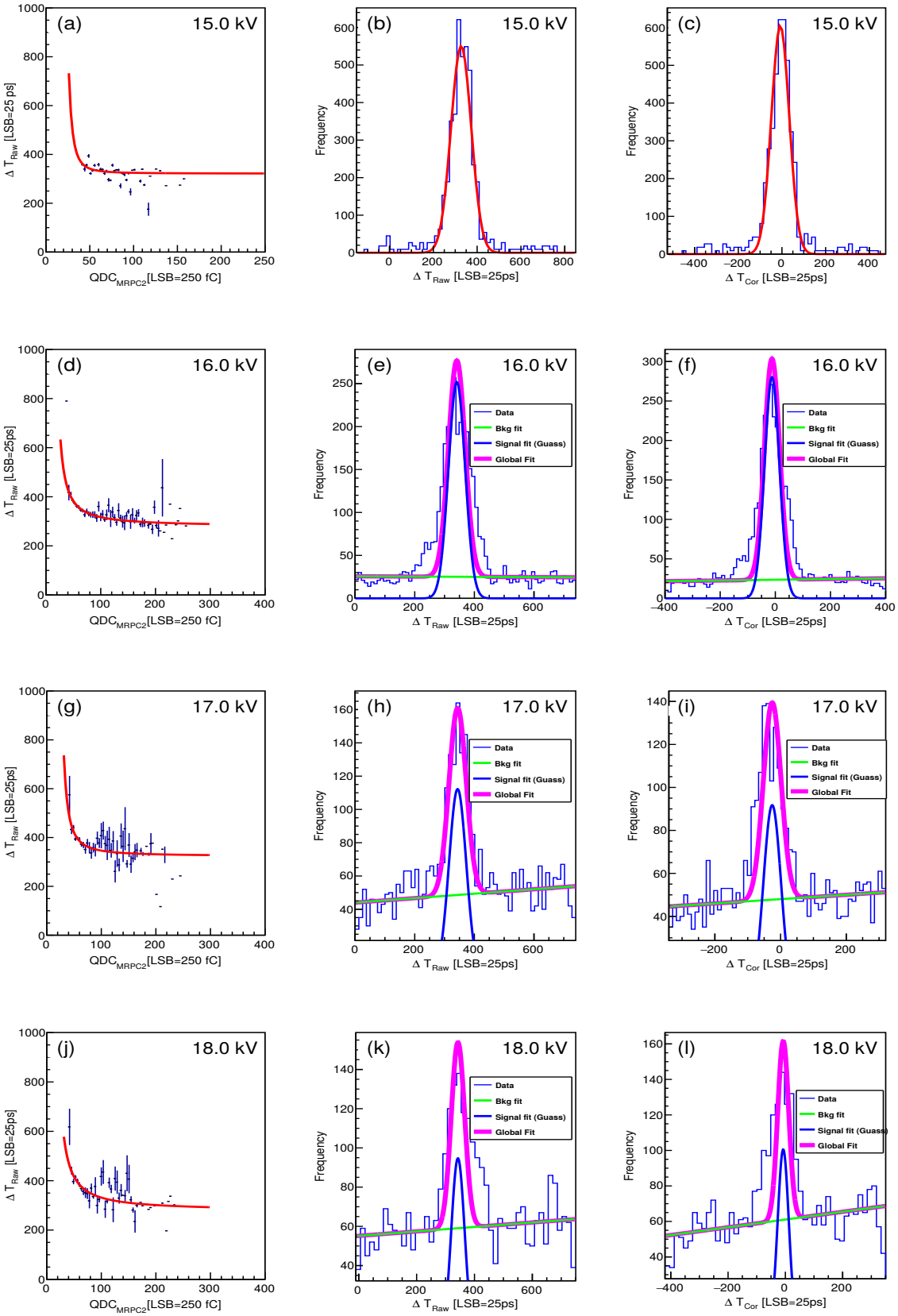

FIGURE 9.12: First column shows the ΔT versus QDC_{MRPC2} profile histograms, second column and third column show the raw ΔT distributions and corrected ΔT distributions for different operating voltages.

Distance	ΔT_1 (ns)	ΔT_2 (ns)	TOF (ns)	Exp. TOF (ns)
30 cm	-8.38 $\pm$ 0.05	-6.24 $\pm$ 0.07	1.07 $\pm$ 0.04	1.0
45 cm	-9.24 $\pm$ 0.04	-6.42 $\pm$ 0.04	1.41 $\pm$ 0.03	1.5
60 cm	-9.67 $\pm$ 0.07	-5.60 $\pm$ 0.06	2.03 $\pm$ 0.05	2.0
75 cm	-10.13 $\pm$ 0.07	-5.13 $\pm$ 0.07	2.50 $\pm$ 0.05	2.5

TABLE 9.2: Measurement of the time of flight (TOF) for various distances between MRPCs

9.3.3 Time resolution for 511 keV gammas

The time resolution is the crucial parameter for a TOF-PET device. The Anusparsh boards were used to get both the digital as well as analog information of each event. The analog information is required to apply time walk correction to the TDC data. Data was taken for four values of operating high voltage 15kV, 16 kV, 17 kV and 18 kV with source placed at the bottom MRPC. The separation between the two MRPCs was kept fixed at $\sim$ 30 cm. Figures 9.12 show the results for the data taken at these four high voltages. The first column shows the profile histograms of ΔT_{Raw} versus QDC_{MRPC2}. These profile histograms are fitted to a function $\exp[-p_0/x + p_1] + p_2$. The TDC value of each event is then corrected by using the fit parameters p_0, p_1 and p_2 and the QDC value. The calibration is done using the equation 9.1. The second column shows the raw ΔT distributions. The third column shows the corrected ΔT distributions. The plots in second and third columns are fitted with a combination of a gaussian and a first order polynomial function. The gaussian peak corresponds to the source signal and the linear function fits the unifrom random noise. The time resolution values are listed in table 9.3.

H.V.	σ_T (ps) (Raw)	σ_T (ps) (Corrected)
15 kV	1157.25 $\pm$ 15.00	1022.00 $\pm$ 14.25
16 kV	757.50 $\pm$ 8.50	679.25 $\pm$ 9.00
17 kV	722.75 $\pm$ 5.00	674.50 $\pm$ 7.75
18 kV	583.75 $\pm$ 7.50	480.75 $\pm$ 5.00

TABLE 9.3: Time resolution at different high voltages

9.4 Geant4 simulation of Efficiency for 511 keV gammas

MRPCs are gas filled detectors and have excellent effeciency for minimum ionising particles (muons). Efficiency study of our detector for cosmic muons can be found in [18]. MRPCs have very low efficiency for gammas. Since our experiment involves 511 keV gammas produced by ^{22}Na source, we did a Geant4 simulation study to estimate the efficiency of our detector for 511 keV gammas. The MRPC was simulated according to the design details described in section 9.2. Gammas of energy 511 keV generated by Geant4 monte carlo were showered within a solid angle which covered the entire active detector area. 50,000 photons were used to generate a set of data. Ten such data samples were created and the efficiency was calculted for each data set and then their mean and standard deviation was calulated. We repeated this exercise by varying the number of gas gaps from 1 to 30. Figure 9.13(a) shows the plot of effeciency versus the number of gaps in the MRPC. The data points are the mean values of efficiency and the errors are given by $\sigma/\sqrt{(\mathrm{N}-1)}$ (where "σ" is the standard deviation and "N" is the number data samples). As it can be seen that the efficiency is very low for 511 keV gammas. Our detector has six gaps which corresponds to an efficiency of $\sim$ 1%. Efficency increases with the increase in the number of gaps.

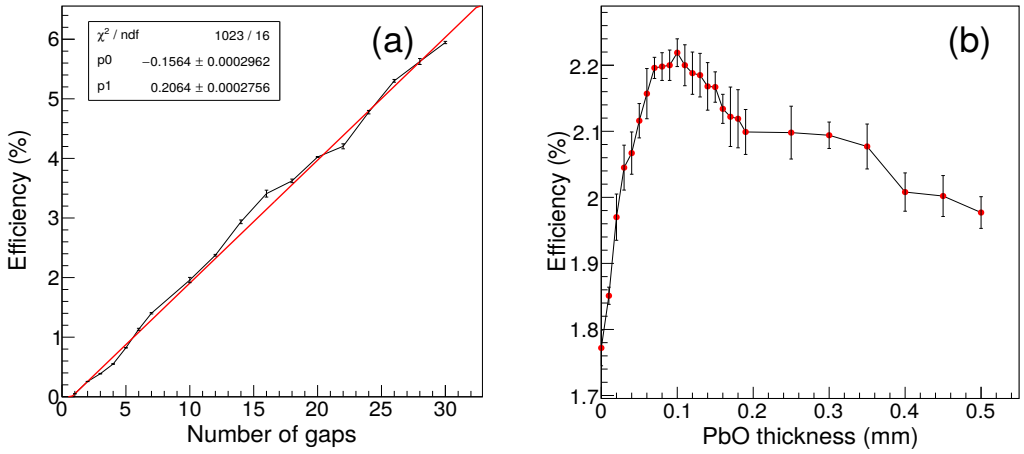

FIGURE 9.13: (a) Efficiency vs number of gaps and (b) efficiency vs thickness of the PbO coat.

The efficiency can be improved if a high "Z" material is used as a converter, which converts gammas into electrons through photoelectric effect or compton scattering. We did a simulation study to estimate the improvement in efficiency by using PbO as a converter material. A PbO coat was applied on the inner side of an outside electrode. The thickness of the coat was varied from 0.00 mm to 0.50 mm. Ten data sets were obtained for each thickness by shooting 50,000 photons on the coated electrode side of the MRPC. Efficiency was obtained in similar way as obtained above. Figure 9.13(b) shows the efficiency versus PbO coat thickness plot. The data points are the mean values obtained from the ten data sets and the errors are given by $\sigma/\sqrt{(\mathrm{N}-1)}$. We see an improvement in effeciency near 0.1 mm thickness of the coat. The number of gaps (6 gaps) was kept fixed for this study.

9.5 Conclusion

We measured Time Of Flight (TOF) of 511 keV gammas produced by (^{22}Na) source between the two MRPCs for different distances between the two detectors. The time resolution of our detector for 511 keV photons at 18 kV operating volatges is $\sim$ 480 ps which includes electronic jitter of $\sim$ 120 ps. We did Geant4 simulation to estimate the efficiency of our detector for 511 keV gammas for different number of gaps in an MRPC. The efficency increases with increasing number of gas gaps. A PbO coat on the inner side of one of the outer electrodes which acts as a converter material can also improve the efficiency of our detector.

Chapter 10

Summary

10.1 Hadron Energy Estimation

In this work, we attempted to obtain an estimate of the energy of hadrons produced in a charged current interaction of an atmospheric muon neutrino/anti-neutrino in ICAL at INO. This was done by doing a full Geant4 simulation of atmospheric neutrino events generated by NUANCE. We have used the un-oscillated data simulated for a period of 100 years. We have established the following results:

- For $E_{had} < 5$ GeV, almost all of the hadron energy is carried by the baryons.
- The relation between the number of hits and the energy of hadrons is very different for the two cases when the hadrons are mesons and when the hadrons are baryons.
- When the events are classified into bins with different number of hadron hits, the resulting spectra are reasonably well described by Vavilov distributions.
- There is a good correlation between the number of hits and the mean value of E_{Ehad} of the Vavilov distributions.
- The width (σ) of the Vavilov distributions is related to the mean energy ($E_{\mathrm{had-mean}} = E$) through the expected relation $\sigma(E)/E = \sqrt{(a^2/E + b^2)}$.

It will be interesting to redo the analysis of the physics sensitivities of ICAL at INO using the hadron energy estimates and resolution functions presented here.

10.2 Tension between the data of T2K & NOνA

The two long baseline accelerator neutrino experiments, T2K and NOνA, have taken significant amount of data both in the neutrino channel as well as in the anti-neutrino channel. The disappearance data of T2K prefers $\sin^2\theta_{23}$ close to 0.5 whereas that of prefers $\sin^2\theta_{23}$ to be non-maximal. T2K has observed 89 ν_e appearance events but the number of $\bar{\nu}_e$ appearance events is not statistically significant. NOνA has observed 58 ν_e and 18 $\bar{\nu}_e$ appearance events and has established $\bar{\nu}_e$ appearance at 4 σ.

To understand the constraints imposed by the appearance data on the three unknown parameters of neutrino oscillations, we define a reference point: no matter effects, $\sin^2\theta_{23} = 0.5$ and $\delta_{\rm CP} = 0$. We consider the change induced in $P_{\mu e}$ and $P_{\bar{\mu}\bar{e}}$ by the inclusion of matter effect due to NH/IH, by the change of $\sin^2\theta_{23}$ to HO/LO and by the effect of CP-violation with $\delta_{\rm CP}$ in LHP/UHP. Both matter effects and non-zero $\delta_{\rm CP}$ induced opposite deviations in $P_{\mu e}$ and in $P_{\bar{\mu}\bar{e}}$. But the octant of θ_{23} changes both the probabilities the same way. The observed ν_e appearance events in T2K are about 50% more than what is expected for the reference point. Such a large excess is possible only if the change in $P_{\mu e}$ is positive due to the changes in all the three unknowns. That is if hierarchy is NH, θ_{23} is in HO and $\delta_{\rm CP} \approx -90^\circ$. The best-fit point of T2K finds the unknowns to be: hierarchy is NH, $\sin^2\theta 23 = 0.53$ and $\delta_{\rm CP} = -107^\circ$. The value of $\sin^2\theta 23$ is a compromise value of the best-fit values of the disappearance and the appearance data. T2K appearance data requires $\delta_{\rm CP}$ to be in the neighbourhood of -90° quite strongly. In the case of NOνA, the observed ν_e and $\bar{\nu}_e$ appearance events are in moderate excess relative to the reference point. Such an observation can be explained only if the changes induced by hierarchy and $\delta_{\rm CP}$ in $P_{\mu e}$ and $P_{\bar{\mu}\bar{e}}$ nearly cancel each

other and the increase is due to θ_{23} being in HO. This is why NOνA obtains two nearly degenerate solutions: hierarchy is NH, θ23 in HO and $\delta_{\rm CP} \approx 30^\circ$ and hierarchy is IH, θ_{23} in HO and $\delta_{\rm CP} \approx -90^\circ$. The large excess of ν_e appearance events in T2K rules out both these points at 95% C.L. On the other hand, the moderate excess of ν_e and $\bar{\nu}_e$ appearance events in NOνA disfavours enhancement of $P_{\mu e}$ due to both hierarchy and $\delta_{\rm CP}$.

The analysis of NOνA data picks $\sin^2\theta_{23} = 0.58$ as the best-fit value. In the combined analysis of the appearance and the disappearance data of the two experiments the best-fit value of $\sin^2\theta_{23}$ is pulled a little lower by the disappearance data of T2K. The best-fit value of $\delta_{\rm CP}$ for the NH solution is in the LHP at -130°. This value is the result of the large excess of ν_e appearance events seen by T2K which force $\delta_{\rm CP}$ to take a large value in LHP. Values of $\delta_{\rm CP}$ in UHP, for NH, are ruled out at 2 σ, even though the best-fit point of is in this region. This also is a result of the large excess of ν_e appearance events observed by T2K. Values of $\delta_{\rm CP}$ in UHP predict the number of ν_e appearance events for T2K to be close to or below that of the reference point. Such values are strongly disfavoured by T2K because the observed number of events is significantly larger. Even though this region is preferred by NOνA appearance data, the conflict between its predictions and T2K data is ruling it out at 2 σ in the combined fit.

Even though T2K barely allows an IH solution at 2 σ, the combined fit has a nearly degenerate IH solution which is the common IH solution of each experiment, with $\delta_{\rm CP} = -90^\circ$ and $\sin^2\theta_{23} = 0.56$. If the hierarchy is IH and $\delta_{\rm CP}$ is in UHP $P_{\mu e}$ is doubly suppressed by matter effects and by $\delta_{\rm CP}$. There is a corresponding double enhancement of $P_{\bar{\mu}\bar{e}}$. Such a feature is not seen by either experiment hence this possibility is ruled out at 3 σ.

10.3 Feasibility study of MRPC based PET device

We developed and characterized several six-gap glass MRPCs and extensively studied their performance over a long period of time. We obtained

a time resolution of $\sim$ 390 ps with a cosmic muon telescope with orthogonal pickup panels. We also recorded data in an oscilloscope from both ends of the strips with parallel pickup panels. The time resolution obtianed from this setup is $\sim$ 286 ps. We measured Time Of Flight (TOF) of 511 keV gammas produced by (^{22}Na) source between the two MRPCs for different distances between the two detectors. We studied the time resolution of our detector for 511 keV photons at different operating high volatges. The time resolution improves with incresing high voltage. We could go upto 18 kV and the time resolution at this high voltage is $\sim$ 480 ps which includes electronic jitter of $\sim$ 120 ps. The time walk correction using the analog information from the Anusparsh boards significantly improves the time resolution. We did Geant4 simulation to estimate the efficiency of our detector for 511 keV gammas for different number of gaps in an MRPC. The efficency increases with increasing number of gas gaps. A PbO coat on the inner side of one of the outer electrodes which acts as a converter material can also improve the efficiency of our detector.

Bibliography

[1] Shakeel Ahmed et al. "Physics Potential of the ICAL detector at the India-based Neutrino Observatory (INO)". In: *Pramana* 88.5 (2017), p. 79. DOI: 10.1007/s12043-017-1373-4. arXiv: 1505.07380 [physics.ins-det].

[2] Ali Ajmi et al. "Improving the hierarchy sensitivity of ICAL using neural network". In: *J. Phys. Conf. Ser.* 888.1 (2017), p. 012151. DOI: 10.1088/1742-6596/888/1/012151. arXiv: 1510.02350 [physics.ins-det].

[3] Anushree Ghosh, Tarak Thakore, and Sandhya Choubey. "Determining the Neutrino Mass Hierarchy with INO, T2K, NOvA and Reactor Experiments". In: *JHEP* 04 (2013), p. 009. DOI: 10.1007/JHEP04(2013)009. arXiv: 1212.1305 [hep-ph].

[4] Tarak Thakore et al. "The Reach of INO for Atmospheric Neutrino Oscillation Parameters". In: *JHEP* 05 (2013), p. 058. DOI: 10.1007/JHEP05(2013)058. arXiv: 1303.2534 [hep-ph].

[5] S. Seth et al. "Update of INO-ICAL reconstruction algorithm". In: *Journal of Instrumentation* 13 (2018), P09015.

[6] Lakshmi S. Mohan et al. "Simulation studies of hadron energy resolution as a function of iron plate thickness at INO-ICAL". In: *JINST* 9.09 (2014), T09003. DOI: 10.1088/1748-0221/9/09/T09003. arXiv: 1401.2779 [physics.ins-det].

[7] D. Casper. "The Nuance neutrino physics simulation, and the future". In: *Nucl. Phys. Proc. Suppl.* 112 (2002). [,161(2002)], pp. 161–170. DOI: 10.1016/S0920-5632(02)01756-5. arXiv: hep-ph/0208030 [hep-ph].

[8] P. V. Vavilov. "Ionization losses of high-energy heavy particles". In: *Sov. Phys. JETP* 5 (1957). [Zh. Eksp. Teor. Fiz.32,920(1957)], pp. 749–751.

[9] M M Devi et al. "Hadron energy response of the Iron Calorimeter detector at the India-based Neutrino Observatory". In: *Journal of Instrumentation* 8 (2013), P11003.

[10] Y. Itow et al. "The JHF-Kamioka neutrino project". In: *Neutrino oscillations and their origin. Proceedings, 3rd International Workshop, NOON 2001, Kashiwa, Tokyo, Japan, December 508, 2001*. 2001, pp. 239–248. arXiv: hep-ex/0106019 [hep-ex].

[11] T2K Collaboration (K. Abe et al.) "Precise Measurement of the Neutrino Mixing Parameter θ_{23} from Muon Neutrino Disappearance in an Off-Axis Beam". In: *Phys. Rev. Lett.* 112 (2014), p. 181801.

[12] K. Abe et al. "Observation of Electron Neutrino Appearance in a Muon Neutrino Beam". In: *Phys. Rev. Lett.* 112 (6 Feb. 2014), p. 061802. DOI: 10.1103/PhysRevLett.112.061802. URL: https://link.aps.org/doi/10.1103/PhysRevLett.112.061802.

[13] D. S. Ayres et al. "The NOvA Technical Design Report". In: (2007). DOI: 10.2172/935497.

[14] K. Abe et al. "Search for CP Violation in Neutrino and Antineutrino Oscillations by the T2K Experiment with 2.2×10^{21} Protons on Target". In: *Phys. Rev. Lett.* 121.17 (2018), p. 171802. DOI: 10.1103/PhysRevLett.121.171802. arXiv: 1807.07891 [hep-ex].

[15] M. A. Acero et al. "First Measurement of Neutrino Oscillation Parameters using Neutrinos and Antineutrinos by NOvA". In: (2019). arXiv: 1906.04907 [hep-ex].

[16] Patrick Huber, M. Lindner, and W. Winter. "Simulation of long-baseline neutrino oscillation experiments with GLoBES (General Long Baseline Experiment Simulator)". In: *Comput. Phys. Commun.* 167 (2005), p. 195. DOI: 10.1016/j.cpc.2005.01.003. arXiv: hep-ph/0407333 [hep-ph].

[17] Patrick Huber et al. "New features in the simulation of neutrino oscillation experiments with GLoBES 3.0: General Long Baseline Experiment Simulator". In: *Comput. Phys. Commun.* 177 (2007), pp. 432–438. DOI: 10.1016/j.cpc.2007.05.004. arXiv: hep-ph/0701187 [hep-ph].

[18] Moon Moon Devi et al. "Design, development and performance study of six-gap glass MRPC detectors". In: *Eur. Phys. J.* C76.12 (2016), p. 711. DOI: 10.1140/epjc/s10052-016-4570-2. arXiv: 1509.08586 [physics.ins-det].

[19] E. Fermi. "An attempt of a theory of beta radiation. 1." In: *Ric. Sci.* 4 (1933), pp. 491–495.

[20] E. Fermi. "Tentativo di una teoria dell'emissione dei raggi beta". In: *Z. Phys.* 88 (1934), pp. 161–177.

[21] E. Fermi. "Tentativo di una teoria dei raggi beta". In: *Il Nuovo Cimento (1924-1942)* 11 (2008), p. 1.

[22] P. J. Mohr and B. N. Taylor D. B. Newell. "CODATA Recommended Values of the Fundamental Physical Constants: 2014". In: *Rev. Mod. Phys.* 88 (2016), no. 3 035009.

[23] M. Tanabashi et al. "Review of Particle Physics". In: *Phys. Rev. D* 98.3 (2018), p. 030001. DOI: 10.1103/PhysRevD.98.030001.

[24] F. Reines and C. L. Cowan. "A Proposed Experiment to Detect the Free Neutrino". In: *Physical Review* 90 (1953), pp. 492–493.

[25] F. Reines, F. B. Harrison C. L. Cowan, and H. W. Kruse A. D. McGuire. "Detection of the free antineutrino". In: *Phys. Rev.* 117 (1960), pp. 159–173.

[26] F. Reines. "The neutrino: From poltergeist to particle". In: *Rev. Mod. Phys* 68 (1996), pp. 317–327.

[27] R. Davis. "Attempt to detect the antineutrinos from a nuclear reactor by the $Cl^{37}(\nu,e^{-})A^{37}$ reaction". In: *Phys. Rev.* 97 (1955), pp. 766–769.

[28] G. Danby et al. "Observation of High-Energy Neutrino Reactions and the Existence of Two Kinds of Neutrinos". In: *Phys. Rev. Lett.* 9 (1962), pp. 36–44.

[29] M. Schwartz. "Feasibility of Using High-Energy Neutrinos to Study the Weak Interactions". In: *Phys. Rev. Lett.* 4 (1960), pp. 306–307.

[30] H. L. Anderson et al. “Branching Ratio of the Electronic Mode of Positive Pion Decay”. In: *Phys. Rev.* 119 (1960), pp. 2050–2067.

[31] G. Danby et al. “Remarks Concerning the Recent High-Energy Neutrino Experiment”. In: *Phys. Rev. Lett.* 10 (1963), pp. 260–262.

[32] M. L. Perl et. al. “Evidence for Anomalous Lepton Production in e^+ - e^- Annihilation”. In: *Phys. Rev. Lett.* 35 (1975), pp. 1489–1492.

[33] Martin L. Perl. “Review of Heavy Lepton Production in e^+ e^- Annihilation”. In: *Reflections on experimental science* SLAC-PUB-2022 (1977), pp. 197–216.

[34] M L Perl. “The Tau Lepton”. In: *Annual Review of Nuclear and Particle Science* 30 (1980), pp. 299–335.

[35] S. Schael et. al. “Precision electroweak measurements on the Z resonance”. In: *Physics Reports* 427 (2006), pp. 257–454.

[36] K. Kodama et. al. **DONUT** Collaboration. “Observation of tau neutrino interactions”. In: *Physics Letters B* 504 (2001), pp. 218–224.

[37] R. Schwienhorst. “Appendix A”. In: *Ph.D. Thesis* University of Minnesota (2000).

[38] K. Kodama et. al. “Final tau-neutrino results from the DONuT experiment”. In: *Phys. Rev. D* 78 (2008), p. 052002.

[39] K. Kodama et. al. **DONUT** Collaboration. “First direct observation of the tau-neutrino”. In: *Europhys. News* 32 (2001), pp. 56–57.

[40] C. Weinheimer. “Direct determination of Neutrino Mass from Tritium Beta Spectrum”. In: (). arXiv: 0912.1619 [hep-ex].

[41] R. P. Feynman and M. Gell-Mann. “Theory of the fermi interaction”. In: *Phys. Rev.* 109 (1958), pp. 193–198.

[42] E. C. G. Sudarshan and R. E. Marshak. “Chirality invariance and the universal fermi interaction”. In: *Phys. Rev.* 109 (1958), pp. 1860–1862.

[43] A. Salam. “On parity conservation and neutrino mass”. In: *Il Nuovo Cimento* (1955-1965) 5 (1957), pp. 299–301.

[44] L. D. Landau. "On the conservation laws for weak interactions". In: *Nucl. Phys.* 3 (1957), pp. 127–131.

[45] J. J. Sakurai. "Mass reversal and weak interactions". In: *Il Nuovo Cimento* (1955-1965) 7 (1958), pp. 649–660.

[46] L. Grodzins M. Goldhaber and A. W. Sunyar. "Helicity of Neutrinos". In: *Phys. Rev.* 109 (1958), pp. 1015–1017.

[47] E Fermi. In: *Nuovo Cim.* 11 (1934), pp. 1–19.

[48] R G Hamish Robertson. "Direct determination of neutrino mass". In: *Journal of Physics: Conference Series* 173.1 (2009), p. 012016.

[49] V. M. Lobashev et. al. "Direct search for mass of neutrino and anomaly in the tritium beta spectrum". In: *Phys. Lett.* B460 (1999), pp. 227–235.

[50] C. Kraus et. al. "Final results from phase II of the Mainz neutrino mass search in tritium beta decay". In: *Eur. Phys. J.* C40 (2005), pp. 447–468.

[51] H. Daniel K. H. Hiddemann and O. Schwentker. "Limits on neutrino masses from the tritium beta spectrum". In: *Journal of Physics G: Nuclear and Particle Physics* 21 (1995), no. 5639.

[52] A. Oscipowicz et. al. **KATRIN** Collaboration. "KATRIN: A Next generation tritium beta decay experiment with sub-eV sensitivity for the electron neutrino mass." In: (). arXiv: hep-ex/0109033.

[53] K. Assamagan et al. "Upper limit of the muon-neutrino mass and charged-pion mass from momentum analysis of a surface muon beam". In: *Phys. Rev. D* 53 (1996), pp. 6065–6077.

[54] ALEPH Collaboration and R. Barate et al. "An upper limit on the τ neutrino mass from three- and five-prong tau decays". In: *The European Physical Journal C - Particles and Fields* 2 (1998), pp. 395–406.

[55] Carlo Giunti and Chung W. Kim. *Fundamentals of Neutrino Physics and Astrophysics*. 2007. ISBN: 9780198508717.

[56] J. A. Formaggio et al. "From eV to EeV: Neutrino Cross Sections Across Energy Scales". In: *Rev. Mod. Phys.* 84 (2012), pp. 1307–1341.

[57] Y. Fukuda et al. "Evidence for Oscillation of Atmospheric Neutrinos". In: *Phys. Rev. Lett.* 81 (1998), pp. 1562–1567.

[58] Q. R. Ahmad et al. "Direct Evidence for Neutrino Flavor Transformation from Neutral-Current Interactions in the Sudbury Neutrino Observatory". In: *Phys. Rev. Lett.* 89 (2002), p. 011301.

[59] B. T. Cleveland et al. "Measurement of the Solar Electron Neutrino Flux with the Homestake Chlorine Detector". In: *apj* 496 (1998), pp. 505–526.

[60] M. Altmann et al. "Complete results for five years of GNO solar neutrino observations". In: *Physics Letters B* 616 (2005), pp. 174–190.

[61] J. N. Abdurashitov and SAGE Collaboration. "Solar neutrino flux measurements by the Soviet-American gallium experiment (SAGE) for half the 22-year solar cycle". In: *Journal of Experimental and Theoretical Physics* 95 (2002), pp. 181–193.

[62] K2K Collaboration (M. H. Ahn et al.) "Measurement of neutrino oscillation by the K2K experiment". In: *Phys. Rev. D* 74 (2006), p. 072003.

[63] MINOS Collaboration (P. Adamson et al.) "Measurement of Neutrino and Antineutrino Oscillations Using Beam and Atmospheric Data in MINOS". In: *Phys. Rev. Lett.* 110 (2013), p. 251801.

[64] T. Araki et al. "Measurement of Neutrino Oscillation with KamLAND: Evidence of Spectral Distortion". In: *Phys. Rev. Lett.* 94 (2005), p. 081801.

[65] Daya Bay Collaboration (F. An et al.) "Spectral Measurement of Electron Antineutrino Oscillation Amplitude and Frequency at Daya Bay". In: *Phys. Rev. Lett.* 112 (2014), p. 061801.

[66] RENO Collaboration (S.-B. Kim et al.) "Observation of Reactor Electron Antineutrinos Disappearance in the RENO Experiment". In: *Phys. Rev. Lett.* 108 (2012), p. 191802.

[67] Double Chooz Collaboration (Y. Abe et al.) "First measurement of θ_{13} from delayed neutron capture on hydrogen in the Double Chooz experiment". In: *Physics Letters B* 723 (2013), pp. 66–70.

[68] M. Gell-Mann and A. Pais. "Behavior of neutral particles under charge conjugation". In: *Physical Review* 97 (1955), pp. 1387–1389.

[69] B. Pontecorvo. "Mesonium and anti-mesonium". In: *Sov. Phys. JETP* 6 (1957). [Zh. Eksp. Teor. Fiz.33,549(1957)], p. 429.

[70] B. Pontecorvo. "Inverse beta processes and nonconservation of lepton charge". In: *Sov. Phys. JETP* 7 (1958). [Zh. Eksp. Teor. Fiz.34,247(1957)], pp. 172–173.

[71] Ziro Maki, Masami Nakagawa, and Shoichi Sakata. "Remarks on the Unified Model of Elementary Particles". In: *Progress of Theoretical Physics* 28 (1962), pp. 870–880.

[72] Stephen F. King. "Neutrino mass and mixing in the seesaw playground". In: *Nuclear Physics B* 908 (2016), pp. 456–466.

[73] Shalom Eliezer and Arthur R. Swift. "Experimental Consequences of electron Neutrino-Muon-neutrino Mixing in Neutrino Beams". In: *Nucl. Phys.* B105 (1976), pp. 45–51.

[74] Harald Fritzsch and Peter Minkowski. "Vector-Like Weak Currents, Massive Neutrinos, and Neutrino Beam Oscillations". In: *Phys. Lett.* 62B (1976), pp. 72–76.

[75] Samoil M. Bilenky and B. Pontecorvo. "The Quark-Lepton Analogy and the Muonic Charge". In: *Yad. Fiz.* 24 (1976). [Sov. J. Nucl. Phys.24,316(1976)], pp. 603–608.

[76] Samoil M. Bilenky and B. Pontecorvo. "Again on Neutrino Oscillations". In: *Lett. Nuovo Cim.* 17 (1976), p. 569.

[77] Samoil M. Bilenky and B. Pontecorvo. "Lepton Mixing and Neutrino Oscillations". In: *Phys. Rept.* 41 (1978), pp. 225–261.

[78] X. Qian and P. Vogel. "Neutrino mass hierarchy". In: *Progress in Particle and Nuclear Physics* 83 (2015), pp. 1–30.

[79] M. Apollonio et al. "Limits on neutrino oscillations from the CHOOZ experiment". In: *Phys. Lett.* B466 (1999), pp. 415–430. DOI: 10.1016/S0370-2693(99)01072-2. arXiv: hep-ex/9907037 [hep-ex].

[80] P. Adamson et al. "Measurement of the Neutrino Mass Splitting and Flavor Mixing by MINOS". In: *Phys. Rev. Lett.* 106 (2011), p. 181801. DOI: 10.1103/PhysRevLett.106.181801. arXiv: 1103.0340 [hep-ex].

[81] P. Adamson. "Measurement of Neutrino Oscillations with the MINOS Detectors in the NuMI Beam". In: *Phys. Rev. Lett.* 101 (2008), p. 131802.

[82] David M. Webber. "An Improved Measurement of Electron Antineutrino Disappearance at Daya Bay". In: *Nuclear Physics B - Proceedings Supplements* 233 (2012), pp. 96–101.

[83] J. K. Ahn et al. "Observation of Reactor Electron Antineutrino Disappearance in the RENO Experiment". In: *Phys. Rev. Lett.* 108 (2012), p. 191802. DOI: 10.1103/PhysRevLett.108.191802. arXiv: 1204.0626 [hep-ex].

[84] Y. Abe et al. "First Measurement of θ_{13} from Delayed Neutron Capture on Hydrogen in the Double Chooz Experiment". In: *Phys. Lett.* B723 (2013), pp. 66–70. DOI: 10.1016/j.physletb.2013.04.050. arXiv: 1301.2948 [hep-ex].

[85] Y. Abe et al. "Improved measurements of the neutrino mixing angle θ_{13} with the Double Chooz detector". In: *JHEP* 10 (2014). [Erratum: JHEP02,074(2015)], p. 086. DOI: 10.1007/JHEP02(2015)074, 10.1007/JHEP10(2014)086. arXiv: 1406.7763 [hep-ex].

[86] Yu-Feng Li et al. "Unambiguous determination of the neutrino mass hierarchy using reactor neutrinos". In: *Phys. Rev. D* 88 (1 July 2013), p. 013008. DOI: 10.1103/PhysRevD.88.013008. URL: https://link.aps.org/doi/10.1103/PhysRevD.88.013008.

[87] L. Wolfenstein. "Neutrino oscillations in matter". In: *Phys. Rev. D* 17 (9 May 1978), pp. 2369–2374. DOI: 10.1103/PhysRevD.17.2369. URL: https://link.aps.org/doi/10.1103/PhysRevD.17.2369.

[88] S. P. Mikheyev and A. Yu. Smirnov. "Resonance Amplification of Oscillations in Matter and Spectroscopy of Solar Neutrinos". In: *Sov. J. Nucl. Phys.* 42 (1985). [,305(1986)], pp. 913–917.

[89] S. P. Mikheev and A. Yu. Smirnov. "Resonant amplification of neutrino oscillations in matter and solar neutrino spectroscopy". In: *Nuovo Cim.* C9 (1986), pp. 17–26. DOI: 10.1007/BF02508049.

[90] H. A. Bethe. "Possible Explanation of the Solar-Neutrino Puzzle". In: *Phys. Rev. Lett.* 56 (12 Mar. 1986), pp. 1305–1308. DOI: 10.1103/PhysRevLett.56.1305. URL: https://link.aps.org/doi/10.1103/PhysRevLett.56.1305.

[91] V. Barger et al. "Matter effects on three-neutrino oscillations". In: *Phys. Rev. D* 22 (11 Dec. 1980), pp. 2718–2726. DOI: 10.1103/PhysRevD.22.2718. URL: https://link.aps.org/doi/10.1103/PhysRevD.22.2718.

[92] Ara Ioannisian and Stefan Pokorski. "Three neutrino oscillations in matter". In: *Physics Letters B* 782 (2018), pp. 641–645. ISSN: 0370-2693. DOI: https://doi.org/10.1016/j.physletb.2018.06.001. URL: http://www.sciencedirect.com/science/article/pii/S0370269318304428.

[93] A. Cervera et al. "Golden measurements at a neutrino factory". In: *Nuclear Physics B* 579.1 (2000), pp. 17–55. ISSN: 0550-3213. DOI: https://doi.org/10.1016/S0550-3213(00)00221-2. URL: http://www.sciencedirect.com/science/article/pii/S0550321300002212.

[94] V. Barger, D. Marfatia, and K. Whisnant. "Breaking eightfold degeneracies in neutrino CP violation, mixing, and mass hierarchy". In: *Phys. Rev. D* 65 (7 Mar. 2002), p. 073023. DOI: 10.1103/PhysRevD.65.073023. URL: https://link.aps.org/doi/10.1103/PhysRevD.65.073023.

[95] Takaaki KAJITA. "Atmospheric neutrinos and discovery of neutrino oscillations". In: *Proceedings of the Japan Academy, Series B* 86.4 (2010), pp. 303–321. DOI: 10.2183/pjab.86.303.

[96] M. Honda et al. "Atmospheric neutrino flux calculation using the NRLMSISE-00 atmospheric model". In: *Phys. Rev.* D92.2 (2015), p. 023004. DOI: 10.1103/PhysRevD.92.023004. arXiv: 1502.03916 [astro-ph.HE].

[97] G. Battistoni et al. "The FLUKA atmospheric neutrino flux calculation". In: *Astropart. Phys.* 19 (2003). [Erratum: Astropart. Phys.19,291(2003)], pp. 269–

290. DOI: 10.1016/S0927-6505(02)00246-3. arXiv: hep-ph/0207035 [hep-ph]. URL: http://www.mi.infn.it/~battist/neutrino.html.

[98] Morihiro Honda et al. "A New calculation of the atmospheric neutrino flux in a 3-dimensional scheme". In: *Phys. Rev.* D70 (2004), p. 043008. DOI: 10.1103/PhysRevD.70.043008. arXiv: astro-ph/0404457 [astro-ph]. URL: http://www.icrr.u-tokyo.ac.jp/%E2%88%BCmhonda/.

[99] G. D. Barr et al. "A Three - dimensional calculation of atmospheric neutrinos". In: *Phys. Rev.* D70 (2004), p. 023006. DOI: 10.1103/PhysRevD.70.023006. arXiv: astro-ph/0403630 [astro-ph]. URL: http://www-pnp.physics.ox.ac.uk/%E2%88%BCbarr/fluxfiles/.

[100] Jurgen Wentz et al. "Simulation of atmospheric muon and neutrino fluxes with CORSIKA". In: *Phys. Rev.* D67 (2003), p. 073020. DOI: 10.1103/PhysRevD.67.073020. arXiv: hep-ph/0301199 [hep-ph].

[101] Yong Liu, L. Derome, and M. Buenerd. "Atmospheric muon and neutrino flux from 3-dimensional simulation". In: *Phys. Rev.* D67 (2003), p. 073022. DOI: 10.1103/PhysRevD.67.073022. arXiv: astro-ph/0211632 [astro-ph].

[102] Jean Favier, R. Kossakowski, and J. P Vialle. "A 3-D simulation of the atmospheric neutrinos". In: *Phys. Rev.* D68 (2003), p. 093006. DOI: 10.1103/PhysRevD.68.093006. arXiv: astro-ph/0305460 [astro-ph].

[103] T. K. Gaisser and M. Honda. "Flux of atmospheric neutrinos". In: *Ann. Rev. Nucl. Part. Sci.* 52 (2002), pp. 153–199. DOI: 10.1146/annurev.nucl.52.050102.090645. arXiv: hep-ph/0203272 [hep-ph].

[104] G. D. Barr et al. "Uncertainties in Atmospheric Neutrino Fluxes". In: *Phys. Rev.* D74 (2006), p. 094009. DOI: 10.1103/PhysRevD.74.094009. arXiv: astro-ph/0611266 [astro-ph].

[105] C. V. Achar et al. "Detection of muons produced by cosmic ray neutrinos deep underground". In: *Phys. Lett.* 18 (1965), pp. 196–199. DOI: 10.1016/0031-9163(65)90712-2.

[106] F. Reines et al. "Evidence for High-Energy Cosmic-Ray Neutrino Interactions". In: *Phys. Rev. Lett.* 15 (9 Aug. 1965), pp. 429–433. DOI: 10.1103/PhysRevLett.15.429. URL: https://link.aps.org/doi/10.1103/PhysRevLett.15.429.

[107] D. Casper et al. "Measurement of atmospheric neutrino composition with IMB-3". In: *Phys. Rev. Lett.* 66 (1991), pp. 2561–2564. DOI: 10.1103/PhysRevLett.66.2561.

[108] K. S. Hirata et al. "Experimental Study of the Atmospheric Neutrino Flux". In: *Phys. Lett.* B205 (1988). [,447(1988)], p. 416. DOI: 10.1016/0370-2693(88)91690-5.

[109] Y. Fukuda et al. "Evidence for oscillation of atmospheric neutrinos". In: *Phys. Rev. Lett.* 81 (1998), pp. 1562–1567. DOI: 10.1103/PhysRevLett.81.1562. arXiv: hep-ex/9807003 [hep-ex].

[110] Takaaki Kajita. "Atmospheric neutrinos". In: *New Journal of Physics* 6 (Dec. 2004), pp. 194–194. DOI: 10.1088/1367-2630/6/1/194. URL: https://doi.org/10.1088%2F1367-2630%2F6%2F1%2F194.

[111] D. H. Perkins. "PROTON DECAY EXPERIMENTS". In: *Ann. Rev. Nucl. Part. Sci.* 34 (1984), pp. 1–52. DOI: 10.1146/annurev.ns.34.120184.000245.

[112] R. Becker-Szendy et al. "IMB-3: a large water Cherenkov detector for nucleon decay and neutrino interactions". In: *Nuclear Instruments and Methods in Physics Research Section A: Accelerators, Spectrometers, Detectors and Associated Equipment* 324.1 (1993), pp. 363–382. ISSN: 0168-9002. DOI: https://doi.org/10.1016/0168-9002(93)90998-W. URL: http://www.sciencedirect.com/science/article/pii/016890029390998W.

[113] W. Gajewski. "A search for oscillation of atmospheric neutrinos with the IMB detector". In: *Nucl. Phys. Proc. Suppl.* 28A (1992). [,161(1992)], pp. 161–164. DOI: 10.1016/0920-5632(92)90164-N.

[114] M. Fukugita and A. Suzuki, eds. *Physics and astrophysics of neutrinos*. 1994.

[115] Y. Fukuda et al. "Atmospheric muon-neutrino / electron-neutrino ratio in the multiGeV energy range". In: *Phys. Lett.* B335 (1994), pp. 237–245. DOI: 10.1016/0370-2693(94)91420-6.

[116] Y. Fukuda et al. "The Super-Kamiokande detector". In: *Nucl. Instrum. Meth.* A501 (2003), pp. 418–462. DOI: 10.1016/S0168-9002(03)00425-X.

[117] Y. Fukuda et al. "Measurement of a small atmospheric muon-neutrino / electron-neutrino ratio". In: *Phys. Lett.* B433 (1998), pp. 9–18. DOI: 10.1016/S0370-2693(98)00476-6. arXiv: hep-ex/9803006 [hep-ex].

[118] Y. Fukuda et al. "Evidence for oscillation of atmospheric neutrinos". In: *Phys. Rev. Lett.* 81 (1998), pp. 1562–1567. DOI: 10.1103/PhysRevLett.81.1562. arXiv: hep-ex/9807003 [hep-ex].

[119] K. Abe et al. "Atmospheric neutrino oscillation analysis with external constraints in Super-Kamiokande I-IV". In: *Phys. Rev.* D97.7 (2018), p. 072001. DOI: 10.1103/PhysRevD.97.072001. arXiv: 1710.09126 [hep-ex].

[120] K. Abe et al. "Hyper-Kamiokande Design Report". In: (2018). arXiv: 1805.04163 [physics.ins-det].

[121] Christophe Bronner. "Physics potential of Hyper-Kamiokande for neutrino oscillation measurements". In: *PoS* NuFact2017 (2018), p. 053. DOI: 10.22323/1.295.0053.

[122] João Pedro Athayde MarconExpected sensitivity to NMH after 3 years of data taking as reported in KM3Net LoIdes de André. "PINGU". In: *PoS* NUFACT2014 (2015), p. 033. DOI: 10.22323/1.226.0033.

[123] Sirin Odrowski. "Atmospheric neutrino oscillations with PINGU". In: *J. Phys. Conf. Ser.* 598.1 (2015), p. 012026. DOI: 10.1088/1742-6596/598/1/012026.

[124] Liam Quinn. "Status and Perspectives of KM3NeT/ORCA". In: *PoS* EPS-HEP2017 (2017), p. 130. DOI: 10.22323/1.314.0130.

[125] M. Sajjad Athar et al. "India-based Neutrino Observatory: Project Report. Volume I." In: 2006. URL: http://www.imsc.res.in/~ino/OpenReports/INOReport.pdf.

[126] S. P. Behera et al. "Simulation Studies for Electromagnetic Design of INO ICAL Magnet and Its Response to Muons". In: *IEEE Transactions on Magnetics* 51.2 (Feb. 2015), pp. 1–9. ISSN: 0018-9464. DOI: 10.1109/TMAG.2014.2344624.

[127] S. D. Kalmani et al. "Design validation and performance of closed loop gas recirculation system". In: *JINST* 11.11 (2016), p. C11026. DOI: 10.1088/1748-0221/11/11/C11026.

[128] S. D. Kalmani et al. "Some studies using capillary for flow control in a closed loop gas recirculation system". In: *Springer Proc. Phys.* 203 (2018), pp. 913–915. DOI: 10.1007/978-3-319-73171-1_223. arXiv: 1702.01654 [physics.ins-det].

[129] R. Santonico and R. Cardarelli. "Development of Resistive Plate Counters". In: *Nucl. Instrum. Meth.* 187 (1981), pp. 377–380. DOI: 10.1016/0029-554X(81)90363-3.

[130] R. Santonico et al. "Progress in Resistive Plate Counters". In: *Nucl. Instrum. Meth.* A263 (1988), pp. 20–25. DOI: 10.1016/0168-9002(88)91011-X.

[131] W. R. Leo. *Techniques for Nuclear and Particle Physics Experiments: A How to Approach*. 1987. ISBN: 9783540572800.

[132] Hugh Gallagher, Yoshinari Hayato, and Jan Sobczyk. "Discussion: Confronting theory and experiment". In: *AIP Conference Proceedings* 1663.1 (2015), p. 110004. DOI: 10.1063/1.4919506. URL: https://aip.scitation.org/doi/abs/10.1063/1.4919506.

[133] Askhat Gazizov and Marek P. Kowalski. "ANIS: High energy neutrino generator for neutrino telescopes". In: *Comput. Phys. Commun.* 172 (2005), pp. 203–213. DOI: 10.1016/j.cpc.2005.03.113. arXiv: astro-ph/0406439 [astro-ph].

[134] C. Andreopoulos et al. "The GENIE Neutrino Monte Carlo Generator". In: *Nucl. Instrum. Meth.* A614 (2010), pp. 87–104. DOI: 10.1016/j.nima.2009.12.009. arXiv: 0905.2517 [hep-ph].

[135] O. Buss et al. "Transport-theoretical Description of Nuclear Reactions". In: *Phys. Rept.* 512 (2012), pp. 1–124. DOI: 10.1016/j.physrep.2011.12.001. arXiv: 1106.1344 [hep-ph].

[136] L. AlvarezRuso et al. "GiBUU and NeutrinoNucleus scattering". In: *AIP Conference Proceedings* 1382.1 (2011), pp. 170–172. DOI: 10.1063/1.3644303. URL: https://aip.scitation.org/doi/abs/10.1063/1.3644303.

[137] D. Autiero. "The OPERA event generator and the data tuning of nuclear re-interactions". In: *Nucl. Phys. Proc. Suppl.* 139 (2005). [,253(2005)], pp. 253–259. DOI: 10.1016/j.nuclphysbps.2004.11.168.

[138] Y. Hayato. "NEUT". In: *Nucl. Phys. Proc. Suppl.* 112 (2002). [,171(2002)], pp. 171–176. DOI: 10.1016/S0920-5632(02)01759-0.

[139] G. Battistoni et al. "The FLUKA atmospheric neutrino flux calculation". In: *Astropart. Phys.* 19 (2003). [Erratum: Astropart. Phys.19,291(2003)], pp. 269–290. DOI: 10.1016/S0927-6505(02)00246-3. arXiv: hep-ph/0207035 [hep-ph].

[140] Arthur Ankowski and Jan Sobczyk. "Neutrino interactions: From theory to Monte Carlo simulations. Proceedings, 45th Karpacz Winter School in Theoretical Physics, Ladek-Zdroj, Poland, February 2-11, 2009". In: (2009). [Acta Phys. Polon.B40,pp.2389(2009)], pp. 2389–2672.

[141] Cezary Juszczak, Jaroslaw A. Nowak, and Jan T. Sobczyk. "Simulations from a new neutrino event generator". In: *Nucl. Phys. Proc. Suppl.* 159 (2006). [,211(2005)], pp. 211–216. DOI: 10.1016/j.nuclphysbps.2006.08.069. arXiv: hep-ph/0512365 [hep-ph].

[142] *Fundamental Physics at the Intensity Frontier*. 2012. DOI: 10.2172/1042577. arXiv: 1205.2671 [hep-ex]. URL: http://lss.fnal.gov/archive/preprint/fermilab-conf-12-879-ppd.shtml.

[143] F. Cavanna and O. Palamara. "GENEVE: a Montecarlo generator for neutrino interactions in the intermediate energy range". In: *Nuclear Physics B - Proceedings Supplements* 112.1 (2002), pp. 183–187. ISSN: 0920-5632. DOI: https://doi.org/10.1016/S0920-5632(02)01767-X. URL: http://www.sciencedirect.com/science/article/pii/S092056320201767X.

[144] H. Gallagher. "The NEUGEN neutrino event generator". In: *Nuclear Physics B - Proceedings Supplements* 112.1 (2002), pp. 188–194. ISSN: 0920-5632. DOI: https://doi.org/10.1016/S0920-5632(02)01775-9. URL: http://www.sciencedirect.com/science/article/pii/S0920563202017759.

[145] Jarosław A. Nowak, Cezary Juszczak, and Jan T. Sobczyk. "Comparison of predictions for nuclear effects in the Marteau model with the NUX+FLUKA

scheme". In: *Nuclear Physics B - Proceedings Supplements* 139 (2005). Proceedings of the Third International Workshop on Neutrino-Nucleus Interactions in the Few-GeV Region, pp. 272–277. ISSN: 0920-5632. DOI: https://doi.org/10.1016/j.nuclphysbps.2004.11.215. URL: http://www.sciencedirect.com/science/article/pii/S0920563204007844.

[146] S. Agostinelli et al. "GEANT4: A Simulation toolkit". In: *Nucl. Instrum. Meth.* A506 (2003), pp. 250–303. DOI: 10.1016/S0168-9002(03)01368-8.

[147] https://www.mentor.com/products/mechanical/magnet/magnet/.

[148] Satyanarayana Bheesette. "Design and Characterisation Studies of Resistive Plate Chambers". PhD thesis. Indian Inst. Tech., Mumbai, 2009. URL: http://www.ino.tifr.res.in/ino/theses/satya_thesis.pdf.

[149] John Stuart Marshall. "A study of muon neutrino disappearance with the MINOS detectors and the NuMI neutrino beam". PhD thesis. Cambridge U., 2008. DOI: 10.2172/935002. URL: http://lss.fnal.gov/cgi-bin/find_paper.pl?thesis-2008-20.

[150] E. J. Wolin and L. L. Ho. "Covariance matrices for track fitting with the Kalman filter". In: *Nucl. Instrum. Meth.* A329 (1993), pp. 493–500. DOI: 10.1016/0168-9002(93)91285-U.

[151] H. Bethe and J. Ashkin. In: *Experimental Nuclear Physics, Ed. E. Segré,J. Wiley, New York* (1953), p. 253.

[152] Kolahal Bhattacharya et al. "Error propagation of the track model and track fitting strategy for the Iron CALorimeter detector in India-based neutrino observatory". In: *Comput. Phys. Commun.* 185 (2014), pp. 3259–3268. DOI: 10.1016/j.cpc.2014.09.003. arXiv: 1510.02792 [physics.ins-det].

[153] Animesh Chatterjee et al. "A Simulations Study of the Muon Response of the Iron Calorimeter Detector at the India-based Neutrino Observatory". In: *JINST* 9 (2014), P07001. DOI: 10.1088/1748-0221/9/07/P07001. arXiv: 1405.7243 [physics.ins-det].

[154] M M Devi et al. "Enhancing sensitivity to neutrino parameters at INO combining muon and hadron information". In: *Journal of High Energy Physics* 2014 (2014), p. 189.

[155] Tarak Thakore. "Physics Potential of the India-based Neutrino Observatory (INO)". PhD thesis. TIFR, Mumbai, DHEP, 2014. URL: http://www.ino.tifr.res.in/ino/theses/Thesis_Tarak01.pdf.

[156] D. G. Michael et al. "Observation of muon neutrino disappearance with the MINOS detectors and the NuMI neutrino beam". In: *Phys. Rev. Lett.* 97 (2006), p. 191801. DOI: 10.1103/PhysRevLett.97.191801. arXiv: hep-ex/0607088 [hep-ex].

[157] P. Adamson et al. "Improved search for muon-neutrino to electron-neutrino oscillations in MINOS". In: *Phys. Rev. Lett.* 107 (2011), p. 181802. DOI: 10.1103/PhysRevLett.107.181802. arXiv: 1108.0015 [hep-ex].

[158] Suman Bharti et al. "Understanding the degeneracies in NOνA data". In: *JHEP* 09 (2018), p. 036. DOI: 10.1007/JHEP09(2018)036. arXiv: 1805.10182 [hep-ph].

[159] E Cerron Zeballos et al. "A new type of resistive plate chamber: The multigap RPC". In: *Nuclear Instruments and Methods in Physics Research* 374 (1996), pp. 132–135. DOI: https://doi.org/10.1016/0168-9002(96)00158-1.

[160] P. Fonte, A. Smirnitsky, and M. C. S. Williams. "A New high resolution TOF technology". In: *Nucl. Instrum. Meth.* A443 (2000), pp. 201–204. DOI: 10.1016/S0168-9002(99)01008-6.

[161] M. C. S. Williams. "The Multigap RPC: The Time-of-flight detector for the ALICE experiment". In: *Nucl. Instrum. Meth.* A478 (2002), pp. 183–186. DOI: 10.1016/S0168-9002(01)01753-3.

[162] K. Doroud et al. "MRPC-PET: A new technique for high precision time and position measurements". In: *Nuclear Instruments and Methods in Physics Research Section A: Accelerators, Spectrometers, Detectors and Associated Equipment* 660.1 (2011), pp. 73–76. ISSN: 0168-9002. DOI: https://doi.org/10.1016/

j.nima.2011.09.008. URL: http://www.sciencedirect.com/science/article/pii/S0168900211017530.

[163] B. Sharifi and S. Saramad. "Design and experimental test of a novel double stack MRPC detector for medical imaging applications". In: *Nucl. Instrum. Meth.* A908 (2018), pp. 35–42. DOI: 10.1016/j.nima.2018.08.010.

[164] G. Belli et al. "Multigap RPC time resolution to 511 keV annihilation photons". In: *Nucl. Instrum. Meth.* A781 (2015), pp. 26–33. DOI: 10.1016/j.nima.2015.01.082. arXiv: 1406.2119 [physics.ins-det].

[165] L. Shi et al. "A high time and spatial resolution MRPC designed for muon tomography". In: *Journal of Instrumentation* 9.12 (Dec. 2014), pp. C12038–C12038. DOI: 10.1088/1748-0221/9/12/c12038. URL: https://doi.org/10.1088%2F1748-0221%2F9%2F12%2Fc12038.

[166] V. B. Chandratre et al. "ANUSPARSH-II frontend ASIC for avalanche mode of RPC detector using regulated cascode trans-impedance amplifier". In: *DAE Symp. Nucl. Phys.* 60 (2015), pp. 928–929.

[167] U. Amaldi et al. "Development of TOF-PET detectors based on the Multi-Gap Resistive Plate Chambers". In: *Nuclear Instruments and Methods in Physics Research Section A: Accelerators, Spectrometers, Detectors and Associated Equipment* 778 (2015), pp. 85–91. ISSN: 0168-9002. DOI: https://doi.org/10.1016/j.nima.2015.01.018. URL: http://www.sciencedirect.com/science/article/pii/S0168900215000443.

[168] P. Moskal et al. "Novel detector systems for the Positron Emission Tomography". In: *Bio-Algorithms Med-Syst.* 7.2 (2011), p. 73. arXiv: 1305.5187 [physics.med-ph].